

Mathematical Aspects of Cell-Based and Agent-Based Modelling for Skin Contraction after Deep Tissue Injury

Peng, Q.

DOI

[10.4233/uuid:8c624c7a-15c4-41a1-8cc6-7eb8a9b36a86](https://doi.org/10.4233/uuid:8c624c7a-15c4-41a1-8cc6-7eb8a9b36a86)

Publication date

2021

Document Version

Final published version

Citation (APA)

Peng, Q. (2021). *Mathematical Aspects of Cell-Based and Agent-Based Modelling for Skin Contraction after Deep Tissue Injury*. <https://doi.org/10.4233/uuid:8c624c7a-15c4-41a1-8cc6-7eb8a9b36a86>

Important note

To cite this publication, please use the final published version (if applicable). Please check the document version above.

Copyright

Other than for strictly personal use, it is not permitted to download, forward or distribute the text or part of it, without the consent of the author(s) and/or copyright holder(s), unless the work is under an open content license such as Creative Commons.

Takedown policy

Please contact us and provide details if you believe this document breaches copyrights. We will remove access to the work immediately and investigate your claim.

**MATHEMATICAL ASPECTS OF CELL-BASED AND
AGENT-BASED MODELLING FOR SKIN
CONTRACTION AFTER DEEP TISSUE INJURY**

MATHEMATICAL ASPECTS OF CELL-BASED AND AGENT-BASED MODELLING FOR SKIN CONTRACTION AFTER DEEP TISSUE INJURY

Dissertation

for the purpose of obtaining the degree of doctor
at Delft University of Technology
by the authority of the Rector Magnificus Prof. dr. ir. T. H. J. van der Hagen;
Chair of the Board for Doctorates
to be defended publicly on
Friday 8 October 2021 at 10:00 o'clock

by

Qiyao PENG

Master of Science in Statistics,
Lancaster University, United Kingdom,
born in Nanchang Jiangxi, China.

This dissertation has been approved by the promotor:

Promotor: Prof. dr. ir. C. Vuik

Promotor: Prof. dr. ir. F. J. Vermolen

Composition of the doctoral committee:

Rector Magnificus,	chairperson
Prof. dr. ir. C. Vuik	Delft University of Technology, promotor
Prof. dr. ir. F. J. Vermolen	Hasselt University, promotor

Independent Members:

Prof. dr. A. A. Zadpoor	Delft University of Technology, Leiden University Medical Center
Prof. dr. R. M. H. Merks	Leiden University
Prof. dr. A. Gefen	Tel Aviv University
Dr. N. V. Budko	Delft University of Technology
Prof. dr. ir. G. Jongbloed	Delft University of Technology, reserve member

Other Members:

Dr. D. Weihs	Technion - Israel Institute of Technology
--------------	---



This research was supported by the China Scholarship Council (CSC).

Keywords: Skin Contractions, Agent-Based Model, Cellular Traction Forces, Morphoelasticity, Dirac Delta Distributions, Cell Geometry

Printed by: proefschriftMaken || proefschriftmaken.nl

Front & Back: The cover is designed by Lingyun Li and Susana Vieira based on the topic of the thesis.

Copyright © 2021 by Q. PENG

ISBN 978-94-6384-253-2

An electronic version of this dissertation is available at
<http://repository.tudelft.nl/>.

*To my beloved family,
without whom I would never be the person I am today.*

CONTENTS

Summary	xi
Samenvatting	xiii
1 Introduction	1
1.1 Biological Background	1
1.1.1 Skin and Wound Healing	1
1.1.2 Cell geometry	4
1.2 Mathematical Modelling in Biology	5
1.3 Motivation and Objectives	6
1.4 Outline	7
I Agent-Based Modelling of Skin Contraction	9
2 Agent-Based Modelling and Parameter Sensitivity Analysis with a Finite-Element Method for Skin Contraction	11
2.1 Introduction	12
2.2 Mathematical Models	12
2.2.1 Biological Assumptions	12
2.2.2 Semi-Stochastic Cell-Based Model	16
2.2.3 Initial Settings of the Model	25
2.3 Numerical Results.	25
2.3.1 Displacements of Cells.	26
2.3.2 Concentration of Signalling Molecules and Density of Tissue Bundles	26
2.3.3 Strain Energy in the Wound	31
2.3.4 Wound Area Reduction	31
2.3.5 Sensitivity Test of the Model	35
2.4 Monte Carlo Simulations	41
2.5 Discussions and Conclusion	44
3 Comparison between a Phenomenological Approach and a Morphoelasticity Approach regarding the Displacement of Extracellular Matrix	49
3.1 Introduction	49
3.2 Mathematical Models	50
3.2.1 Phenomenological Approach	50
3.2.2 Morphoelasticity Approach	51

3.3	Sensitivity Test of Morphoelasticity Approach.	52
3.4	Comparison between the Phenomenological Approach and the Morphoelasticity Approach.	54
3.5	Monte Carlo Simulations with Morphoelasticity Approach	57
3.6	Conclusions.	61
II	Point Forces and Their Alternative Approaches in Cell-Based Models for Skin Contraction	63
4	Point Forces and Their Alternatives in Cell-Based Models for Skin Contraction in One Dimension	65
4.1	Introduction	65
4.2	Mathematical Model	66
4.3	Numerical Results.	71
4.4	Conclusion	74
5	Point Forces in Elasticity Equation and Their Alternatives in Multiple Dimensions	75
5.1	Introduction	76
5.2	Elasticity Equation with Point Sources in Two Dimensions	76
5.2.1	The Mixed Approach.	78
5.2.2	The 'Hole' Approach	79
5.2.3	The Smoothed Particle Approach	79
5.3	Elasticity Equation with Point Sources in Multiple Dimensions	86
5.3.1	The 'Hole' Approach	93
5.3.2	The Smoothed Particle Approach	96
5.4	Numerical Results.	103
5.5	Conclusion	106
6	Upscaling between an Agent-Based Model (Smoothed Particle Approach) and a Continuum-Based Model for Skin Contractions	109
6.1	Introduction	109
6.2	Mathematical Models in One Dimension	110
6.2.1	Smoothed Particle Approach.	110
6.2.2	Cell Density Approach	111
6.2.3	Consistency between Two Models	111
6.3	Mathematical Models in Two Dimensions	116
6.3.1	Smoothed Particle Approach and Cell Density Approach	116
6.3.2	Consistency between Two Approaches in Finite-Element Method	117
6.4	Results	118
6.4.1	One-Dimensional Results	118
6.4.2	Two-Dimensional Results	125
6.5	Conclusions.	126

III	Modelling the Evolution of Cell Geometry during Cell Migration	129
7	A Formalism for Modelling Traction forces and Cell Shape Evolution during Cell Migration in Various Biomedical Processes	131
7.1	Introduction	131
7.2	Mathematical Modelling	132
7.2.1	Concentration of Generic Signal	133
7.2.2	Passive Convection of Substrate	134
7.2.3	Cell Deformation	137
7.3	Applications and Numerical Results	140
7.3.1	Finite-Element Methods	141
7.3.2	Cells Moving towards the Point Source	141
7.3.3	Differentiation of Cells	142
7.3.4	Repulsion between Two Colliding Cells	146
7.3.5	Cell Moving through a Microtubule	146
7.4	Conclusions.	154
8	Conclusions and Discussions	155
8.1	General Conclusions	155
8.2	Conclusions on Part I	155
8.3	Conclusions on Part II.	156
8.4	Conclusions on Part III	157
8.5	Discussions and Outlook	157
	References	161
	Acknowledgements	169
	Curriculum Vitæ	175
	Publications and Scientific Activities	177

SUMMARY

Burns and other skin traumas occur at various intensities regarding the depth and area of the skin, as well as the involvement of the different skin layers. Worldwide, an estimated six million patients need hospitalisation for burns annually. Furthermore, most severe burn injuries will develop morbidity and unaesthetic scars like contractures and hypertrophic scars, which cause a significantly negative impact on the patients' life. Contractures, which usually concur with disabilities and disfunctionings of the joints, are recognized as excessive contractions. Contractions are caused by the pulling forces exerted on the extracellular matrix (ECM) by the (myo)fibroblasts in the proliferation stage.

To have a better understanding and insight into the occurrences of contractions and other biological phenomena, mathematical modelling is a useful tool for visualization and prediction. Using mathematical models, it is possible to simulate important biological mechanisms and track the cellular activities and positions of each individual cell.

The research described in the thesis is divided into three parts: (1) agent-based modelling for skin contractions after burn injuries; (2) the numerical treatment of point forces and their alternatives in cell-based models for skin contractions; (3) cell-based modelling for the evolution of cell geometry during migration.

The skin contraction model is able to reproduce important trends that are observed in clinical settings. The Monte Carlo based parameter sensitivity analysis reveals significant correlations between several stages in the contraction process. These correlations can be used by clinicians to predict scar characteristics on the basis of earlier observations. The flexibility in adjusting parameter values allows the model to be used as patient-oriented simulation tool for the prediction of the evolution of skin after serious trauma.

To model the traction forces exerted by the (myo)fibroblasts, we use point forces that are described by the Dirac Delta distributions, which is an important feature of the so-called *immersed boundary approaches*. For the case of linear elasticity, the superposition argument is used in the analysis of the solution to the linear set of partial differential equations. However, for the dimensionalities that are higher than one, the Dirac Delta distributions result into singular solutions. Hence, we developed various alternatives to get around the singular behaviour of the solutions which allows classical finite-element techniques to be applied to the current agent-based formulations. All the alternatives have been proved to be consistent with the immersed boundary approach. One of the alternatives is the smoothed particle approach that is also proposed in this thesis. This approach is optimal in its use regarding the straightforward numerical treatment since it allows classical solutions in the sense of smoothness, which makes it attractive from a computational point of view. Furthermore, this formalism is a bridge between the continuum (fully partial differential equations-based) approach and the agent-based approach.

Besides the agent-based models, the thesis contains the development and extension of cell-based models. In this modelling type, the geometry of the cell is computed during cell migration and differentiation. This is initialized in order to simulate the differentiation of fibroblasts (spindle shaped) to myofibroblasts (dendric shaped), which are known to produce excess collagen and to exert larger pulling forces on their immediate environment. This differentiation process, which involves the alteration of the cell geometry, causes a larger contraction of the scar. Furthermore, the evolution of cell geometry determines the ability of cancer cells to (trans)migrate to other parts of the body. A phenomenological model for the evolution of cell geometry has been developed by dividing the cell boundary into mesh points that are connected to the cell centre by a series of springs. Furthermore, the impact of cellular forces exerted on the immediate environment of cells is taken into account using a morphoelastic formulation. The model is provided as a basis to be extended to simulate more complicated microscopic experiments and it can be implemented into various models where the evolution of cells is involved, for instance, reepithelialization and cancer cell invasion.

SAMENVATTING

Brandwonden en andere huidtrauma's doen zich voor met wisselende ernst, zowel qua diepte en grootte van het aangetaste huidoppervlak als het aantal huidlagen dat betrokken is. Op jaarbasis wordt wereldwijd een geschat aantal van zes miljoen patiënten vanwege brandwonden opgenomen in het ziekenhuis. Bovendien gaan veel ernstige brandwonden gepaard met morbiditeit en niet-esthetische littekens zoals contracturen en hypertrofische littekens, die een significant negatieve invloed op het leven van patiënten hebben. Contracturen zijn extreme samentrekkingen die meestal samen gaan met het beperkt functioneren van de gewrichten. Samentrekkingen worden veroorzaakt door de trekkrachten die de (myo)fibroblasten, die zich in de fase van celdeling bevinden, uitoefenen op de extracellulaire matrix (ECM).

Om meer inzicht en begrip te verkrijgen wat betreft het optreden van samentrekkingen en andere biologische fenomenen, is wiskundig modelleren een nuttig instrument voor visualisatie en het voorspellen.. Door wiskundige modellen te gebruiken is het mogelijk om belangrijke biologische mechanismen te simuleren en de cellulaire activiteiten en posities van individuele cellen te volgen.

Het onderzoek zoals beschreven in deze dissertatie is onderverdeeld in drie delen: (1) agent-based modelleren voor huidsamentrekkingen die optreden na brandwonden; (2) de numerieke behandeling van puntkrachten en hun alternatieven in cell-based modellen voor huidsamentrekkingen; (3) cell-based modelleren voor de ontwikkeling van de celvorm gedurende de migratie.

Het model, dat de samentrekking van de huid beschrijft, is in staat belangrijke trends die men in de kliniek waarneemt te reproduceren. De parametergevoelgeheidsanalyse gebaseerd op Monte Carlo simulaties laat significante correlaties zien tussen verschillende fasen in het samentrekkingsproces. Deze correlaties kunnen door artsen worden gebruikt om op basis van eerdere waarnemingen de eigenschappen van littekens te voorspellen. De mogelijkheid om de parameterwaarden aan te passen geeft het model genoeg flexibiliteit om gebruikt te worden als instrument voor het simuleren en voorspellen van de ontwikkeling van de huid van een patiënt na een serieus trauma. Om de trekkrachten die uitgeoefend worden door de (myo)fibroblasten te modelleren, gebruiken we puntkrachten die beschreven worden door Dirac-Delta verdelingen. Dit is een belangrijk aspect van de zogeheten immersed boundary methode. In het geval van lineaire elasticiteit gebruiken we het superpositie beginsel in onze analyse van de oplossing van het lineaire stelsel van partiële differentiaalvergelijkingen. Als de dimensionaliteit groter is dan één, resulteert het gebruik van Dirac-Delta verdelingen echter in singuliere oplossingen. We hebben meerdere alternatieven ontwikkeld om het singuliere gedrag van de oplossingen te omzeilen. Deze stellen ons in staat om klassieke eindige-elementenmethoden toe te passen op de huidige agent-based formuleringen. We hebben bewezen dat alle alternatieven consistent zijn met de immersed boundary aanpak. Eén van de alternatieven is de smoothed particle methode, die ook wordt gebruikt in

deze dissertatie. Deze aanpak is optimaal vanwege de eenvoudige numerieke behandeling die gebruikt kan worden: aangezien qua gladheid de oplossingen klassiek zijn, is deze methode rekentechnisch gezien aantrekkelijk. Bovendien slaat dit formalisme een brug tussen de continue aanpak (die volledig gebaseerd is op partiële differentiaalvergelijkingen) en de agent-based aanpak.

Naast agent-based modellen beschrijft deze dissertatie ook de ontwikkeling en uitbreiding van cel-based modellen, waarbij de celvorm wordt berekend gedurende de celmigratie en -differentiatie. Dit doen we om de differentiatie te simuleren van fibroblasten (spilvormig) naar myofibroblasten (dendrietvormig), die, zoals bekend is, een teveel aan collageen produceren en grotere trekkrachten uitoefenen op hun directe omgeving. Dit differentiatieproces, dat gepaard gaat met een verandering in de celvorm, veroorzaakt een sterkere samentrekking van littekens. Ook bepaalt de ontwikkeling van de celvorm het vermogen van kankercellen om zich naar andere delen van het lichaam te verplaatsen. Een fenomenologisch model is ontwikkeld dat de evolutie van de celvorm beschrijft door het celmembraan in een netwerk van punten te verdelen die door middel van veren verbonden zijn met het midden van de cel. Ook wordt een morfoelastische formulering gebruikt om de invloed van celkrachten die uitgeoefend worden op de directe omgeving mee te kunnen nemen. Het model wordt voorzien als basis waarop voortgeborduurd kan worden om ingewikkeldere microscopische experimenten te simuleren. Ook kan het worden verwerkt in verschillende modellen waarin de ontwikkeling van cellen een rol speelt zoals bijvoorbeeld re-epithelialisatie en de invasie van kankercellen.

1

INTRODUCTION

1.1. BIOLOGICAL BACKGROUND

1.1.1. SKIN AND WOUND HEALING

Wound healing is the spontaneous process of the skin to cure itself after an injury. It is a complex cascade of cellular events which contribute to resurfacing, reconstitution and restoration of the tensile strength of injured skin.

Roughly speaking, skin consists of three layers: the epidermis, the dermis and the hypodermis. Superficial wounds will heal without any problem, since the trauma only occurs on the epidermis. However, if it is a severe, deeper injury at the dermis, which causes a significant loss of soft tissue, then the dermal wounds may lead to various pathological problems. Therefore, it is vital for the skin that (secondary) deep wound healing proceeds speedy and effective. During secondary healing, the formation of a blood clot, the regeneration of collagen (in extracellular matrix) and re-vascularisation take place [2]. In most cases of serious skin trauma, excessive healing reactions, such as the development of wound contractures, known as excessive and pathological contractions, or hypertrophic scars, takes place.

Contractions are caused by mechanical interactions between cells and extracellular matrix (ECM), that is, (myo)fibroblasts exert pulling forces on their immediate surroundings. By this contractile mechanism, large, severe wounds in human skin reduce by 5-10 % of its original size. Furthermore, the polymeric structure and orientation of regenerated collagen will be different from embryonic, undamaged skin [2].

Wound healing entails four partially overlapping phases: hemostasis, inflammation, proliferation and maturation/ remodelling [2]; see Figure 1.1. During hemostasis, mainly platelets are responsible for blood clot formation so that the clot can prevent more blood loss and also provides the provisional scaffold (connective tissue) for cell migration towards the wound [3]. Subsequently, the inflammatory cells (white blood cells) are attracted to the wound to remove the bacteria and debris in inflammatory phase. When it

Parts of this chapter have been published in *Biomech Model Mechanobiol* **19**, 2525–2551 (2020) [1] and submitted to *Biomech Model Mechanobiol* and *Journal of Computational and Applied Mathematics*.

WOUND HEALING

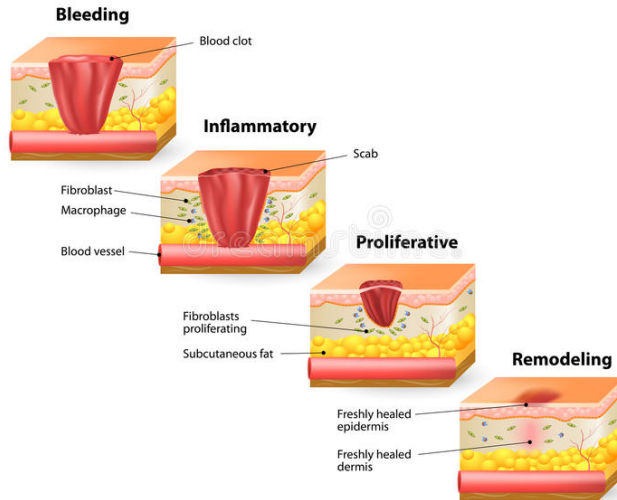


Figure 1.1: Four partially overlapping stages of wound healing [4]

comes to the next proliferative phase, different entities like vessels, fibrin and granulation tissues etc. start being regenerated and the wound begins to contract. In the final remodelling stage, collagen forms tight cross-links, which increases the tensile strength of the scar. The remodelling phase can take from months to years depending on the wound.

The four phases will be explained in more detail in the coming paragraphs. Since the evolution of skin entails a complicated sequence of biological processes, we can only summarize the biological dynamics.

Immediately after injury, hemostasis starts, which is characterised by vasoconstriction—a process to stop bleeding by closing damaged blood vessels [3, 5]. If the lining of the blood vessels is broken, then the nearby uninjured blood vessels will constrict in order to limit blood loss. As a result, a blood clot is developed to seal off the wound from its surroundings, so that the invasion of other hazardous contaminants and pathogens into the skin is prevented. In the meanwhile, the platelets are activated and aggregating, which lead to the formation of a blood clot. The activation facilitates platelets to degranulate and to release chemotactic growth factors into the extracellular space [2].

Inflammation can be split into early (24-48 hours) and late (48-72 hours) phases. The main process during the inflammatory phase is characterised by an increased activity of the immune system. In other words, the inflammatory cells, including neutrophils, macrophages and T lymphocytes, will enter the wound to clean the damaged region, specifically by removing the bacteria and debris through phagocytosis [3, 6]. In the early stage of the phase, neutrophils are the first immune cells arriving at the wound,

followed by tissue macrophages which result from differentiation from monocytes [6]. Macrophages are the most important cells in the later inflammatory phase since they are the original producers of cytokines, especially of transforming growth factor beta (TGF-beta), which stimulates the chemotaxis and proliferation of fibroblasts and smooth muscle cells [2]. At the final stage of the inflammatory phase, chemokines released by macrophages attract endothelial cells to the wound and stimulate angiogenesis, which is the formation of a blood vessel network. During this stage, T-lymphocytes, which mainly effect the cell-mediated response and release signalling molecules, also start moving to the wound area. Additionally, skin resident mast cells migrate to the wound area [6].

The subsequent phase is proliferation, which will continue for 2-4 weeks after wounding, depending on the wound size [2]. It includes epithelialization, fibroplasia, angiogenesis and the development of granulation tissue. Redifferentiation of the keratinocytes in the neo-epidermis is activated before completing wound closure and leads to efficient reconstitution of the epidermal barrier [6]. After epithelialization, the injured dermis starts being repaired. Within four days, the clot will be broken by proteins like plasmins, of which the production is effected by the presence of tissue plasminogen activator (tPA). Subsequently, the clot is replaced by granulation tissue, which consists of cells and connective tissues [3]. During this process, fibroblasts are attracted to the wound area from the wound surroundings by a number of factors like platelet-derived growth factor (PDGF) and transforming growth factor-beta (TGF-beta) [2]. Once within the wound, fibroblasts sometimes differentiate into myofibroblasts, which pull the extracellular matrix with higher forces and cause deformation of the tissue [6, 7]. In the meanwhile, fibroblasts release collagen to rebuild the ECM. However, the tensile and strength properties of the newly built collagen differ from the properties of uninjured skin. In the course of time, the tensile strength will increase as a result of a tight cross-link of the collagen molecules. Additionally, since the newly released collagen is deposited according to the direction of migration of the fibroblasts, the orientation of newly regenerated collagen is anisotropic. In summary, wound contraction takes place due to myofibroblasts exerting pulling forces on the surrounding extracellular matrix and results into the formation of (permanent) stresses and strain in and around the wound area. The amount of contraction is related to the size, shape, depth and anatomical location of the wound, for instance, tissues with stronger laxity contract more comparing to loose tissues, and square-shaped wounds contract more than circular ones [2, 8]. Due to the occurrence of contraction, the exposed surface area of the wound decreases without the production of new wound-covering tissues. Notably, contraction must be distinguished from contracture, which is a pathological process of excessive contraction. Usually, contractures concur with disfunctioning and disabilities of the patients.

The late stage of new tissue formation overlaps with maturation/remodelling which can last several years. At last, the dermal tissue has a low cell density for both macrophages and fibroblasts [2], and the tensile strength of new tissue will increase but it will never reach the level of undamaged tissue [2, 3, 6]. On the other hand, the main factors in the maturation/remodelling phase are collagen and cytokines. As mentioned earlier, the collagen molecules connect to other collagen molecules to strengthen the bundles. Cytokines are released from a variety of cells and bind to cell surface receptors to stimulate a cell response.

The aforementioned stages of wound healing partly overlap each other and intracellular communication drives the initiation and termination of the subsequent stages. The inflammatory phase is initiated by the platelets that originate from the blood vessels and form the blood clot. The platelets secrete PDGF that is detected by the immune cells (white blood cells) in the blood circulatory system (for example, neutrophils, monocytes, macrophages and T-lymphocytes). The immune cells transmigrate through the walls of the blood vessels to arrive at the wound site [9], where they clear up debris and other pathogens through phagocytosis [3, 6]. These immune cells secrete the transforming growth factor TGF-beta. We bear in mind that the immune cells release several types of TGF-beta chemokines, and that some types of these chemokines initiate the formation of a newly generated blood vessel network (also referred to as angiogenesis). Migration of the fibroblasts and immune cells takes place via various biological mechanisms. The most important biological mechanisms for cell migration are random walk, which takes place as a result of unpredictable inhomogeneities and anisotropies in the extracellular matrix of skin, chemo (hapto)taxis, which characterises cellular migration in the direction of (or opposite to) the gradient of a chemical and tensotaxis, which represents cellular migration driven by mechanical cues.

1.1.2. CELL GEOMETRY

Cells may attain various shapes and sizes, for example, stem cells can differentiate and adopt the shape and functionality of many different cell types in our body: fan-like keratocytes, hand-shaped nerve growth cones and spindle-shaped fibroblasts [10, 11]. It has been recognized that cell geometry influences cellular activities like cell growth and death, cell mobility and adhesion to the direct environment [10, 12–15]. The shape of a mobile cell is determined by its boundaries, which dynamically vary with a local balance between retraction and protrusion [16]. There are multiple constituent elements affecting the cell shape, for instance, the cytoskeleton and the cell-substrate adhesions, which have been studied in depth in the past years. However, it is still a great challenge to understand the mechanisms that determine the global cell morphology in the context of its function [10, 13].

Signalling molecules play an important role in cell migration and cell shape. During wound healing, chemotaxis is one of the most important cues for migration of immune cells and fibroblasts in inflammatory and proliferative phases [1–3, 17]. Metastasis of cancer cells can be induced by nutrients and oxygen, since tumour growth requires an adequate supply of oxygen and nutrients. Under most pathological circumstances, oxygen and nutrients are supplied through the local blood vasculature [18, 19]. Commonly, signalling molecules are activated at the plasma membrane, and de-activated in the cytoplasm. On the other hand, the concentration of signalling molecules determines the cytoskeletal dynamics [10].

In wound healing, cells migrate and change shape in both the epidermis and the dermis layers. Re-epithelialization is the most essential part for the skin to re-establish its barrier function [20–22]. However, the mechanisms of re-epithelialization are poorly understood. In the early stage of the epidermis closure in a wound, the basement membrane between the epidermis and dermis extends slightly over the ends of the incised dermis, creating an “extension membrane” (or so-called epidermal tongue) [23]. The

mechanism of the occurrence of the epidermal tongue is still unclear. A possible explanation is that, the suprabasal cells (which lie upon the layer of basal cells) form the tongue by migrating over the leading basal cells and dedifferentiating to basal cells (which are adhered to the basement membrane between the epidermis and dermis) to form new leaders [20, 23–25]. When epidermal epithelial cells are "crawling" and "climbing up" to reestablish the epidermis, they elongate and flatten [20]. In the dermis, it has been widely documented that the differentiation of fibroblasts is one of the key events during wound healing. Differentiation changes the spindle-shaped fibroblast to dendritic-shaped myofibroblasts. Subsequently, cells' mechanobiology is modified considerably as well. The differentiated myofibroblasts exert much larger forces on the extracellular matrix (ECM) than fibroblasts [1]. Excessive numbers of myofibroblasts will result in contractures, which are morbid and pathological macro-scale contractions. Usually, contractures concur with disabilities and dysfunction, and have a grave impact on patients' daily life.

Another circumstance where cell geometry has a significant impact is cancer cell invasion and cancer metastasis, when the cancer cell deforms such that it can go through various sizes of pores or vessels. Cancer metastasis has been reported as the main reason of death in cancer patients [14]. During the migration of a cancer cell to its destination, especially migrating through a narrow and stiff cavity, it has to deform to adapt to the obstacles. More invasive cancer cells, appear to be more pliable and dynamic both internally [26] and externally [27–29], and thus able to adjust their cytoskeleton and morphology, which might provide a possible cause for cancer. In addition to that, cancer cells are known to apply a significantly larger traction force on the substrate, compared to benign cells [14], yet the specific mechanisms that induce these increased forces are still poorly understood.

1.2. MATHEMATICAL MODELLING IN BIOLOGY

In 1952, a mathematical model was developed in biology by Turing [30] to describe the occurrence of natural patterns such as strips and spots, and since then, a bridge has been built between experimental work and mathematical modelling. As Bonner [31] said in his book already in 1974: "*We have arrived at the stage where models are useful to suggest experiments, and the facts of the experiments in turn lead to new and improved models that suggest new experiments. By this rocking back and forth between the reality of experimental facts and the dream world of hypotheses, we can move slowly toward a satisfactory solution of the major problems of developmental biology*". Mathematical modelling in biology advances both mathematics and biology, and it has had a crucial impact on biological and medical research.

Even though there have been significant successes in mathematical biology over the last fifty years, mathematical biology is not widely accepted [32, 33]. Therefore, various researchers argued how useful mathematics is in biology [32–35]. Firstly, mathematical modelling has been proven to be an important tool to have a deeper insight into many biological processes that are potentially difficult to control in experiments. Furthermore, if the global patterns are lacking, mathematical models are capable of exposing the hidden correlation between the parameters. Secondly, when a model is able to reproduce experimental results, it can be further considered to suggest new hypothesis. In other

words, mathematical modelling turns blurred concepts and ideas into testable and rigorous hypotheses. Subsequently, potential treatments can be developed, for instance, the improvement of the efficiency of drug delivery. Thirdly, mathematical modelling can simulate various biological phenomena, for example, wound healing and cancer metastasis, such that the model is capable of predicting as a simulation tool. Furthermore, thanks to the flexibility of altering parameters and parameter values in the simulation, mathematical models can be patient-oriented, which strengthen their predicting power further. Last but not least, the using of mathematical models reduces the number of animal experiments significantly. We note that in this context, both animal experiments and computation are model descriptions of reality, since also in the case of animal experiments, the translation between animal and human pathologies is often obscure.

Depending on the scale of the observed domain, continuum models and agent-based models are widely used. Continuum models, developed by Tranquillo and Murray [36], among many others, in which all the behaviours of species are described by partial differential equations (PDEs). Therefore, cells are represented by densities rather than by entities of their own. They have the advantage of modelling a larger scale, however, the model neglects the individual cellular activity and cells are not tracked [37]. The other class of models is hybrid framework based, or called agent-based model in which the cells are treated as individual, discrete entities and the extracellular matrix (ECM) is treated as a continuous variable. Agent-based models are suitable to model cellular activities of every cell, for instance, cell migration and cell deformation, even though agent-based models are more suited for the micro-scale due to their computational cost. On the other hand, agent-based models are helpful to understand and develop a better insight into biological scenarios at the level of cells.

Hence, agent-based modelling is preferred in this thesis to simulate wound healing and the dynamics of cell geometry. Compared with cell density models, agent-based models have several advantages. Firstly, agent-based models are experiment-based (measurable parameters like cell stiffness, cell mobility, cell forces are used directly), and therefore, the influence of cellular properties on the surroundings can be evaluated immediately. The second advantage is the ability to visualize the computational results, so that this can easily be developed into a user-friendly simulation tool. Thirdly, it is straightforward to involve the stochastic processes in various cellular events (like cell migration and cell proliferation etc.).

In this thesis, there are multiple mechanisms determining the displacement and the geometry of the cell, namely, interactions between cells, chemotaxis, passive convection and random walk. In other words, a semi-stochastic partial differential equation (PDE) is used to model the displacement of cells. For chemotaxis and passive convection, we mainly incorporate PDEs solved by finite-element methods.

1.3. MOTIVATION AND OBJECTIVES

Burns and other skin traumas occur at various intensities regarding the depth and area of the skin, as well as the involvement of the different skin layers. Worldwide, an estimated six million patients need hospitalisation for burns annually. In most hospitalized populations with severe burn injuries, the mortality rate is between 1.4% and 18% with the maximum rate 34% [38]. Furthermore, most severe burn injuries will develop morbidity

and unaesthetic scars like contractures and hypertrophic scars, which cause a significantly bad impact on the patients' life.

Globally, cancer is the second leading causes of deaths: about one in six deaths is resulted from cancer [39]. Cancer metastasis that is has been reported as one of the most dreadful reasons of patients' death. In solid tumor, 66.7% of cancer deaths are due to metastasis [40].

Even though technology has been developing in the last decades, these diseases and complications are still incurable. As it has been mentioned earlier, mathematical models can be helpful and beneficial to reproduce and simulate various biological scenarios. Hence, they are a useful tool to discover hidden explanations of phenomena, since only significant features are elected to develop the model. Furthermore, mathematical models are not based on additional animal experiments and as an additional simulation tool, these models can contribute to a further reduction of the number of animal experiments.

In this thesis, firstly, we are keen on developing a more accurate model for wound healing, as a preliminary phase for a user-friendly simulation tool. Subsequently, the physicians and surgeons can use the tool to predict the healing procedure of every patient. In the meantime, the accuracy of the model is attached to the solution to the equations. Hence, we investigate various approaches to improve the accuracy of the solution, in particular in higher dimensions. On the other hand, it is acknowledged that cell geometry plays an important role in cancer metastasis. We begin with developing a model including traction forces exerted by the cell, such that the model is able to reproduce some laboratory experiments.

1.4. OUTLINE

This dissertation contains three parts excluding introductions and conclusions. The first part is about agent-based modelling on wound contractions after deep tissue injuries. In Chapter 2, we describe an agent-based model for wound contractions, where a phenomenological model is selected to describe the permanent deformation of the wound. Chapter 3 treats a morphoelasticity model, in which the permanent deformation of the substrate is connected to the strain. In addition to embed morphoelasticity in the wound healing model, we also compare these two models in terms of the dynamics of the wound. The second part is devoted to point sources and point forces, as well as superpositions of them. These point sources and point forces are modelled by the use of Dirac Delta distributions. The point forces are typically applied to model cell traction force over the cell boundary. This is done by a superposition of point forces over the boundary of the cell. A major issue with these point sources and forces is the singular nature of the solution for the dimensionality exceeding one. Hence, alternative approaches are needed and are proved to be consistent with the immersed boundary approach in one dimension (Chapter 4) and multiple dimensions (Chapter 5). In Chapter 6, we managed to upscale the agent-based model and the continuum-based model and establish the consistency between these two categories of models, regarding the traction forces exerted by the cells. The last part of this thesis is about the cell geometry. Chapter 7 states a cell-based model including the cell traction force to simulate the dynamics of the cell geometry evolution. Last but not least, we summarize this thesis and present some recommendations for the future work.

I

AGENT-BASED MODELLING OF SKIN CONTRACTION

2

AGENT-BASED MODELLING AND PARAMETER SENSITIVITY ANALYSIS WITH A FINITE-ELEMENT METHOD FOR SKIN CONTRACTION

In this chapter, we extend the model of wound healing by Boon et al. [41]. In addition to explaining the model explicitly regarding every component, namely cells, signalling molecules and tissue bundles, we categorised fibroblasts as regular fibroblasts and myofibroblasts. We do so since it is widely documented that myofibroblasts play a significant role during wound healing and skin contraction, and that they are the main phenotype of cells that is responsible for the permanent deformations. Furthermore, we carried out some sensitivity tests of the model by modifying certain parameter values, and we observe that the model shows some consistency with several biological phenomena.

Using Monte Carlo simulations, we found that the model predicts a significant strong positive correlation between the final wound area and the minimal wound area. The high correlation between the wound area after four days and the final/minimal wound area makes it possible for physicians to predict the most probable time evolution of the wound of the patient. However, the collagen density ratio at the time when the wound area reaches its equilibrium and minimum, cannot indicate the degree of skin contraction, whereas at the 4th day post-wounding, when the collagen is accumulating from null, there is a strong negative correlation between the area and the collagen density ratio. Further, under the circumstances that we modelled, the probability that patients will end up with 5% contraction is about 0.627.

2.1. INTRODUCTION

In this chapter, we will use the hybrid cell-based model developed by Vermolen and Gefen [42] and improved by Boon *et al.* [41]. The innovations are the following: in this modelling study, a six-species model for the second and third phases of wound healing processes is selected, including multiple types of cells, cytokines and tissues; see Cumming *et al.* [3] and Koppenol [17]. In the current text, we have improved the model by modelling the proliferation and differentiation of both fibroblasts and myofibroblasts by the use of stochastic sampling from exponential distributions. In the model, cells are taken as spherical individuals which become circles after projection in two spatial dimensions, cytokines and tissues are treated as continuous variables. Furthermore, we have done sensitivity tests to validate the model and Monte Carlo simulations to assess the impact of uncertainty and parameter variation.

The chapter is structured as follows. In Section 2.2, we present the biological assumptions and the semi-stochastic cell-based model. Section 2.3 treats the numerical results of the model from various aspects, like the positions of the cells, variations of the concentration of cytokines and strain energy of the wound, and the wound area changing over time, which is taken as an indicator of the contractions. Furthermore, the effect of applying different parameter values on wound healing is probed. The results from the Monte Carlo simulations are presented in Section 2.4. Finally, the conclusions and some remarks for the model are shown in Section 2.5.

2.2. MATHEMATICAL MODELS

2.2.1. BIOLOGICAL ASSUMPTIONS

To regenerate new and healthy tissue in the wound, the importance of cell proliferation, migration and differentiation has been documented [5]. However, the activities of viable cells are much more complex than they were observed in the laboratory. In other words, it is infeasible to depict and contain every aspect of cellular activity into the model. Therefore, to encode a mathematical model, we have to make some simplifications of biological system and until now we mainly work in two spatial dimensions. Under this circumstance, the domain we are working on is denoted by $\Omega \in \mathbb{R}^2$. Furthermore, we use the following assumptions for the cells—in this report, namely macrophages, regular fibroblasts and myofibroblasts:

- cells are in a circular shape with a fixed radius;
- distortion of cell geometry is not taken into consideration, however, cells are allowed overlap in a reasonable range;
- once two cells mechanically contact and even (partly) overlap, they will repel each other and exert a repulsion force which is in the opposite direction of the vector connecting the cells; additionally, the remote traction forces between any two cells are neglected;
- each cell is either viable or dead and once a cell dies, it disappears immediately from the computational domain; we note that the finite-element method is ap-

plied over the entire domain, and hence the only thing that changes in the algorithm is the disappearance of a force or source as soon as a cell dies;

- when cell division occurs, the centre of the original cell moves randomly to the circumference and the new cell's center is on the opposite side of the circumference; the process is depicted in Figure 2.1 [42];
- each cell needs time to grow before it is allowed to differentiate or divide after its birth; the daughter cell needs more time than the mother cell [43], but cell death/apoptosis can always occur due to excessive mechanical forcing;
- cell division and death rates follow the exponential distribution; see Chen *et al.* [44] for more details, of which the probability rate for these processes depends on the concentration of TGF-beta and strain energy density;
- in this model, the division of macrophages and myofibroblasts are neglected, hence, only regular fibroblasts are allowed to proliferate;
- each viable (myo)fibroblast exerts a force on the substrate where it is living on.

Note that in fact cells are not overlapping but they collide against each other. Subsequently, they repel each other. We use a Hertz contact model to simulate repulsion against cells. This model is based on the indentation of a sphere, which we model by 'overlapping'. Similar approaches by different authors can be found in for instance Yamao *et al.* [45]. Some papers report about the quantification of cell forces, however, the experimental values of intracellular forces are characterized by very large uncertainties. The magnitude of intracellular forces, which effects the 'overlapping region' between cells does not effect our computed results in terms of contractile behaviour of burn injuries that much.

The solution of the partial differential equations that will be presented in this section is approximated by the use of the finite element method. The finite element method is applied over the entire domain of computation to approximate the solution of the equations for the concentrations and force balance. The individual cells act as sources for the regeneration of chemical agents and exert forces to the immediate surroundings. To this extent, the whole domain of computation is triangulated and linear basis functions are used. Since the cells exert forces to their surroundings, the region is deformed, which is incorporated into the finite element method. The finite-element method is implemented within the FEniCS package [46]. For completeness, we present the Galerkin formulations of the partial differential equations that we numerically solve.

Regarding the cell repelling force, a Hertz contact force is used to take cells as isotropic homogeneous elastic bodies, which are deformed if two cells repel each other. The difference between the sum of the radius of two cells and the distance between two cell centres is defined as overlapping distance [42, 44, 47]. This overlapping region is fictitious since in real situations cells do not overlap. The overlapping distance is used to quantify the indentation, which in turn, determines the repulsive force. We have used the Hertz contact force model for soft spheres.

We consider a two-dimensional computational domain that is filled with cells and substrate. Since the predominant mode of cellular migration is by chemotaxis, we only

incorporate direct mechanical (repulsion) forces between cells that are in physical contact. For more details about modelling the traction forces using strain energy density, see Vermolen and Gefen [42] and Dudaie *et al.* [48].

Strain energy density is the mechanical energy per unit volume and it quantifies the magnitude of the strain by which a cell will migrate.

The strain energy density from the repulsive force that is exerted by colliding cells is modelled by, see [42]:

$$M^{ij}(\mathbf{r}_i) = \frac{1}{30} \frac{E_c}{\pi} \left(\frac{h_{ij}}{R} \right)^{\frac{5}{2}}, \quad (2.1)$$

where

$$h_{ij} = \max\{2R - \|\mathbf{r}_i - \mathbf{r}_j\|, 0\},$$

is known as the overlapping distance of two cells. We consider cell i as a cell that collides with other cells, then the total repulsion energy density is the sum of the repulsion energy densities which results from the cells contacting cell i mechanically. Suppose cells $j \in \{i_1, \dots, i_k\} \subseteq \{1, \dots, n(t)\}$ contact mechanically with cell i at time t , then the total repulsion energy is

$$M^{mc}(\mathbf{r}_i) = \sum_{j=i_1}^{i_k} M^{ij}(\mathbf{r}_i), \quad \text{for } i \in \{1, \dots, n\}. \quad (2.2)$$

Based on the cell assumptions, the total energy density is

$$\hat{M}(\mathbf{r}_i) = \begin{cases} 0, & \text{if } h_{ij} = 0, \\ -M^{mc}(\mathbf{r}_i), & \text{if } h_{ij} > 0. \end{cases} \quad (2.3)$$

According to Vermolen and Gefen [42], the displacement of cell i over a time step Δt is a linear combination of all the unit vectors connecting to the rest with the total strain energy density as the weight factor. Hereby, we use the unit vector connecting cell i to cell j

$$\mathbf{e}_{ij} = \frac{\mathbf{r}_j - \mathbf{r}_i}{\|\mathbf{r}_j - \mathbf{r}_i\|}, \quad \text{where } i \neq j,$$

and according to the biological assumption of no more traction force, the weight of the direction of displacement is given by

$$M_z(\mathbf{r}_i) = \begin{cases} 0, & \text{if } h_{ij} = 0, \\ -M^{ij}(\mathbf{r}_i), & \text{if } h_{ij} > 0. \end{cases} \quad (2.4)$$

Then the overall moving direction of cell i is given by the following equation:

$$\mathbf{z}_i = \sum_{j=1, j \neq i}^n M_z(\mathbf{r}_i) \mathbf{e}_{ij} = \sum_{j=i_1}^{i_k} M_z(\mathbf{r}_i) \mathbf{e}_{ij}. \quad (2.5)$$

Then we normalize the vector again to obtain

$$\hat{\mathbf{z}}_i = \frac{\mathbf{z}_i}{\|\mathbf{z}_i\|}.$$

Based on the model of displacement of cell i , developed by Vermolen and Gefen [42], the direction is determined by $\hat{\mathbf{z}}_i$ and the magnitude of the displacement is proportional to the total energy density $\hat{M}(\mathbf{r}_i)$.

To improve the computational efficiency, we use another method modelling the proliferation and apoptosis of cells, which is extended from the one used in Chen *et al.* [44]. Each viable cell has a certain possibility to proliferate or die due to its surroundings and its internal environment. In this chapter, for proliferation and differentiation of regular fibroblasts, we consider the effects from the surroundings on each cell, namely the strain energy density due to forces exerted by other cells and the concentration of TGF-beta.

Following the approach in Vermolen and Gefen [49], the probability of cell proliferation, differentiation and apoptosis follow a (memoryless) exponential distribution, of which the probability density function is defined by

$$f_{t_n}(\lambda, t) = \lambda \exp\{-\lambda(t - t_n)\},$$

in the time interval $(t_n, t_n + \Delta t)$. Here, Δt is the timestep, which is fixed in this chapter. Hence,

$$\mathbb{P}(t \in (t_n, t_n + \Delta t)) = \int_{t_n}^{t_n + \Delta t} \lambda \exp\{-\lambda(t - t_n)\} dt = 1 - \exp\{-\lambda \Delta t\},$$

and hence the probability is determined by the $\lambda \Delta t$. The division and apoptosis rates were used on the basis of earlier studies in Vermolen and Gefen [49] and on the basis of Chen *et al.* [44], where it has been specified how proliferation and death rates change with mechanical signals. These rates are incorporated in the exponential distribution, which we describe in Section 2.2.2. The actual values were based on 'educated guesses' and the sensitivity of the model. The probability rate is set according to the following relation with the strain energy density and the concentration of TGF-beta:

$$\lambda_d = 20 \times c_{TGF}^2(\mathbf{x}, t) + \begin{cases} 2, & \text{if } \|\hat{M}(\mathbf{r}_i)\| < 0.05 \text{ kg}/(\mu\text{m} \cdot \text{h}^2), \\ 0, & \text{otherwise,} \end{cases}$$

where $c_{TGF}(\mathbf{x}, t)$ is the concentration of TGF-beta at position \mathbf{x} and time t , and

$$\lambda_a = \begin{cases} 10, & \text{if } \|\hat{M}(\mathbf{r}_i)\| \geq 0.07 \text{ kg}/(\mu\text{m} \cdot \text{h}^2), \\ 0, & \text{otherwise,} \end{cases}$$

for proliferation and apoptosis respectively. From a biological point of view, when fibroblasts enter the wound region, they can differentiate into myofibroblasts, which pull the extracellular matrix even harder and cause the contractions of the wound. Thus, to describe the probability differentiating into myofibroblasts, exponential distribution is still applied with different parameter value λ , based on the fact that the exponential distribution is memoryless. Similarly, we use the same exponential distribution model to describe the probability of differentiation from a regular fibroblast to myofibroblast with

$$\lambda_{myo} = \begin{cases} 60 \times c_{TGF}^2(\mathbf{x}, t) + 10, & \text{if } c_{TGF}(\mathbf{x}, t) > 0.01 \text{ g}/(\mu\text{m})^3, \\ 0, & \text{otherwise.} \end{cases}$$

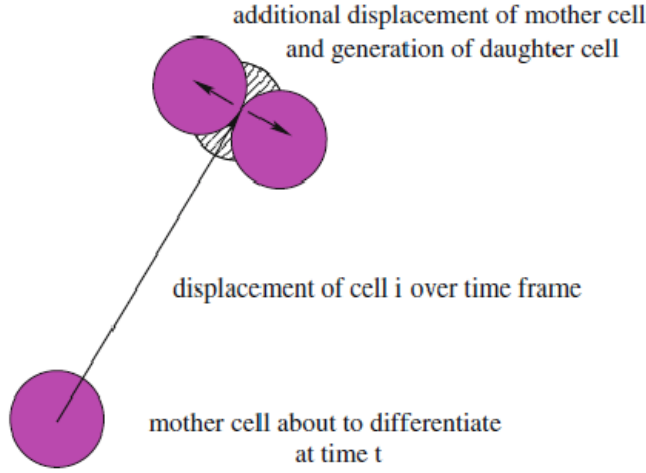


Figure 2.1: The process of cell division combined with the cell displacement [42]

At each time step, we generate a random number ξ from a uniform distribution in $[0, 1]$. The cell will divide or die or differentiate if and only if $\xi < \mathbb{P}(t \in (t_n, t_n + \Delta t))$ with corresponding λ .

Additionally, for each cell, it needs some time to grow mature first and then it can divide. We assume that a cell will not divide unless the growth time exceeds some time step threshold but there is no restriction for cell death.

The related parameter values of cells used in this study are shown in Table 2.1. The values in the table below are mainly from Chen *et al.* [44] and Koppenol [17]. Note that some of the parameter values, such as the dimensions of the cells, are fictitious and that the current paper mainly focusses on evaluating the sensitivity of the model.

2.2.2. SEMI-STOCHASTIC CELL-BASED MODEL

CONCENTRATION OF SIGNALLING MOLECULES

In the model, the fields of the several growth factors are modelled by reaction-diffusion equations of the form:

$$\frac{\partial c(\mathbf{x}, t)}{\partial t} + \nabla \cdot [\mathbf{v}(t, \mathbf{x}(t)) \cdot c(\mathbf{x}, t)] - \nabla \cdot (D \nabla c(\mathbf{x}, t)) = F, \quad (2.6)$$

where c is the concentration, D is the diffusion rate, which is either a positive constant or a function of fibre and collagen concentration, and $\mathbf{v}(t, \mathbf{x}(t))$ is the displacement velocity of the substrate that results from the cellular forces exerted on their surroundings. To derive the corresponding Galerkin's form, Reynold's Transport Theorem [50, 51] is applied to dismiss the term with the displacement velocity $\mathbf{v}(t, \mathbf{x}(t))$. Define material derivative as

$$\frac{Df(\mathbf{x}(t), t)}{Dt} = \frac{\partial f(\mathbf{x}(t), t)}{\partial t} + \mathbf{v}(t, \mathbf{x}(t)) \cdot \nabla f(\mathbf{x}(t), t)$$

for any tensor field $f(\mathbf{x}(t), t)$, where $\mathbf{v}(t, \mathbf{x}(t))$ is the velocity of the field.

Table 2.1: Parameter values of cells which will be used in the calculation of this chapter

Parameter	Description	Value	Dimension	Reference
E_s	Substrate elasticity	50	$kg/(\mu m \cdot h^2)$	Dudaie <i>et al.</i> [48]
E_c	Cell elasticity	5	$kg/(\mu m \cdot h^2)$	Dudaie <i>et al.</i> [48]
F_i	Traction force between cells	10	$kg \cdot \mu m/h^2$	Chen <i>et al.</i> [44]
R	Cell radius	2.5	μm	Dudaie <i>et al.</i> [48]
μ	Cell friction coefficient	0.2	–	Vermolen and Gefen [49]
β_i	Mobility of the cell surface	1	h^{-1}	Vermolen and Gefen [49]
P_f	Magnitude of temporary force of regular fibroblasts	8.32	$kg \cdot \mu m/h^2$	Koppenol [17]
Q_0	Magnitude of plastic force of myofibroblasts	33	$kg \cdot \mu m/h^2$	Koppenol [17]
α_ρ	Coefficient related to collagen and fibrin	10^4	–	Koppenol [17]
v	Speed of biased movement of cells	2.5	$\mu m/h$	Koppenol [17]
c_{PDGF}^0	Initial concentration of PDGF	1	$g/(\mu m)^3$	Koppenol [17]
c_{tPA}^0	Initial concentration of tPA	1	$g/(\mu m)^3$	Koppenol [17]
D_{TGF}^{min}	Minimum diffusion rate of TGF-beta	10.6	$\mu m^2/h$	Koppenol [17]
D_{TGF}^{max}	Maximum diffusion rate of TGF-beta	100.6	$\mu m^2/h$	Koppenol [17]
k_{TGF}	Secretion rate of TGF-beta molecules by macrophages	2.5	$kg/(\mu m^3 h)$	Koppenol [17]
D_{PDGF}	Diffusion rate of PDGF	10	$\mu m^2/h$	Koppenol [17]
D_{tPA}^{min}	Minimum diffusion rate of tPA	0.711	$\mu m^2/h$	Koppenol [17]
D_{tPA}^{max}	Maximum diffusion rate of tPA	14.1	$\mu m^2/h$	Koppenol [17]
k_{tPA}	Secretion rate of tPA by damaged endothelial cells	0.5	$kg/(\mu m^3 h)$	Koppenol [17]
δ_ρ	Degradation rate of fibrin bundles	0.15	$\mu m^2/h$	Koppenol [17]
x_0	Length of the computational domain in x direction	120	μm	Estimated in this study
y_0	Length of the computational domain in y direction	80	μm	Estimated in this study
x_w	Length of the wound region in x direction	40	μm	Estimated in this study
y_w	Length of the wound region in y direction	30	μm	Estimated in this study
Δt	Time step	0.1	h	Estimated in this study
ν	Poisson's ratio of the substrate	0.48	–	Estimated in this study
P_m	Magnitude of temporary force of myofibroblasts	33.28	$kg \cdot \mu m/h^2$	Estimated in this study
κ	Parameter in Robin's boundary condition to solve Eq (2.6)	100	$1/\mu m$	Estimated in this study
κ_f	Parameter in Robin's boundary condition to solve Eq (2.9)	3	$1/\mu m$	Estimated in this study
σ_{rw}	Weight of random walk	0.01	–	Estimated in this study

Theorem 2.1. Let Ω_t be a time-dependent domain in \mathbb{R}^d , and let $\partial\Omega_t$ be the boundary of Ω_t , further, let $f, \frac{\partial f}{\partial t} \in L^2(\Omega_t)$ be a given function and let \mathbf{v} represent the velocity of moving boundary $\partial\Omega_t$, then

$$\frac{d}{dt} \int_{\Omega_t} f(\mathbf{x}(t), t) d\Omega_t = \int_{\Omega_t} \frac{\partial f}{\partial t}(\mathbf{x}(t), t) d\Omega_t + \int_{\partial\Omega_t} f(\mathbf{x}(t), t) \mathbf{v}(t, \mathbf{x}(t)) \cdot \mathbf{n} d\Gamma,$$

where \mathbf{n} is the outward-pointing unit normal vector.

Robin's boundary conditions are used here since it models a balance between the diffusive flux from the domain of computation and the mass transfer into the surroundings around the domain of computation. The symbol κ , which is non-negative, represents the mass transfer coefficient. Note that as $\kappa \rightarrow 0$ then the Robin condition tends to a homogeneous Neumann condition, which represents no flux (hence isolation). Whereas as $\kappa \rightarrow \infty$ represents the case that $c \rightarrow 0$ on the boundary, which, physically, is reminiscent to having an infinite mass flow rate at the boundary into the surroundings. The Robin condition, also referred to as a mixing boundary condition, is able to deal with both these two limits and all cases between these limits.

With Robin's boundary condition and applying Reynold's theorem (Th. 2.1), the Galerkin's form of Eq (2.6) is

$$\left\{ \begin{array}{l} \text{Find } c_h(\mathbf{x}, t) \in C_h^1([0, T] \times H_h^1(\Omega_t)) \cap C_h^0([0, T] \times H_h^1(\Omega_t)), \text{ such that} \\ \frac{d}{dt} \int_{\Omega_t} c_h(\mathbf{x}, t) \phi_h(\mathbf{x}(t)) d\Omega_t + \int_{\Omega_t} D \nabla \phi_h(\mathbf{x}(t)) \nabla c_h(\mathbf{x}, t) d\Omega_t + \int_{\partial\Omega_t} \kappa c_h(\mathbf{x}, t) \phi_h(\mathbf{x}(t)) d\Gamma_t \\ = \int_{\Omega_t} F \phi_h(\mathbf{x}(t)) d\Omega_t, \\ \forall \phi_h(\mathbf{x}(t)) \in H_h^1(\Omega_t), \end{array} \right.$$

where $c_h(\mathbf{x}, t)$ is the numerical solution of the concentration at time t .

Furthermore, linear triangular basis functions are utilised to derive Galerkin's form. Since the basis function is attached to vertices, it can be concluded that for the basis function at any mesh point i , we have $\frac{D\phi_j(\mathbf{x}(t))}{Dt} = 0$ [52] for all $j \in \{1, \dots, N_h\}$ where N_h is the number of nodal points in the domain. In our computational implementation, the backward Euler method is applied to integrate over time, and we only give the time dependence here in the Galerkin's form:

$$\left\{ \begin{array}{l} \text{Find } c_h(\mathbf{x}, t) \in C^1([0, T] \times H_h^1(\Omega_t)) \cap C^0([0, T] \times H_h^1(\Omega_t)), \text{ such that} \\ \frac{1}{\Delta t} \left(\int_{\Omega_{t+\Delta t}} c_h(t + \Delta t) \phi_h(\mathbf{x}(t + \Delta t)) d\Omega_{t+\Delta t} - \int_{\Omega_t} c_h(t) \phi_h(\mathbf{x}(t)) d\Omega_t \right) \\ + \int_{\Omega_{t+\Delta t}} D \nabla \phi_h(\mathbf{x}(t + \Delta t)) \nabla c_h(t + \Delta t) d\Omega_{t+\Delta t} \\ + \int_{\partial\Omega_{t+\Delta t}} \kappa c_h(t + \Delta t) \phi_h(\mathbf{x}(t + \Delta t)) d\Gamma_{t+\Delta t} = \int_{\Omega_{t+\Delta t}} F \phi_h(\mathbf{x}(t + \Delta t)) d\Omega_{t+\Delta t}, \\ \forall \phi_h(\mathbf{x}(t)) \in H_h^1(\Omega_t), \end{array} \right.$$

where $c_h(\mathbf{x}, t)$ is the numerical solution of the concentration at time t . To distinguish between the cytokines, we add the subscript "PDGF", "TGF" or "tPA" if it is necessary. As for the velocity of the environment (i.e. the extracellular matrix) where all the biological elements live on, We, indeed, compute the displacement from the solution of the balance of momentum. Subsequently, the velocity is post-processed from the numerical time derivative, where following [53] $\mathbf{v}(t, \mathbf{x}(t)) = \frac{D\mathbf{u}(t, \mathbf{x}(t))}{Dt}$, and hence we get

$$\mathbf{v}(t, \mathbf{x}(t)) \approx \frac{\mathbf{u}(t + \Delta t, \mathbf{x}(t + \Delta t)) - \mathbf{u}(t, \mathbf{x}(t))}{\Delta t}.$$

The platelet derived signalling molecules have been regenerated by the platelets. We assume that the platelets are no longer active and therefore the platelet derived signalling molecules are only subject to diffusion. Alternative processes such as regeneration and decay are neglected. Thus, the equation to determine the concentration of PDGF is given by

$$\frac{\partial c_{PDGF}}{\partial t} + \nabla \cdot [c_{PDGF} \cdot \mathbf{v}(t, \mathbf{x}(t))] - D_{PDGF} \Delta c_{PDGF} = 0, \quad (2.7)$$

where D_{PDGF} is the diffusion coefficient given in Table 2.1.

Regarding the concentration of TGF-beta, it is widely documented that macrophages are the one of the main sources [2, 3, 41]. Therefore, each viable macrophage is a point source of TGF-beta and hence Dirac Delta distributions are used. Furthermore, we assume that the diffusion coefficient of the signalling molecule is linearly dependent on the local density of the fibrin molecules [9]. All these assumptions yield the following equation to determine the concentration of TGF-beta:

$$\frac{\partial c_{TGF}}{\partial t} + \nabla \cdot [c_{TGF} \cdot \mathbf{v}(t, \mathbf{x}(t))] - \nabla \cdot [D_{TGF}(\rho^f) \nabla c_{TGF}] = k_{TGF} \sum_{i=1}^{T_M(t)} \delta(\mathbf{x} - \mathbf{x}_i), \quad (2.8)$$

with

$$D_{TGF}(\rho^f) = (\alpha_\rho \rho^f) D_{TGF}^{min} + (1 - \alpha_\rho \rho^f) D_{TGF}^{max}.$$

Here, D_{TGF}^{min} and D_{TGF}^{max} are the minimum and maximum diffusion coefficient of tPA, k_{TGF} is the secretion coefficient of TGF-beta of each macrophage and α_ρ is a given positive constant. All the parameter values are given in Table 2.1.

FORCE BALANCE

The (myo)fibroblasts exert pulling forces on their immediate surroundings in the extracellular matrix. These forces are directed towards the cell centre and cause local displacements and deformation of the extracellular matrix. The combination of all these forces causes a net contraction of the tissue around the region where the fibroblasts are actively exerting forces. The (myo)fibroblast exert pulling forces on their immediate environment. Next to these forces, they change the local environment in a way that residual forces remain after their presence. Therefore we consider two types of forces: temporary force (\mathbf{f}_t) and plastic force (\mathbf{f}_p).

As it is stated before, the force results in the deformation of the skin surrounding the wound. Neglecting inertia, the balance of momentum in Ω_t reads as:

$$-\nabla \cdot \underline{\underline{\sigma}} = \mathbf{f}_t + \mathbf{f}_p. \quad (2.9)$$

From a mechanical point of view, we treat the computational domain as continuous, linear and isotropic. Further, as a result of the presence of liquid phases in the tissue, the mechanical balance is also subject to viscous, that is friction, effects. Therefore, we use Kelvin-Voigt's viscoelastic dashpot model, which in essence reads as

$$\underline{\underline{\sigma}} = \underline{\underline{E}} \underline{\underline{\epsilon}} + \underline{\underline{\mu}} \dot{\underline{\underline{\epsilon}}},$$

where $\dot{\underline{\epsilon}}$ denotes the time derivative of $\underline{\epsilon}$, \underline{E} and $\underline{\mu}$ are linear tensors and they will be specified now. We decompose the total stress by

$$\underline{\sigma} = \underline{\sigma}_{elas} + \eta \underline{\sigma}_{visco} \quad (2.10)$$

where η is the weight of the viscoelasticity stress tensor, $\underline{\sigma}_{elas}$ is

$$\underline{\sigma}_{elas} = \frac{E_s}{1+\nu} \left\{ \underline{\epsilon} + tr(\underline{\epsilon}) \left[\frac{\nu}{1-2\nu} \right] \underline{I} \right\}, \quad (2.11)$$

and $\underline{\sigma}_{visco}$ is

$$\underline{\sigma}_{visco} = \frac{E_s}{2(1+\nu)} \dot{\underline{\epsilon}} + \frac{2}{3} \times \frac{E_s}{2(1+\nu)} \nabla \cdot \dot{\underline{\mathbf{u}}}. \quad (2.12)$$

In the above equations, E_s is the Young's modulus of the domain, ν is Poisson's ratio, $\underline{\epsilon}$ is the infinitesimal strain tensor and $\dot{\underline{\mathbf{u}}}$ is the time derivative of $\underline{\mathbf{u}}$, that is,

$$\underline{\epsilon} = \frac{1}{2} [\nabla \underline{\mathbf{u}} + (\nabla \underline{\mathbf{u}})^T]. \quad (2.13)$$

The above PDE provides a good approximation if the strains are relatively small. Combined with Robin's boundary condition

$$\underline{\sigma} \cdot \mathbf{n} + \kappa_f \underline{\mathbf{u}} = \mathbf{0},$$

where κ_f is a non-negative constant representing a spring force constant between the computational domain and its far away surroundings, the displacement $\underline{\mathbf{u}}$ of the extracellular matrix where all the biological components are, can be determined by Eq (2.9). Note that if $\kappa_f \rightarrow \infty$, then $\underline{\mathbf{u}} \rightarrow \mathbf{0}$ which represents a fixed boundary, and $\kappa_f \rightarrow 0$ represents a free boundary in the sense that no external force is exerted on the boundary.

Temporary Force

Temporary forces are characterised by (myo)fibroblasts exerting forces from the boundary of the cell onto their immediate surroundings. Once there is no cell, the deformation caused by the forces will disappear. For cell i , the cell boundary Γ^i is divided into finite line segments in two-dimensional case. We assume that an inward directed force is exerted as a point force at the midpoint of every line segment in the normal direction to the line segment. The total force is a linear combination of every force at every segment. Hence, at time t , the total temporary force is expressed by

$$\mathbf{f}_t(t) = \sum_{i=1}^{T_N(t)} \sum_{j=1}^{N_S^i} P(\mathbf{x}_j^i, t) \mathbf{n}(\mathbf{x}_j^i(t)) \delta(\mathbf{x} - \mathbf{x}_j^i(t)) \Delta \Gamma_N^{i,j}, \quad (2.14)$$

where $T_N(t)$ is the number of cells at time t , N_S^i is the number of line segments of cell i , $P(\mathbf{x}, t)$ is the magnitude of the pulling force exerted at point \mathbf{x} and time t per length, $\mathbf{n}(\mathbf{x})$ is the unit inward pointing normal vector (towards the cell centre) at position \mathbf{x} , $\mathbf{x}_j^i(t)$ is the midpoint on line segment j of cell i at time t and $\Delta \Gamma_N^{i,j}$ is the length of line segment

j. This method is also used in fluid dynamics, and is known as the immersed boundary method. Theoretically, as $N_S^i \rightarrow \infty$, i.e. $\Delta\Gamma_N^{i,j} \rightarrow 0$, Eq (2.14) becomes [41]

$$\mathbf{f}_t(t) = \sum_{i=1}^{N(t)} \int_{\partial\Omega_N^i} P(\mathbf{x}^i, t) \mathbf{n}(\mathbf{x}^i(t)) \delta(\mathbf{x} - \mathbf{x}^i(t)) d\Gamma_N^i, \quad (2.15)$$

Here, $\mathbf{x}^i(t)$ is a point on the cell boundary of cell *i* at time *t*.

For the sake of computational efficiency, each cell is divided into three boundary segments [54]. Therefore, $N_S^i = 3$ in Equation (2.14).

Plastic Force

Plastic forces occur as a result of the changes that myofibroblasts inflict on their immediate surroundings. On the one hand, these forces are caused by large deformations, but also by the chemical decomposition of collagen chains into shorter chains. The shortening of the chains causes stresses and strains in the cross-linked network of collagen molecules. The modelling of the permanent forces proceeds similarly to the modelling of the temporary forces with the only difference that the forces are not acting on the cellular boundary but on the boundary of an element of the finite-element mesh. Similarly to the temporary forces, the total plastic force on the boundary segments of the elements of the mesh at time *t* is expressed by [41]

$$\mathbf{f}_p = \sum_{i=1}^{N_E} \sum_{e=1}^{N_e^i} Q(\tau^i) \mathbf{n}(\mathbf{x}) \delta(\mathbf{x} - \mathbf{x}_e^i(t)) \Delta\Gamma_E^{i,e}, \quad (2.16)$$

where N_E is the total number of mesh triangular elements, N_e^i is the total number of edges of the mesh triangular elements, $Q(\tau^i)$ is the magnitude of the plastic force density at efficient exposure time τ^i of myofibroblast, $\mathbf{n}(\mathbf{x})$ is the unit inward pointing normal vector, $\mathbf{x}_e^i(t)$ is the midpoint and $\Delta\Gamma_E^{i,e}$ is the length of the edge respectively. We note that this framework is sufficiently general to extend to different element shapes.

Note that here the magnitude of the force is a function of the exposure time τ^i of the element by the myofibroblasts, denoted by $Q(\tau^i)$. In Koppenol [17], it was hypothesized that the effective exposure of each element on the finite-element mesh was expressed by

$$\frac{d\tau^i}{dt} = c_{TGF}(\mathbf{x}_E^i) (1 - \alpha_\rho \rho^c(\mathbf{x}_E^i)) \frac{A(\Omega_C \cap \Omega_{e_i})}{A(\Omega_{e_i})}, \quad (2.17)$$

where \mathbf{x}_E^i is the central point of the mesh element *i*, $\rho^c(\mathbf{x}_E^i)$ is the density of collagen at \mathbf{x}_E^i , $A(\Omega_C \cap \Omega_{e_i})$ is the area of the intersection of the cell and mesh element *i* and $A(\Omega_{e_i})$ is the area of mesh element *i*. Note that the area ratio $\frac{A(\Omega_C \cap \Omega_{e_i})}{A(\Omega_{e_i})}$ will not exceed unity. However, to implement into the computation, it is hard to calculate this ratio explicitly. Therefore, we rewrite Equation (2.17). Since it is not straightforward from a computational point of view to compute the area of overlap, we simplify this operation by

$$\frac{d\tau^i}{dt} = c_{TGF}(\mathbf{x}_E^i) (1 - \alpha_\rho \rho^c(\mathbf{x}_E^i)) N_{m_{yo}}^i, \quad (2.18)$$

where N_{myo}^i is the number of myofibroblasts that the central point of mesh element i is in.

The magnitude of the plastic force density is a function of exposure time τ^i :

$$Q(\tau^i) = Q_{max}(1 - e^{-\tau^i}), \quad (2.19)$$

where Q_{max} is the maximal magnitude of the plastic force density.

ORIENTATION OF TISSUES

Dallon *et al.* [55] and Cumming *et al.* [3] introduced vector-based representations of collagen and fibrin. The approach by Cumming *et al.* [3] is tensor-based and since this makes it straightforward to incorporate the impact from the orientation on the migration path of the cells, we use the formalism by Cumming *et al.* [3].

The orientation of the bundles and the density of collagen molecules at position \mathbf{x} and time t are determined by the general symmetric tensor:

$$\underline{\Omega}^k(\mathbf{x}, t) = \int_0^\pi \mathbf{p}(\theta) \mathbf{p}(\theta)^T \rho(\mathbf{x}, t, \theta) d\theta, \quad (2.20)$$

where k indicates the type of the tissue: f for fibrin and c for collagen, $\mathbf{p}(\theta)^T = [\cos\theta, \sin\theta]$ is the unit vector in the direction θ , and $\rho(\mathbf{x}, t, \theta)$ is the density of collagen at position \mathbf{x} and time t . Note that in this chapter, $\underline{\Omega}^k$ and $\Omega_{i,j}^k$ denotes the tensor of fibrin or collagen and the entries in the tensor, respectively. The density of collagen can be determined by the trace of $\underline{\Omega}^k$, that is, the summation of the eigenvalues or diagonal entries. Since the tensor is symmetric positive definite, it can be decomposed as the sum of weighed outer products of orthonormal eigenvectors, which in the two-dimensional case gives:

$$\underline{\Omega}^k(\mathbf{x}, t) = \lambda_1(\mathbf{x}, t) \mathbf{v}_1(\mathbf{x}, t) \mathbf{v}_1(\mathbf{x}, t)^T + \lambda_2(\mathbf{x}, t) \mathbf{v}_2(\mathbf{x}, t) \mathbf{v}_2(\mathbf{x}, t)^T,$$

where $\lambda_1(\mathbf{x}, t)$ and $\lambda_2(\mathbf{x}, t)$ are eigenvalues. The orientation of the eigenvectors illustrates the direction of alignment, and

$$e = 1 - \frac{\lambda_{min}}{\lambda_{max}},$$

represents the degree of anisotropy. Note that if both eigenvalues are equal, then the dermal layer is completely isotropic, which renders $e = 0$.

We incorporate the breakdown of the provisional fibrin-based extracellular matrix into the model. Assuming the degradation rate of the fibrin bundles to be determined by the concentration of tPA and the concentration of the fibrin bundles themselves [17], then for any entry in the fibrin orientation tensor, we have

$$\frac{\partial \Omega_{ij}^f}{\partial t} + \nabla \cdot [\Omega_{ij}^f \cdot \mathbf{v}(t, \mathbf{x}(t))] = -\delta_\rho [c_{tPA} \Omega_{ij}^f], \quad (2.21)$$

for any $i, j \in \{1, 2\}$ and δ_ρ represents the degradation rate of fibrin bundles. Note that the \mathbf{v} -term accounts for the mesh movement velocity.

The concentration of tPA, is assumed that it is only secreted on the edge between the injured and uninjured regions. In addition, based on Koppenol [17], the diffusion

coefficient of tPA is related to the local concentration of fibrin molecules. Hence, the equation below is used to derive the concentration of tPA:

$$\frac{\partial c_{tPA}}{\partial t} + \nabla \cdot [c_{tPA} \cdot \mathbf{v}(t, \mathbf{x}(t))] = \nabla \cdot [D_{tPA}(\rho^f) \nabla c_{tPA}] + k_{tPA} \delta_{\partial\Omega_w}, \quad (2.22)$$

where

$$D_{tPA}(\rho^f) = (\alpha_\rho \rho^f) D_{tPA}^{\min} + (1 - \alpha_\rho \rho^f) D_{tPA}^{\max}.$$

Here, D_{tPA}^{\min} and D_{tPA}^{\max} are the minimum and maximum diffusion coefficient of tPA, k_{tPA} is the secretion rate of tPA by damaged endothelial cells and α_ρ is a given positive constant. We define the distributions $\delta_{\partial\Omega_w}$ as

$$\delta_{\partial\Omega_w}(\mathbf{x}) \begin{cases} = 0, & \text{if } \mathbf{x} \notin \partial\Omega_w, \\ > 0, & \text{if } \mathbf{x} \in \partial\Omega_w, \end{cases}$$

such that for any region $A \subset \Omega$, there is

$$\int_A \delta_{\partial\Omega_w}(\mathbf{x}) d\Omega = \frac{\mu(A \cap \partial\Omega_w)}{\mu(\partial\Omega_w)},$$

in which the measure $\mu: \partial\Omega_w \rightarrow \mathbb{R}^+$ is the length of the curve $\partial\Omega_w$.

The collagen bundles are deposited by the (myo)fibroblasts in the direction of **active** migration. Since the cells are much smaller than the computational domain, we use Dirac Delta functions to model the secretion of the collagen bundles. Furthermore, the secretion rate depends on the amount of total density including fibrin and collagen. This amounts (see also Cumming *et al.* [3], Koppelol [17], Boon *et al.* [41])

$$\begin{aligned} & \frac{\partial \Omega_{ij}^c}{\partial t} + \nabla \cdot [\Omega_{ij}^c \cdot \mathbf{v}(t, \mathbf{x}(t))] \\ &= \sum_{k=1}^{T_N(t)} \left(1 - \alpha_\rho [\rho^f(\mathbf{x}_N^k(t)) + \rho^c(\mathbf{x}_N^k(t))] \right) [\mathbf{r}_N^k(t) (\mathbf{r}_N^k(t))^T]_{ij} \delta(\mathbf{x} - \mathbf{x}_N^k(t)), \end{aligned} \quad (2.23)$$

where $\mathbf{r}_N^k(t) = (d\mathbf{x}_N^k(t) - \mathbf{v}dt) / \|d\mathbf{x}_N^k(t) - \mathbf{v}dt\|$ is the unit vector of the direction of active displacement of (myo)fibroblast k at time t for any $i, j \in \{1, 2\}$, and $\mathbf{x}_N^k(t)$ is the centre position of (myo)fibroblast with index k , see Eq (2.26).

As collagen bundles are one of the main components of the healthy ECM, the collagen density ratio is an important indicator of the healing progress. In our model, we assume that the ECM is composed of fibrin bundles and collagen bundles. Hence, we introduce the collagen density ratio as the proportion of all the tissue bundles in the wound:

$$\hat{\rho}^c(t) = \frac{\int_{\Omega_w(t)} \rho^c d\Omega}{\int_{\Omega_w(t)} \rho_0^c d\Omega}, \quad (2.24)$$

where ρ^c and ρ_0^c denotes the density of collagen bundles in the injured skin and undamaged skin respectively. Note that initially, the ratio is 0 since the fibrin bundles occupy the wound in the form of blood clot. As time proceeds, the fibrin bundles are degenerated by tPA, and collagen is expressed by the (myo)fibroblasts, and therewith, the collagen density ratio increases to 1 finally.

DISPLACEMENT OF VARIOUS CELL PHENOTYPES

Generally speaking, to determine the position of any cell in the semi-stochastic cell-based model is a combination of interactions between cells, namely repulsion when there is mechanic contact for any two cells; chemotaxis, which is related to the signalling molecules; passive convection due to the displacement of the substrate and random walk. In addition, random walk, is also embedded within the displacement model. Let $d\mathbf{W}(t)$ represent a vector Wiener process in which the contributions to the different coordinate directions are treated as independent events. This Wiener process models random walk, that is diffusion, of the cell. Note that $\sigma_{rw} = \sqrt{2D_c}$, where D_c represents the diffusion coefficient of the cell phenotype of cell i .

For the immune cells, chemotaxis is associated with PDGF, then the displacement of the center position of i -th macrophage is given by

$$\begin{aligned} d\mathbf{r}_i(t) = & \alpha_i \hat{M}(\mathbf{r}_i) \hat{\mathbf{z}}_i dt + \mu_c \frac{\nabla c_{PDGF}}{\|\nabla c_{PDGF}\| + \gamma} dt + \mathbf{v} dt \\ & + \sigma_{rw} d\mathbf{W}(t), \text{ for all } i \in \{1, \dots, n\}, \end{aligned} \quad (2.25)$$

where μ_c is the constant representing the weight of chemotaxis, which is expressed by

$$v \left(1 - \alpha_\rho \frac{\rho^f + \rho^c}{2} \right),$$

here, v is the speed of biased movement of cells, c_{PDGF} is the concentration of PDGF which is initially high in injured region and low in uninjured region, γ is a small positive constant to prevent the denominator being zero and \mathbf{v} is the displacement velocity of the substrate, which follows from solving the momentum balance.

For (myo)fibroblasts, except the concentration part is related to TGF-beta, the rest is the same as for macrophages, i.e. for i -th (myo)fibroblast, the new position is derived by

$$\begin{aligned} d\mathbf{r}_i(t) = & \alpha_i \hat{M}(\mathbf{r}_i) \hat{\mathbf{z}}_i dt + \mu_c \left\{ [1 - \alpha_\rho \rho^c(\mathbf{r}_i(t))] \underline{I} \right. \\ & \left. + [\alpha_\rho \rho^c(\mathbf{r}_i(t)) \underline{\Omega}^c(\mathbf{r}_i(t))] \right\} \frac{\nabla c_{TGF}}{\|\nabla c_{TGF}\| + \gamma} dt \\ & + \mathbf{v} dt + \sigma_{rw} d\mathbf{W}(t), \text{ for all } i \in \{1, \dots, n\}, \end{aligned} \quad (2.26)$$

where μ_c is the same expression as before, c_{TGF} is the concentration of TGF-beta secreted by macrophages.

In Eq (2.25) and Eq (2.26), α_i stands for a cell motility parameter with dimension $\left[\frac{h \cdot \mu m}{kg} \right]$ of which the expression is

$$\alpha_i = \frac{\beta_i R^3}{\mu F_i},$$

as outlined in Gefen [56]. Here, β_i represents a coefficient for the mobility of the portion of the cell surface that is in physical contact with the substrate of another cell, and dimensionless parameter μ is the friction coefficient between the cell surface and the underlying substrate [56]. The values of the parameters have been listed in Table 2.1.

2.2.3. INITIAL SETTINGS OF THE MODEL

Initially, there are no myofibroblasts. The TGF-beta concentration determines the differentiation rate of fibroblasts to myofibroblasts. Macrophages are uniformly distributed on the edge between wound and the undamaged region. The fibroblasts are initially distributed randomly in the undamaged region.

It is assumed that the concentration of PDGF is higher in the injured region and lower in the undamaged region. In order to specify the concentration, we introduce the following indicator function

$$\mathbb{1}_{\Omega_w} = \begin{cases} 1, & \mathbf{x} \in \Omega_w, \\ 0, & \mathbf{x} \notin \Omega_w, \end{cases} \quad (2.27)$$

where Ω_w is the wound region as a subdomain in the computational domain. Subsequently, the initial setting of PDGF is

$$c_{PDGF}^0(\mathbf{x}) = \mathbb{1}_{\Omega_w} c_{PDGF}^0,$$

where c_{PDGF}^0 is given in Table 2.1. Since TGF-beta is mainly secreted by macrophages, the initial condition of it is zero everywhere over the computational domain, that is,

$$c_{TGF}^0(\mathbf{x}) = 0, \quad \text{in } \Omega_t.$$

As for tPA, the concentration is higher on the edge between injured and uninjured region and lower in the rest part:

$$c_{tPA}^0(\mathbf{x}) = \begin{cases} c_{tPA}^{\Gamma_w}, & \mathbf{x} \in \partial\Omega_w, \\ 0, & \text{otherwise,} \end{cases}$$

where $\partial\Omega_w$ is the edge between wound and healthy skin, and $c_{tPA}^{\Gamma_w}$ is given in Table 2.1.

Initially, the material is assumed to be in mechanical equilibrium. Therefore, there are no stresses and strains.

It is assumed that the initial collagen and fibrin are isotropic. Therefore, we have

$$\frac{\underline{\Omega}^f}{0} = \frac{\mathbb{1}_{\Omega_w}}{2\alpha_\rho} \underline{I} = \frac{\mathbb{1}_{\Omega_w}}{2\alpha_\rho} \begin{bmatrix} 1 & 0 \\ 0 & 1 \end{bmatrix}, \quad (2.28)$$

and

$$\frac{\underline{\Omega}^c}{0} = \frac{1 - \mathbb{1}_{\Omega_w}}{2\alpha_\rho} \underline{I} = \frac{1 - \mathbb{1}_{\Omega_w}}{2\alpha_\rho} \begin{bmatrix} 1 & 0 \\ 0 & 1 \end{bmatrix}, \quad (2.29)$$

where $\mathbb{1}_{\Omega_w}$ is the indicator function that was introduced in Eq (2.27) and α_ρ is a positive constant.

2.3. NUMERICAL RESULTS

The finite-element method has been embedded within the FEniCS [46] package that has been implemented in Python. Based on the size of the computational domain (see Figure 2.2), averagely each time iteration takes 5–7 seconds depending on the total number of cells in the domain as well. Since the computational efficiency is not the focus of this chapter, the algorithm has not been optimized yet. Computations have been done on an Intel(R) Core(TM) i7-6500U CPU @ 2.50GHz computer.

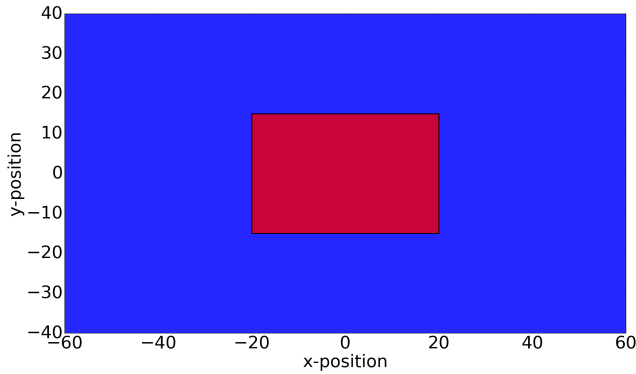


Figure 2.2: The computational domain in two dimensions is $(-60, 60) \times (-40, 40)$, in which the wound region is $(-20, 20) \times (-15, 15)$ depicted by red and the undamaged tissue is depicted by blue.

2.3.1. DISPLACEMENTS OF CELLS

Firstly, we study the dynamics of the different cell phenotypes as a function of time. In Figure 2.3, we show the different cell phenotypes that are indicated by different colours. The red, green and blue circles represent the immune cells, myofibroblasts and fibroblasts, respectively. In the early stages, it can be seen that the fibroblasts are only distributed over the undamaged domain and that the immune cells are scattered over the interface between the wound and undamaged area. As time proceeds, the immune cells migrate into the wound where they release the growth factor TGF-beta. The build-up of the TGF-beta triggers the ingress of fibroblasts, which in turn differentiate to myofibroblasts. In the intermediate stages, it can be seen that the wound region contains myofibroblasts, which are responsible for the largest portion of temporary forces and displacements and which also facilitate the permanent displacements. During this stage, the immune cells are subject to apoptosis and therewith disappear. At the later stages, the myofibroblasts are subject to apoptosis and the wound region is occupied by fibroblasts.

In Figure 2.4, the cell counts for the various phenotypes are shown. The figure shows 10 runs of simulations. It can be seen that in the early stages the immune cells accumulate and the damaged region is cleaned. The immune cells trigger the ingress of fibroblasts, and upon decreasing cell counts of immune cells, the counts of myofibroblasts accumulate. Subsequently, after having regenerated collagen, the counts of myofibroblasts decrease as a result of apoptosis. The increased counts of fibroblasts drop back to numbers that are reminiscent to the undamaged state.

2.3.2. CONCENTRATION OF SIGNALLING MOLECULES AND DENSITY OF TISSUE BUNDLES

Initially the PDGF concentration is maximal near the interface between the undamaged region and wounded region. This can be seen in Figure 2.5(a). As time proceeds, diffusion flattens the profiles of the PDGF concentration and the concentration tends to

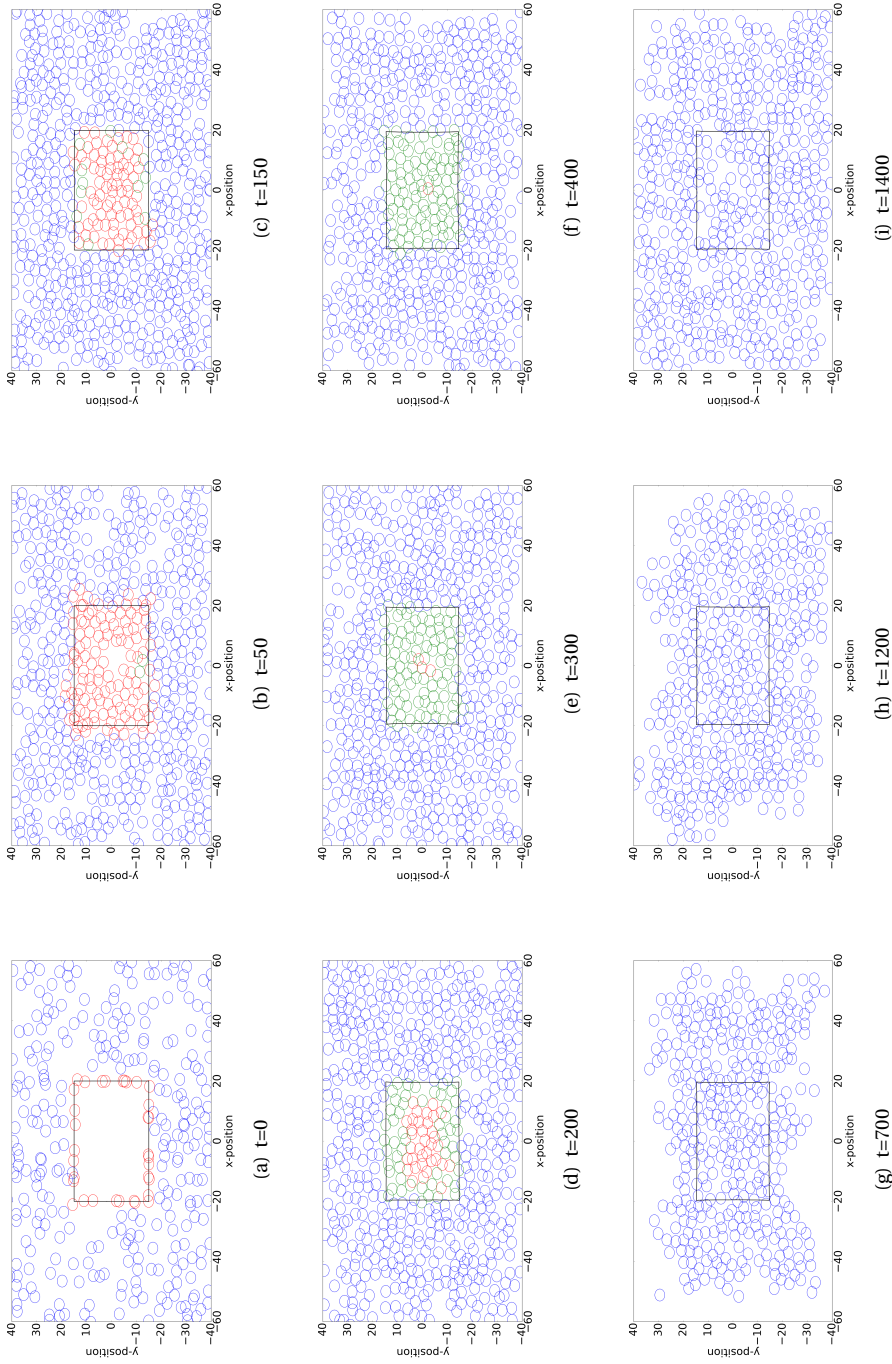


Figure 2.3: The plots show the positions of three categories of cells in the computational domain. Red, blue and green circles represent macrophages, regular fibroblasts and myofibroblasts respectively. The rectangular shape in the middle is the wound region at different time. The parameter values used to solve the partial differential equations are taken from Table 2.1.

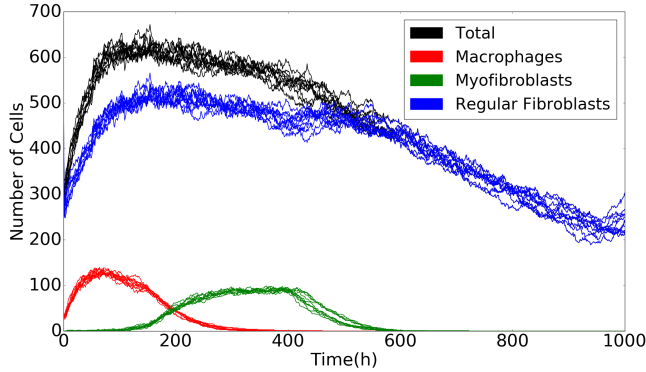


Figure 2.4: The plot shows the number of various phenotypes of cells changes over time with multiple simulations. The blue, red and green curves represent regular fibroblasts, macrophages and myofibroblasts respectively. The black curves represent the total count of all the cells in the computational domain. The parameter values used to solve the partial differential equations are taken from Table 2.1.

zero due to diffusion to the outer surroundings. The TGF-beta is regenerated by the immune cells and hence as long as the immune cells are in the wounded region, then the concentration increases. At later stages, the immune cells disappear and therewith the concentration of TGF-beta no longer increases and starts decreasing and flattening as a result of diffusion. The gradient of the TGF-beta makes the fibroblasts migrate to the wound site. The peak of the TGF-beta concentration is at around 100 hours post wounding, which is in line with the experimental observations from Dallon *et al.* [57].

As cells are proliferating, migrating and subject to apoptosis, they secrete chemicals like PDGF and TGF-beta. Hence, next to diffusion, these chemicals are subject to regeneration and decay. Since PDGF is present initially as a result of platelets, this agent is active during a relatively short time since the platelets are subject to apoptosis shortly after wounding. Due to diffusion into the tissue and due to lack of regeneration, PDGF vanishes shortly after wounding. The immune cells are attracted towards the wound region by PDGF and the immune cells secrete TGF-beta. Hence, the peak in TGF-beta follows the peak of the PDGF. After a while, the immune cells disappear, which also makes the source of TGF-beta vanish and hence due to long distance diffusion, the concentration of TGF-beta decays down to zero. The dynamics of the fields of PDGF and TGF-beta can be seen in Figures 2.5 and Figure 2.6, respectively.

The damage on skin is characterised by loss of extracellular matrix and cells. A pivotal aspect of wound healing is the restoration of collagen. Before collagen is deposited, first a fibrin network is established by the platelets by means of polymerisation. In the modelling, we assume the fibrin network to have laid down by the platelets. Initially we assume the fibrin network (blood cloth) to exist in the damaged region. In the first stage the fibrin network is decomposed by the agent tPA. Subsequently, the fibrin network is replaced with collagen by the fibroblasts. The orientation of the deposited collagen is determined by the direction of migration of the (myo)fibroblasts. The dynamics of the fibrin and collagen density are shown in Figures 2.7 and Figure 2.8, respectively.

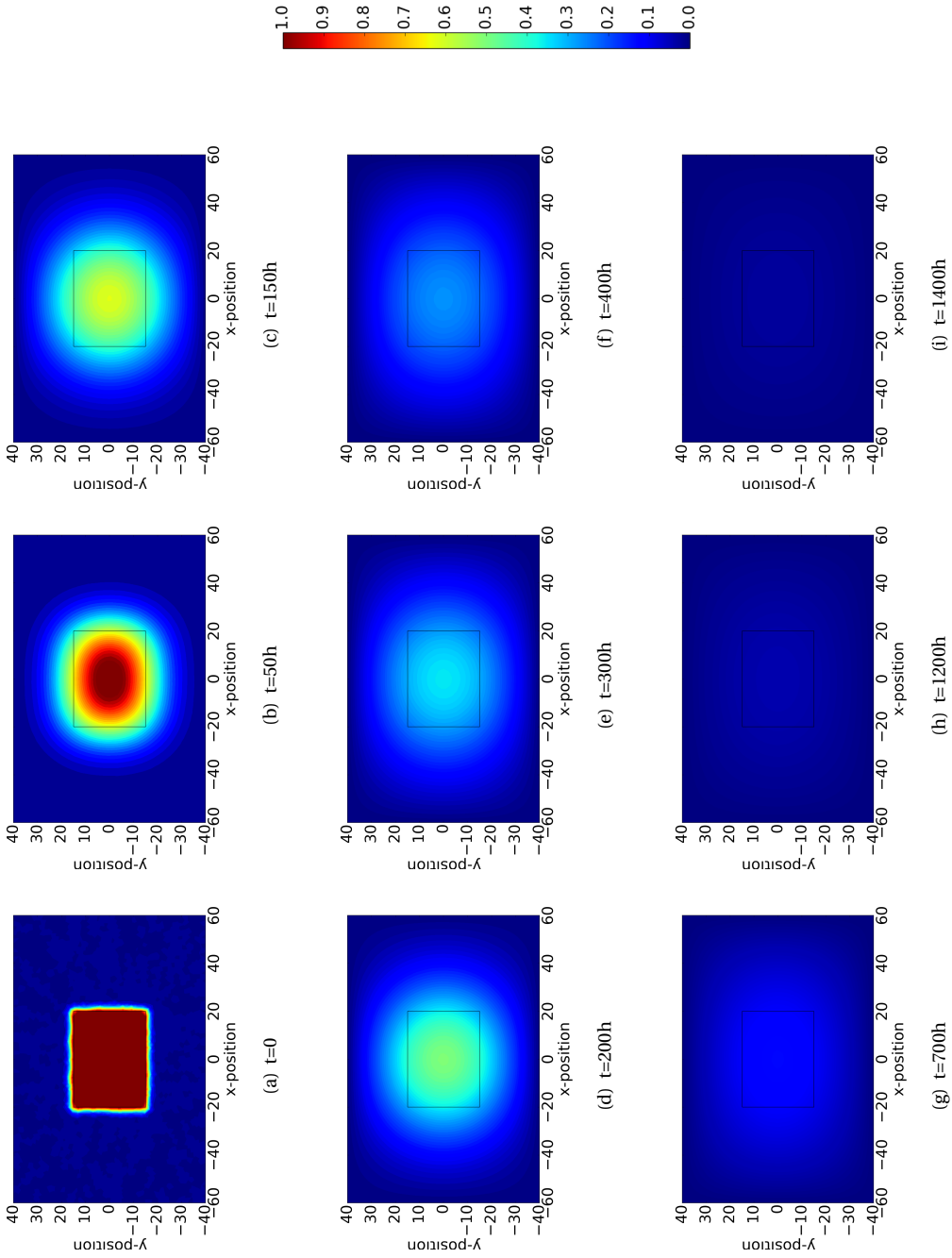


Figure 2.5: The plots show the dynamics of PDGF, which induces the displacements of macrophages. The results are derived by solving Eq (2.7) with Robin's boundary condition. The parameter values used to solve the partial differential equations are taken from Table 2.1.

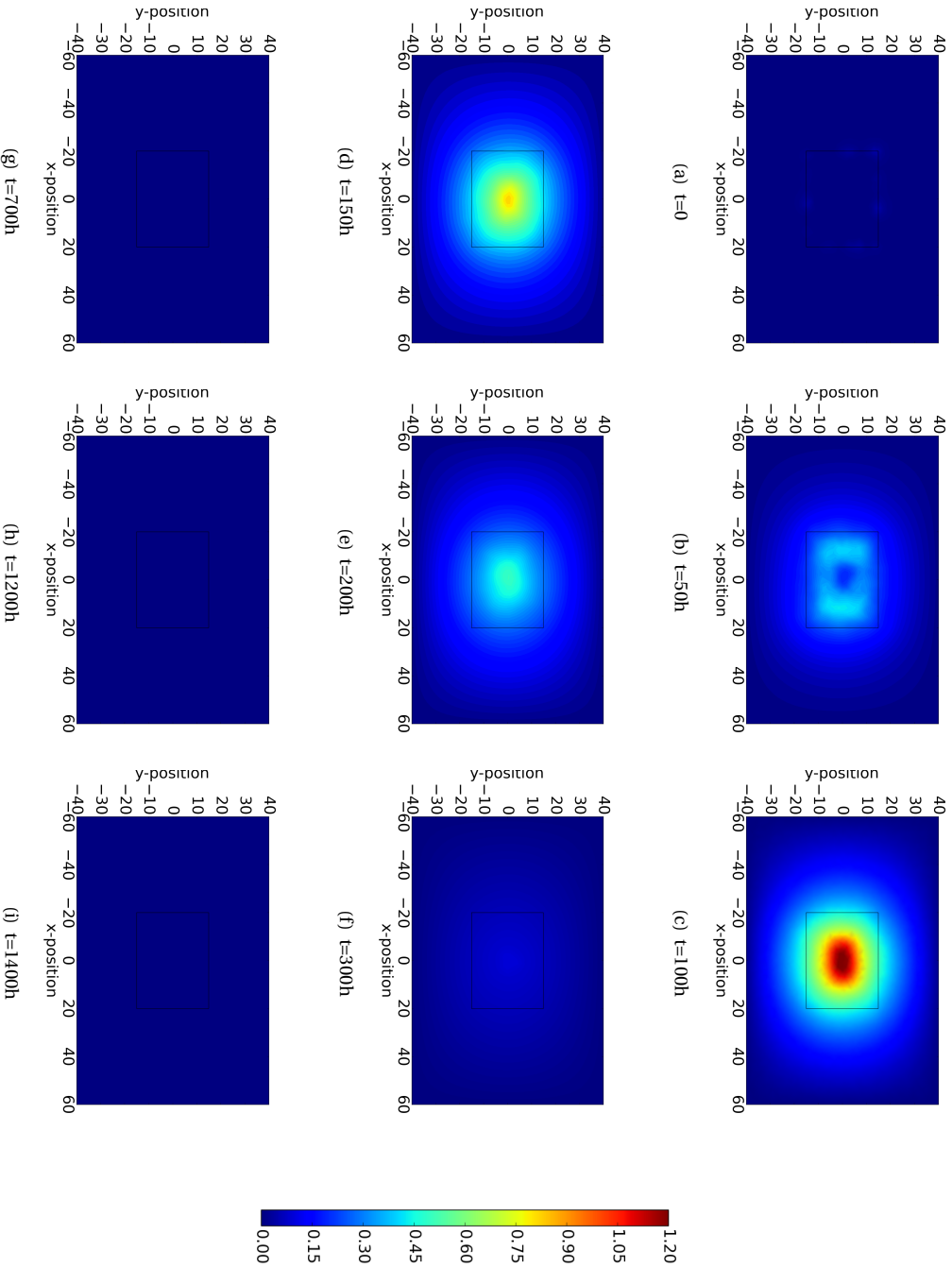


Figure 2.6: The plots show the dynamics of TGF- β , which induces the displacements of (myo)fibroblasts and the differentiation from the regular fibroblasts to the myofibroblasts. The results are derived by solving Eq (2.8) with Robin's boundary condition. The parameter values used to solve the partial differential equations are taken from Table 2.1.

Figure 2.7 illustrates the initial occupance of the wound region by the fibrin network and in the undamaged region there is no fibrin. Gradually, the fibrin network is subject to decay as a result of the tPA agent. Figure 2.8 shows that initially the collagen density is zero in the wounded region, whereas the undamaged region possesses the equilibrium value of collagen. As time proceeds the fibrin network decays in the wounded region, whereas the collagen density increases due to regeneration by the (myo)fibroblasts. The orientation of the collagen bundles guide the migration of (myo)fibroblasts, see [3, 17, 58], which is shown by Figures 2.8(d) and 2.8(e).

2.3.3. STRAIN ENERGY IN THE WOUND

Strain energy represents a measure of potential energy that is present in the tissue region. This potential energy results due to deformation and is computed by the integral over the computational region of half of the tensor inner product of the strain and stress tensors. Since it is believed that strain causes pain or itchy sensations to the patient, we use this quantity as a measure of pain that a patient has. Therefore we are interested in the dynamics of this parameter, as well as the parameter yields understanding to the dynamics of the deformation and contraction of the wound.

The (myo)fibroblasts are responsible for the deformation of the tissue and hence these cells make the strain energy density increase locally and globally. Since initially the tissue is in mechanical equilibrium and since initially there are no (myo)fibroblasts present in the wound area, the strain energy density is zero in the wound initially. As time proceeds, the fibroblasts enter the wound region and myofibroblasts appear there, the strain energy locally increases in the wound area. The dynamics of the strain energy density field can be seen in Figure 2.9. In Figure 2.9(c) the local increase due to appearance of (myo)fibroblasts has been visualised. After this stage, the strain energy density steadily increases in the wound region, and around 400h, it peaks then decreases because of the apoptosis of the myofibroblasts, which removes the temporary deformation produced by them. However, since the permanent deformation caused by the myofibroblasts and the presenting of regular fibroblasts, the strain energy density of the wound will be positive constantly.

2.3.4. WOUND AREA REDUCTION

We consider a two-dimensional representation of the wound and we are interested in the contraction of the wound. To this extent, we compute the area of the wound over time and we compute the reduction of wound area over time by

$$r = \frac{A_{\Omega}}{A_{\Omega}^0}, \quad (2.30)$$

where the area subject to deformation and reduction at any time is denoted by A_{Ω} and the initial wound area is represented by A_{Ω}^0 .

We use the shoelace theorem derived by Meister [59] in 1769 to compute the wound area, since adjacent vertices on the wound boundary are connected and it results in a polygon. Suppose we have a polygon with n vertices, then the area is calculated by

$$A_{\Omega} \approx A_{SL} = \frac{1}{2} \left\| \sum_{i=1}^n (x_i y_{i+1} - x_{i+1} y_i) \right\|, \quad (2.31)$$

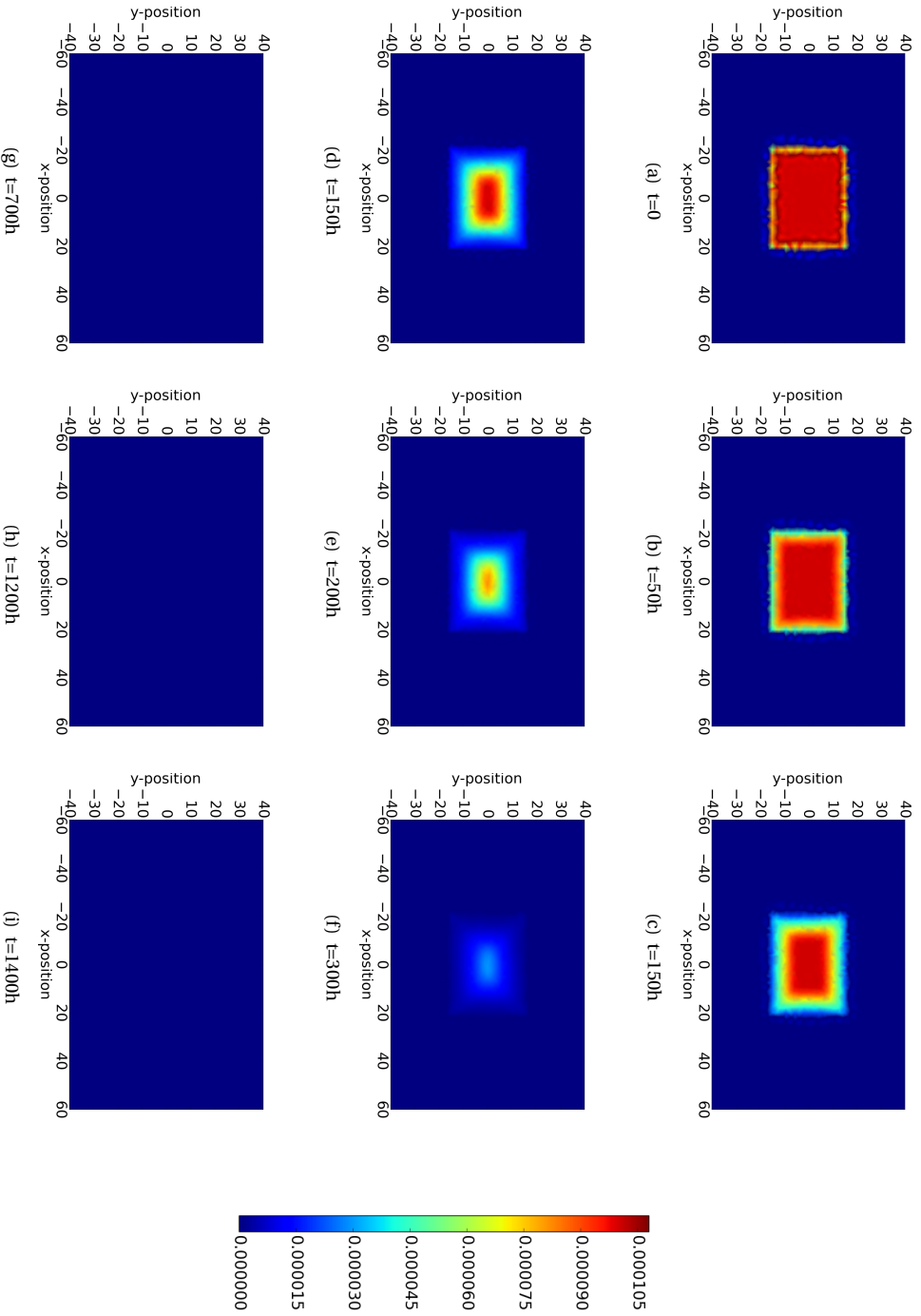


Figure 2.7: The plots show the density of fibrin bundles over time. The results are derived by solving Eq (2.21). The parameter values used to solve the partial differential equations are taken from Table 2.1.

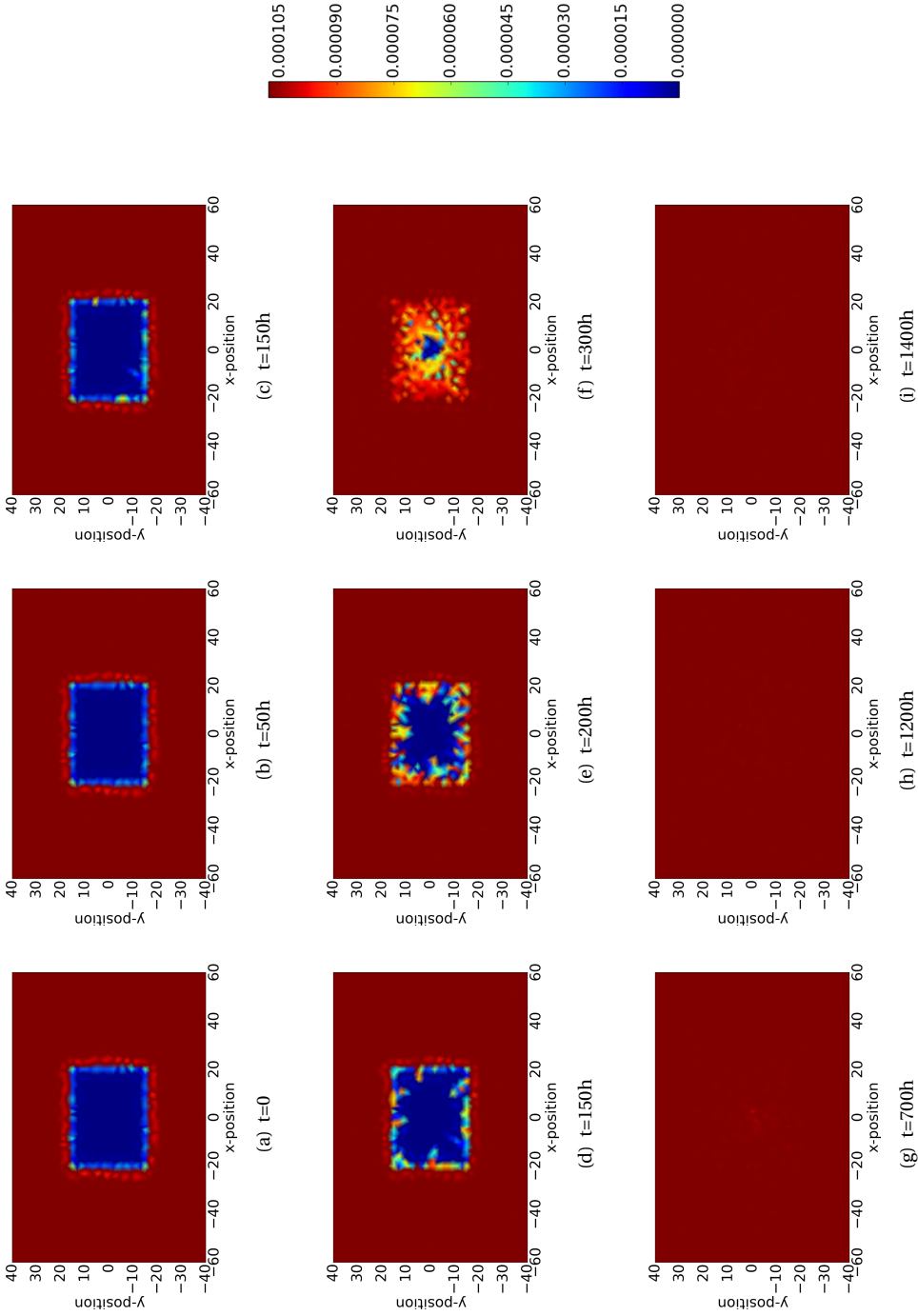


Figure 2.8: The plots show the density of collagen bundles over time. The results are derived by solving Eq (2.23). The parameter values used to solve the partial differential equations are taken from Table 2.1.

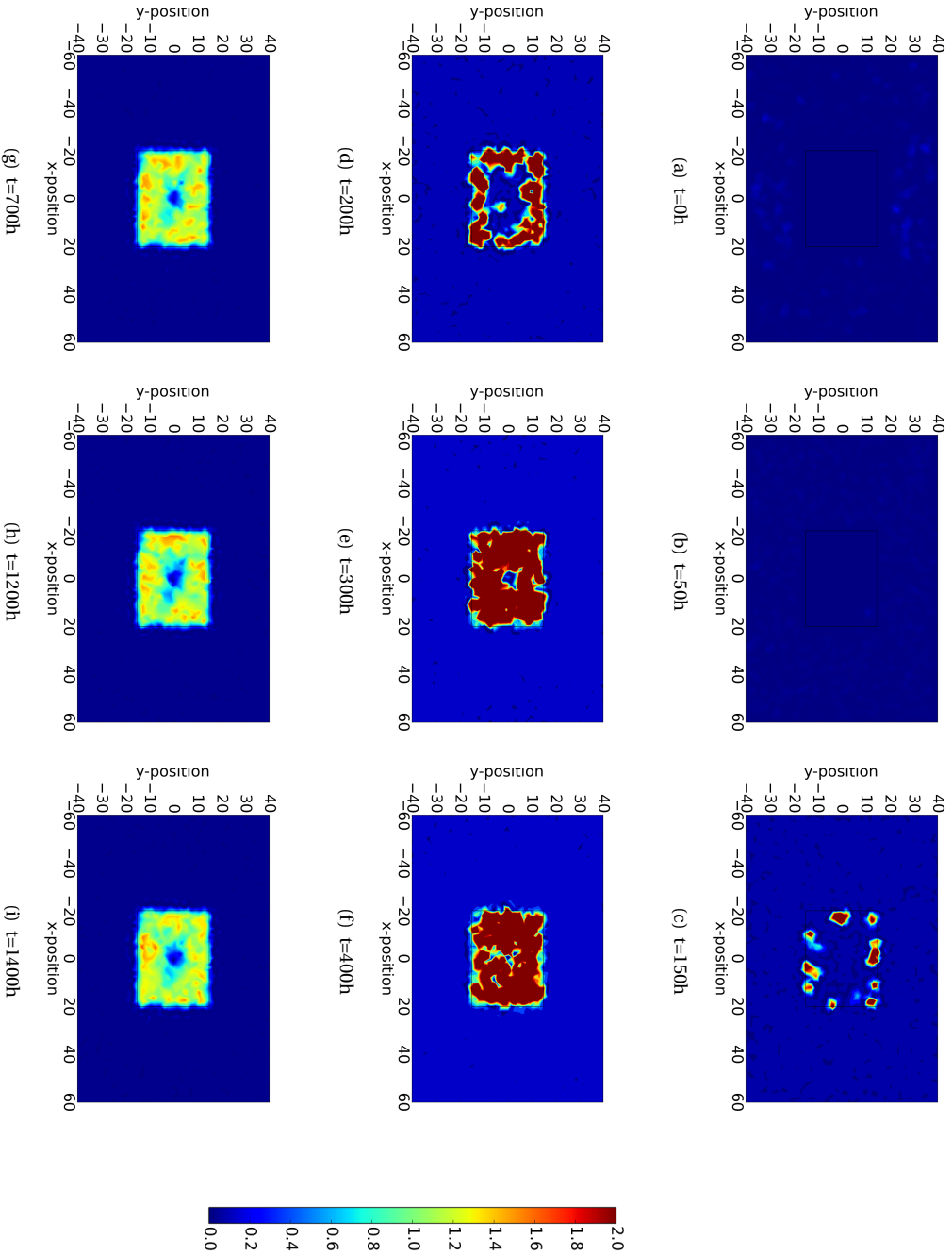


Figure 2.9: The plots show the strain energy distribution in the wound region, which is defined by $\int_{\Omega} \frac{1}{2} \underline{\underline{\sigma}}(u) : \underline{\underline{\epsilon}}(u)$. The displacement of the extracellular matrix can be derived by solving Eq (2.9) with Robin's boundary condition. The parameter values used to solve the partial differential equations are taken from Table 2.1.

where (x_i, y_i) , $i = 1, \dots, n$ is the coordinate of vertex i and $(x_{n+1}, y_{n+1}) = (x_1, y_1)$. Note that the vertices should be sorted in either a counter clockwise or clockwise direction.

We plot the wound area as a function of time in Figure 2.10, where various parameters have been varied in the different subplots. As an example, we consider Figure 2.10(a). The results in the other plots will be discussed in the next section. It can be seen that at the very early stages there is a slight increase of the wound area due to the pulling forces that are exerted by the fibroblasts that surround the wound region. After a while the fibroblasts migrate into the wound region and they start contracting the wound. This contraction is amplified after differentiation to myofibroblasts takes place. At the final stages of the simulations, the myofibroblasts and fibroblasts are subject to apoptosis and the myofibroblasts vanish, whereas the fibroblasts reach an equilibrium density, which is roughly equal to the density in the initial undamaged state (see also Figure 2.4). At this stage the wound region retracts towards the initial state, but since permanent strains and deformations remain, see Fig 2.9, it can be seen that there is a permanent reduction of the wound area, see Figure 2.10(a). Note that we have conducted multiple simulations in order to illustrate the impact of uncertainties that originate from the stochastic parts of the model (cell division, cell differentiation, cell death and cell migration).

2.3.5. SENSITIVITY TEST OF THE MODEL

Wound healing involves a cascade of biological processes in which many cellular phenomena take place and all changes in these cellular phenomena, either caused by diseases such as diabetes, or alternatively caused by genetic constitution or patients' lifestyle can have significant impact on the evolution of the skin after wounding. The healing time, which is the time needed for the regeneration of collagen, but also contraction times and intensities are important parameters that are used to describe the physiological condition of the skin of the patient. Therefore, a sensitivity analysis of the model is indispensable. Since the complicated nature of the underlying model makes it impossible for us to find closed form expressions for the parameters of interest, we need to carry out computer simulations in which we change one or more of the input parameters. In Figure 2.10, we show several simulation runs in which we use a basis set of parameter values from Table 2.1, and in which we change one of the input parameters. Since our model contains random processes for cell division, cell differentiation, cell appearance, and for cell migration, we conduct multiple simulations for some of the changes in the input parameters to see whether changes in the input parameter lead to significant changes in the behaviour of the solution.

The signalling molecules are crucially important for the sake of (long distance) intracellular communication. As a result of uncertainties from measurement and variation among patients and over time and tissue composition, diffusion coefficients vary unpredictably. Therefore, we vary the diffusion coefficient of these agents. In Figure 2.10(b), the diffusion coefficient of PDGF has been varied in several runs. Higher values of the diffusion coefficient of PDGF result into a faster transport of PDGF towards the immune cells, which are triggered earlier to migrate towards the wound region. Therefore, contraction takes place earlier as the PDGF diffusion coefficient increases, but the intensity of contraction both as a maximum and at the very long time range does not depend on the value of PDGF. Hence, the value of the PDGF diffusion coefficient does not effect the

intensity of the contraction, it only impacts the length of the time-interval of the contraction process.

Skin tissue contains solid polymeric matter as well as liquid phases in the form of blood and fluidic substances in cells. Hence, viscous (friction) effects are of crucial importance to deal with. Viscous phenomena have a damping effect on the mechanical behavior of the system. The forces that are exerted by the (myo)fibroblasts are damped by viscosity. This makes the deformation evolve more smoothly and it makes the wound area evolve more smoothly over time. This can be seen in Figure 2.10(d), where large viscosities increase the damping component in the solution, and it can be seen that if the viscosity part in mechanics is very large, then the transition to the final contracted state proceeds even monotonic, without the presence of the minimum wound area at a finite time. Decreasing the viscosity, makes the wound area exhibit a deeper minimum. Hence having a large viscosity, which corresponds to a higher degree of moisture, is beneficial for the patient at the short run, but does not change anything on the long run if therapy is not reconsidered. Since skin tends to become less moisture as skin ages, elderly people may suffer from a larger intermediate maximum degree of contraction [60].

We noticed that in Figure 2.10(e), the curves are not monotonic from the beginning of time. If the patient has a strong immune system, then more immune cells will appear on the edge between the wound and undamaged area. A large number of immune cells build up a "cell wall" surrounding the wound and prevent fibroblasts entering the wound, despite the fact that the immune cells release large amount of TGF-beta to attract fibroblasts. On the other hand, if the patient has a weaker immune system, then the number of immune cells is not sufficient to promote fibroblasts entering, and hence the concentration of TGF-beta is not high enough to trigger efficient displacement of fibroblasts towards the wound. Hence, two different cases are investigated: the fixed production of TGF-beta of each immune cell and the fixed amount of production of TGF-beta of all the immune cells. In other words, we denote $N_0(t)$ and $N_1(t)$ as the number of immune cells at time t with different rate of immune cells random appearing, and k_0 and k_1 is the production of TGF-beta of each immune cell. Therefore, since we assume all the immune cells are identical, the two cases are: 1) $k_0 = k_1$; 2) $N_0 k_0 = N_1 k_1$, respectively. The wound area changes, the density of collagen ratio and the strain energy of wound are displaced in Figure 2.11. We plot several curves that correspond to various strength of the immune system to have a better insight into the effect of the immune system on wound healing.

The stiffness of skin influences the magnitude of the displacement if a certain force is applied. Lower values of the Young's modulus (stiffness) increase the magnitude of the displacement for a given forcing [8]. Hence, lower values of the stiffness make the skin contract more severely, which can be seen Figure 2.10(f). Similar experimental results are observed in Wells [61]. However, the overall strain energy does not necessarily increase since the strain energy is proportional to the skin stiffness. Skin stiffness can be related to age and other genetic patterns of the patient. Age, however, is a complicated, but important, parameter since it may incur simultaneous changes of several parameters [62].

Based on the simulations that we have done so far, the results seem to reproduce most of the measured trends and can be explained by an intuitive point of view. In

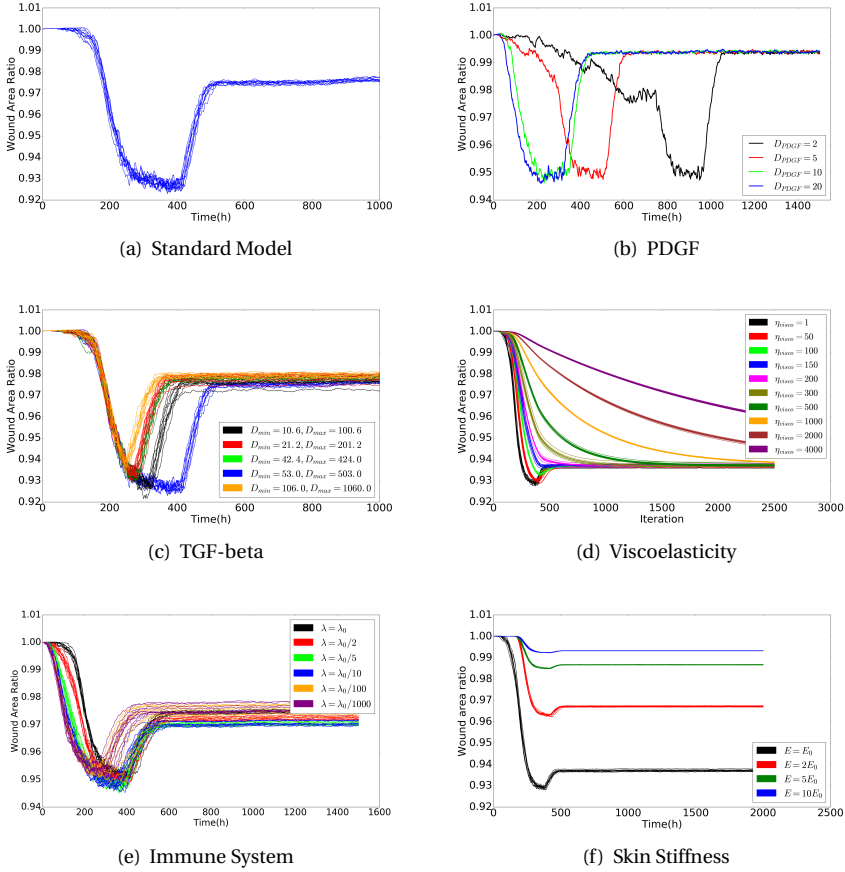


Figure 2.10: To investigate the influence of parameter values on wound healing, we use various values for the diffusion rate of PDGF and TGF-beta, the weight of viscoelasticity term for the force balance, the rate of immune cells random appearing, and the stiffness of the extracellular matrix in the model. The results are derived by solving the partial differential equations. The parameter values used to solve the partial differential equations are taken from Table 2.1, except the parameter under the sensitivity test.

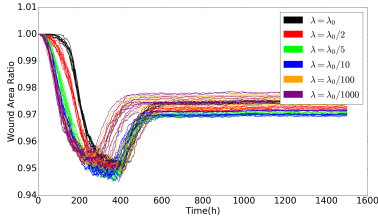
the next section, we will present the results from Monte Carlo simulations in which a Bayesian parameter sensitivity (I prefer this word here) study has been carried out.

2

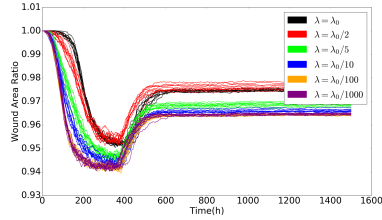
In every subplot of Figure 2.11 the probability rate for the appearance of the immune cells (macrophages) has been varied. Comparing the curves in each row of the subplots, it can be concluded that the collagen density ratio cannot indicate the degree of the wound contractions, but the wound strain energy dynamics follows the same tendency of wound area change. This conclusion can also be derived from the correlation in Monte Carlo simulations, which will be discussed in the next section. In other words, the correlation between the wound strain energy and the wound area is almost linear and significant.

More importantly, it can be seen that if this probability rate of macrophages appearance is large, then the count of immune cells is large. This implies that the concentration of TGF-beta is larger and hence the (myo)fibroblasts arrive into the wound site at earlier stages and in larger numbers. Therefore, at larger probability rates of macrophage appearance, the wound area decreases faster and earlier and to lower values, which implies that the maximal degree of contraction is larger. In fact, we expected that the permanent (plastic) deformations are also larger and hence the final degree of contraction is also larger, which corresponds to a smaller final wound area, since the counts of fibroblasts and hence also myofibroblasts are larger for larger values of the probability rate. However, the results in either Figure 2.11(a) or Figure 2.11(b) are not monotonic, which results from that larger number of immune cells will build up a barrier on the boundary of the wound, preventing the fibroblasts entering the wound to cure it. Therefore, above some threshold of probability rates of macrophage appearance, the larger the rates, the less the contraction; when the rates are below the threshold, the less the rates, the less the contraction. In other words, there is an (non-favorable) optimum for the degree of contraction with respect to the probability rate of macrophage appearance; see Figure 2.12. From the patient's point of view, a lower value of lambda decreases the onset of wound healing and regeneration of collagen, which hence delays wound healing, however, wound contraction is inhibited by lower lambda values. Hence, a slower immune reaction could be beneficial to the patient in this sense. A similar conclusion was drawn in Koppenol [17], Larouche *et al.* [63].

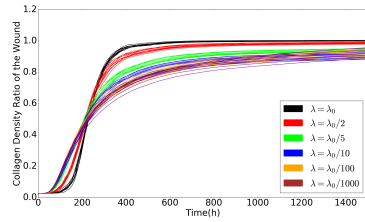
Besides the barrier built up by large number of immune cells, the main effect of the probability rate of immune cells appearance is the production of TGF-beta. Hence, we conduct another series of simulations where the TGF-beta production rate (denoted by k_{TGF}) per macrophage has been varied. A low value of k_{TGF} corresponds to a relatively weak immune system. In this case, we avoid the scenario of having a wall of immune cells that prevent fibroblasts to enter the damaged region. Figure 2.13 shows the wound area and the strain energy of the wound against time. The results in both subplots are monotonic, which indicates that the more production of TGF-beta, the more contraction and the larger strain energy of the wound, as well as shorter healing time, since the fibroblasts proliferate more and differentiate more into myofibroblasts and get stronger signals to move towards the wound. In other words, in our model, TGF-beta is the key factor why the strength of the immune system influences the healing process.



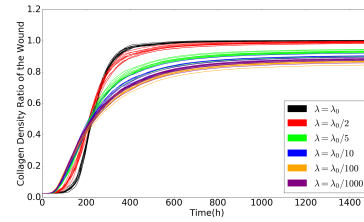
(a) Wound area change of the same production of TGF-beta of each macrophage



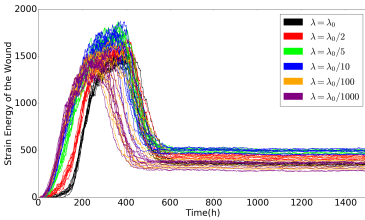
(b) Wound area change of the same production of TGF-beta of all macrophages



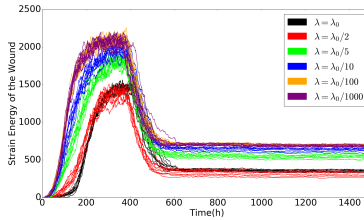
(c) Collagen density ratio of the same production of TGF-beta of each macrophage



(d) Collagen density ratio of the same production of TGF-beta of all macrophages



(e) Strain energy of the wound of the same production of TGF-beta of each macrophage



(f) Strain energy of the wound of the same production of TGF-beta of all macrophages

Figure 2.11: The left column shows the case when the production of TGF-beta of each immune cell is the same. The right column shows the case when the production of TGF-beta of all immune cells is the same. The results are derived by solving the partial differential equations. The parameter values used to solve the partial differential equations are taken from Table 2.1.

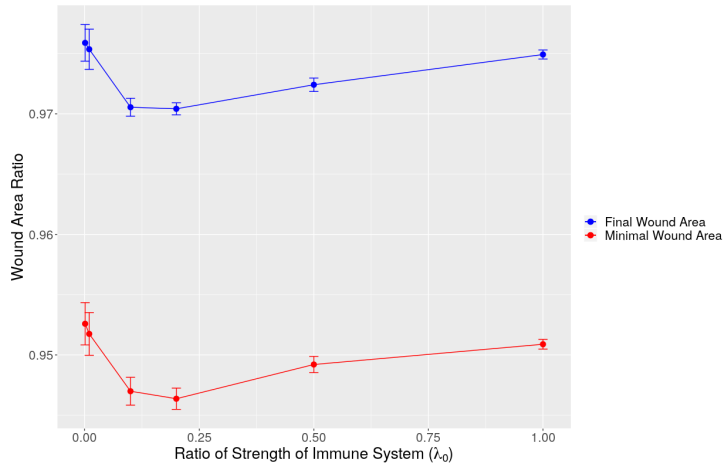


Figure 2.12: Minimal and final wound area ratio with respect to various probability rates of immune cells appearance. The blue curves and points stand for the final wound area, and the red curves and points present the minimal wound area. The parameter values used to solve the partial differential equations are taken from Table 2.1.

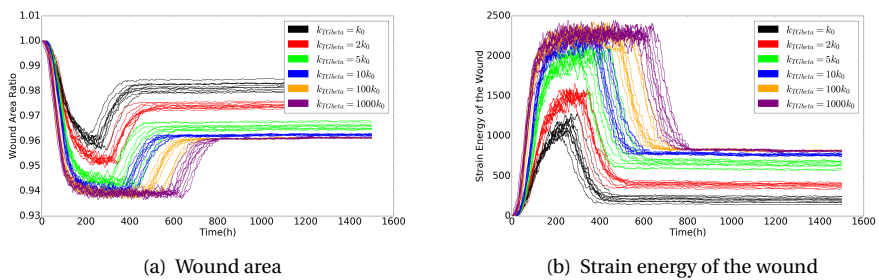


Figure 2.13: The area and the strain energy of the wound with various values of the production rate of TGF-beta. The parameter values used to solve the partial differential equations are taken from Table 2.1.

2.4. MONTE CARLO SIMULATIONS

As we mentioned earlier in Table 2.1, the parameter values are mostly selected based on the sensitivity of the model. Additionally, due to the limited literature sources of *in vivo* data for these parameters, and the discrepancy between the values collected by different measurements in the laboratory [64–67], Monte Carlo simulations will be beneficial to probe the hidden correlation between the parameters. The input parameters (see Table 3.3) represent different characteristics of patients, for instance, age, strength of immune system etc. [62]. We are interested in the contractions, which is indicated by the volume change. For each category, we recorded the final (equilibrium), minimal area (most intensified contraction) and the scar area at the 4th day after wounding.

Table 2.2: Distributions of the input parameters in Monte Carlo simulations

Input Parameters Parameter	Description	Distributions
E_s	Substrate elasticity	log normal(log50,0.1)
λ_d	Division rate of regular fibroblasts related to strain energy density	uniform(1.5,2.5)
λ_a	Apoptosis rate of myofibroblasts	normal(10,0.1)
λ_{immune_random}	Rate of Point Poisson Process of macrophages random appearing on the edge between the wound and undamaged skin	log normal(log0.04, 10^{-5})
Responses/Outputs Parameter	Description	Mean (Standard Deviation)
n	The time when the model reaches equilibrium	626.4(38.46908)
n_{min}	The time when the wound has minimal volume	380.1(27.64454)
$Area_final$	The equilibrium wound area	1142(4.658205)
$Area_min$	The minimal wound area	1090(8.324712)
$Area_4days$	The wound area at 4th day after wounding	1198(1.448219)
$\rho_{c_hat_final}$	The ratio of average density of collagen when the model reaches equilibrium	0.9950(0.003062998)
$\rho_{c_hat_min}$	The ratio of average density of collagen when the wound area is minimal	0.9336(0.02632869)

We collected 1210 observations via the simulations. The description of the data is shown in Table 3.3. Regarding the effect from inputs on the outputs, the stiffness of the skin has a significant correlation with the minimal and final area (0.97 and 0.96 respectively), as well as the ratio of the average density of collagen over the wound (0.39). The death rate of myofibroblasts does have a relatively less significant correlation and weak correlation (0.048) with the ratio of the average density of collagen over the wound.

However, the responses show more significant correlations. With respect to the final area of the wound, it has a significant correlation with many other outputs. In particular, it has an almost linear correlation with the minimal wound area, whereas the correlation is 0.17 with the wound area at the 4th day after wounding. Therefore, it would be beneficial for physicians to predict the final healed wound with these data known.

Table 2.3: The Weibull distribution to fit the reversed data of wound area at the 4th day

	Estimate	Standard Error
Shape	1.92876	4.42490×10^{-2}
Scale	2.51742×10^{-3}	1.49013×10^{-5}
Log-Likelihood: 6492.219	AIC=-12980.44	

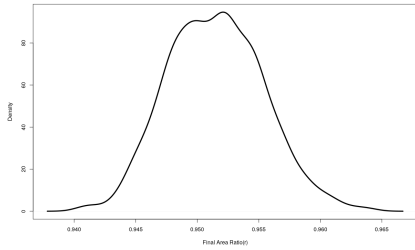
Further we investigate the correlation between the final density of collagen and several other parameters. Even though it shows mostly a significant correlation with other output, all the correlations are relatively low—the absolute values are all below 0.4, except the one with the time when the model reaches its equilibrium. Thus, regarding the wound contractions, the final density ratio cannot provide much information about the degree of the wound contractions.

We investigate the statistical distributions of the wound area at multiple times. This gives an indication of the severeness of contractions that patients will develop. Hereby, we use the ratio described in Eq (2.30). The density plots and the cumulative probability function plots are shown in Figure 2.14.

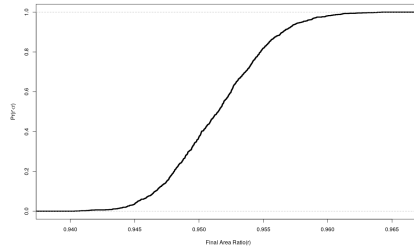
The curves in Figure 2.14(a) and 2.14(c) show the Gaussian shape. However, according to the Shapiro normality tests [68], neither of them come from a normal distribution. For the data of the wound area at the 4th day, we use the Weibull model to fit the reversed data, that is, we investigate the maximum of the data plus a small positive number subtracting every data, since the Weibull distribution requires all the positive data. We used 2-parameter Weibull distribution. The estimates of the parameters are shown in Table 2.3 and the diagonalized plots are displayed in Figure 2.15. It can be concluded that the Weibull distribution fits the reversed data quite well.

From Figure 2.14(b), patients have 0.627 probability to recover at most 95% of the original wound volume. Figure 2.14(d) indicates that for the largest contraction in small-scaled wound, the possibility that patients lose 9% of the volume is 0.585.

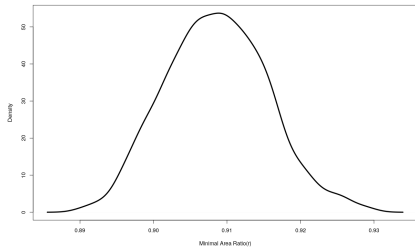
In the first batch of the Monte Carlo simulations, we have already concluded that the stiffness plays an important role in influencing the outcomes of the wound healing, in spite of a relatively small range that was used for the skin stiffness E_s . In the second round, we keep every distribution of the input the same as in the previous batch except for the stiffness. Herewith, we use the uniform distribution ranged from 23.90 to 300.00 from Liang *et al.* [65]. Additionally, the collagen density ratio at three different time points (i.e. when the wound area reaches equilibrium, minimal and at the 4th day) has been recorded as well as outcome. We plot some significant and interesting correlation results in Figure 2.16. Mostly, the correlation relations do not vary a lot. Furthermore, the final area and the minimal area has a correlation of 1.0, and the correlation between the wound area at the 4th day and the final/minimal wound area is 0.53, which is much larger than the one before. Between the final/minimal wound area and the collagen density ratio at the corresponding time point, it shows a non-monotonic "valley" shape, which matches the results in the sensitivity test before, that is, the collagen density ratio cannot indicate how severe the wound contraction is. However, when the new collagen is still regenerated from null, there exists a strongly negative linear correlation (-0.64) between the wound area and the collagen ratio density, which can be



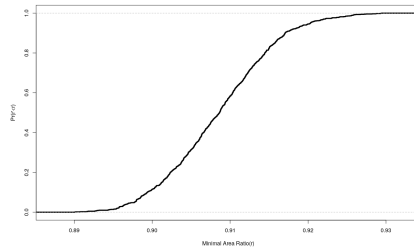
(a) Density plot of final wound area



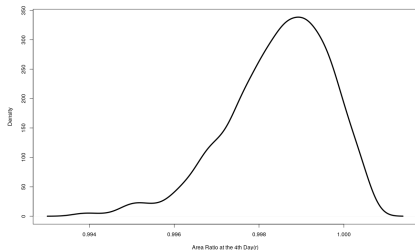
(b) Cumulative probability plot of final wound area



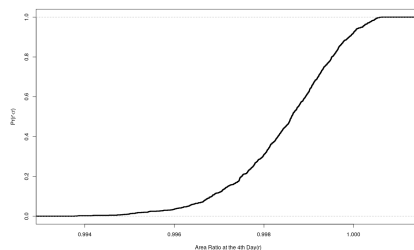
(c) Density plot of minimal wound area



(d) Cumulative probability plot of minimal wound area



(e) Density plot of wound area at the 4th day



(f) Cumulative probability plot of wound area at the 4th day

Figure 2.14: Left column shows the density plots of the wound area at different time. Right column shows the probability function plots of the wound area at different time. The parameter values used to solve the partial differential equations are taken from Table 2.1 and the random variable value are from Table 3.3.

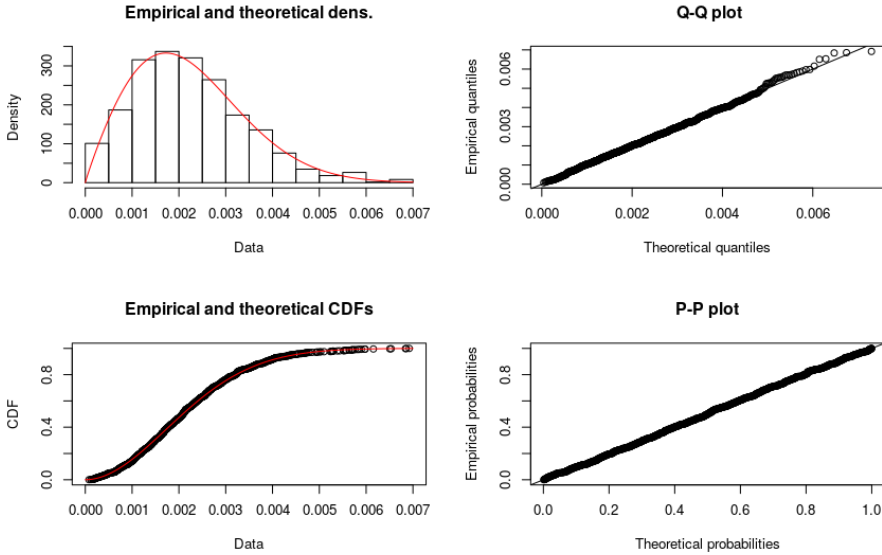


Figure 2.15: The diagonal plots of the Weibull distribution fitting the reversed data of the wound area at the 4th day.

seen from the data at the 4th day post wounding. Next to it, we noticed that the distribution of final/minimal wound area is more like an inverse Weibull distribution than a Gaussian distribution, which illustrates how significantly important the skin stiffness is to the wound healing, with respect to contraction.

2.5. DISCUSSIONS AND CONCLUSION

In this chapter, we mainly implement the semi-stochastic model to mimic the wound healing processes, and in particular the chained processes of inflammation and subsequent collagen regeneration. In the model, the displacements of cells, the dynamics of signalling molecules and wound area contractions over time are all described by PDEs. The model seems to reproduce the trends and biological observations reasonably well.

As it is seen from the results, macrophages play an important role in the early stage and they are the first arriving in the wound. In the meanwhile, TGF-beta is secreted by macrophages and this chemical attracts regular fibroblasts, as well as trigger the differentiation from regular fibroblasts to myofibroblasts. The number of macrophages and myofibroblasts follows the same pattern, i.e. increasing first then drop down to zero, whereas the number of regular fibroblasts will drop down to a certain level.

Signalling molecules are crucial for the chemotaxis of cells. Starting from higher concentration in the wound area and lower values in healthy tissues, PDF declined to zero over the whole observed domain in the end. Since macrophages are the main source of TGF-beta, the dynamics of the concentration is the same as the number of macrophages.

The wound contractions are illustrated by the area change of the wound. Initially,

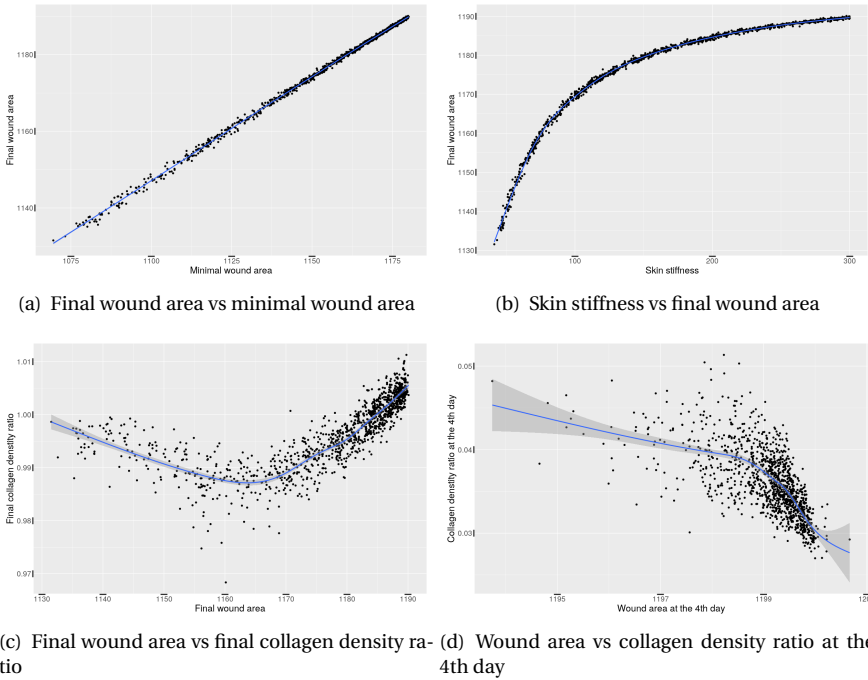


Figure 2.16: The plots show the correlation plot of two parameters from the Monte Carlo simulations. The curve in each plot is the smoothed line with the confidential interval. In each subplot, the p-value of the correlation is less than 0.001. The parameter values used to solve the partial differential equations are taken from Table 2.1 and the random variable values are from Table 3.3.

fibroblasts are outside of the wound, hence the forces they exert first enlarge the wound area a little. Due to the high concentration of TGF-beta, they gradually move into the wound and cause the deformation, that is, the reduction of wound area and accumulation of strain energy over the wound region. As the number of fibroblasts eventually stabilizes, the area of the wound and strain energy also tend to reach a stable equilibrium..

Under practical circumstances, the fibrin and collagen will affect the activities of the cells. To be more specific, they provide the guidance of the direction of the displacements of the cells. In addition, the bundles of these tissues will increase the strain of the wound and yield to the problematic complications after the wound healing. We have incorporated the tissues and related signalling molecules like tissue plasminogen activator (tPA) to improve the model.

To some extent, the model matches certain important time points with clinical data, for example, the maximal concentration of TGF-beta occurs around 100h after wounding [3, 57], the regular fibroblasts started arriving in the wound region in two to five days after the injury and the number of (myo)fibroblasts peaks at one to two weeks post-wounding [69], whereas in our model, (myo)fibroblasts appear in the wound around the fourth days after wounding and the peak of the sum of myofibroblasts and regular fibroblasts appears 12 days after wounding. In addition, after the sensitivity tests of the model, the conclusions drawn are matched with other experimental observations like O'Leary *et al.* [8], Larouche *et al.* [63] and Wells [61] etc.

According to the sensitivity tests, we found out that most factors have a monotonic influence on the wound contractions except the probability rate of immune cells appearance. Since the probability rate of immune cells appearance is related to the number of immune cells and subsequently decides the production of TGF-beta, there exists an optimal possibility rates of immune cells appearance. This is attributed to the fact that as too few immune cells do not release enough TGF-beta whereas too many immune cells build up a barrier on the edge of the wound preventing the fibroblasts entering the wound region. Therefore, below some threshold, a weaker immune system will extend the healing time but also, favorably, result into a less contracted wound.

The model is the basis to do Monte Carlo simulations, which are meant to figure out the effect of certain components on the healing process. We found out that the stiffness has a significant influence on wound healing regarding the contractions, which is also verified by *in vivo* and experimental observations. The distribution of the equilibrium and the minimal area is highly dependent on the distribution of skin stiffness, and there is a (nearly) significantly linear correlation between them. According to the significant correlations between the area at the 4th days after wounding and the equilibrium and minimal area, the area at the 4th day, is supposed to provide some information about the healing process afterwards. However, the relation between the wound area and the corresponding collagen density ratio is not monotonic, while for the 4th day the collagen density ratio can be used to indicate the degree of the wound contractions.

Since the cell-based model is mainly for the small-scale wound, the area reduction ratio is relatively small. The probability that patients will end up with 5% contraction or less is about 0.627, and have the worst contraction with losing 9% of the volume is around 0.585, with a small range of skin stiffness.

We bear in mind that the model is currently only in two dimensions, which has the benefits of efficient computations for a large number of simulations. In particular, obtaining results from Monte Carlo simulations is more efficient than modelling in three dimensions. On the other hand, one could work on extending the model into three dimensions, which is more realistic but more expensive from a computational perspective.

3

COMPARISON BETWEEN A PHENOMENOLOGICAL APPROACH AND A MORPHOELASTICITY APPROACH REGARDING THE DISPLACEMENT OF EXTRACELLULAR MATRIX

Plastic (permanent) deformations are modeled in Chapter 2 by a phenomenological model. In this chapter, we consider a more physics-based formulation that is based on morphoelasticity. We firstly introduce the morphoelasticity approach and investigate the impact of significant parameters by sensitivity analysis. As both formulations are able to model the scar contraction, we implement the two approaches in the skin contraction model and they appear to give similar computed results. Furthermore, we carry out Monte Carlo simulations of the skin contraction model containing the morphoelasticity approach. Most results are similar to the ones where the phenomenological approach is utilized, however, the collagen density is predicted to have a more significant impact on the degree of the wound contraction if the morphoelasticity model is selected.

3.1. INTRODUCTION

In Chapter 2, we modelled the traction forces exerted by the (myo)fibroblasts with a phenomenological approach, in which the forces are applied at the line segments of the

This chapter has been submitted to the journal together with W.S. Gorter.

mesh. An alternative approach to model the plastic deformation is by the use of morphoelasticity, which is a more advanced model. Morphoelasticity is widely used in biological modelling to describe elastic growth, for instance, the growth of tumors [70], the growth of seashells [71] and contractions of scars after an injury [17, 72] etc. Morphoelasticity provides a description of the evolution of plastic (permanent) deformation.

This chapter is structured as follows: we firstly introduce both approaches in Section 3.2. Section 3.3 describes the investigation of the impact of various parameters on the morphoelasticity approach. Subsequently, we show some numerical results in two dimensions to compare these two approaches in Section 3.4. In Section 3.5, we perform a Monte Carlo based parameter sensitivity analysis on the basis of the morphoelastic approach for the displacement of the extracellular matrix (ECM). Finally, Section 3.6 presents the conclusions.

3

3.2. MATHEMATICAL MODELS

To model the plastic deformation of the skin during wound healing, one can consider two approaches, namely a phenomenological approach and a morphoelasticity approach. In this section, both approaches will be introduced in the cellular scale.

3.2.1. PHENOMENOLOGICAL APPROACH

In Section 2.2, a phenomenological model is developed to simulate the permanent deformation of the skin, where we phenomenologically defined plastic forces by artificial forces that were exerted on the faces (that is boundary segments) of the mesh elements. This approach is motivated by the fact that it is known that myofibroblasts shorten the polymeric chains that constitute the extracellular matrix. This chapter is devoted to the comparison of the phenomenological model and the morphoelastic model. In the phenomenological model, the plastic displacements and deformations are modelled by the introduction of virtual forces. These virtual forces are motivated by the shortening of the polymeric chains in the extracellular matrix by the myofibroblasts. In this chapter, the virtual forces are also sometimes referred to as 'plastic forces'. The magnitude of the virtual force is assumed to be constant and to be equal to Q . For the plastic forces in the phenomenological model, we set

$$\mathbf{f}_p = \sum_{i=1}^{N_E} \sum_{e=1}^{N_e^i} Q \mathbf{n}(\mathbf{x}) \delta(\mathbf{x} - \mathbf{x}_e^i(t)) \Delta \Gamma_E^{i,e}, \quad (3.1)$$

where N_E is the total number of mesh triangular elements, N_e^i is the total number of edges of mesh elements (hence for triangular elements, $N_e^i = 3$), Q is the magnitude of the plastic force density of myofibroblast, $\mathbf{n}(\mathbf{x})$ is the unit inward (hence directed towards the center of the mesh element) pointing normal vector, $\mathbf{x}_e^i(t)$ is the midpoint of the boundary segment in consideration and $\Delta \Gamma_E^{i,e}$ is the length of the boundary segment, respectively. We note that this framework is sufficiently general to extend to different element shapes. Furthermore, instead of a Robin boundary condition, a homogeneous Dirichlet boundary condition is utilised. Hence, the boundary value problem is

expressed by

$$\begin{cases} -\nabla \cdot \boldsymbol{\sigma} = \mathbf{f}_t + \mathbf{f}_p, & \text{in } \Omega, \\ \mathbf{u}(\mathbf{x}, t) = \mathbf{0}, & \text{on } \partial\Omega. \end{cases} \quad (3.2)$$

Here, $\boldsymbol{\sigma}$ contains both elastic and viscoelastic part, that is,

$$\begin{aligned} \boldsymbol{\sigma} &= \boldsymbol{\sigma}_{elas} + \eta \boldsymbol{\sigma}_{visco} \\ &= \frac{E_s}{1+\nu} \left\{ \boldsymbol{\epsilon} + \text{tr}(\boldsymbol{\epsilon}) \left[\frac{\nu}{1-2\nu} \right] \mathbf{I} \right\} + \eta [\mu_1 \dot{\boldsymbol{\epsilon}} + \mu_2 \nabla \cdot \dot{\mathbf{u}} \mathbf{I}]. \end{aligned} \quad (3.3)$$

Furthermore, $\boldsymbol{\epsilon}$ is the infinitesimal strain tensor as defined by Eq (2.13), $\text{tr}(\boldsymbol{\epsilon})$ is the trace of $\boldsymbol{\epsilon}$, and \mathbf{f}_t and \mathbf{f}_p are defined by Eq (2.14) and Eq (3.1), respectively.

Since a homogeneous boundary condition is used, the boundary does not move. To model a wound, a subdomain $\Omega_w \subset \Omega$ (strict subset) is chosen. Further, zero initial displacement is assumed, that is $\mathbf{u}(\mathbf{x}, t) = \mathbf{0}$.

3.2.2. MORPHOELASTICITY APPROACH

Whereas the phenomenological approach is based on directly solving the equations for the local displacement of the tissue, the morphoelastic approach represents partial differential equations for the displacement velocity and the strain. To this extent, the equations for the balance of momentum and the evolution of the strain tensor are given by:

$$\begin{cases} \rho \left[\frac{D\mathbf{v}}{Dt} + \mathbf{v}(\nabla \cdot \mathbf{v}) \right] - \nabla \cdot \boldsymbol{\sigma} = \mathbf{f}_t, & \text{in } \Omega, \\ \frac{D\boldsymbol{\epsilon}}{Dt} + \boldsymbol{\epsilon} \text{skw}(\mathbf{L}) - \text{skw}(\mathbf{L})\boldsymbol{\epsilon} + [\text{tr}(\boldsymbol{\epsilon}) - 1] \text{sym}(\mathbf{L}) = -\alpha \boldsymbol{\epsilon}, & \text{in } \Omega, \\ \mathbf{v}(\mathbf{x}, t) = \mathbf{0}, & \text{on } \partial\Omega, \end{cases} \quad (3.4)$$

where ρ is the density of the extracellular matrix, \mathbf{f}_t is the temporary force described in Eq (2.14), $\mathbf{L} = \nabla \mathbf{v}$ and α is a non-negative constant. Here, $\frac{D\mathbf{y}}{Dt} = \frac{\partial \mathbf{y}}{\partial t} + \mathbf{v} \nabla \mathbf{y}$ is the material derivative for any tensor field \mathbf{y} and \mathbf{v} is the flow velocity. Furthermore, $\text{skw}(\mathbf{L}) = \frac{1}{2}(\mathbf{L} - \mathbf{L}^T)$ is the skew-symmetric and $\text{sym}(\mathbf{L}) = \frac{1}{2}(\mathbf{L} + \mathbf{L}^T)$ is the symmetric part of the matrix, respectively, and $\text{tr}(\boldsymbol{\epsilon})$ represents the trace of $\boldsymbol{\epsilon}$. The definition of stress tensor in the morphoelasticity approach has the same components as phenomenological approach in Eq (3.3). Since one solves the displacement velocity in the morphoelastic approach, the viscous part in Eq (3.3) is replaced with

$$\boldsymbol{\sigma}_{visco} = \mu_1 \text{sym}(\mathbf{L}) + \mu_2 \text{tr}(\text{sym}(\mathbf{L})) \mathbf{I}. \quad (3.5)$$

The initial boundary value problem for morphoelasticity is nonlinear and requires the solution of the displacement velocity \mathbf{v} and the strain tensor $\boldsymbol{\epsilon}$. This is in contrast to the boundary value problem in Eq (3.2). Since we are interested in the contraction of the wound region Ω_w , we approximate the displacement by integrating the velocity over time: $\mathbf{u}(t) = \int_0^t \mathbf{v}(s) ds$.

In a phenomenological approach, the plastic forces are responsible for the permanent deformation, which is the deformation after releasing all actual, physical forces

Table 3.1: Parameter values and the range of values of the parameters in the sensitivity test.

Parameter	Description	Value or Range of the Values		Unit
x_0	Length of the computational domain in x direction	0.2		cm
y_0	Length of the computational domain in y direction	0.2		cm
x_w	Length of the wound region in x direction	0.04		cm
y_w	Length of the wound region in y direction	0.04		cm
Δt	Time step	0.02		day
ρ	Density of the ECM	1.02		g/cm^3
μ_1	Shear viscosity	100		$g/(cm \cdot day)$
μ_2	Bulk viscosity	100		$g/(cm \cdot day)$
P	Magnitude of the cellular traction force	200		$g \cdot cm/day$
E_s	Young's modulus of the ECM	31	[20.0, 200.0]	$g/(cm \cdot day^2)$
η	Weight of viscosity in viscoelasticity	1	[0.6, 3]	–
α	Degree of the permanent deformation	0.2	[0.0, 1.0]	day^{-1}
ν	Poisson ratio of the ECM	0.48	[0.118, 0.495]	–

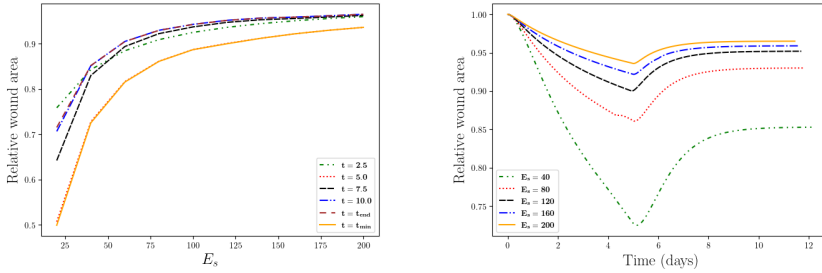
that are exerted by the (myo)fibroblasts. The right-hand side of the equation for the evolution of the strain tensor models the amount of permanent deformation. If $\alpha = 0$ at all times, then the tissue will gradually recover its original shape and volume over time after release of all forces.

3.3. SENSITIVITY TEST OF MORPHOELASTICITY APPROACH

To have a better insight into the model, we carry out a sensitivity analysis regarding different parameters in the morphoelasticity approach. As the model is mainly for the deformation of the wound, we define a subdomain (as wound region) in the centre of the computational domain and we investigate the relative wound area at different times. Since we are interested in the impact of the input parameters, we carry out the sensitivity tests where we only change the value of one parameter. The parameter values are displayed in Table 3.1. In this section, we assume that the shapes and sizes of the cells are identical, and they are at fixed positions that are strictly within the wound region $\Omega_w \subset \Omega$. The traction forces are removed from $t = 5$ day. Furthermore, we define t_{min} and t_{end} as the time point when the skin has the maximal contraction and when the model reaches its equilibrium.

The Young's modulus E_s indicates the stiffness of the ECM. According to clinical observations [8], softer skins will develop a more serious skin contraction compared with stiffer skin. In other words, since the amount of contraction and displacement decreases with increasing stiffness (E_s), the scar area stays larger if the stiffness is larger. We show the results in Figures 3.1 with various values of E_s . In Figure 3.1(a), the relative wound area is plotted as a function of E_s and various colors of the curves stand for different

time points. Figure 3.1(b) shows the relative wound area as a function of time and various colors of the curves stand for different values of E_s . It is concluded that a stiffer skin develops a less contracted wound. Furthermore, Figure 3.1(a) shows a hyperbolic correlation between the wound area and the stiffness.



(a) Relative wound area ratio against the stiffness of ECM at different times (b) Relative wound area ratio against time with various stiffnesses of the ECM

Figure 3.1: The impact of the stiffness E_s is shown in the figure. Different curves stand for various times in subfigure (a) and various values of E_s in subfigure (b), respectively.

Skin is taken as a viscoelastic material [73], that is, skin has both viscous and elastic properties. Viscosity is related to delayed recovery (or damping) from deformation, while elasticity is related to rebounding and quick recovery from deformation. Hence, we are interested in the impact of the damping property of the skin on the wound contraction. As it is shown in Figure 3.2, with a larger viscosity η , the wound reaches its minimal area later and develops less contraction. In particular, there is an approximate linear correlation between the minimal wound area and the value of η . Similarly, for the recovering phase, a smaller viscosity results into faster recovery, that is, the model reaches the equilibrium earlier, i.e. at a smaller t_{end} . It can be seen from Figure 3.3 that scar contraction takes place over a longer period with a linear tendency as η increases. However, less significant differences appear in the final stages of scar contraction, and this tendency may be attributed to the fact that the range of η is not above the threshold when the damping is too large so that the skin cannot recover.

The Poisson ratio ν indicates how much a material will deform in the direction perpendicular to the force direction. We vary ν here between (0.118, 0.495). Note that for incompressible materials, we have $\nu = 0.5$. As the ECM becomes more incompressible, the wound area stays constant and this yields small contractions regardless of the time point post wounding. Furthermore, the curves in Figure 3.4(a) show a hyperbolic behaviour. In general, a more compressible ECM indicates a higher degree of skin contraction and a larger healing time; see Figure 3.4(b).

Different from the phenomenological approach, the degree of the permanent deformation in the morphoelasticity approach is determined by α in Eq (3.4). Figure 3.5 displays the results with different values of α . Generally speaking, a smaller value of α is beneficial to the scar since this leads to smaller final contractions. Note that when $\alpha = 0$, theoretically the wound will recover to its original size.

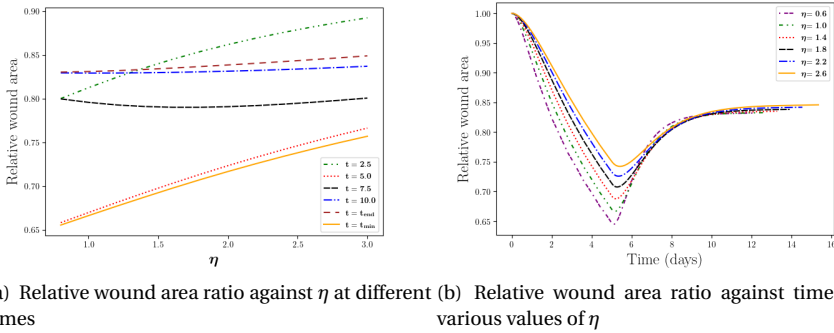


Figure 3.2: The impact of the weight of viscosity η is shown in the figure. Different curves stand for various times in subfigure (a) and various values of η in subfigure (b), respectively.

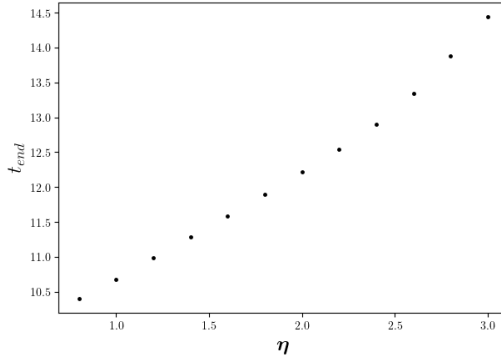
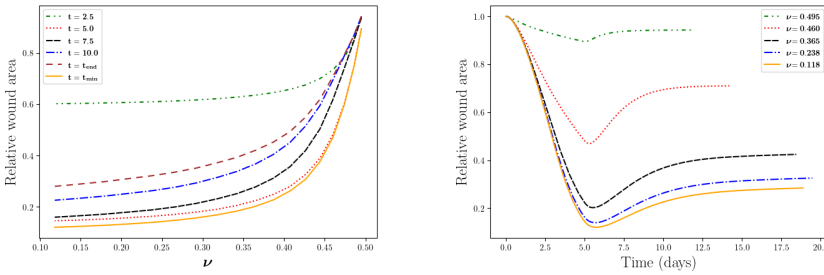


Figure 3.3: The impact of η on the duration of scar contraction. As η increases, the damping effects become more significant, hence, the model takes longer time to reach the equilibrium.

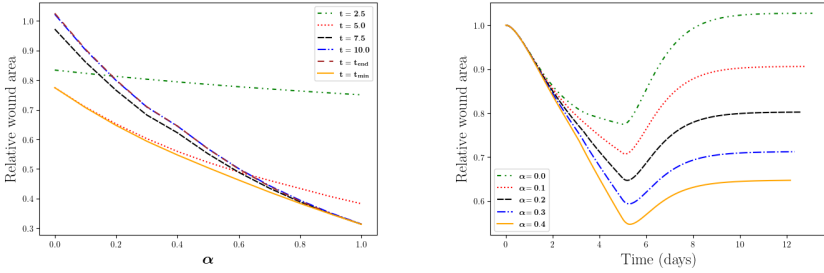
3.4. COMPARISON BETWEEN THE PHENOMENOLOGICAL APPROACH AND THE MORPHOELASTICITY APPROACH

As both approaches are capable of reproducing the permanent plastic deformation during skin contraction, we are interested in whether they are numerically consistent, when both boundary value problems are solved by the finite-element methods with Lagrangian piecewise linear basis functions. We altered the skin contraction model in Chapter 2 by modelling the wound deformation in the phenomenological model (see Eq (3.2)) and morphoelasticity model (see Eq (3.4)), respectively. To ensure the modelling settings are the same as much as possible, we inherit the parameter values from Chapter 2 mostly. Hence, we only display the parameter values used in force balance of the wound healing model in this sections in Table 3.2. The results of the relative wound area against time are shown in Figure 3.6.



(a) Relative wound area ratio against the Poisson ratio ν at different times (b) Relative wound area ratio against time with various values of Poisson ratio ν

Figure 3.4: The impact of the Poisson ratio ν is shown in the figure. Different curves stand for various times in subfigure (a) and various values of ν in subfigure (b), respectively. As ν increases, the ECM becomes less compressible, subsequently, it results into less skin contraction.



(a) Relative wound area ratio against α at different times (b) Relative wound area ratio against time with various values of α

Figure 3.5: The impact of the degree of permanent deformation α is shown in the figure. Different curves stand for various times in subfigure (a) and various values of α in subfigure (b), respectively.

We run several simulations with each approach since the model contains random processes. Figure 3.6 presents a case without and with permanent deformations (left and right subfigures, respectively). In other words, Figure 3.6(a) shows the case when plastic forces are not active in the phenomenological approach and the case that $\alpha = 0$ in the morphoelastic approach. Figure 3.6(b) shows the results using the corresponding parameter values from Table 2.1 and 3.2. In Figure 3.6(a), the curves of both colors are mostly overlapping, which indicates that both approaches can be used to describe scar contraction and as long as the main parameter values are the same, the models are more or less consistent. The inclusion of permanent deformations in both models by setting α and Q to positive values shows the same qualitative trends. However, it has turned out to be very difficult to make the curves from the two different models overlap, that is, make them agree quantitatively.

Regarding computational efficiency, these two approaches take more or less the same

Table 3.2: Parameter values of cells which will be used in the calculation of this report

Parameter	Description	Value	Dimension	Reference
E_s	Substrate elasticity	100	$kg/(\mu m \cdot h^2)$	Liang <i>et al.</i> [65]
E_c	Cell elasticity	5	$kg/(\mu m \cdot h^2)$	Dudaie <i>et al.</i> [48]
R	Cell radius	2.5	μm	Dudaie <i>et al.</i> [48]
P_f	Magnitude of temporary force of regular fibroblasts	2.08	$kg \cdot \mu m/h^2$	Koppenol [17]
Q	Magnitude of plastic force of myofibroblasts in phenomenological approach	33	$kg \cdot \mu m/h^2$	Koppenol [17]
x_0	Length of the computational domain in x direction	120	μm	Estimated in this study
y_0	Length of the computational domain in y direction	80	μm	Estimated in this study
x_w	Length of the wound region in x direction	40	μm	Estimated in this study
y_w	Length of the wound region in y direction	30	μm	Estimated in this study
Δt	Time step	0.1	h	Estimated in this study
ν	Poisson's ratio of the substrate	0.48	–	Estimated in this study
η	Weight of viscosity in viscoelasticity	10	–	Estimated in this study
μ_1	Shear viscosity	16.89	$kg/(\mu m \cdot h)$	Estimated in this study
μ_2	Bulk viscosity	11.26	$kg/(\mu m \cdot h)$	Estimated in this study
P_m	Magnitude of temporary force of myofibroblasts	10.4	$kg \cdot \mu m/h^2$	Estimated in this study
α	Weight of the growth tensor in morphoelasticity approach if the permanent deformation exists	0.01	h^{-1}	Estimated in this study

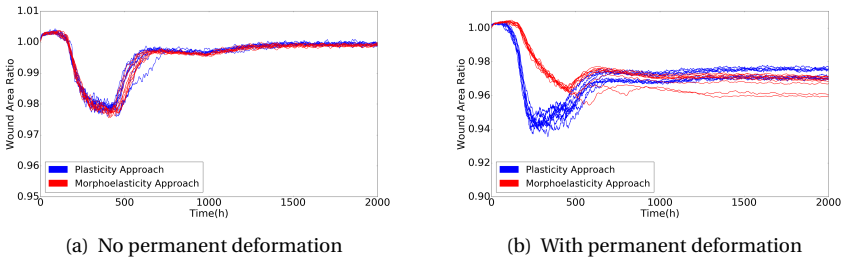


Figure 3.6: The plots show the wound area ratio with both phenomenological and morphoelasticity approach with and without permanent deformation respectively. Red curves represent the morphoelasticity approach and blue curves represent the phenomenological approach. The parameter values are given in Table 2.1 and 3.2.

CPU time for each iteration (around 4–7s on an Intel(R) Core(TM) i7-6500U CPU @ 2.50GHz computer). Hence in terms of computation time, there is no preference between either two models.

3.5. MONTE CARLO SIMULATIONS WITH MORPHOELASTICITY APPROACH

The model contains a large amount of randomness due to the random processes like cell division and migration, and due to the uncertainty in the values of the large number of input parameters. The input parameters are descriptive for the cells, signalling molecules and tissue bundles. The outputs of interest include the scar area and collagen density at different times. We are, for instance, interested in the time at which the scar area reaches its (modified) equilibrium, the time at which the contraction is maximal and the time at which the total amount of collagen reaches a certain threshold value. Note that, in this chapter, the size of cells and the scar have been set to academic values due to the limitation of computational resources. The values, as well as the statistical distributions of the input values are listed in Table 3.3. Other input values have been taken from Chapter 2.

In total, 1005 samples are collected and the basic statistics, being the obtained output sample mean and output sample standard deviation, are shown in Table 3.3. With respect to the input variables, only the stiffness has significant impact on the outputs, which is reasonable since stiffness is one of the most important properties of skin. Regarding the outputs, they can be categorized as wound area, specific time point and ratio of the density of collagen. Here, we define the ratio of the density of collagen by

$$\hat{\rho}_c(t) = \frac{\int_{\Omega_w(t)} \rho_c d\Omega}{\int_{\Omega_w(t)} \rho_c^0 d\Omega},$$

where ρ_c is the density of the collagen and ρ_c^0 is the density of collagen in the undamaged skin. This indicator illustrates the difference between the injured and uninjured skin regarding the regeneration of collagen.

In Table 3.3, we show the Monte Carlo error, which is defined by the standard deviation divided by the square root of the sample size, and the relative Monte Carlo error (denoted by *r.e.*), which is defined by the Monte Carlo error divided by the sample mean. As the number of samples increases, one can approximate the relative Monte Carlo error by

$$r.e. = \frac{\hat{\sigma}}{|\hat{\mu}|\sqrt{n}},$$

where $\hat{\sigma}$ and $\hat{\mu}$ are the sample standard deviation and sample mean, respectively and n is the sample size. By the Central Limit Theorem [74], one can obtain immediately that the quantity $\frac{\hat{\mu} - \mu}{\sigma/\sqrt{n}}$ follows the standard normal distribution, where μ and σ^2 are the population mean and variance, respectively. Given $\theta, \delta > 0$, we suppose

$$\mathbb{P}\left(\frac{|\hat{\mu} - \mu|}{\sigma/\sqrt{n}} \geq \theta\right) = \delta,$$

then

$$\mathbb{P}\left(\frac{\hat{\mu} - \mu}{\sigma/\sqrt{n}} \leq \theta\right) = 1 - \frac{\delta}{2}.$$

Table 3.3: Distributions of the input parameters in Monte Carlo simulations when morphoelasticity approach is collaborated.

Input Parameters Parameter	Description	Distributions		
E_s	Substrate elasticity	log normal(log50, 0.1)		
λ_d	Division rate of regular fibroblasts related to strain energy density	uniform(1.5, 2.5)		
λ_a	Apoptosis rate of myofibroblasts	normal(10, 0.1)		
λ_{immune_random}	Rate of Point Poisson Process of macrophages random appearing on the edge between the wound and undamaged skin	log normal(log0.04, 10^{-5})		

Responses/Outputs				
Parameter	Description	Mean (Standard Deviation)	Monte Carlo Error	Relative Monte Carlo Error
n	The time when the model reaches equilibrium	657(46.23974)	1.458587	0.00222
n_{min}	The time when the wound has minimal volume	467.6(39.80696)	1.255671	0.00269
$n_{rho_0.5}$	The first time when the ratio of average density of collagen exceeds 0.5	207.8(4.77877)	0.150741	0.00073
$n_{rho_0.8}$	The first time when the ratio of average density of collagen exceeds 0.8	258.1(5.292965)	0.641850	0.00249
$Area_final$	The equilibrium wound area	1091.8(46.70199)	1.473168	0.00135
$Area_min$	The minimal wound area	1083.5(47.81659)	1.508327	0.00139
$Area_4d$	The wound area at 4th day after wounding	1199(1.038872)	0.032770	0.00003
$Area_rho_0.5$	The wound area when the ratio of average density of collagen firstly exceeds 0.5	1171(11.92360)	0.376118	0.00032
$Area_rho_0.8$	The wound area when the ratio of average density of collagen firstly exceeds 0.8	1149(20.34776)	0.641850	0.00059
$rho_c_hat_final$	The ratio of average density of collagen when the model reaches equilibrium	1.061(0.0022738)	0.000173	0.00016
$rho_c_hat_min$	The ratio of average density of collagen when the wound area is minimal	1.065(0.0023577)	0.000744	0.00070
$rho_c_hat_4d$	The ratio of average density of collagen at 4th day after wounding	0.05485(0.00097955)	0.000309	0.00564

We note that $(n-1)\frac{\hat{\sigma}^2}{\sigma^2}$ follows a χ^2 distribution with $n-1$ degrees of freedom, and there-with $\sqrt{n}\frac{\hat{\mu}-\mu}{\hat{\sigma}}$ follows a t-distribution. However, as $n \rightarrow \infty$, $\hat{\sigma}$ converges to σ (consistent estimator). Hence, for n very large, it follows that

$$|\hat{\mu} - \mu| \leq \frac{\hat{\sigma}}{\sqrt{n}} \Phi^{-1} \left(1 - \frac{\delta}{2} \right),$$

where $\Phi(z)$ is the cumulative probability function of standard normal distribution. We write the above inequality in terms of the relative Monte Carlo error (denoted by *r.e.*), then one obtains

$$\frac{|\hat{\mu} - \mu|}{|\mu|} \leq \frac{\hat{\sigma}}{\sqrt{n}|\mu|} \Phi^{-1} \left(1 - \frac{\delta}{2} \right) = r.e. \cdot \Phi^{-1} \left(1 - \frac{\delta}{2} \right).$$

The above inequality in terms of an interval of significance says that the sample mean resides within this interval with probability of $(1 - \delta)$. From Table 3.3, all the relative Monte Carlo errors are less than 0.006, which indicates that regarding the sample mean, the sample size is sufficiently large.

Most of the correlations obtained in this chapter for morphoelasticity are consistent with the correlations that were obtained in Chapter 2. The current correlations seem to be a bit more significant, which reflects that the model based on morphoelasticity is more sensitive to parameter variation than the phenomenological model from Chapter 2. At least significant ($p < 0.001$) correlations are observed between many of the output and input parameters. Therefore, the scar area after a short amount of time can be used as indicative for the behavior of the scar area at later times, such as the maximum contraction and the final contraction.

Figure 3.7 shows some correlation plots between various parameters. From Figure 3.7(a), it can be seen that the correlation coefficient is (almost) equal to one, which reflects a very strong correlation between the maximal contraction and the final contraction. In other words, the more the scar contracts, the more the long-term area differs from the initial area. In other words, there is less recovery in the long term if the earliest maximum contraction is more severe. Furthermore, there is a slightly stronger correlation between the final scar area and the scar area on the fourth day post wounding (see Figure 3.7(b)), compared with the results in Chapter 2. This slightly stronger correlation may be a consequence from the fact that the morphoelasticity approach directly connects the scar deformation to the strain tensor. These correlations are useful for clinicians to predict the final contraction of the injured skin.

The stiffness of skin significantly determines the extent of contraction. It has been found that a wound in the buttock contracts more than a wound in the scalp region [8]. In Figure 3.7(c), it can be seen that the model reproduces this biological observation, for example, it is observed in O'Leary *et al.* [8] that the scar contracts less in the scalp than in the buttock. Subsequently, more wound contraction goes with higher collagen density ratio. Therefore, there is a negative correlation between the collagen density ratio and the skin stiffness; see Figure 3.7(d).

Another difference from the phenomenological model in Chapter 2 is the correlation between the final wound area and the final ratio of average collagen density. In Chapter 2, even though the correlation is significant (i.e. p -value is less than 0.001), the scatter plot is not monotonic, therefore, the negative correlation is not convincing to some extent. Nevertheless, in this chapter, we observe, among other correlations, a significant correlation between the scar area and the ratio of density of collagen. In Figure 3.7(e), the final wound area and the final ratio of average collagen density are strongly negatively correlated. In other words, higher collagen density results in a higher degree of contractions (i.e. a smaller final scar area). This also holds for the data from the 4th day

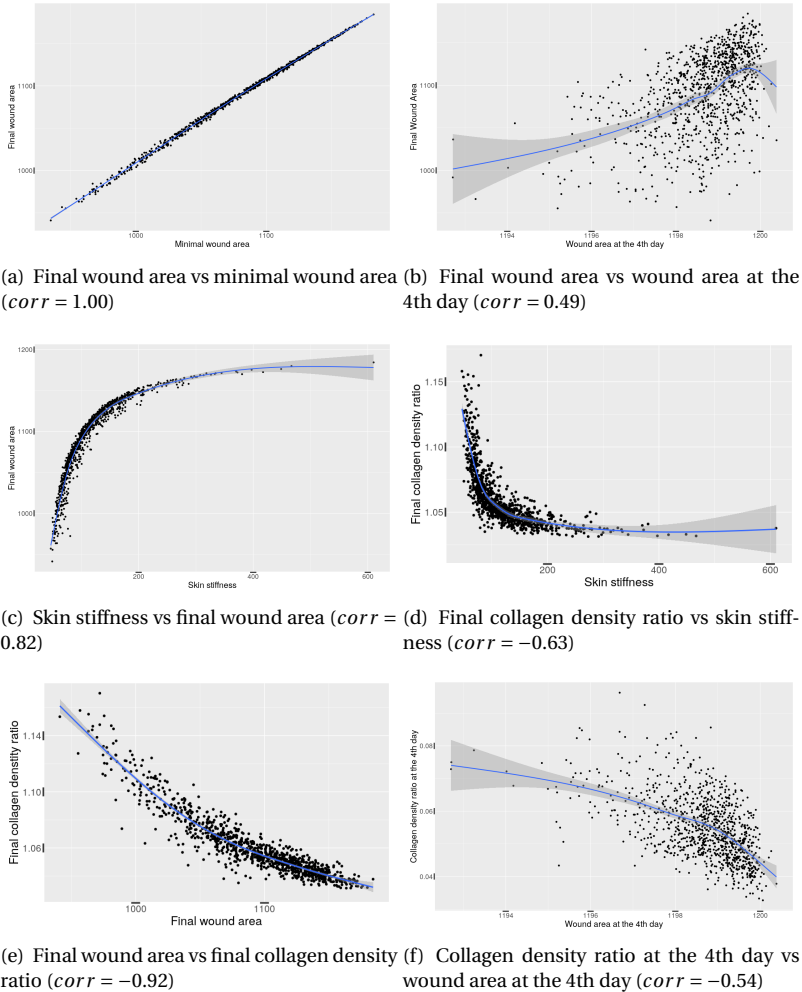


Figure 3.7: The plots show the correlation plot of two parameters from the Monte Carlo simulations. The curve in each plot is the smoothed line with the confidential interval. In each subplot, the p-value of the correlation is less than 0.001.

post wounding; see Figure 3.7(f). This dependence is caused by the fact that the orientation of the collagen bundles guides the migration direction of the (myo)fibroblasts, and since the (myo)fibroblasts are responsible for the regeneration of collagen bundles, as well as for the contractile forces within the scar, the combination of proliferation of (myo)fibroblasts and remodeling of collagen lead to more contraction. This is also observed in [62].

To determine the degree of contraction of post-burned skin, scar area is used as a quantifier. Figure 3.8 shows the estimated probability density distribution of the final

wound area from the Monte Carlo simulations. It is obvious from the shape of this probability density distribution that the final scar area is not normally distributed. A normality test confirms this observation quantitatively. From Figure 3.8(b), it can be concluded, that considering a wound with size $20\mu m \times 15\mu m$, the probability that the wound will develop 10% contraction is around 40% and 15% contraction is around 10%.

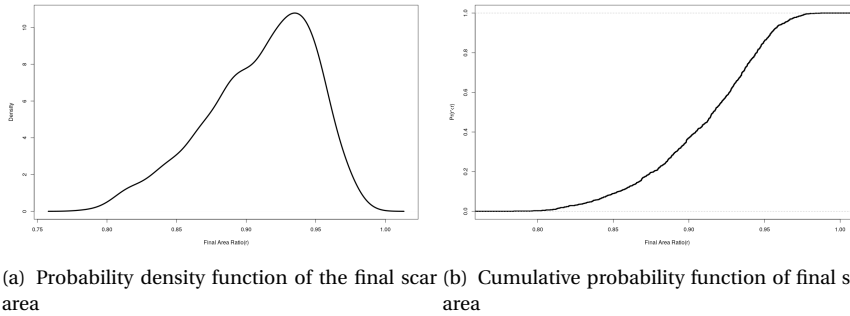


Figure 3.8: Probability density function and cumulative probability function of the final scar area are shown respectively.

3.6. CONCLUSIONS

In this chapter, we considered an alternative formalism to describe the permanent deformation of a scar region by combining morphoelasticity and a cell-based wound healing model. We confirm that both the phenomenological approach (see Chapter 2) and the morphoelasticity qualitatively give similar numerical results. Hence, both model formulations can be used to describe to local plasticity of the wound. The parameter sensitivity analysis showed that the viscosity part in the viscoelastic model for the displacement has a significant damping effect on the evolution of the scar area.

Compared to the phenomenological approach, the model with morphoelasticity is more sensitive to the random processes and parameter variations. Furthermore, with the same magnitude of the cellular forces, the model with morphoelasticity develops larger contractions. Regarding the computation time, the solution of the partial differential equations is more expensive in the case of morphoelasticity than for the phenomenological model. However, for large number of cells, this difference decreases, which implies that the computation time becomes predominantly determined by the cellular processes. These cellular processes entail the cellular force interaction, development of cellular forces, cell proliferation and cell migration. Based on these considerations, the incorporation of morphoelasticity into the modeling framework is also promising in real-world situations where a parallel computing environment is used.

Next to this deterministic parameter variation, a Bayesian (Monte Carlo) approach has been done for the morphoelastic model. Most of the results confirm the correlations that were obtained from the Monte Carlo simulations on the basis of the phenomenological model. However, the correlation between the ratio of average density of collagen and

the scar area is more negatively pronounced in the morphoelastic model. This observation is consistent with the clinical observations in O'Rourke *et al.* [75]. For this reason, the model based on morphoelasticity is preferred for use in future research.

Regarding further research, the focus should be directed towards application of the model to an enlargement of the scale so that the modeling framework is applicable to clinical situations. This enlargement of the modeling scale requires a parallel computing environment. Furthermore, upscaling of the agent-based model to a fully continuum-scale computational framework is also a necessary step.

II

POINT FORCES AND THEIR ALTERNATIVE APPROACHES IN CELL-BASED MODELS FOR SKIN CONTRACTION

4

POINT FORCES AND THEIR ALTERNATIVES IN CELL-BASED MODELS FOR SKIN CONTRACTION IN ONE DIMENSION

We consider a cell-based approach in which the balance of momentum is used to predict the the impact of cellular forces on the surrounding tissue. To this extent, the elasticity equation and the Dirac Delta distributions are combined. In the one dimensional case, the solution to the momemntum balance equation is piecewise linear, and hence, the solution stays in the Hilbert space H^1 . However, in order to avoid the singularity caused by the Dirac Delta distribution for dimensionality exceeding one, alternative approaches are necessary. Thus, a Gaussian distribution is used as a smoothed approach. Based on the application that the pulling force is pointing inward to the cell, the smoothed particle approach is probed as well. In one dimension, it turns out that the aforementioned three approaches are consistent in the sense of the exact solution.

4.1. INTRODUCTION

The Dirac Delta distribution in any dimensionality is defined by

$$\delta(\mathbf{x}) = 0, \text{ for } \mathbf{x} \neq \mathbf{0},$$

and constrained to satisfy the identity that

$$\int_{\Omega} \delta(\mathbf{x}) d\Omega = 1, \text{ if } \mathbf{0} \in \Omega \subset \mathbb{R}^n.$$

This chapter has been published in EUMATH2019 Proceedings and submitted to Journal of Computational and Applied Mathematics.

In the model of wound healing and cell geometry in this thesis, the Dirac Delta distributions are widely used to model the point sources of signalling molecules and point forces exerted by the cells on their direct environment or the obstacles they collide.

We consider the elasticity equation with the Dirac Delta distributions in this thesis. In one dimension, the solution to the PDE with any boundary condition can be expressed precisely, and the solution is piecewise linear, hence, the solution is in Hilbert space H^1 . However, for dimensionality exceeding one, the Dirac Delta distribution will result in singular solution that is not in Hilbert space H^1 . In order to circumvent this complication, the smoothed forces approach is developed, in which we use the Gaussian distributions to replace the Dirac Delta distributions. Especially in our healing model, the forces point towards the centre of the cell. Therefore, we use the gradient of the Gaussian distribution as an alternative.

The boundary value problems for all three methods are displayed in Section 4.2. Section 4.3 shows the numerical results corresponding to the approaches investigated before. In Section 4.4, conclusions are delivered.

4

4.2. MATHEMATICAL MODEL

Considering the force equilibrium in one dimension, the equations are expressed as

$$-\frac{d\sigma}{dx} = f, \quad \text{Equation of Equilibrium,} \quad (4.1)$$

$$\epsilon = \frac{du}{dx}, \quad \text{Strain-Displacement Relation,} \quad (4.2)$$

$$\sigma = E\epsilon, \quad \text{Constitutive Equation.} \quad (4.3)$$

To simplify the equation with $E = 1$ here, the equations above can be combined to Poisson equation in one dimension:

$$-\frac{d^2u}{dx^2} = f. \quad (4.4)$$

WITH DIRICHLET BOUNDARY CONDITION

According to Eq (2.14), we assume there is a cell with size h and centre position c in the computational domain $(0, L)$. Combined with homogeneous Dirichlet boundary conditions, the boundary value problem of the direct approach (or the so-called immersed boundary approach) is given by

$$(BVP_{\delta}^D) \begin{cases} -\frac{d^2u}{dx^2} = \delta(x - (c - \frac{h}{2})) - \delta(x - (c + \frac{h}{2})), & x \in (0, L), \\ u(0) = u(L) = 0, \end{cases} \quad (4.5)$$

where $\delta(x - x')$ is the Dirac Delta distribution. Note that to (BVP_{δ}^D) , the solution is piecewise linear and hence in $H^1(\Omega)$.

The Gaussian distribution is usually used as a replacement for the Dirac Delta distributions to obtain a smoother expression. Here, we denote

$$\delta_{\epsilon}(x - x') = \frac{1}{\sqrt{2\pi\epsilon^2}} \exp\left\{-\frac{(x - x')^2}{2\epsilon^2}\right\},$$

for the Gaussian distribution with mean x' and variance ε^2 . Therefore, the boundary value problem of the smoothed approach is expressed as

$$(BVP_S^D) \begin{cases} -\frac{d^2 u_\varepsilon}{dx^2} = \delta_\varepsilon(x - (c - \frac{h}{2})) - \delta_\varepsilon(x - (c + \frac{h}{2})), & x \in (0, L), \\ u_\varepsilon(0) = u_\varepsilon(L) = 0, \end{cases} \quad (4.6)$$

In (BVP_S^D) , since the right-hand side is smooth, we can rewrite it as

$$\begin{aligned} \delta_\varepsilon(x - (c - \frac{h}{2})) - \delta_\varepsilon(x - (c + \frac{h}{2})) &= h \frac{d\delta_\varepsilon}{dx}(x - c + \eta) \\ \Rightarrow \frac{1}{h}(\delta_\varepsilon(x - (c - \frac{h}{2})) - \delta_\varepsilon(x - (c + \frac{h}{2}))) &= \frac{d\delta_\varepsilon}{dx}(x - c + \eta), \quad \exists \eta \in (-\frac{h}{2}, \frac{h}{2}). \end{aligned} \quad (4.7)$$

As $h \rightarrow 0$, Eq (4.7) turns into

$$\lim_{h \rightarrow 0} \frac{1}{h}(\delta_\varepsilon(x - (c - \frac{h}{2})) - \delta_\varepsilon(x - (c + \frac{h}{2}))) = \frac{d\delta_\varepsilon}{dx}(x - c). \quad (4.8)$$

In other words, the right-hand side of (BVP_S^D) converges to right-hand side of the smoothed particle approach:

$$(BVP_{SP}^D) \begin{cases} -\frac{d^2 v_\varepsilon}{dx^2} = h \frac{d\delta_\varepsilon}{dx}(x - c), & x \in (0, L), \\ v_\varepsilon(0) = v_\varepsilon(L) = 0, \end{cases} \quad (4.9)$$

as $h \rightarrow 0$. This, in turn is combined with the boundary conditions to conclude that the difference between u_ε and v_ε satisfies a homogeneous Laplace equation as $h \rightarrow 0$, and hence $v_\varepsilon \rightarrow u_\varepsilon$ as $h \rightarrow 0$. In fact, we are aware that in the context of the electric dipole moment, especially in three dimensional potential theory, there are similar transformations occurring in expressing the potential of an electric dipole. One applies a Taylor expansion to write the expression of an electric dipole as a one-point charge by the use of the gradient; see Laud [76] for more details.

Hereby, we will prove the convergence of the solutions of (BVP_S^D) and (BVP_{SP}^D) with applying Poincaré's inequality and Taylor's expansion.

Lemma 4.1. (Poincaré's Inequality) *For any function \mathbf{u} in the Sobolev space, and a given bounded domain Ω , such that $\mathbf{u} = \mathbf{0}$ on the boundary of Ω , there exists a constant C such that*

$$\|\mathbf{u}\|_{L^p(\Omega)} \leq C \|\nabla \mathbf{u}\|_{L^p(\Omega)}, \quad (4.10)$$

where $1 \leq p < \infty$.

Theorem 4.1. *Denote u_ε and v_ε as the solutions to the boundary value problems (BVP_S^D) and (BVP_{SP}^D) respectively, then as the length of the cell h turns to zero, $v_\varepsilon \rightarrow u_\varepsilon$.*

Proof. We consider $w_\varepsilon = u_\varepsilon - v_\varepsilon$ and subtract Eq (4.6) and Eq (4.9), a new boundary value problem of w_ε is expressed as

$$\begin{cases} -\frac{d^2 w_\varepsilon}{dx^2} = \delta_\varepsilon(x - (c - \frac{h}{2})) - \delta_\varepsilon(x - (c + \frac{h}{2})) - h \frac{d\delta_\varepsilon}{dx}(x - c), & x \in (0, L), \\ w_\varepsilon(0) = w_\varepsilon(L) = 0. \end{cases} \quad (4.11)$$

By Taylor expansion and there exists $(\eta_1, \eta_2) \in (0, 1)$, such that the above equations become

$$\begin{cases} -\frac{d^2 w_\varepsilon}{dx^2} = \frac{h^3}{48} \left[\delta_\varepsilon^{(3)}\left(x - \left(c - \frac{h}{2}\eta_1\right)\right) + \delta_\varepsilon^{(3)}\left(x - \left(c - \frac{h}{2}\eta_2\right)\right) \right], & x \in (0, L), \\ w_\varepsilon(0) = w_\varepsilon(L) = 0. \end{cases} \quad (4.12)$$

Here, $\delta_\varepsilon^{(3)}$ is the third derivative of the Gaussian distribution with variance ε . Note that

$$\left\| \frac{h^3}{48} \left[\delta_\varepsilon^{(3)}\left(x - \left(c - \frac{h}{2}\eta_1\right)\right) + \delta_\varepsilon^{(3)}\left(x - \left(c - \frac{h}{2}\eta_2\right)\right) \right] \right\| \leq \frac{h^3}{48} \times 2 \times \|\delta_\varepsilon^{(3)}(x-c)\| = \frac{h^3}{24} \times \|\delta_\varepsilon^{(3)}(x-c)\|.$$

Then we multiply $w_\varepsilon(x)$ on both sides and taking integral over $(0, L)$, and it gives

$$\begin{aligned} -\int_0^L w_\varepsilon''(x) w_\varepsilon(x) dx &\leq \frac{h^3}{48} \times 2 \|\delta_\varepsilon^{(3)}(x-c)\| \int_0^L w_\varepsilon(x) dx \\ \Rightarrow -[w_\varepsilon'(x) w_\varepsilon(x)]_0^L + \int_0^L (w_\varepsilon'(x))^2 dx &\leq \frac{h^3}{24} \times \|\delta_\varepsilon^{(3)}(x-c)\| \int_0^L w_\varepsilon(x) dx \\ \Rightarrow \int_0^L (w_\varepsilon'(x))^2 dx &\leq \frac{h^3}{24} \|\delta_\varepsilon^{(3)}(x-c)\| L \|w_\varepsilon(x)\|_{L^2((0,L))} \\ \Rightarrow \int_0^L (w_\varepsilon'(x))^2 dx &\leq \frac{h^3}{24} \|\delta_\varepsilon^{(3)}(x-c)\| L \|w_\varepsilon(x)\|_{L^2((0,L))} \\ \Rightarrow \|w_\varepsilon(x)\|_{L^2((0,L))}^2 &\leq \frac{h^3}{24} \|\delta_\varepsilon^{(3)}(x-c)\| L \|w_\varepsilon(x)\|_{L^2((0,L))}. \end{aligned}$$

Combined with Poincaré's inequality (see Lemma 4.1), we can obtain that there exists a positive constant K , such that

$$\|w_\varepsilon\|_{L^2((0,L))} \leq L \frac{h^3}{24K} \times \|\delta_\varepsilon^{(3)}(x-c)\|.$$

Hence, $\|w_\varepsilon\| \rightarrow 0$, as $h \rightarrow 0$, which implies the convergence between u_ε and v_ε . \square

For the direct approach, the exact solution is the linear combination of the Green' function in one dimension, which is known as

$$G(x, x') = \begin{cases} x'(1 - \frac{x}{L}), & x \geq x', \\ x(1 - \frac{x'}{L}), & x < x'. \end{cases} \quad (4.13)$$

Since the forces are inward pointing to the centre of the cell, the solution to (BVP_δ) is

$$u_\delta(x) = G(x, c - \frac{h}{2}) - G(x, c + \frac{h}{2}). \quad (4.14)$$

The solutions to (BVP_S^D) and (BVP_{Sp}^D) , are, respectively, given by

$$\begin{aligned} u_{S_\varepsilon}(x) &= \frac{x\varepsilon}{\sqrt{2}L} \left(\int_{-\frac{c-h/2}{\sqrt{2\varepsilon}}}^{\frac{L-(c-h/2)}{\sqrt{2\varepsilon}}} \operatorname{erf}(x') dx' - \int_{-\frac{c+h/2}{\sqrt{2\varepsilon}}}^{\frac{L-(c+h/2)}{\sqrt{2\varepsilon}}} \operatorname{erf}(x') dx' \right) \\ &\quad - \frac{\varepsilon}{\sqrt{2}} \left(\int_{-\frac{c-h/2}{\sqrt{2\varepsilon}}}^{\frac{x-(c-h/2)}{\sqrt{2\varepsilon}}} \operatorname{erf}(x') dx' - \int_{-\frac{c+h/2}{\sqrt{2\varepsilon}}}^{\frac{x-(c+h/2)}{\sqrt{2\varepsilon}}} \operatorname{erf}(x') dx' \right), \end{aligned} \quad (4.15)$$

and

$$u_{SP_\varepsilon}(x) = \frac{h}{2} \left\{ \left(\frac{x}{L} - 1 \right) \operatorname{erf} \left(\frac{c}{\sqrt{2\varepsilon}} \right) + \frac{x}{L} \operatorname{erf} \left(\frac{L-c}{\sqrt{2\varepsilon}} \right) - \operatorname{erf} \left(\frac{x-c}{\sqrt{2\varepsilon}} \right) \right\}, \quad (4.16)$$

where $\operatorname{erf}(x)$ is the error function defined as $\operatorname{erf}(x) = \frac{2}{\sqrt{\pi}} \int_0^x \exp(-t^2) dt$ [77].

WITH ROBIN'S BOUNDARY CONDITIONS

We consider the same partial differential equations stated in Eq (4.2), (4.3) and (4.2) with the following Robin's boundary condition:

$$-u'(0) + u(0) = 0 \text{ and } u'(L) + u(L) = 0,$$

for domain $(0, L)$. Following the same assumptions before, there is a cell with size h and centre position c , then the boundary value problem of the direct approach is given by

$$(BVP_\delta^R) \begin{cases} -\frac{d^2 u}{dx^2} = \delta(x - (c + \frac{h}{2})) - \delta(x - (c - \frac{h}{2})), & x \in (0, L), \\ -u'(0) + u(0) = 0, \\ u'(L) + u(L) = 0. \end{cases}$$

The solution is

$$u_\delta(x) = \frac{1+x}{2+L} h - (x - (c - \frac{h}{2}))_+ + (x - (c + \frac{h}{2}))_+, \quad (4.17)$$

where $(x)_+ = \max\{0, x\}$. Substituting $x = 0$, Eq (4.17) delivers $u(0) = \frac{h}{2+L}$. For the smoothed approach, using the Gaussian distribution as an approximation of the Dirac Delta distribution, the boundary value problem is expressed as

$$(BVP_S^R) \begin{cases} -\frac{d^2 u_\varepsilon}{dx^2} = -\delta_\varepsilon(x - (c + \frac{h}{2})) + \delta_\varepsilon(x - (c - \frac{h}{2})), & x \in (0, L), \\ -u'_\varepsilon(0) + u_\varepsilon(0) = 0, \\ u'_\varepsilon(L) + u_\varepsilon(L) = 0. \end{cases} \quad (4.18)$$

The solution to the above problem is

$$u_{S_\varepsilon}(x) = - \left(\frac{\mathcal{G}'_{\varepsilon, c+h/2}(L) + \mathcal{G}_{\varepsilon, c+h/2}(L)}{2+L} (1+x) - \mathcal{G}_{\varepsilon, c+h/2}(x) \right) + \left(\frac{\mathcal{G}'_{\varepsilon, c-h/2}(L) + \mathcal{G}_{\varepsilon, c-h/2}(L)}{2+L} (1+x) - \mathcal{G}_{\varepsilon, c-h/2}(x) \right), \quad (4.19)$$

where $\mathcal{G}_{\varepsilon, c}(x) = \int_0^x \int_0^s \delta_\varepsilon(t-c) dt ds$. Substituting $x = 0$, we obtain

$$u_{S_\varepsilon}(0) = \frac{(\mathcal{G}'_{\varepsilon, c-h/2}(L) + \mathcal{G}_{\varepsilon, c-h/2}(L)) - (\mathcal{G}'_{\varepsilon, c+h/2}(L) + \mathcal{G}_{\varepsilon, c+h/2}(L))}{2+L}.$$

As $\varepsilon \rightarrow 0$, $\delta_\varepsilon(x)$ tends to $\delta(x)$, therefore,

$$\lim_{\varepsilon \rightarrow 0} \mathcal{G}'_{\varepsilon, c}(x) = \lim_{\varepsilon \rightarrow 0} \int_0^x \delta_\varepsilon(t-c) dt = H(x-c), \quad (4.20)$$

$$\lim_{\varepsilon \rightarrow 0} \mathcal{G}_{\varepsilon, c}(x) = \lim_{\varepsilon \rightarrow 0} \int_0^x \int_0^s \delta_{\varepsilon}(t-c) dt ds = \int_0^x H(s-c) ds = (x-c)_+, \quad (4.21)$$

where $H(x)$ is Heaviside step function, defined as the integral of the Dirac Delta distribution. We notice that $u_{\delta} \rightarrow u_{S_{\varepsilon}}$ when ε goes to zero. Combining Eq (4.20) and (4.21) with $x = L$ and $c - h/2, c + h/2 \in (0, L)$, it gives

$$\begin{cases} \lim_{\varepsilon \rightarrow 0} \mathcal{G}'_{\varepsilon, c+h/2}(L) = \lim_{\varepsilon \rightarrow 0} \mathcal{G}'_{\varepsilon, c-h/2}(L) = 1, \\ \lim_{\varepsilon \rightarrow 0} \mathcal{G}_{\varepsilon, c+h/2}(L) = L - (c + h/2), \\ \lim_{\varepsilon \rightarrow 0} \mathcal{G}_{\varepsilon, c-h/2}(L) = L - (c - h/2). \end{cases}$$

Thus,

$$\lim_{\varepsilon \rightarrow 0} u_{S_{\varepsilon}}(0) = \frac{h}{2+L} = u_{\delta}(0).$$

To prove $u_{S_{\varepsilon}}$ converges to u_{δ} as $\varepsilon \rightarrow 0$, we apply Eq (4.20) and (4.21), then

$$\begin{aligned} u_{S_{\varepsilon}}(x) &\rightarrow \frac{1+L-(c-h/2)}{2+L} (1+x) - (x-(c-h/2))_+ \\ &\quad - \frac{1+L-(c+h/2)}{2+L} (1+x) + (x-(c+h/2))_+ \\ &= \frac{h}{2+L} (1+x) - (x-(c-h/2))_+ + (x-(c+h/2))_+ \\ &= u_{\delta}(x), \quad \text{as } \varepsilon \rightarrow 0 \text{ and for all } x \in (0, L). \end{aligned}$$

Next, we consider the smoothed particle approach with Robin's boundary condition, that is

$$(BVP_{SP}) \begin{cases} -\frac{d^2 v_{\varepsilon}}{dx^2} = h \frac{d\delta_{\varepsilon}}{dx}(x-c), & x \in (0, L), \\ -v'_{\varepsilon}(0) + v_{\varepsilon}(0) = 0, \\ v'_{\varepsilon}(L) + v_{\varepsilon}(L) = 0. \end{cases} \quad (4.22)$$

The solution to it is given by

$$\begin{aligned} u_{SP_{\varepsilon}}(x) &= \frac{1+x}{2+L} \left\{ \frac{h}{2} \left[\operatorname{erf}\left(\frac{L-c}{\sqrt{2\varepsilon}}\right) + \operatorname{erf}\left(\frac{c}{\sqrt{2\varepsilon}}\right) + \frac{\sqrt{2}}{\sqrt{\pi\varepsilon^2}} \exp\left\{-\left(\frac{L-c}{\sqrt{2\varepsilon}}\right)^2\right\} \right] \right. \\ &\quad \left. - h(1+L) \frac{1}{\sqrt{2\pi\varepsilon^2}} \exp\left\{-\frac{c^2}{2\varepsilon^2}\right\} \right\} + hx \frac{1}{\sqrt{2\pi\varepsilon^2}} \exp\left\{-\frac{c^2}{2\varepsilon^2}\right\} - \frac{h}{2} \left[\operatorname{erf}\left(\frac{x-c}{\sqrt{2\varepsilon}}\right) + \operatorname{erf}\left(\frac{c}{\sqrt{2\varepsilon}}\right) \right]. \end{aligned} \quad (4.23)$$

Lemma 4.2. (Friedrich's Inequality) For an open bounded domain $\Omega \subset \mathbb{R}^n$ with boundary $\partial\Omega$, there exists a positive constant C , such that for any function $u \in H^1(\Omega)$,

$$\int_{\Omega} u^2 d\Omega \leq C \left[\int_{\Omega} \|\nabla u\|^2 d\Omega + \int_{\partial\Omega} u^2 d\Omega \right].$$

Theorem 4.2. Denote u_{ε} and v_{ε} as the solutions to the boundary value problems (BVP_{SP}^R) and (BVP_{SP}^R) respectively, then as the length of the cell h turns to zero, $v_{\varepsilon} \rightarrow u_{\varepsilon}$.

Proof. To prove the convergence between the solutions of u_{S_ε} and u_{SP_ε} , we will use Taylor expansion and define $w_\varepsilon = u_\varepsilon - v_\varepsilon$ in Eq (4.18) and (4.22) respectively, then we obtain the boundary value problem for w_ε

$$\begin{cases} -\frac{d^2 w_\varepsilon}{dx^2} = \frac{h^3}{48} \left[\delta_\varepsilon^{(3)}(x - (c - \frac{h}{2}\eta_1)) + \delta_\varepsilon^{(3)}(x - (c - \frac{h}{2}\eta_2)) \right], & x \in (0, L), \\ -w'_\varepsilon(0) + w_\varepsilon(0) = 0, \\ w'_\varepsilon(L) + w_\varepsilon(L) = 0, \end{cases} \quad (4.24)$$

where there exists $(\eta_1, \eta_2) \in (0, 1)$. Multiplying $w_\varepsilon(x)$ on both sides and taking the integral over the domain $(0, L)$ gives

$$\begin{aligned} -\int_0^L w_\varepsilon''(x) w_\varepsilon(x) dx &= \int_0^L \frac{h^3}{48} \left[\delta_\varepsilon^{(3)}(x - (c - \frac{h}{2}\eta_1)) + \delta_\varepsilon^{(3)}(x - (c - \frac{h}{2}\eta_2)) \right] w_\varepsilon(x) dx \\ &\Rightarrow -[w'_\varepsilon(x) w_\varepsilon(x)]_0^L + \int_0^L (w'_\varepsilon(x))^2 dx \leq \frac{h^3}{48} \times 2 \|\delta_\varepsilon^{(3)}(x - c)\| \int_0^L w_\varepsilon''(x) dx \\ &\Rightarrow w_\varepsilon^2(L) + w_\varepsilon^2(0) + \int_0^L (w'_\varepsilon(x))^2 dx \leq \frac{h^3}{24} \|\delta_\varepsilon^{(3)}(x - c)\| L \|w_\varepsilon(x)\|_{L^2((0, L))}. \end{aligned}$$

Applying Friedrich's inequality (see Lemma 4.2), there exists $K > 0$, such that

$$\begin{aligned} K \|w_\varepsilon(x)\|_{L^2((0, L))}^2 &\leq w_\varepsilon^2(L) + w_\varepsilon^2(0) + \int_0^L w'_\varepsilon(x) dx \leq \frac{h^3}{24} \|\delta_\varepsilon^{(3)}(x - c)\| L \|w_\varepsilon(x)\|_{L^2((0, L))} \\ &\Rightarrow \|w_\varepsilon(x)\|_{L^2((0, L))} \leq \frac{h^3 L}{24K} \|\delta_\varepsilon^{(3)}(x - c)\| \rightarrow 0, \text{ as } h \rightarrow 0. \end{aligned}$$

Hence, we proved that $v_\varepsilon \rightarrow u_\varepsilon$. \square

4.3. NUMERICAL RESULTS

In this section, the results are presented. We make use of the available exact solutions that are known in the one-dimensional case. Since this chapter is devoted to the comparison of various modelling approaches, the results are generic in the sense that the presentation and the analysis of the modelling is done for a one-dimensional case with dimensionless parameters. Here, we assume that the computational region is $(0, 7)$, where $L = 7$, and the size of the biological cell is equal to the variance of the Gaussian distribution denoted by ε . Figure 4.1 shows the analytical solution of all three approaches from Eq (4.14), (4.15) and (4.16) regarding homogeneous Dirichlet boundary conditions. Figure 4.2 presents the solutions to (BVP_δ^R) , (BVP_S^R) and (BVP_{SP}^R) . In both figures, the red and blue curves, which correspond to the direct and the smoothed Delta approach, mostly overlap regardless the choices of ε . This indicates that the solutions to the smoothed force approach and the smoothed particle approach are consistent. As ε decreases, the solutions to the smoothed approach and the smoothed particle approach converge to the solution to the direct approach. In other words, Figure 4.1 and 4.2 confirm the consistency between all three approaches, as long as ε is efficiently small.

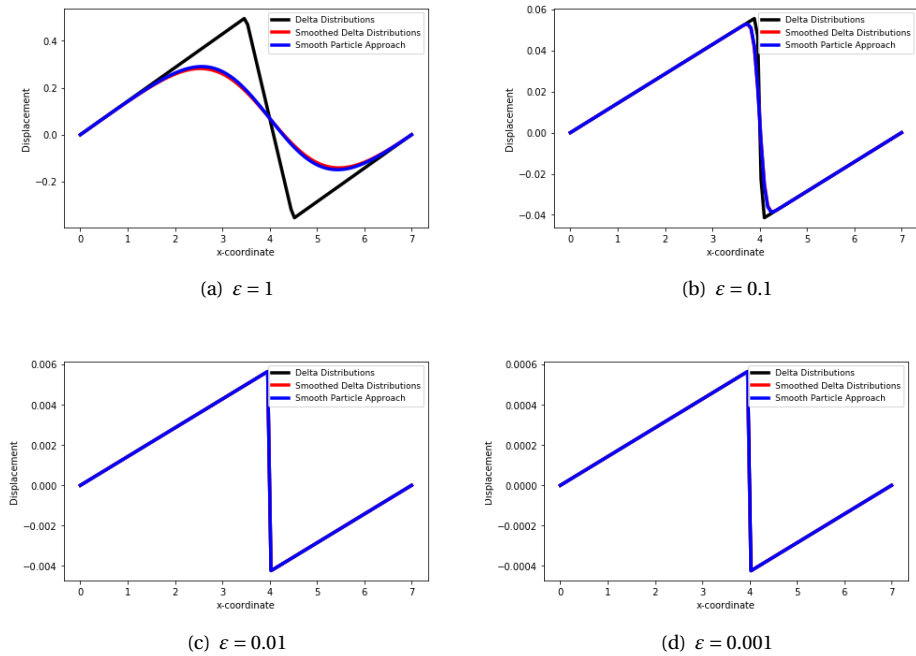


Figure 4.1: For one dimension, different colours of curves show the solution to (BVP_{δ}^D) , (BVP_S^D) and (BVP_{SP}^D) respectively, where homogeneous Dirichlet boundary condition is used. Black curve shows the solution to the direct approach, red curve is the smoothed approach and blue curve is the smoothed particle approach. As $h = \epsilon$ decreases, all the results converge

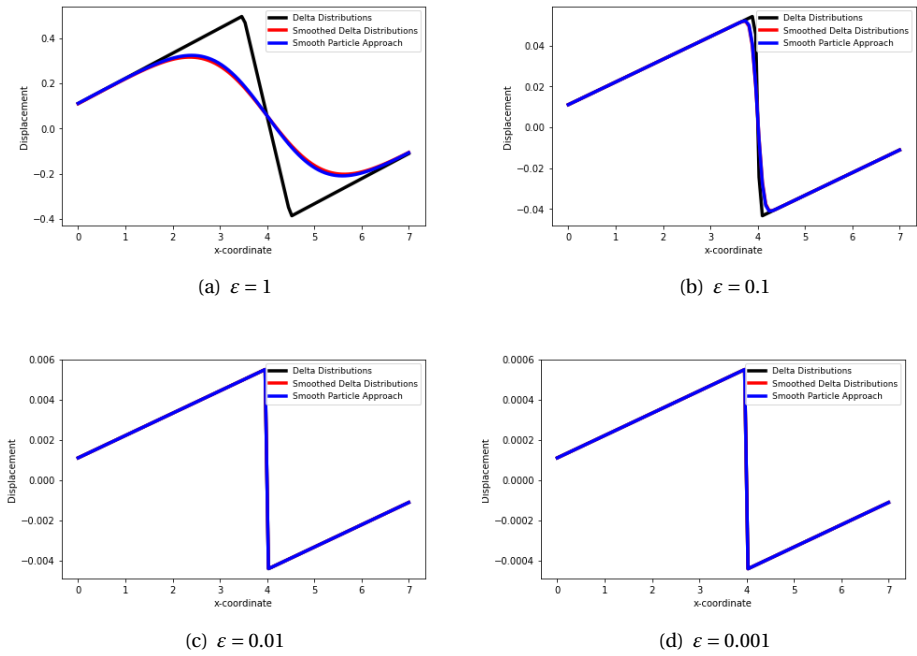


Figure 4.2: For one dimension, different colours of curves show the solution to (BVP_{δ}^R) , (BVP_S^R) and (BVP_{SP}^R) respectively, where Robin's boundary condition is used. Black curve shows the solution to the direct approach, red curve is the smoothed approach and blue curve is the smoothed particle approach. As $h = \epsilon$ decreases, all the results converge

4.4. CONCLUSION

In this chapter, we developed two alternative methods using the Gaussian distributions to replace the Dirac Delta distributions in the point forces. The first method is the smoothed approach, in which the Dirac Delta distributions at the midpoint of boundary segments of the cell are replaced by the Gaussian distributions directly. The second alternative method is the smoothed particle approach, which takes into account the gradient of the Gaussian distribution at the centre of the cell, and it is based on the point forces exerted on the boundary of cells in wound healing. In one dimension, we proved that the smoothed approach and the smoothed particle approach converge to the direct approach, and the numerical results verified consistency. The consistency in one dimension makes it promising to extend the work to higher dimensionalities, which will be discussed in the next chapter.

5

POINT FORCES IN ELASTICITY EQUATION AND THEIR ALTERNATIVES IN MULTIPLE DIMENSIONS

We consider several mathematical issues regarding models that simulate forces exerted by cells. Since the size of cells is much smaller than the size of the domain of computation, one often considers point forces, modelled by the Dirac Delta distributions on boundary segments of cells. In the current chapter, we treat forces that are directed normal to the cell boundary and that are directed toward the cell centre. Since it can be shown that there exists no smooth solution if the dimensionality exceeds one, at least not in H^1 to the governing momentum balance equation, we analyse the convergence and quality of approximation. Furthermore, the expected finite element problems that we get necessitate to scrutinize alternative model formulations, such as the use of smoothed Dirac distributions, or the so-called smoothed particle approach as well as the so-called 'hole' approach where cellular forces are modelled through the use of (natural) boundary conditions. In this chapter, we investigate and attempt to quantify the conditions for consistency between the various approaches. This has resulted into error analyses in the L^2 -norm of the numerical solution based on Galerkin principles that entail Lagrangian basis functions. The chapter also addresses well-posedness in terms of existence and uniqueness. The current analysis has been performed for the linear steady-state (hence neglecting inertia and damping) momentum equations under the assumption of Hooke's law.

This chapter has been published in proceedings of 2020 International Conference on Mathematics and Computers in Science and Engineering (MACISE), IEEE, 2020 [78] and submitted to Journal of Mathematics and Computers in Simulation and Journal of Computational and Applied Mathematics.

5.1. INTRODUCTION

In this chapter, we extend the alternatives developed in Chapter 4 into higher dimensions. The irregular nature of the Dirac Delta distributions makes the elliptic boundary value problem from the balance of momentum have a singular solution in the sense that for dimensionalities larger than one, no formal solutions in the finite-element space H^1 exist. Although in classical finite-element strategies, one uses for instance piecewise linear Lagrangian basis functions, which are in H^1 , and therewith one attempts to approximate the solution, which is not in H^1 , as well as possibly by a function in H^1 . In [79], the convergence of finite-element solutions by means of piecewise linear Lagrangian elements in multiple dimensions has been demonstrated.

We start from the two-dimensional case. Besides the smoothed force approach and the smoothed particle approach that have been developed in Chapter 4, we investigate the mixed finite-element method and the 'hole' approach. The mixed finite-element method is a more advanced finite element method, of which more details can be found in [80]. The 'hole' approach is based on the fact that the formalism of temporary forces in [17] are exerted on a continuous curve. The smoothed force approach, the smoothed particle approach and the 'hole' approach have been proven analytically and numerically to be consistent with the immersed boundary approach, respectively. Furthermore, we extend the proof into general dimensionality.

This chapter is structured as follows: Section 5.2 displays the immersed boundary approach and all the other alternatives in two dimensions, then we prove the consistency. Section 5.3 extends the alternative approaches and the proof to dimensionalities that are larger than one. In Section 5.4, we show the numerical results in two dimensions to illustrate the numerical consistency.

5.2. ELASTICITY EQUATION WITH POINT SOURCES IN TWO DIMENSIONS

To describe the contraction of the tissue, we use the equation for conservation of momentum over the computational domain Ω :

$$-\nabla \cdot \boldsymbol{\sigma} = \mathbf{f}. \quad (5.1)$$

In the above equation, inertia has been neglected. We consider a linear, homogeneous and isotropic material; hence, Hooke's Law is used here to define $\boldsymbol{\sigma}$ for dimensionality exceeding one:

$$\boldsymbol{\sigma} = \frac{E}{1+\nu} \left\{ \boldsymbol{\epsilon} + \text{tr}(\boldsymbol{\epsilon}) \left[\frac{\nu}{1-2\nu} \right] \mathbf{I} \right\}, \quad (5.2)$$

where E is the stiffness of the material or tissue in the computational domain, ν is Poisson's ratio and $\boldsymbol{\epsilon}$ is the infinitesimal Eulerian strain tensor:

$$\boldsymbol{\epsilon} = \frac{1}{2} [\nabla \mathbf{u} + (\nabla \mathbf{u})^T]. \quad (5.3)$$

For the sake of illustration, we consider one relatively big cell which is comparable to the two dimensional domain. The boundary of the cell is divided piecewisely into line

segments, so that we use a polygon as the approximation to compute the area. On the centre of each line segment, a point force pulls the surrounding environment towards the centre of the cell. Hereby, we consider the following forcing that is exerted by the cell on its surroundings [49]:

$$\mathbf{f}_t = \sum_{j=1}^{N_S} P(\mathbf{x}_j, t) \mathbf{n}(\mathbf{x}_j(t)) \delta(\mathbf{x} - \mathbf{x}_j(t)) \Delta S(\mathbf{x}_j(t)), \quad (5.4)$$

where N_S is the number of line segments of the cell, $P(\mathbf{x}, t)$ is the magnitude of the pulling force exerted at point \mathbf{x} and time t per length, $\mathbf{n}(\mathbf{x})$ is the unit inward pointing normal vector (towards the cell centre) at position \mathbf{x} , $\mathbf{x}_j(t)$ is the midpoint on line segment j of the cell at time t and $\Delta S(\mathbf{x}_j(t))$ is the length of line segment j . In this chapter, we will not consider the time iteration. Hence, we will neglect t from the notations in the following contents.

In two dimensions, we are solving the boundary value problems described in Eq (5.1), (5.2) and (5.3) with a Robin's boundary condition. This Robin's boundary condition models the mechanical interaction as a result of a spring force between the computational domain and its surrounding tissue. The temporary force is illustrated in Eq (5.4). Therefore, the PDE we are going to solve is given by

$$(BVP) \begin{cases} -\nabla \cdot \boldsymbol{\sigma}(\mathbf{u}) = \sum_{j=1}^{N_S} P(\mathbf{x}_j) \mathbf{n}(\mathbf{x}_j) \delta(\mathbf{x} - \mathbf{x}_j) \Delta S(\mathbf{x}_j), & \text{in } \Omega, \\ \boldsymbol{\sigma} \cdot \mathbf{n} + \kappa \mathbf{u} = \mathbf{0}, & \text{on } \partial\Omega. \end{cases} \quad (5.5)$$

Since the solution \mathbf{u} is not in $\mathbf{H}^1(\Omega)$ and piecewise linear Lagrangian basis functions $\{\boldsymbol{\phi}^i\}$, $i = \{1, 2, \dots, N\}$ are selected, we consider a subspace of $\mathbf{H}^1(\Omega)$, which is defined by $\mathbf{V}_h(\Omega) = \text{Span}\{\boldsymbol{\phi}^1, \boldsymbol{\phi}^2, \dots, \boldsymbol{\phi}^N\}$ [81]. Note that the linear Lagrangian basis functions are piecewise smooth and continuous over Ω , hence, they are in \mathbf{H}^1 . The corresponding Galerkin's form is given by

$$\left\{ \begin{array}{l} \text{Find } \mathbf{u}_h \in \mathbf{V}_h(\Omega), \text{ such that} \\ \int_{\partial\Omega} \kappa \mathbf{u}_h \boldsymbol{\phi}_h d\Gamma + \int_{\Omega} \boldsymbol{\sigma} : \nabla \boldsymbol{\phi}_h d\Omega \\ = \int_{\Omega} \sum_{j=1}^{N_S} P(\mathbf{x}_j) \mathbf{n}(\mathbf{x}_j) \delta(\mathbf{x} - \mathbf{x}_j) \Delta S(\mathbf{x}_j) \boldsymbol{\phi}_h d\Omega = \int_{\Omega} \int_{\partial\Omega_N} P(\mathbf{x}) \mathbf{n}(\mathbf{x}) \delta(\mathbf{x} - \mathbf{x}_j) \boldsymbol{\phi}_h dS(\mathbf{x}') d\Omega, \\ \text{as } N_S \rightarrow \infty, \text{ for all } \boldsymbol{\phi}_h \in \mathbf{V}_h(\Omega), \end{array} \right.$$

where the length of the line segments on the cell boundary tends to 0, and Γ_C represents the cell boundary.

The boundary value problem shown in Eq (5.5) is an operator equation, which can be written as

$$L\mathbf{u} = \mathbf{f}_t,$$

with boundary conditions. The operator L is self-adjoint, positive definite, linear and the solution lives in a linear space. Therefore, (BVP) can be written in the following

variational form:

$$\begin{cases} \text{Find } \mathbf{u}_h \in \mathbf{V}_h(\Omega), \text{ such that } F(\mathbf{u}_h) \leq F(\mathbf{v}_h), \forall \mathbf{v}_h \in \mathbf{V}_h(\Omega), \text{ where} \\ F(\mathbf{u}_h) = \int_{\Omega} \frac{1}{2} \boldsymbol{\sigma}(\mathbf{u}_h) : \boldsymbol{\epsilon}(\mathbf{u}_h) - \mathbf{u}_h \mathbf{f}_t d\Omega + \int_{\partial\Omega} \frac{1}{2} \kappa \|\mathbf{u}_h\|^2 dS. \end{cases}$$

5.2.1. THE MIXED APPROACH

Subsequently, we apply the mixed approach in the two dimensional case to solve the linear elasticity problem with the convolution of point forces that were described earlier. We use Hooke's Law for the relation between the stress and strain-tensors, and we rewrite it into vector formulation [80]:

$$\begin{bmatrix} \sigma_{11} \\ \sigma_{22} \\ \sigma_{12} \end{bmatrix} = \frac{E}{(1+\nu)(1-2\nu)} \begin{bmatrix} 1-\nu & \nu & 0 \\ \nu & 1-\nu & 0 \\ 0 & 0 & 1-2\nu \end{bmatrix} \begin{bmatrix} \epsilon_{11} \\ \epsilon_{22} \\ \epsilon_{12} \end{bmatrix}, \quad (5.6)$$

or

$$\boldsymbol{\sigma} = \mathcal{C} \boldsymbol{\epsilon}.$$

We rewrite the expression above in the form of

$$\boldsymbol{\epsilon} = \mathcal{C}^{-1} \boldsymbol{\sigma},$$

where

$$\mathcal{C}^{-1} = \frac{1+\nu}{E} \begin{bmatrix} 1-\nu & -\nu & 0 \\ -\nu & 1-\nu & 0 \\ 0 & 0 & 1 \end{bmatrix}. \quad (5.7)$$

Hence, the PDE we are going to solve is

$$(BVP_M^2) \begin{cases} \nabla \cdot \boldsymbol{\sigma}(\mathbf{u}) = - \sum_{j=1}^{N_S} P(\mathbf{x}) \mathbf{n}(\mathbf{x}) \delta(\mathbf{x} - \mathbf{x}_j) \Delta S(\mathbf{x}_j), & \text{in } \Omega, \\ \boldsymbol{\sigma} = \mathcal{C} \boldsymbol{\epsilon}, & \text{in } \Omega, \\ \boldsymbol{\sigma} \cdot \mathbf{n} + \kappa \mathbf{u} = \mathbf{0}, & \text{on } \partial\Omega. \end{cases} \quad (5.8)$$

Let $\mathbf{W}_h(\Omega)$ and $\mathbf{X}_h(\Omega)$ be a completion of $L^2(\Omega)$ containing sufficiently smooth functions [81], and define the inner product of two matrices by $\mathbf{A} : \mathbf{B} = \sum_{i=1}^n \sum_{j=1}^n a_{ij} b_{ij}$, then the Galerkin's form for the general equation is

$$\begin{cases} \text{Find } (\boldsymbol{\sigma}_h, \mathbf{u}_h) \in \mathbf{W}_h(\Omega) \times \mathbf{X}_h(\Omega), \text{ such that} \\ \int_{\Omega} \mathcal{C}^{-1} \boldsymbol{\sigma}(\mathbf{u}_h) : \boldsymbol{\tau} - \boldsymbol{\epsilon}(\mathbf{u}_h) : \boldsymbol{\tau} d\Omega = 0, \\ \int_{\Omega} \boldsymbol{\sigma}(\mathbf{u}_h) : \nabla \boldsymbol{\phi}_h d\Omega + \int_{\partial\Omega} \kappa \mathbf{u}_h \cdot \boldsymbol{\phi}_h d\Gamma = \int_{\Omega} \sum_{j=1}^{N_S} P(\mathbf{x}_j) \mathbf{n}(\mathbf{x}_j) \delta(\mathbf{x} - \mathbf{x}_j) \Delta \Gamma^j \boldsymbol{\phi}_h d\Omega, \\ \forall (\boldsymbol{\tau}_h, \boldsymbol{\phi}_h) \in \mathbf{W}_h(\Omega) \times \mathbf{X}_h(\Omega). \end{cases}$$

This is the mixed method developed by Hellinger and Reisner and this approach solves $(\boldsymbol{\sigma}, \mathbf{u})$, which is due to the fact that $\boldsymbol{\epsilon}$ can be written as $\nabla^{(s)}(\mathbf{u})$; see [80] for more details.

We bear in mind that the spaces in all aforementioned Galerkin's form with subscript h are finite element spaces that represent the span of Lagrangian basis functions.

5.2.2. THE 'HOLE' APPROACH

Since the force is actually applied on a continuous curve, rather than on the complete computational domain, we remove the region occupied by the cell from the computational domain and hence treat the cell as a hole in the computational domain. Then the force on the cell boundary is modelled by a (natural) boundary condition. Therewith, we have boundary conditions on the external boundary, as well as a force boundary condition on the boundary of the cell. The boundary value problem we are working on becomes

$$(BVP_H^2) \begin{cases} -\nabla \cdot \boldsymbol{\sigma}(\mathbf{u}) = 0, & \text{in } \Omega \setminus \Omega_C, \\ \boldsymbol{\sigma} \cdot \mathbf{n} = P(\mathbf{x})\mathbf{n}(\mathbf{x}), & \text{on } \Gamma_C, \\ \boldsymbol{\sigma} \cdot \mathbf{n} + \kappa \mathbf{u} = \mathbf{0}, & \text{on } \partial\Omega, \end{cases} \quad (5.9)$$

where Ω is the complete computational domain including the cell and extracellular regions, Ω_C is the region occupied by the cell, and Γ_C is the boundary of the cell. The current case no longer consists of the Dirac Delta distributions and herewith using the weak form, and appropriate theorems (such as Lax-Milgram and Korn's Inequality) existence and uniqueness of a solution in H^1 is easily demonstrated. The corresponding Galerkin's form for Eq (5.9) is

$$\begin{cases} \text{Find } \mathbf{u}_h \in \mathbf{H}^1(\Omega \setminus \Omega_C), \text{ such that} \\ \int_{\partial\Omega} \kappa \mathbf{u}_h \boldsymbol{\phi}_h d\Gamma + \int_{\Omega \setminus \Omega_C} \boldsymbol{\sigma} : \nabla \boldsymbol{\phi}_h d\Omega = \int_{\Gamma_C} P(\mathbf{x})\mathbf{n}(\mathbf{x}) \boldsymbol{\phi}_h dS, \text{ for all } \boldsymbol{\phi}_h \in \mathbf{H}^1(\Omega \setminus \Omega_C). \end{cases}$$

In [82], we proved the consistency between the 'hole' approach and the immersed boundary approach.

5.2.3. THE SMOOTHED PARTICLE APPROACH

The Gaussian distribution is used here as a replacement for the Dirac Delta distribution. Hereby, we show that in the two dimensions, the Gaussian distribution is a proper approximation for the Dirac Delta distribution.

Lemma 5.1. For an open domain $\Omega = (x_1, x_2) \times (y_1, y_2) \subset \mathbb{R}^2$, let

$$\delta_\varepsilon(x - x', y - y') = \frac{1}{2\pi\varepsilon^2} \exp\left\{-\frac{(x - x')^2 + (y - y')^2}{2\varepsilon^2}\right\},$$

where $(x', y') \in \Omega$, then

(i) $\lim_{\varepsilon \rightarrow 0^+} \delta_\varepsilon(x - x', y - y') \rightarrow 0$, for all $(x, y) \neq (x', y')$;

(ii) $\int_{y_1}^{y_2} \int_{x_1}^{x_2} \delta_\varepsilon(x - x', y - y') dx dy \rightarrow 1$, as $\varepsilon \rightarrow 0^+$;

(iii) Let $f(x, y) \in C^2(\mathbb{R}^2)$ and $\|f(x, y)\| \leq M < +\infty$, then

$$\int_{y_1}^{y_2} \int_{x_1}^{x_2} \delta_\varepsilon(x - x', y - y') f(x, y) dx dy \rightarrow f(x', y'), \text{ as } \varepsilon \rightarrow 0^+.$$

Proof. (i) Since $(x, y) \neq (x', y')$, $\lim_{\varepsilon \rightarrow 0^+} \exp\left\{-\frac{(x - x')^2 + (y - y')^2}{2\varepsilon^2}\right\} \rightarrow 0$. Thus,

$$\lim_{\varepsilon \rightarrow 0^+} \delta_\varepsilon(x - x', y - y') \rightarrow 0, \text{ for all } (x, y) \neq (x', y').$$

(ii) Let $B(\mathbf{x}'; a_L)$ and $B(\mathbf{x}'; a_u)$ be the inscribed and circumscribed circles of the rectangle $[x_1, x_2] \times [y_1, y_2]$, respectively. Since $\delta_\varepsilon(\mathbf{x} - \mathbf{x}') \geq 0$, it follows that

$$\int_{B(\mathbf{x}'; a_L)} \delta_\varepsilon(\mathbf{x} - \mathbf{x}') d\Omega \leq \int_{y_1}^{y_2} \int_{x_1}^{x_2} \delta_\varepsilon(\mathbf{x} - \mathbf{x}') dx dy \leq \int_{B(\mathbf{x}'; a_u)} \delta_\varepsilon(\mathbf{x} - \mathbf{x}') d\Omega.$$

For any circle centred at \mathbf{x}' with radius a , one can derive that

$$\int_{B(\mathbf{x}'; a)} \delta_\varepsilon(\mathbf{x} - \mathbf{x}') d\Omega = \int_0^a \int_0^{2\pi} \frac{1}{2\pi\varepsilon^2} \exp\left\{-\frac{r^2}{2\varepsilon^2}\right\} r d\phi dr = 1 - \exp\left\{-\frac{a^2}{2\varepsilon^2}\right\}.$$

Hence, it follows that

$$1 - \exp\left\{-\frac{a_L^2}{2\varepsilon^2}\right\} \leq \int_{y_1}^{y_2} \int_{x_1}^{x_2} \delta_\varepsilon(\mathbf{x} - \mathbf{x}') dx dy \leq 1 - \exp\left\{-\frac{a_u^2}{2\varepsilon^2}\right\}.$$

Both sides of the inequality tend to 1 as $\varepsilon \rightarrow 0^+$. Subsequently, using the Squeeze Theorem [83], it can be concluded that

$$\int_{y_1}^{y_2} \int_{x_1}^{x_2} \delta_\varepsilon(\mathbf{x} - \mathbf{x}') dx dy \rightarrow 1, \text{ as } \varepsilon \rightarrow 0^+.$$

(iii) Now we consider

$$\begin{aligned} & \int_{y_1}^{y_2} \int_{x_1}^{x_2} \delta_\varepsilon(x - x', y - y') f(x, y) dx dy \\ &= \int_{y_1}^{y_2} \int_{x_1}^{x_2} \frac{1}{2\pi\varepsilon^2} \exp\left\{-\frac{(x - x')^2 + (y - y')^2}{2\varepsilon^2}\right\} f(x, y) dx dy \\ &= \frac{1}{2\pi\varepsilon^2} \int_{y_1}^{y_2} \exp\left\{-\frac{(y - y')^2}{2\varepsilon^2}\right\} \int_{x_1}^{x_2} \exp\left\{-\frac{(x - x')^2}{2\varepsilon^2}\right\} f(x, y) dx dy. \end{aligned}$$

Let $s = \frac{y - y'}{\sqrt{2\varepsilon}} - \frac{y_1 + y_2}{2}$ and $t = \frac{x - x'}{\sqrt{2\varepsilon}} - \frac{x_1 + x_2}{2}$, then

$$\begin{aligned} & \int_{y_1}^{y_2} \int_{x_1}^{x_2} \delta_\varepsilon(x - x', y - y') f(x, y) dx dy \\ &= \frac{1}{\pi} \int \frac{\frac{y_2 - y_1}{2} - y'}{\sqrt{2\varepsilon}} \exp\left\{-\left(s + \frac{y_1 + y_2}{2}\right)^2\right\} \int \frac{\frac{x_2 - x_1}{2} - x'}{\sqrt{2\varepsilon}} \exp\left\{-\left(t + \frac{x_1 + x_2}{2}\right)^2\right\} \times \\ & f\left(\sqrt{2\varepsilon}t + \sqrt{2\varepsilon} \frac{x_1 + x_2}{2} + x', \sqrt{2\varepsilon}s + \sqrt{2\varepsilon} \frac{y_1 + y_2}{2} + y'\right) dt ds. \end{aligned}$$

By Taylor expansion, we obtain

$$\begin{aligned}
 & f\left(\sqrt{2\varepsilon}t + \sqrt{2\varepsilon}\frac{x_1+x_2}{2} + x', \sqrt{2\varepsilon}s + \sqrt{2\varepsilon}\frac{y_1+y_2}{2} + y'\right) \\
 &= f(x', y') + f_x(x', y')\sqrt{2\varepsilon}\left(t + \frac{x_1+x_2}{2}\right) + f_y(x', y')\sqrt{2\varepsilon}\left(s + \frac{y_1+y_2}{2}\right) \\
 &+ \frac{1}{2}\left[f_{xx}(x', y')2\varepsilon^2\left(t + \frac{x_1+x_2}{2}\right)^2 + 2f_{xy}(x', y')2\varepsilon^2\left(t + \frac{x_1+x_2}{2}\right)\left(s + \frac{y_1+y_2}{2}\right) + f_{yy}2\varepsilon^2\left(s + \frac{y_1+y_2}{2}\right)^2\right] \\
 &+ \mathcal{O}(\varepsilon^3) \\
 &= f(x', y') + f_x(x', y')\sqrt{2\varepsilon}\left(t + \frac{x_1+x_2}{2}\right) + f_y(x', y')\sqrt{2\varepsilon}\left(s + \frac{y_1+y_2}{2}\right) + f_{xx}(x', y')\varepsilon^2\left(t + \frac{x_1+x_2}{2}\right)^2 \\
 &+ 2f_{xy}(x', y')\varepsilon^2\left(t + \frac{x_1+x_2}{2}\right)\left(s + \frac{y_1+y_2}{2}\right) + f_{yy}\varepsilon^2\left(s + \frac{y_1+y_2}{2}\right)^2 + \mathcal{O}(\varepsilon^3).
 \end{aligned} \tag{5.10}$$

Let $\xi = t + \frac{x_1+x_2}{2}$ and $\eta = s + \frac{y_1+y_2}{2}$, and for any non-negative integer n ,

$$\int_{-\infty}^{+\infty} z^n e^{-z^2} dz = \begin{cases} 0, & \text{if } n \text{ is odd,} \\ \Gamma\left(\frac{n+1}{2}\right), & \text{if } n \text{ is even.} \end{cases}$$

5

Then, we calculate

$$\begin{aligned}
 & \int_{-\infty}^{+\infty} \int_{-\infty}^{+\infty} \delta_\varepsilon(x-x', y-y') f(x, y) dx dy \\
 &= \frac{1}{\pi} \int_{-\infty}^{+\infty} \exp\{-\eta^2\} \int_{-\infty}^{+\infty} \exp\{-\xi^2\} \times f(\sqrt{2\varepsilon}\xi + x', \sqrt{2\varepsilon}\eta + y') d\xi d\eta \\
 &= \frac{1}{\pi} \int_{-\infty}^{+\infty} \exp\{-\eta^2\} \int_{-\infty}^{+\infty} \exp\{-\xi^2\} \times [f(x', y') + f_x(x', y')\sqrt{2\varepsilon}\xi + f_y(x', y')\sqrt{2\varepsilon}\eta + f_{xx}(x', y')\varepsilon^2\xi^2 \\
 &+ 2f_{xy}(x', y')\varepsilon^2\xi\eta + f_{yy}(x', y')\varepsilon^2\eta^2 + \mathcal{O}(\varepsilon^3)] d\xi d\eta \\
 &= f(x', y') + \frac{\varepsilon^2}{\sqrt{\pi}} \Gamma\left(\frac{3}{2}\right) [f_{xx}(x', y') + f_{yy}(x', y')] + \mathcal{O}(\varepsilon^3) \\
 &\rightarrow f(x', y'), \text{ as } \varepsilon \rightarrow 0^+.
 \end{aligned}$$

According to the substitution of t, s, ξ, η , the integral over domain $(x_1, x_2) \times (y_1, y_2)$ can be rewritten as

$$\begin{aligned}
 & \int_{y_1}^{y_2} \int_{x_1}^{x_2} \cdots dx dy = 2\varepsilon^2 \int_{\frac{y_1-y'}{\sqrt{2\varepsilon}} - \frac{y_1+y_2}{2}}^{\frac{y_2-y'}{\sqrt{2\varepsilon}} - \frac{y_1+y_2}{2}} \int_{\frac{x_1-x'}{\sqrt{2\varepsilon}} - \frac{x_1+x_2}{2}}^{\frac{x_2-x'}{\sqrt{2\varepsilon}} - \frac{x_1+x_2}{2}} \cdots dt ds \\
 &= 2\varepsilon^2 \int_{\frac{y_1-y'}{\sqrt{2\varepsilon}}}^{\frac{y_2-y'}{\sqrt{2\varepsilon}}} \int_{\frac{x_1-x'}{\sqrt{2\varepsilon}}}^{\frac{x_2-x'}{\sqrt{2\varepsilon}}} \cdots d\xi d\eta \\
 &= 2\varepsilon^2 \left[\int_{-\infty}^{+\infty} \int_{-\infty}^{+\infty} \cdots d\xi d\eta - \int_{-\infty}^{+\infty} \int_{-\infty}^{\frac{x_1-x'}{\sqrt{2\varepsilon}}} \cdots d\xi d\eta - \int_{-\infty}^{+\infty} \int_{\frac{x_2-x'}{\sqrt{2\varepsilon}}}^{+\infty} \cdots d\xi d\eta \right. \\
 &\quad \left. - \int_{-\infty}^{\frac{y_1-y'}{\sqrt{2\varepsilon}}} \int_{\frac{x_1-x'}{\sqrt{2\varepsilon}}}^{\frac{x_2-x'}{\sqrt{2\varepsilon}}} \cdots d\xi d\eta - \int_{\frac{y_2-y'}{\sqrt{2\varepsilon}}}^{+\infty} \int_{\frac{x_1-x'}{\sqrt{2\varepsilon}}}^{\frac{x_2-x'}{\sqrt{2\varepsilon}}} \cdots d\xi d\eta \right].
 \end{aligned} \tag{5.11}$$

Subsequently, by Eq (5.11),

$$\begin{aligned}
& \left| \int_{y_1}^{y_2} \int_{x_1}^{x_2} \delta_\varepsilon(x-x', y-y') f(x, y) dx dy - f(x', y') \right| \\
&= \left| \frac{\varepsilon^2}{\sqrt{\pi}} \Gamma\left(\frac{3}{2}\right) [f_{xx}(x', y') + f_{yy}(x', y')] + \mathcal{O}(\varepsilon^3) \right. \\
&\quad - \int_{-\infty}^{+\infty} \int_{-\infty}^{\frac{x_1-x'}{\sqrt{2\varepsilon}}} \exp\{-(\xi^2 + \eta^2)\} f(\sqrt{2\varepsilon}\xi + x', \sqrt{2\varepsilon}\eta + y') d\xi d\eta \\
&\quad - \int_{-\infty}^{+\infty} \int_{\frac{x_2-x'}{\sqrt{2\varepsilon}}}^{+\infty} \exp\{-(\xi^2 + \eta^2)\} f(\sqrt{2\varepsilon}\xi + x', \sqrt{2\varepsilon}\eta + y') d\xi d\eta \\
&\quad - \int_{-\infty}^{\frac{y_1-y'}{\sqrt{2\varepsilon}}} \int_{\frac{x_1-x'}{\sqrt{2\varepsilon}}}^{\frac{x_2-x'}{\sqrt{2\varepsilon}}} \exp\{-(\xi^2 + \eta^2)\} f(\sqrt{2\varepsilon}\xi + x', \sqrt{2\varepsilon}\eta + y') d\xi d\eta \\
&\quad \left. - \int_{\frac{y_2-y'}{\sqrt{2\varepsilon}}}^{+\infty} \int_{\frac{x_1-x'}{\sqrt{2\varepsilon}}}^{\frac{x_2-x'}{\sqrt{2\varepsilon}}} \exp\{-(\xi^2 + \eta^2)\} f(\sqrt{2\varepsilon}\xi + x', \sqrt{2\varepsilon}\eta + y') d\xi d\eta \right| \\
&\leq \frac{\varepsilon^2}{\sqrt{\pi}} \Gamma\left(\frac{3}{2}\right) [f_{xx}(x', y') + f_{yy}(x', y')] + \mathcal{O}(\varepsilon^3) \\
&\quad + \int_{-\infty}^{+\infty} \int_{-\infty}^{\frac{x_1-x'}{\sqrt{2\varepsilon}}} \exp\{-(\xi^2 + \eta^2)\} |f(\sqrt{2\varepsilon}\xi + x', \sqrt{2\varepsilon}\eta + y')| d\xi d\eta \\
&\quad + \int_{-\infty}^{+\infty} \int_{\frac{x_2-x'}{\sqrt{2\varepsilon}}}^{+\infty} \exp\{-(\xi^2 + \eta^2)\} |f(\sqrt{2\varepsilon}\xi + x', \sqrt{2\varepsilon}\eta + y')| d\xi d\eta \\
&\quad + \int_{-\infty}^{\frac{y_1-y'}{\sqrt{2\varepsilon}}} \int_{\frac{x_1-x'}{\sqrt{2\varepsilon}}}^{\frac{x_2-x'}{\sqrt{2\varepsilon}}} \exp\{-(\xi^2 + \eta^2)\} |f(\sqrt{2\varepsilon}\xi + x', \sqrt{2\varepsilon}\eta + y')| d\xi d\eta \\
&\quad + \int_{\frac{y_2-y'}{\sqrt{2\varepsilon}}}^{+\infty} \int_{\frac{x_1-x'}{\sqrt{2\varepsilon}}}^{\frac{x_2-x'}{\sqrt{2\varepsilon}}} \exp\{-(\xi^2 + \eta^2)\} |f(\sqrt{2\varepsilon}\xi + x', \sqrt{2\varepsilon}\eta + y')| d\xi d\eta \\
&\leq \frac{\varepsilon^2}{\sqrt{\pi}} \Gamma\left(\frac{3}{2}\right) [f_{xx}(x', y') + f_{yy}(x', y')] + \mathcal{O}(\varepsilon^3) + \frac{M}{4} \left[\operatorname{erf}\left(\frac{x_1-x'}{\sqrt{2\varepsilon}}\right) - \operatorname{erf}\left(\frac{x_2-x'}{\sqrt{2\varepsilon}}\right) + 2 \right] \\
&\quad + \frac{M}{8} \left[\operatorname{erf}\left(\frac{x_1-x'}{\sqrt{2\varepsilon}}\right) - \operatorname{erf}\left(\frac{x_2-x'}{\sqrt{2\varepsilon}}\right) \right] \times \left[\operatorname{erf}\left(\frac{y_1-y'}{\sqrt{2\varepsilon}}\right) - \operatorname{erf}\left(\frac{y_2-y'}{\sqrt{2\varepsilon}}\right) + 2 \right].
\end{aligned}$$

Therefore,

$$\begin{aligned}
& \left| \int_{y_1}^{y_2} \int_{x_1}^{x_2} \delta_\varepsilon(x-x', y-y') f(x, y) dx dy - f(x', y') \right| \\
&\leq \left| \frac{\varepsilon^2}{\sqrt{\pi}} \Gamma\left(\frac{3}{2}\right) [f_{xx}(x', y') + f_{yy}(x', y')] + \mathcal{O}(\varepsilon^3) + \frac{M}{4} \left[\operatorname{erf}\left(\frac{x_1-x'}{\sqrt{2\varepsilon}}\right) - \operatorname{erf}\left(\frac{x_2-x'}{\sqrt{2\varepsilon}}\right) + 2 \right] \right. \\
&\quad \left. \frac{M}{8} \left[\operatorname{erf}\left(\frac{x_1-x'}{\sqrt{2\varepsilon}}\right) - \operatorname{erf}\left(\frac{x_2-x'}{\sqrt{2\varepsilon}}\right) \right] \times \left[\operatorname{erf}\left(\frac{y_1-y'}{\sqrt{2\varepsilon}}\right) - \operatorname{erf}\left(\frac{y_2-y'}{\sqrt{2\varepsilon}}\right) + 2 \right] \right| \rightarrow 0, \text{ as } \varepsilon \rightarrow 0^+.
\end{aligned}$$

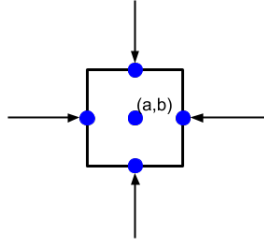


Figure 5.1: We consider a square shape cell, with the centre position at (a, b) . The forces exerted on the boundary are indicated by arrows

□

5

We start with analysing only one relatively big cell in the computational domain. According to the model described in Eq (5.4), the forces released on the boundary of the cell are the superposition of point forces on the midpoint of each line segment. For example, if we use a square shape to approximate the cell, then the forces are depicted in Figure 5.1. Therefore, in this circumstance, the forces can be rewritten as

$$\begin{aligned}
 \mathbf{f}_t &= P \left\{ \begin{bmatrix} 1 \\ 0 \end{bmatrix} \Delta y \delta \left(x - \left(a - \frac{\Delta x}{2} \right), y - b \right) - \begin{bmatrix} 1 \\ 0 \end{bmatrix} \Delta y \delta \left(x - \left(a + \frac{\Delta x}{2} \right), y - b \right) \right. \\
 &\quad \left. + \begin{bmatrix} 0 \\ 1 \end{bmatrix} \Delta x \delta \left(x - a, y - \left(b - \frac{\Delta y}{2} \right) \right) - \begin{bmatrix} 0 \\ 1 \end{bmatrix} \Delta x \delta \left(x - a, y - \left(b + \frac{\Delta y}{2} \right) \right) \right\} \\
 &\approx P \left\{ \begin{bmatrix} 1 \\ 0 \end{bmatrix} \Delta y \left[\delta_\varepsilon \left(x - \left(a - \frac{\Delta x}{2} \right), y - b \right) - \delta_\varepsilon \left(x - \left(a + \frac{\Delta x}{2} \right), y - b \right) \right] \right. \\
 &\quad \left. + \begin{bmatrix} 0 \\ 1 \end{bmatrix} \Delta x \left[\delta_\varepsilon \left(x - a, y - \left(b - \frac{\Delta y}{2} \right) \right) - \delta_\varepsilon \left(x - a, y - \left(b + \frac{\Delta y}{2} \right) \right) \right] \right\},
 \end{aligned} \tag{5.12}$$

where we set $\delta(x) \approx \delta_\varepsilon(x)$. Thanks to the continuity of the Gaussian distribution δ_ε , there exists $(\eta_x, \eta_y) \in (-\Delta x/2, \Delta x/2) \times (-\Delta y/2, \Delta y/2)$ such that, Eq (5.12) yields into

$$\begin{aligned}
 \mathbf{f}_t &\approx P \left\{ \begin{bmatrix} 1 \\ 0 \end{bmatrix} \Delta y \Delta x \frac{\partial \delta_\varepsilon}{\partial x} (x - a + \eta_x, y - b) + \begin{bmatrix} 0 \\ 1 \end{bmatrix} \Delta y \Delta x \frac{\partial \delta_\varepsilon}{\partial y} (x - a, y - b + \eta_y) \right\} \\
 &\rightarrow P \Delta x \Delta y \nabla \delta_\varepsilon (x - a, y - b), \text{ as } \Delta x, \Delta y \rightarrow 0.
 \end{aligned} \tag{5.13}$$

The above procedure implies that as $\Delta x, \Delta y \rightarrow 0$, the right-hand side of the regularized Dirac Delta Distributions converges to $P \Delta x \Delta y \nabla \delta_\varepsilon (x - a, y - b)$. This implies that the Laplacian of the difference between the solutions from both approaches converges to zero.

Lemma 5.2. (Korn's Inequality [80]) Let $\Omega \subset \mathbb{R}^n$ be an open, connected domain. Then there exists a positive constant K , such that for any function $\mathbf{u} \in H^1(\Omega)$,

$$\int_{\Omega} \left[\frac{1}{2} (\nabla \mathbf{u} + \nabla \mathbf{u}^T) \right]^2 d\Omega + \int_{\Omega} \mathbf{u}^2 d\Omega \geq K \|\mathbf{u}\|_{H^1(\Omega)}^2.$$

Lemma 5.3. (Korn's Second Inequality [80]) Let $\Omega \subset \mathbb{R}^n$ be an open, connected domain, and denote $\boldsymbol{\epsilon}(\mathbf{u})$ as it is defined in Eq (5.3). Then there exists a positive constant K' , such that for any function $\mathbf{u} \in H^1(\Omega)$,

$$\int_{\Omega} \boldsymbol{\epsilon}(\mathbf{u}) : \boldsymbol{\epsilon}(\mathbf{u}) d\Omega \geq K' \|\mathbf{u}\|_{H^1(\Omega)}^2,$$

where $\mathbf{A} : \mathbf{B} = \sum_{i=1}^n \sum_{j=1}^n a_{ij} b_{ij}$ is the inner product of two matrices.

Corollary 5.1. Let $\Omega \subset \mathbb{R}^n$ be an open, connected domain, and denote $\boldsymbol{\epsilon}(\mathbf{u})$ as it is defined in Eq (5.3) and $\boldsymbol{\sigma}(\mathbf{u})$ as in Eq (5.2). Then there exists a positive constant K' , such that for any function $\mathbf{u} \in H^1(\Omega)$,

$$\int_{\Omega} \boldsymbol{\sigma}(\mathbf{u}) : \boldsymbol{\epsilon}(\mathbf{u}) d\Omega \geq K' \|\mathbf{u}\|_{H^1(\Omega)}^2.$$

Proof. According to the definition of $\boldsymbol{\sigma}$, the integral is given by

$$\begin{aligned} & \int_{\Omega} \boldsymbol{\sigma}(\mathbf{u}) : \boldsymbol{\epsilon}(\mathbf{u}) d\Omega \\ &= \int_{\Omega} \frac{E}{1+\nu} \|\boldsymbol{\epsilon}\|^2 + \frac{E\nu}{(1+\nu)(1-2\nu)} \text{tr}(\boldsymbol{\epsilon}) \mathbf{I} : \boldsymbol{\epsilon} d\Omega \\ &= \int_{\Omega} \frac{E}{1+\nu} \|\boldsymbol{\epsilon}\|^2 + \frac{E\nu}{(1+\nu)(1-2\nu)} \text{tr}(\boldsymbol{\epsilon})^2 d\Omega \\ &\geq \frac{E}{1+\nu} \int_{\Omega} \|\boldsymbol{\epsilon}\|^2 d\Omega. \end{aligned}$$

Applying Korn's second inequality (Lemma 5.3), it can be concluded that there exists a positive constant K' such that

$$\int_{\Omega} \boldsymbol{\sigma}(\mathbf{u}) : \boldsymbol{\epsilon}(\mathbf{u}) \geq K' \|\mathbf{u}\|_{H^1(\Omega)}^2.$$

□

Theorem 5.1. Let \mathbf{u} the solution to the boundary value problems

$$(BVP^2) \begin{cases} -\nabla \cdot \boldsymbol{\sigma}(\mathbf{u}) = P \left\{ \begin{bmatrix} 1 \\ 0 \end{bmatrix} \Delta y \left[\delta \left(x - \left(a - \frac{\Delta x}{2} \right), y - b \right) - \delta \left(x - \left(a + \frac{\Delta x}{2} \right), y - b \right) \right] \right. \\ \left. + \begin{bmatrix} 0 \\ 1 \end{bmatrix} \Delta x \left[\delta \left(x - a, y - \left(b - \frac{\Delta y}{2} \right) \right) - \delta \left(x - a, y - \left(b + \frac{\Delta y}{2} \right) \right) \right] \right\}, \mathbf{x} \in \Omega, \\ \boldsymbol{\sigma}(\mathbf{u}_{\boldsymbol{\epsilon}}) \cdot \mathbf{n} + \kappa \mathbf{u}_{\boldsymbol{\epsilon}} = \mathbf{0}, \mathbf{x} \in \partial\Omega, \end{cases}$$

(5.14)

and \mathbf{u}_ε the solution to

$$(BVP_\varepsilon^2) \left\{ \begin{array}{l} -\nabla \cdot \boldsymbol{\sigma}(\mathbf{u}_\varepsilon) = P \left\{ \begin{array}{l} \left[\begin{array}{l} 1 \\ 0 \end{array} \right] \Delta y \left[\delta_\varepsilon \left(x - \left(a - \frac{\Delta x}{2} \right), y - b \right) - \delta_\varepsilon \left(x - \left(a + \frac{\Delta x}{2} \right), y - b \right) \right] \\ + \left[\begin{array}{l} 0 \\ 1 \end{array} \right] \Delta x \left[\delta_\varepsilon \left(x - a, y - \left(b - \frac{\Delta y}{2} \right) \right) - \delta_\varepsilon \left(x - a, y - \left(b + \frac{\Delta y}{2} \right) \right) \right] \end{array} \right\}, \mathbf{x} \in \Omega, \\ \boldsymbol{\sigma}(\mathbf{u}_\varepsilon) \cdot \mathbf{n} + \kappa \mathbf{u}_\varepsilon = \mathbf{0}, \mathbf{x} \in \partial\Omega. \end{array} \right. \quad (5.15)$$

Then \mathbf{u}_ε converges to \mathbf{u} , as $\varepsilon \rightarrow 0^+$.

Proof. Let $\mathbf{w} = \mathbf{u} - \mathbf{u}_\varepsilon$, and subtract the equations above. It yields into a new boundary value problem of \mathbf{w} :

$$(BVP_w^2) \left\{ \begin{array}{l} -\nabla \cdot \boldsymbol{\sigma}(\mathbf{w}) = P \left\{ \begin{array}{l} \left[\begin{array}{l} 1 \\ 0 \end{array} \right] \Delta y \left[\delta \left(x - \left(a - \frac{\Delta x}{2} \right), y - b \right) - \delta_\varepsilon \left(x - \left(a - \frac{\Delta x}{2} \right), y - b \right) \right. \\ \left. - \delta \left(x - \left(a + \frac{\Delta x}{2} \right), y - b \right) + \delta_\varepsilon \left(x - \left(a + \frac{\Delta x}{2} \right), y - b \right) \right] \\ + \left[\begin{array}{l} 0 \\ 1 \end{array} \right] \Delta x \left[\delta \left(x - a, y - \left(b - \frac{\Delta y}{2} \right) \right) - \delta_\varepsilon \left(x - a, y - \left(b - \frac{\Delta y}{2} \right) \right) - \delta \left(x - a, y - \left(b + \frac{\Delta y}{2} \right) \right) \right. \\ \left. + \delta_\varepsilon \left(x - a, y - \left(b + \frac{\Delta y}{2} \right) \right) \right] \right\}, \mathbf{x} \in \Omega, \\ \boldsymbol{\sigma}(\mathbf{w}) \cdot \mathbf{n} + \kappa \mathbf{w} = \mathbf{0}, \mathbf{x} \in \partial\Omega. \end{array} \right. \quad (5.16)$$

We multiply the above PDE by \mathbf{w} and integrate over the computational domain Ω . Due to the symmetry of strain tensor $\boldsymbol{\varepsilon}$ and the boundary condition, $-\int_\Omega \nabla \cdot \boldsymbol{\sigma}(\mathbf{w}) \mathbf{w} d\Omega = \int_\Omega \boldsymbol{\sigma}(\mathbf{w}) : \boldsymbol{\varepsilon}(\mathbf{w}) d\Omega + \int_{\partial\Omega} \kappa \mathbf{w}^2 dS$. For the convenience, we denote \mathbf{f}_w for the right-hand side of the equation in (BVP_w^2) as force. According to Lemma 5.1, the integral over the right-hand side converges with quadratic order. Therefore, combined with coerciveness and Korn's Inequality (Lemma 5.2 and 5.3), we derive that there exists a positive constant K , such that

$$\begin{aligned} K \int_\Omega \mathbf{w}^2 d\Omega &\leq \int_\Omega \boldsymbol{\sigma}(\mathbf{w}) : \boldsymbol{\varepsilon}(\mathbf{w}) d\Omega + \int_{\partial\Omega} \kappa \mathbf{w}^2 dS \\ &= - \int_\Omega \nabla \cdot \boldsymbol{\sigma}(\mathbf{w}) \mathbf{w} d\Omega = \int_\Omega \mathbf{f}_w \mathbf{w} d\Omega \\ &= \mathcal{O}(\varepsilon^2) \rightarrow 0, \text{ as } \varepsilon \rightarrow 0^+. \end{aligned}$$

Hence, we can conclude that \mathbf{u} converges to \mathbf{u}_ε with the order of ε^2 . \square

Theorem 5.2. Let \mathbf{u}_ε the solution to the boundary value problems in Eq (5.15), and \mathbf{v}_ε the solution to

$$(BVP_{SP}^2) \left\{ \begin{array}{l} -\nabla \cdot \boldsymbol{\sigma}(\mathbf{v}_\varepsilon) = P \Delta x \Delta y \nabla \delta_\varepsilon(x - a, y - b), \quad \mathbf{x} \in \Omega, \\ \boldsymbol{\sigma}(\mathbf{v}_\varepsilon) \cdot \mathbf{n} + \kappa \mathbf{v}_\varepsilon = \mathbf{0}, \quad \mathbf{x} \in \partial\Omega. \end{array} \right. \quad (5.17)$$

As the size of the cell (i.e. $\Delta x, \Delta y$) turns to zero, \mathbf{v}_ε converges to \mathbf{u}_ε .

Proof. Similarly, let $\mathbf{w}_\varepsilon = \mathbf{u}_\varepsilon - \mathbf{v}_\varepsilon$, and subtract the equations above. There exists $(\eta_x, \eta_y) \in (0, 1) \times (0, 1)$, such that applying a Taylor expansion on the smoothed delta-functions, we obtain

$$\left\{ \begin{array}{l} -\nabla \cdot \boldsymbol{\sigma}(\mathbf{w}_\varepsilon) = P \frac{1}{48} \Delta x^3 \Delta y \begin{bmatrix} 1 \\ 0 \end{bmatrix} \left[\frac{\partial^3 \delta_\varepsilon}{\partial x^3}(x - (a - \frac{h}{2}\eta_x), y - b) - \frac{\partial^3 \delta_\varepsilon}{\partial x^3}(x - (a - \frac{h}{2}\eta_x), y - b) \right] \\ + P \frac{1}{48} \Delta x \Delta y^3 \begin{bmatrix} 0 \\ 1 \end{bmatrix} \left[\frac{\partial^3 \delta_\varepsilon}{\partial y^3}(x - a, y - (b - \frac{h}{2}\eta_y)) - \frac{\partial^3 \delta_\varepsilon}{\partial y^3}(x - a, y - (b - \frac{h}{2}\eta_y)) \right], \mathbf{x} \in \Omega, \\ \boldsymbol{\sigma}(\mathbf{w}_\varepsilon) \cdot \mathbf{n} + \kappa \mathbf{w}_\varepsilon = \mathbf{0}, \mathbf{x} \in \partial\Omega. \end{array} \right. \quad (5.18)$$

Following the same procedures in Th 5.1, it results in

$$\kappa \int_{\Omega} \mathbf{w}_\varepsilon^2 d\Omega \leq \int_{\Omega} \boldsymbol{\sigma}(\mathbf{w}_\varepsilon) : \boldsymbol{\varepsilon}(\mathbf{w}_\varepsilon) d\Omega + \int_{\partial\Omega} \kappa \mathbf{w}_\varepsilon^2 dS = - \int_{\Omega} \nabla \cdot \boldsymbol{\sigma}(\mathbf{w}_\varepsilon) \mathbf{w}_\varepsilon d\Omega.$$

The above equation followed as a result of coerciveness and Korn's Inequality (see Lemma 5.2 and 5.3). Using the right-hand side of Eq (5.18) with an L^2 -inner product with w_ε , implies that, we obtain that there exists a positive constant α such that

$$\|\mathbf{w}_\varepsilon\|_{L^2(\Omega)} \leq \alpha \Delta x \Delta y \sqrt{\Delta x^4 + \Delta y^4} \|D^3 \delta_\varepsilon(x - a, y - b)\|_\infty \rightarrow 0, \text{ as } \Delta x, \Delta y \rightarrow 0,$$

where $D^3 \delta_\varepsilon(x - a, y - b)$ is the third derivative of the Gaussian distribution. Hence, $\|\mathbf{w}_\varepsilon\| \rightarrow 0$, as $h \rightarrow 0$, which implies the convergence between \mathbf{u}_ε and \mathbf{v}_ε . \square

With the two theorems above, we have proved that the solution to (BVP_ε^2) converges to the solution to (BVP^2) , and the solution to (BVP_{SP}^2) converges to the solution to (BVP_ε^2) . Hence, we can derive the following theorem:

Theorem 5.3. *Let \mathbf{u} be the solution to (BVP^2) and \mathbf{v}_ε be the solution to (BVP_{SP}^2) , as $\varepsilon \rightarrow 0^+$ and $\Delta x, \Delta y \rightarrow 0$, \mathbf{v}_ε converges to \mathbf{u} .*

Proof. Combining Th 5.1 and Th 5.2, making use of the triangle inequality, we calculate

$$\|\mathbf{u} - \mathbf{v}_\varepsilon\| = \|\mathbf{u} - \mathbf{u}_\varepsilon - \mathbf{v}_\varepsilon + \mathbf{u}_\varepsilon\| \leq \|\mathbf{u} - \mathbf{u}_\varepsilon\| + \|\mathbf{v}_\varepsilon - \mathbf{u}_\varepsilon\| \rightarrow 0,$$

since both term converges to zero respectively, when $\varepsilon \rightarrow 0^+$ and $\Delta x, \Delta y \rightarrow 0$. \square

5.3. ELASTICITY EQUATION WITH POINT SOURCES IN MULTIPLE DIMENSIONS

In the n -dimensional case, we are solving the boundary value problems described in Eq (5.1), (5.2) and (5.3). The body force is given in Eq (5.4), and we consider a homogeneous Dirichlet boundary condition here. Therefore, the immersed boundary value problem that we are going to consider is given by

$$(BVP^n) \left\{ \begin{array}{ll} -\nabla \cdot \boldsymbol{\sigma}(\mathbf{x}) = \sum_{j=1}^{N_S} P(\mathbf{x}_j) \mathbf{n}(\mathbf{x}_j) \delta(\mathbf{x} - \mathbf{x}_j) \Delta S(\mathbf{x}_j), & \text{in } \Omega, \\ \mathbf{u} = \mathbf{0}, & \text{on } \partial\Omega. \end{array} \right.$$

Next to this boundary value problem, we consider the continuous immersed boundary counterpart, given by

$$(BVP_\infty^n) \begin{cases} -\nabla \cdot \boldsymbol{\sigma}(\mathbf{x}) = \int_{\Gamma_C} P(\mathbf{x}') \mathbf{n}(\mathbf{x}') \delta(\mathbf{x} - \mathbf{x}') dS(\mathbf{x}'), & \text{in } \Omega, \\ \mathbf{u} = \mathbf{0}, & \text{on } \partial\Omega, \end{cases}$$

where we take $N_s \rightarrow \infty$. Thus, the body force reads as

$$\mathbf{f}_t^\infty = \int_{\Gamma_C} P(\mathbf{x}') \mathbf{n}(\mathbf{x}') \delta(\mathbf{x} - \mathbf{x}') dS(\mathbf{x}'). \quad (5.19)$$

Due to the irregular nature of the Dirac Delta distributions, the solutions do not exist in \mathbf{H}^1 . We attempt to approximate the solution by the functions in \mathbf{H}^1 via the Galerkin form of (BVP^n) and (BVP_∞^n) . In this chapter, piecewise linear Lagrangian basis functions are selected. Further, the convergence of the finite-element solutions using linear Lagrangian elements in general dimensionality has been proved in [79].

To construct the Galerkin form, we introduce the bilinear form $a(\cdot, \cdot)$

$$a(\mathbf{u}_h, \boldsymbol{\phi}_h) = \int_{\Omega} \boldsymbol{\sigma}(\mathbf{u}_h) : \nabla \boldsymbol{\phi}_h d\Omega = \int_{\Omega} \boldsymbol{\sigma}(\mathbf{u}_h) : \boldsymbol{\epsilon}(\boldsymbol{\phi}_h) d\Omega, \quad (5.20)$$

where the last step is motivated by symmetry of the stress tensor $\boldsymbol{\sigma}$. Recall the definition of $\mathbf{V}_h(\Omega) = \text{Span}\{\boldsymbol{\phi}^1, \boldsymbol{\phi}^2, \dots, \boldsymbol{\phi}^N\}$ [81], where $\boldsymbol{\phi}^i$ for $i = \{1, 2, \dots, N\}$ is the linear Lagrangian basis function over Ω . Subsequently, the Galerkin form is

$$(GF^n) \begin{cases} \text{Find } \mathbf{u}_h \in \mathbf{V}_h(\Omega), \text{ such that} \\ a(\mathbf{u}_h, \boldsymbol{\phi}_h) = (\boldsymbol{\phi}_h, \mathbf{f}_t) = \sum_{j=1}^{N_s} P(\mathbf{x}_j) \mathbf{n}(\mathbf{x}_j) \boldsymbol{\phi}_h(\mathbf{x}_j) \Delta S(\mathbf{x}_j), \\ \text{for all } \boldsymbol{\phi}_h \in \{\boldsymbol{\phi}^1, \boldsymbol{\phi}^2, \dots, \boldsymbol{\phi}^N\} \subset \mathbf{V}_h(\Omega). \end{cases}$$

We further consider the solution to the continuous immersed boundary problem, with the following Galerkin form:

$$(GF_\infty^n) \begin{cases} \text{Find } \mathbf{u}_h \in \mathbf{V}_h(\Omega), \text{ such that} \\ a(\mathbf{u}_h, \boldsymbol{\phi}_h) = (\boldsymbol{\phi}_h, \mathbf{f}_t^\infty) = \int_{\Gamma_C} P(\mathbf{x}') \mathbf{n}(\mathbf{x}') \boldsymbol{\phi}_h(\mathbf{x}') dS(\mathbf{x}'), \\ \text{for all } \boldsymbol{\phi}_h \in \{\boldsymbol{\phi}^1, \boldsymbol{\phi}^2, \dots, \boldsymbol{\phi}^N\} \subset \mathbf{V}_h(\Omega). \end{cases}$$

We note that Korn's Second Inequality can be generalised to cases in which the boundary condition $\mathbf{u} = \mathbf{0}$ is imposed only on a non-zero measure part of the boundary. Using Korn's Second inequality gives the following lemma:

Lemma 5.4. *Let $\Omega \subset \mathbb{R}^n$ be an open, bounded and connected domain. Then there exists a positive constant K , such that for any vector-valued function $\mathbf{u} \in \mathbf{H}_0^1(\Omega)$,*

$$a(\mathbf{u}, \mathbf{u}) = \int_{\Omega} \boldsymbol{\sigma}(\mathbf{u}) : \boldsymbol{\epsilon}(\mathbf{u}) d\Omega \geq K \|\mathbf{u}\|_{\mathbf{H}^1(\Omega)}^2.$$

Proof. The lemma directly follows from the definition of the stress tensor, let $\mathbf{u} \in \mathbf{H}_0^1(\Omega)$:

$$\begin{aligned} a(\mathbf{u}, \mathbf{u}) &= \int_{\Omega} \boldsymbol{\sigma}(\mathbf{u}) : \boldsymbol{\varepsilon}(\mathbf{u}) d\Omega \\ &= \int_{\Omega} \frac{E}{1+\nu} \left\{ \boldsymbol{\varepsilon}(\mathbf{u}) + \text{tr}(\boldsymbol{\varepsilon}(\mathbf{u})) \frac{\nu}{1-2\nu} \mathbf{I} \right\} : \boldsymbol{\varepsilon}(\mathbf{u}) d\Omega \\ &= \int_{\Omega} \frac{E}{1+\nu} \|\boldsymbol{\varepsilon}(\mathbf{u})\|^2 + \frac{E\nu}{(1+\nu)(1-2\nu)} (\text{tr}(\boldsymbol{\varepsilon}(\mathbf{u})))^2 d\Omega \\ &\geq \frac{E}{1+\nu} K \|\mathbf{u}\|_{\mathbf{H}^1(\Omega)}^2. \end{aligned}$$

The last step follows from Lemma 5.3. Hence, redefining $K := \frac{E}{1+\nu} K$ concludes the proof the lemma. \square

Herewith, coerciveness of the linear form $a(\cdot, \cdot)$ has been demonstrated, which is needed for the proof of existence and uniqueness of the Galerkin finite-element solution.

5

Theorem 5.4. Let $\{\boldsymbol{\phi}^i\}$ be piecewise Lagrangian basis field functions and let \mathbf{F} be a vector in \mathbb{R}^n with unit length, further let $P \in C(\bar{\Omega})$, and let $|P| \leq M_2$ for some $M_2 > 0$. We define $\mathbf{V}_h(\Omega) = \text{Span}\{\boldsymbol{\phi}^1, \boldsymbol{\phi}^2, \dots, \boldsymbol{\phi}^{N_s}\} \subset \mathbf{H}_0^1(\Omega)$, then

- $\exists! \mathbf{u}_h^G(\mathbf{x}; \mathbf{x}'; \mathbf{F}) \in \mathbf{V}_h(\Omega)$ such that $a(\mathbf{u}_h, \boldsymbol{\phi}_h) = \mathbf{F}(\mathbf{x}') \cdot \boldsymbol{\phi}_h(\mathbf{x}')$ for all $\boldsymbol{\phi}_h \in \mathbf{V}_h$;
- $\exists! \mathbf{u}_h \in \mathbf{V}_h(\Omega)$ such that

$$a(\mathbf{u}_h, \boldsymbol{\phi}_h) = \sum_{j=1}^{N_s} P(\mathbf{x}_j) \mathbf{n}(\mathbf{x}_j) \boldsymbol{\phi}_h(\mathbf{x}_j) \Delta S(\mathbf{x}_j),$$

for all $\boldsymbol{\phi}_h \in \mathbf{V}_h$, and

$$\mathbf{u}_h = \sum_{j=1}^{N_s} P(\mathbf{x}_j) \mathbf{u}_h^G(\mathbf{x}; \mathbf{x}_j; \mathbf{n}(\mathbf{x}_j)) \Delta S(\mathbf{x}_j);$$

- $\exists! \mathbf{u}_h \in \mathbf{V}_h(\Omega)$ such that

$$a(\mathbf{u}_h, \boldsymbol{\phi}_h) = \int_{\Gamma_C} P(\mathbf{x}') \mathbf{n}(\mathbf{x}') \boldsymbol{\phi}_h(\mathbf{x}') dS(\mathbf{x}'),$$

for all $\boldsymbol{\phi}_h \in \mathbf{V}_h$, and

$$\mathbf{u}_h = \int_{\Gamma_C} P(\mathbf{x}') \mathbf{u}_h^G(\mathbf{x}; \mathbf{x}'; \mathbf{n}(\mathbf{x}')) dS(\mathbf{x}');$$

Proof. • It is immediately clear that $a(\cdot, \cdot)$ is a bilinear form. We have $\mathbf{V}_h \subset \mathbf{H}_0^1(\Omega)$, and $a(\cdot, \cdot)$ is bounded in $\mathbf{H}_0^1(\Omega)$ (see for instance [84]). Furthermore, Lemma 5.4 says that $a(\cdot, \cdot)$ is coercive in $\mathbf{H}_0^1(\Omega)$. Regarding the right-hand side, we have $|\boldsymbol{\phi}_h| \leq$

M_1 for some $M_1 > 0$ since $\boldsymbol{\phi}_h$ is a Lagrangian function, and hence the magnitude of the right-hand side can be bounded from above by

$$|\mathbf{F} \cdot \boldsymbol{\phi}_h(\mathbf{x}')| \leq M_1.$$

Note that $\|\mathbf{F}\| = 1$. Hence the right-hand side is bounded, since we are looking for a solution in a finite dimensional space \mathbf{V}_h , the system

$$\mathbf{A}\mathbf{c} = \mathbf{b},$$

where the coefficients of the symmetric matrix \mathbf{A} are defined by $a_{ij} = a(\phi_i, \phi_j)$, and where a limited number of entries of \mathbf{b} are non-zero and given by $\mathbf{F} \cdot \boldsymbol{\phi}_h(\mathbf{x}')$, which is finite. Since \mathbf{b} is finite, and \mathbf{A} is invertible, existence and uniqueness of \mathbf{u}_h follow (one could apply Lax-Milgram's theorem on the space \mathbb{R}^n in this context) from the algebraic system. For the case of a Hilbert space, boundedness of $\mathbf{F} \cdot \boldsymbol{\phi}_h$ in the H^1 -norm does not hold. This boundedness can only be proved in the one-dimensional case.

- Existence and uniqueness follow analogously, only boundedness of the right-hand side, which is a linear functional in $\boldsymbol{\phi}_h \in \mathbf{V}_h(\Omega)$ has to be checked:

$$\begin{aligned} \left| \sum_{j=1}^{N_S} P(\mathbf{x}_j) \mathbf{n}(\mathbf{x}_j) \cdot \boldsymbol{\phi}_h(\mathbf{x}_j) \Delta S(\mathbf{x}_j) \right| &\leq \sum_{j=1}^{N_S} |P(\mathbf{x}_j)| \|\mathbf{n}(\mathbf{x}_j)\| \|\boldsymbol{\phi}_h(\mathbf{x}_j)\| \Delta S(\mathbf{x}_j) \\ &= \sum_{j=1}^{N_S} |P(\mathbf{x}_j)| \|\boldsymbol{\phi}_h(\mathbf{x}_j)\| \Delta S(\mathbf{x}_j) \leq M_1 M_2 \sum_{j=1}^{N_S} \Delta S(\mathbf{x}_j). \end{aligned}$$

Note that \mathbf{n} has unit length. The summation gives the polygonal length or polyhedral area of the cell boundary. Hence the right-hand side is bounded, then existence and uniqueness follow for the algebraic system. Further by substitution, it follows that that

$$\begin{aligned} a(\mathbf{u}_h, \boldsymbol{\phi}_h) &= a\left(\sum_{j=1}^{N_S} P(\mathbf{x}_j) \mathbf{u}_h^G(\mathbf{x}, \mathbf{x}_j, \mathbf{n}(\mathbf{x}_j)) \Delta S(\mathbf{x}_j), \boldsymbol{\phi}_h\right) \\ &= \sum_{j=1}^{N_S} P(\mathbf{x}_j) a(\mathbf{u}_h^G(\mathbf{x}, \mathbf{x}_j, \mathbf{n}(\mathbf{x}_j)), \boldsymbol{\phi}_h) \Delta S(\mathbf{x}_j) \\ &= \sum_{j=1}^{N_S} P(\mathbf{x}_j) \mathbf{n}(\mathbf{x}_j) \cdot \boldsymbol{\phi}_h(\mathbf{x}_j) \Delta S(\mathbf{x}_j). \end{aligned}$$

The last step uses the first part of the theorem, and finally the assertion is proved similarly to the first assertion.

- We proceed similarly, by boundedness of the right-hand side:

$$\left| \int_{\Gamma_C} P(\mathbf{x}') \mathbf{n}(\mathbf{x}') \cdot \boldsymbol{\phi}_h(\mathbf{x}') dS(\mathbf{x}') \right| \leq M_1 M_2 |\Gamma_C|,$$

where $|\Gamma_C|$ is the measure of the boundary surface of the biological cell. It again shows that the right-hand side is a bounded linear functional in $V_h(\Omega)$. We proceed by substitution:

$$\begin{aligned} a(\mathbf{u}_h, \boldsymbol{\phi}_h) &= a\left(\int_{\Gamma_C} P(\mathbf{x}') \mathbf{u}_h^G(\mathbf{x}, \mathbf{x}', \mathbf{n}(\mathbf{x}')) dS(\mathbf{x}'), \boldsymbol{\phi}_h\right) \\ &= \int_{\Gamma_C} P(\mathbf{x}') a(\mathbf{u}_h^G(\mathbf{x}, \mathbf{x}', \mathbf{n}(\mathbf{x}')), \boldsymbol{\phi}_h) dS(\mathbf{x}') \\ &= \int_{\Gamma_C} P(\mathbf{x}') \mathbf{n}(\mathbf{x}') \cdot \boldsymbol{\phi}_h(\mathbf{x}') dS(\mathbf{x}'). \end{aligned}$$

Note that, formally, it was not necessary to prove boundedness, since coerciveness implies uniqueness and the existence was proved by construction and by combining the result for the existence of \mathbf{u}_h^G . \square

5

Note that for the 'continuous' weak formulation, there is no solution in \mathbf{H}^1 , hence the above claim demonstrates the existence and uniqueness of a Galerkin-based approximation in a subset of \mathbf{H}^1 to a function that is not in \mathbf{H}^1 . The situation is somewhat comparable to approximating $\sqrt{2} \notin \mathbb{Q}$ arbitrarily accurately by a sequence of successive approximations in \mathbb{Q} . Further in two- and three- dimensional case, the convergence between the solution to (GF^n) and (GF_∞^n) can be proved. Similar work has been done in [85] regarding Stokes problem with the Delta distribution term.

Theorem 5.5. *Let Γ_C be a polygon or polyhedron embedded in $\Omega \subset \mathbb{R}^n$ and let $P(\mathbf{x})$ be sufficiently smooth. Further, let \mathbf{x}_j be the midpoint of surface element $\Delta S(\mathbf{x}_j)$. Denote $\mathbf{u}_h^{\Delta S}$ as the Galerkin solution to (GF^n) and the \mathbf{u}_h^∞ as the Galerkin solution to (GF_∞^n) , respectively. In two dimensions, for any $\mathbf{x} \notin \Gamma_C$, there exists a positive constant C , such that for each component of \mathbf{u}_h^∞ we have*

$$|\mathbf{u}_h^{\Delta S} - \mathbf{u}_h^\infty| \leq C \Delta S_{max}^2,$$

where $\Delta S_{max} = \max\{\Delta S(\mathbf{x}_j)\}$ for any $j = \{1, 2, \dots, N_S\}$. In three dimensions, for any $\mathbf{x} \notin \Gamma_C$, there exists a positive constant C , such that for each component of \mathbf{u}_h^∞ we have

$$|\mathbf{u}_h^{\Delta S} - \mathbf{u}_h^\infty| \leq C h_{max}^2,$$

where h_{max} is the maximal diameter among all the triangular elements over Γ_C .

Proof. Away from Γ_C , the function \mathbf{u}_h^G is smooth, and since $P(\mathbf{x})$ is smooth as well, the integrand, given by $P(\mathbf{x}) \mathbf{u}_h^G$ is smooth as well. For ease of notation, we set $\mathbf{f}(\mathbf{x}) = P(\mathbf{x}) \mathbf{u}_h^G(\mathbf{x}; \mathbf{x}', \mathbf{n})$. We start with the 2D-case. Given the i -th boundary element ΔS_i on Γ_C with the endpoints \mathbf{x}_i and \mathbf{x}_{i+1} and we denote its midpoint by $\mathbf{x}_{i+1/2}$, where $i \in \{1, 2, \dots, N_S\}$. We consider

$$\mathbf{x}(s) = \mathbf{x}_{i+1/2} + s \frac{\mathbf{x}_{i+1} - \mathbf{x}_i}{2}, \quad -1 \leq s \leq 1,$$

Hence, $\mathbf{x}(0) = \mathbf{x}_{i+1/2}$ and $\mathbf{x}'(s) = \frac{1}{2}(\mathbf{x}_{i+1} - \mathbf{x}_i)$, and subsequently

$$\|\mathbf{x}'(s)\| = \frac{1}{2} \|\mathbf{x}_{i+1} - \mathbf{x}_i\|.$$

We calculate the contribution over ΔS_i to the integral, where Taylor's Theorem and the Mean Value Theorem for integration are used to warrant the existence of a $\hat{s} \in (-1, 1)$, such that

$$\begin{aligned}
 \int_{\Delta S_i} \mathbf{f}(\mathbf{x}) dS &= \int_{-1}^1 \mathbf{f}(\mathbf{x}(s)) \|\mathbf{x}'(s)\| ds \\
 &= \frac{1}{2} \|\mathbf{x}_{i+1} - \mathbf{x}_i\| \int_{-1}^1 \mathbf{f}(\mathbf{x}(s)) ds \\
 \text{(Taylor Expansion)} &= \frac{1}{2} \|\mathbf{x}_{i+1} - \mathbf{x}_i\| \int_{-1}^1 \mathbf{f}(\mathbf{x}(0)) + s \frac{\mathbf{x}_{i+1} - \mathbf{x}_i}{2} \nabla \mathbf{f}(\mathbf{x}(s))|_{s=0} \\
 &\quad + \frac{1}{2} s^2 \left(\frac{\mathbf{x}_{i+1} - \mathbf{x}_i}{2} \right)^T \mathbf{H}(\mathbf{x}(\hat{s})) \left(\frac{\mathbf{x}_{i+1} - \mathbf{x}_i}{2} \right) ds \\
 &= \frac{1}{2} \|\mathbf{x}_{i+1} - \mathbf{x}_i\| [2\mathbf{f}(\mathbf{x}_{i+1/2}) + 0 + \frac{1}{12} (\mathbf{x}_{i+1} - \mathbf{x}_i)^T \mathbf{H}(\mathbf{x}(\hat{s})) (\mathbf{x}_{i+1} - \mathbf{x}_i)] \\
 &= \|\mathbf{x}_{i+1} - \mathbf{x}_i\| \mathbf{f}(\mathbf{x}_{i+1/2}) + \frac{1}{24} \|\mathbf{x}_{i+1} - \mathbf{x}_i\| (\mathbf{x}_{i+1} - \mathbf{x}_i)^T \mathbf{H}(\mathbf{x}(\hat{s})) (\mathbf{x}_{i+1} - \mathbf{x}_i),
 \end{aligned}$$

where $\mathbf{H}(\mathbf{x}(s))$ is the Hessian matrix of $\mathbf{f}(\mathbf{x}(s))$. Therefore, we obtain that

$$\begin{aligned}
 \left| \int_{\Delta S_i} \mathbf{f}(\mathbf{x}) dS - \|\mathbf{x}_{i+1} - \mathbf{x}_i\| \mathbf{f}(\mathbf{x}_{i+1/2}) \right| &= \frac{1}{24} \|\mathbf{x}_{i+1} - \mathbf{x}_i\| \cdot |(\mathbf{x}_{i+1} - \mathbf{x}_i)^T \mathbf{H}(\mathbf{x}(\hat{s})) (\mathbf{x}_{i+1} - \mathbf{x}_i)| \\
 &\leq \frac{1}{24} \|\mathbf{x}_{i+1} - \mathbf{x}_i\| \tilde{K} \|\mathbf{x}_{i+1} - \mathbf{x}_i\|^2.
 \end{aligned}$$

Since $\mathbf{f}(\mathbf{x}) \in C^2(\Omega)$, it follows that there exists a $\tilde{K} > 0$, such that

$$|(\mathbf{x}, \mathbf{H}(\mathbf{x}))| \leq \tilde{K} \|\mathbf{x}\|^2.$$

Therefore, considering the summation of the boundary elements over Γ_C ,

$$\begin{aligned}
 \left| \int_{\Delta S_i} \mathbf{f}(\mathbf{x}) dS - \sum_{i=1}^{N_S} \|\mathbf{x}_{i+1} - \mathbf{x}_i\| \mathbf{f}(\mathbf{x}_{i+1/2}) \right| &\leq \sum_{i=1}^{N_S} \frac{1}{24} \|\mathbf{x}_{i+1} - \mathbf{x}_i\| \tilde{K} \|\mathbf{x}_{i+1} - \mathbf{x}_i\|^2 \\
 &\leq \frac{1}{24} \tilde{K} \Delta S_{max}^2 \sum_{i=1}^{N_S} \|\mathbf{x}_{i+1} - \mathbf{x}_i\| \\
 &\leq \frac{1}{24} \tilde{K} \Delta S_{max}^2 |\Gamma_C|,
 \end{aligned}$$

where $\Delta S_{max} = \max_{i \in \{1, \dots, N_S\}} \|\mathbf{x}_{i+1} - \mathbf{x}_i\|$ is the maximal length of the line segment over Γ_C , and $|\Gamma_C|$ is the perimeter of the polygon Γ_C . It can be concluded that there exists a positive constant K , such that

$$|\mathbf{u}_h^\infty - \mathbf{u}_h^{\Delta S}| \leq K \Delta S_{max}^2.$$

In three dimensions, the surface element is a triangle. We map the triangle in (x, y, z) -space to the reference triangle in (s, t) -space with points $(0, 0)$, $(0, 1)$ and $(1, 0)$. Suppose there is a surface element e_j with nodal points \mathbf{x}_1 , \mathbf{x}_2 and \mathbf{x}_3 , then the centre point of e_j

is $\mathbf{x}_c = (\mathbf{x}_1 + \mathbf{x}_2 + \mathbf{x}_3)/3$. The map from the reference triangle e_0 to the physical triangle e_j is given by

$$\mathbf{x}(s, t) = \mathbf{x}_1(1 - s - t) + s\mathbf{x}_2 + t\mathbf{x}_3, \quad 0 \leq s, t \leq 1.$$

For any function $\mathbf{f}(\mathbf{x}) \in C^2(\Omega)$, the integral over the original triangle is given by

$$\int_{e_j} \mathbf{f}(\mathbf{x}) d\mathbf{x} = \int_{e_0} \mathbf{f}(\mathbf{x}(s, t)) |\sqrt{\det(\mathbf{J}^T \mathbf{J})}| d(s, t),$$

where \mathbf{J} is the Jacobian matrix, given by

$$\mathbf{J} = \frac{\partial(x, y, z)}{\partial(s, t)} = \begin{pmatrix} x_2 - x_1 & x_3 - x_1 \\ y_2 - y_1 & y_3 - y_1 \\ z_2 - z_1 & z_3 - z_1 \end{pmatrix},$$

and $\sqrt{|\det(\mathbf{J}^T \mathbf{J})|}$ is twice the area of the original triangle e_j , i.e.

$$|\Delta_j| := \sqrt{|\det(\mathbf{J}^T \mathbf{J})|} = \|(\mathbf{x}_2 - \mathbf{x}_1) \times (\mathbf{x}_3 - \mathbf{x}_1)\|.$$

We conduct the same process as for the two dimensional case, we obtain, where $\mathbf{x}(\frac{1}{3}, \frac{1}{3}) = \mathbf{x}_c$ coincides with the midpoint of element e_j , and where Taylor's Theorem for multivariate functions is used with $0 \leq \hat{s} \leq 1, 0 \leq t \leq 1 - s$:

$$\begin{aligned} \int_{e_j} \mathbf{f}(\mathbf{x}) d\mathbf{x} &= \int_{e_0} \mathbf{f}(\mathbf{x}(s, t)) |\Delta_j| d(s, t) \\ &= |\Delta_j| \int_{e_0} \mathbf{f}(\mathbf{x}(s, t)) d(s, t) \\ &= |\Delta_j| \int_{e_0} \mathbf{f}(\mathbf{x}_c) + (\mathbf{x}(s, t) - \mathbf{x}_c) \cdot \nabla \mathbf{f}(\mathbf{x}_c) \\ &\quad + \frac{1}{2} (\mathbf{x}(s, t) - \mathbf{x}_c)^T \mathbf{H}(\mathbf{x}(\hat{s}, \hat{t})) (\mathbf{x}(s, t) - \mathbf{x}_c) d(s, t) \\ &= |\Delta_j| \left[\frac{1}{2} \mathbf{f}(\mathbf{x}_c) + 0 + \frac{1}{2} \int_{e_0} (\mathbf{x}(s, t) - \mathbf{x}_c)^T \mathbf{H}(\mathbf{x}(\hat{s}, \hat{t})) (\mathbf{x}(s, t) - \mathbf{x}_c) d(s, t) \right]. \end{aligned}$$

Due to $\mathbf{f}(\mathbf{x}) \in C^2(\Omega)$, then for the Hessian matrix of $\mathbf{f}(\mathbf{x})$, there exists $\tilde{K} > 0$, such that

$$|(\mathbf{x}, \mathbf{H}(\mathbf{x}))| \leq \tilde{K} \|\mathbf{x}\|^2.$$

It yields

$$\begin{aligned} \left| \int_{e_j} \mathbf{f}(\mathbf{x}) d\mathbf{x} - \frac{|\Delta_j|}{2} \mathbf{f}(\mathbf{x}_c) \right| &\leq \left| \frac{|\Delta_j|}{2} \int_{e_0} (\mathbf{x}(s, t) - \mathbf{x}_c)^T \mathbf{H}(\mathbf{x}(\hat{s}, \hat{t})) (\mathbf{x}(s, t) - \mathbf{x}_c) d(s, t) \right| \\ &\leq \frac{|\Delta_j|}{4} \tilde{K} h_{max}^2, \end{aligned}$$

where h_{max}^2 is the largest diameter in the original triangle e_j . Considering all the surface elements over Γ_C , we compute

$$\left| \int_{\Gamma_C} \mathbf{f}(\mathbf{x}) d\mathbf{x} - \sum_{j=1}^{N_S} \frac{|\Delta_j|}{2} \mathbf{f}(\mathbf{x}_j) \right| \leq \frac{\tilde{K}}{4} h_{max}^2 \sum_{j=1}^{N_S} \frac{|\Delta_j|}{2} \leq \frac{\tilde{K}}{4} h_{max}^2 |\Gamma_C|,$$

where h_{max}^2 is the maximal diameter among all the surface element (i.e. triangle) and $|\Gamma_C|$ is the sum of the measure (area in \mathbb{R}^3) of all the surface elements over Γ_C . Therefore, in three dimensions, we can conclude that there exists a positive constant K , such that for the unique Galerkin solution to both (GF^n) and (GF_∞^n) ,

$$|\mathbf{u}_h^\infty - \mathbf{u}_h^{\Delta S}| \leq Kh_{max}^2.$$

□

The above proof and theorem can easily be extended to higher dimensionalities.

5.3.1. THE 'HOLE' APPROACH

A different approach is based on considering cellular forces on the cell boundary by means of a boundary condition. In this alternative approach, one 'removes' the cell region from the domain of computation. Herewith, one creates a 'hole' in the domain. We consider the balance of momentum over $\Omega \setminus \overline{\Omega}_C$. This gives the following boundary value problem:

$$(BVP_H^n) \begin{cases} -\nabla \cdot \boldsymbol{\sigma} = 0, & \text{in } \Omega \setminus \overline{\Omega}_C, \\ \boldsymbol{\sigma} \cdot \mathbf{n} = P(\mathbf{x}) \mathbf{n}(\mathbf{x}), & \text{on } \Gamma_C, \\ \mathbf{u} = \mathbf{0}, & \text{on } \partial\Omega, \end{cases}$$

where $\boldsymbol{\sigma}$ is defined in Eq (5.2) with stiffness E . Let $D \subset \Omega$, then we introduce the following notation:

$$a_{D,E}(\mathbf{u}, \mathbf{v}) := \int_D \boldsymbol{\sigma}(\mathbf{u}) : \boldsymbol{\epsilon}(\mathbf{v}) d\Omega.$$

Note that the stiffness can be a constant or a function of space over the domain D . The corresponding weak form is stated below:

$$(WF_H^n) \begin{cases} \text{Find } \mathbf{u}^H \in \mathbf{H}^1(\Omega \setminus \Omega_C) \text{ such that} \\ a_{\Omega \setminus \Omega_C, E}(\mathbf{u}^H, \boldsymbol{\phi}) = \int_{\Gamma_C} P(\mathbf{x}) \mathbf{n}(\mathbf{x}) \cdot \boldsymbol{\phi} dS(\mathbf{x}), \text{ for all } \boldsymbol{\phi} \in \mathbf{H}^1(\Omega \setminus \Omega_C). \end{cases}$$

Since $\boldsymbol{\phi} \in \mathbf{H}^1(\Omega \setminus \Omega_C)$, it follows from the Trace Theorem [80], and by noting that $\boldsymbol{\phi}|_{\partial\Omega} = 0$, that there is a $C_1 > 0$ such that $\|\boldsymbol{\phi}\|_{L^2(\Gamma_C)} \leq C_1 \|\boldsymbol{\phi}\|_{\mathbf{H}^1(\Omega)}$, which implies that the right-hand side in the weak form is bounded. Subsequently one combines Korn's Inequality with Lax-Milgram's Lemma to conclude that a unique solution in \mathbf{H}^1 exists.

We compare the immersed boundary method with the 'hole' approach by taking $\beta \geq 0$, then we adjust the immersed boundary method such that

$$E(\mathbf{x}) = \begin{cases} \beta E, & \text{in } \Omega_C, \\ E, & \text{in } \Omega \setminus \overline{\Omega}_C. \end{cases} \quad (5.21)$$

Regarding the adjusted immersed boundary approach where the stiffness is given by Eq (5.21), we have the following Galerkin form

$$(GF_\beta^n) \begin{cases} \text{Find } \mathbf{u}_h^\beta \in \mathbf{V}_h(\Omega) \text{ such that} \\ \beta a_{\Omega_C, E}(\mathbf{u}_h^\beta, \boldsymbol{\phi}_h) + a_{\Omega \setminus \Omega_C, E}(\mathbf{u}_h^\beta, \boldsymbol{\phi}_h) = \int_{\Gamma_C} P(\mathbf{x}) \mathbf{n}(\mathbf{x}) \cdot \boldsymbol{\phi}_h(\mathbf{x}) dS(\mathbf{x}), \text{ for all } \boldsymbol{\phi}_h \in \mathbf{V}_h(\Omega), \end{cases}$$

where $V_h(\Omega)$ is defined in Theorem 5.4 in Section 5.3.

For the 'hole' approach, we have the following Galerkin form

$$(GF_H^n) \begin{cases} \text{Find } \mathbf{u}_h^H \in V_h(\Omega \setminus \Omega_C) \text{ such that} \\ a_{\Omega \setminus \Omega_C, E}(\mathbf{u}_h^H, \boldsymbol{\phi}_h) = \int_{\Gamma_C} P(\mathbf{x}) \mathbf{n}(\mathbf{x}) \cdot \boldsymbol{\phi}_h dS(\mathbf{x}), \text{ for all } \boldsymbol{\phi}_h \in V_h(\Omega \setminus \Omega_C). \end{cases}$$

We will prove that the adjusted immersed boundary method is a perturbation of the 'hole' approach:

Proposition 5.1. *Let \mathbf{u}_h^H and \mathbf{u}_h^β , respectively, satisfy Galerkin forms (GF_H^n) and (GF_β^n) , then there is a $C > 0$ such that*

$$\|\mathbf{u}_h^H - \mathbf{u}_h^\beta\|_{\mathbf{H}^1(\Omega \setminus \Omega_C)} \leq C \sqrt{\beta} \|\mathbf{u}_h^\beta\|_{\mathbf{H}^1(\Omega_C)}^{1/2}.$$

Proof. First we note that, as in the spirit of Theorem 5.4, we consider Galerkin solutions in a subset of \mathbf{H}^1 whereas the solution to the 'continuous' weak formulation is not in \mathbf{H}^1 . Formally (GF_H^n) and (GF_β^n) hold for test functions $\boldsymbol{\phi}_h$ from different sets, namely $V_h(\Omega)$ and $V_h(\Omega \setminus \Omega_C)$. If we choose $V_h(\Omega_C)$ to correspond to Lagrangian basis functions associated to internal nodes in Ω_C , then these basis functions vanish at Γ_C . Furthermore, within the set of Lagrangian basis functions that are associated with $\Omega \setminus \Omega_C$, there are Lagrangian basis functions associated with Γ_C , which have a compact, hence limited, support over Ω_C and in $\Omega \setminus \Omega_C$, then let $\mathbf{v} = \mathbf{u}_h^\beta - \mathbf{u}_h^H$, then subtraction of problems (GF_H^n) and (GF_β^n) gives

$$a_{\Omega \setminus \Omega_C, E}(\mathbf{v}, \boldsymbol{\phi}_h) = -\beta a_{\Omega_C, E}(\mathbf{u}_h^\beta, \boldsymbol{\phi}_h).$$

The left-hand side is a bounded and coercive form on which we can apply Korn's Inequality. Furthermore, boundedness of the right-hand side in $V_h(\Omega \setminus \Omega_C)$ follows by application of the Cauchy-Schwartz Inequality, hence there is an $L > 0$ such that $|a_{\Omega_C, E}(\mathbf{u}_h^\beta, \boldsymbol{\phi}_h)| \leq L \|\mathbf{u}_h^\beta\|_{\mathbf{H}^1(\Omega_C)} \|\boldsymbol{\phi}_h\|_{\mathbf{H}^1(\Omega_C)}$. Herewith, we arrive at

$$-\beta L \|\mathbf{u}_h^\beta\|_{\mathbf{H}^1(\Omega_C)} \|\boldsymbol{\phi}_h\|_{\mathbf{H}^1(\Omega_C)} \leq a_{\Omega \setminus \Omega_C, E}(\mathbf{v}, \boldsymbol{\phi}_h) \leq \beta L \|\mathbf{u}_h^\beta\|_{\mathbf{H}^1(\Omega_C)} \|\boldsymbol{\phi}_h\|_{\mathbf{H}^1(\Omega_C)},$$

for all $\boldsymbol{\phi}_h \in V_h(\Omega \setminus \Omega_C)$.

Note that the $a_{\Omega \setminus \Omega_C}(\mathbf{v}, \boldsymbol{\phi}_h)$ contains \mathbf{v} and $\boldsymbol{\phi}_h$ in $\Omega \setminus \Omega_C$, whereas the right-hand side of the inequality contains norms over Ω_C . Using Korn's Inequality, and upon setting $\boldsymbol{\phi}_h = \mathbf{v}$ in $\Omega \setminus \Omega_C$, we arrive at

$$\begin{aligned} K \|\mathbf{v}\|_{\mathbf{H}^1(\Omega \setminus \Omega_C)}^2 &\leq a_{\Omega \setminus \Omega_C, E}(\mathbf{v}, \mathbf{v}) \leq \beta L \|\mathbf{u}_h^\beta\|_{\mathbf{H}^1(\Omega_C)} \|\mathbf{v}\|_{\mathbf{H}^1(\Omega_C)} \\ \Rightarrow \|\mathbf{v}\|_{\mathbf{H}^1(\Omega \setminus \Omega_C)} &\leq C \sqrt{\beta} \|\mathbf{u}_h^\beta\|_{\mathbf{H}^1(\Omega_C)}^{1/2}, \text{ where } C = \sqrt{\frac{L}{K}} \|\boldsymbol{\phi}_h\|_{\mathbf{H}^1(\Omega_C)}^{1/2}. \end{aligned}$$

□

For the case of a spring-force boundary condition on $\partial\Omega$ one can derive a compatibility condition. To this extent, we consider the following boundary value problems, for the 'hole' problem:

$$(BVP_{H'}^n) \begin{cases} -\nabla \cdot \boldsymbol{\sigma} = 0, & \text{in } \Omega \setminus \bar{\Omega}_C, \\ \boldsymbol{\sigma} \cdot \mathbf{n} = P(\mathbf{x})\mathbf{n}(\mathbf{x}), & \text{on } \Gamma_C, \\ \boldsymbol{\sigma} \cdot \mathbf{n} + \kappa \mathbf{u} = \mathbf{0}, & \text{on } \partial\Omega, \end{cases}$$

and for the immersed boundary problem:

$$(BVP_I^n) \begin{cases} -\nabla \cdot \boldsymbol{\sigma} = \int_{\Gamma_C} P(\mathbf{x}')\mathbf{n}(\mathbf{x}')\delta(\mathbf{x} - \mathbf{x}')dS(\mathbf{x}'), & \text{in } \Omega, \\ \boldsymbol{\sigma} \cdot \mathbf{n} + \kappa \mathbf{u} = \mathbf{0}, & \text{on } \partial\Omega, \end{cases}$$

Next we give a proposition regarding compatibility for the 'hole' approach and the immersed boundary method for the case of a spring boundary condition:

Proposition 5.2. *Let \mathbf{u}_H and \mathbf{u}_I , respectively, be solutions to the 'hole' approach, see $(BVP_{H'}^n)$ and to the immersed boundary approach, see (BVP_I^n) . Let Γ_C denote the boundary of the cell, over which internal forces are exerted, and let $\partial\Omega$ be the outer boundary of Ω . Then*

$$\int_{\partial\Omega} \kappa \mathbf{u}_H dS = \int_{\partial\Omega} \kappa \mathbf{u}_I dS = \int_{\Gamma_C} P(\mathbf{x})\mathbf{n}(\mathbf{x})dS.$$

Proof. To prove that the above equation holds true, we integrate the PDE of both approaches over the computational domain Ω .

For the immersed boundary approach, we get

$$-\int_{\Omega} \nabla \cdot \boldsymbol{\sigma} d\Omega = \int_{\Omega} \sum_{j=1}^{N_S} P(\mathbf{x}_j)\mathbf{n}(\mathbf{x}_j)\delta(\mathbf{x} - \mathbf{x}_j)\Delta S(\mathbf{x}_j)d\Omega,$$

then after applying Gauss Theorem in the LHS and simplifying the RHS, we obtain

$$-\int_{\partial\Omega} \boldsymbol{\sigma} \cdot \mathbf{n}(\mathbf{x})dS = \sum_{j=1}^{N_S} P(\mathbf{x}_j)\mathbf{n}(\mathbf{x}_j)\Delta S(\mathbf{x}_j).$$

By substituting the Robin's boundary condition and letting $N_S \rightarrow \infty$, i.e. $\Delta S(\mathbf{x}_j) \rightarrow 0$, the equation becomes

$$\int_{\partial\Omega} \kappa \mathbf{u}_I dS = \int_{\Gamma_C} P(\mathbf{x})\mathbf{n}(\mathbf{x})dS. \quad (5.22)$$

Subsequently, we do the same thing for the 'hole' approach. Then, we get

$$-\int_{\Omega} \nabla \cdot \boldsymbol{\sigma} d\Omega = 0,$$

and we apply Gauss Theorem:

$$-\int_{\partial\Omega \cup \Gamma_C} \boldsymbol{\sigma} \cdot \mathbf{n}(\mathbf{x})dS = 0,$$

which implies

$$-\int_{\partial\Omega} \boldsymbol{\sigma} \cdot \mathbf{n}(\mathbf{x}) dS - \int_{\Gamma_C} \boldsymbol{\sigma} \cdot \mathbf{n}(\mathbf{x}) dS = 0.$$

Using the boundary conditions, we get

$$\int_{\partial\Omega} \kappa \mathbf{u}_H dS = \int_{\Gamma_C} P(\mathbf{x}) \mathbf{n}(\mathbf{x}) dS,$$

which is exactly the same as Eq (5.22). Hence we proved that

$$\int_{\partial\Omega} \kappa \mathbf{u}_H dS = \int_{\partial\Omega} \kappa \mathbf{u}_I dS = \int_{\Gamma_C} P(\mathbf{x}) \mathbf{n}(\mathbf{x}) dS.$$

□

Hence, the two different approaches are consistent in the sense of global conservation of momentum and therefore the results from both approaches should be comparable.

5

5.3.2. THE SMOOTHED PARTICLE APPROACH

The Gaussian distribution is used here as an approximation for the Dirac Delta distribution. Hereby, we show that in the n -dimensional case, the multivariate Gaussian distribution is a proper approximation for the Dirac Delta distribution. Firstly, we introduce Chebyshev's Inequality and the Empirical Rule for normal distributions. We realize that the Dirac Delta distribution represents a probability distribution. First we will motivate why the Dirac Delta distribution can be approximated by a Gaussian (normal) distribution with a small variance. The idea is to generalize this to multiple dimensions, which reflects the introduction of joint probability distributions of independent identically distributed (iid) stochastic variables.

Lemma 5.5. (Chebyshev's Inequality [86]) Denote X as a random variable with finite mean μ and finite variance σ^2 . Then for any positive $k \in \mathbb{R}$, the following inequality holds:

$$\mathbb{P}(|X - \mu| \geq k) \leq \frac{\sigma^2}{k^2},$$

where $\mathbb{P}(A)$ is the probability of event A . The above inequality can also be rephrased as

$$\mathbb{P}(|X - \mu| \leq k) \geq 1 - \frac{\sigma^2}{k^2}.$$

Lemma 5.6. (Empirical Rule [87]) Given the Gaussian distribution with mean μ and variance ε^2 :

$$\delta_\varepsilon(x - \mu) = 1/\sqrt{2\pi\varepsilon^2} \exp\{-(x - \mu)^2/(2\varepsilon^2)\},$$

then the following integrals are approximated by:

1. $\int_{\mu-\varepsilon}^{\mu+\varepsilon} \delta_\varepsilon(x - \mu) dx \approx 0.6827$;
2. $\int_{\mu-2\varepsilon}^{\mu+2\varepsilon} \delta_\varepsilon(x - \mu) dx \approx 0.9545$;

$$3. \int_{\mu-3\epsilon}^{\mu+3\epsilon} \delta_\epsilon(x-\mu) dx \approx 0.9973.$$

Lemma 5.7. For an open domain

$$\Omega = (x_{1,1}, x_{1,2}) \times (x_{2,1}, x_{2,2}) \times \cdots \times (x_{n,1}, x_{n,2}) \subset \mathbb{R}^n, n \geq 2,$$

let

$$\delta_\epsilon(\mathbf{x} - \mathbf{x}') = \frac{1}{(2\pi\epsilon^2)^{n/2}} \exp\left\{-\frac{\|\mathbf{x} - \mathbf{x}'\|^2}{2\epsilon^2}\right\},$$

where $\mathbf{x}' = (x'_1, \dots, x'_n) \in \Omega$, then

$$(i) \lim_{\epsilon \rightarrow 0^+} \delta_\epsilon(\mathbf{x} - \mathbf{x}') \rightarrow 0, \text{ for all } \mathbf{x} \neq \mathbf{x}';$$

$$(ii) \int_\Omega \delta_\epsilon(\mathbf{x} - \mathbf{x}') d\Omega \rightarrow 1, \text{ as } \epsilon \rightarrow 0^+.$$

(iii) Let $f(\mathbf{x}) \in \mathbb{C}^2(\mathbb{R}^d)$ and $\|f(\mathbf{x})\| \leq M < +\infty$, then there is a $C > 0$ such that

$$\left| \int_\Omega \delta_\epsilon(\mathbf{x} - \mathbf{x}') f(\mathbf{x}) d\Omega - f(\mathbf{x}') \right| \leq C\epsilon^2, \text{ as } \epsilon \rightarrow 0^+.$$

Proof. (i) Since $\mathbf{x} \neq \mathbf{x}'$, $\lim_{\epsilon \rightarrow 0^+} \exp\left\{-\frac{\|\mathbf{x} - \mathbf{x}'\|^2}{2\epsilon^2}\right\} \rightarrow 0$. Thus,

$$\lim_{\epsilon \rightarrow 0^+} \delta_\epsilon(\mathbf{x} - \mathbf{x}') \rightarrow 0, \text{ for all } \mathbf{x} \neq \mathbf{x}'.$$

(ii) We consider the integral over the computational domain $\Omega = (x_{1,1}, x_{1,2}) \times (x_{2,1}, x_{2,2}) \times \cdots \times (x_{n,1}, x_{n,2})$, then we compute

$$\begin{aligned} \int_\Omega \delta_\epsilon(\mathbf{x} - \mathbf{x}') d\Omega &= \int_{x_{1,1}}^{x_{1,2}} \cdots \int_{x_{n,1}}^{x_{n,1}} \delta_\epsilon(\mathbf{x} - \mathbf{x}') dx_n \cdots dx_1 \\ &= \int_{x_{1,1}}^{x_{1,2}} \delta_\epsilon(x_1 - x'_1) dx_1 \times \cdots \times \int_{x_{n,1}}^{x_{n,2}} \delta_\epsilon(x_n - x'_n) dx_n \end{aligned}$$

Let $s_i = x_i - \frac{x_{i,1} + x_{i,2}}{2}$, then we obtain

$$\begin{aligned} \int_\Omega \delta_\epsilon(\mathbf{x} - \mathbf{x}') d\Omega &= \int_{x_{1,1}}^{x_{1,2}} \cdots \int_{x_{n,1}}^{x_{n,1}} \delta_\epsilon(\mathbf{x} - \mathbf{x}') dx_n \cdots dx_1 \\ &= \int_{-\frac{x_{1,2}-x_{1,1}}{2}}^{\frac{x_{1,2}-x_{1,1}}{2}} \delta_\epsilon\left(s_1 - \left(x'_1 + \frac{x_{1,2} + x_{2,2}}{2}\right)\right) ds_1 \times \cdots \times \int_{-\frac{x_{n,2}-x_{n,1}}{2}}^{\frac{x_{n,2}-x_{n,1}}{2}} \delta_\epsilon\left(s_n - \left(x'_n + \frac{x_{n,1} + x_{n,2}}{2}\right)\right) ds_n \\ &= \prod_{i=1}^n \mathbb{P}\left(\left|s - \left(x'_i + \frac{x_{i,2} + x_{i,2}}{2}\right)\right| \leq \frac{x_{i,2} - x_{i,1}}{2}\right) \end{aligned}$$

According to Chebyshev's Inequality (see Lemma 5.5), there exists a series positive constants $\{k_i\}$, $i = \{1, \dots, n\}$, such that for any i ,

$$\mathbb{P}\left(\left|s - \left(x'_i + \frac{x_{i,1} + x_{i,2}}{2}\right)\right| \leq \frac{x_{i,2} - x_{i,1}}{2}\right) \geq 1 - \frac{4\epsilon^2}{(x_{i,2} - x_{i,1})^2} \geq 0.$$

Hence, it follows that

$$\int_{\Omega} \delta_{\varepsilon}(\mathbf{x} - \mathbf{x}') d\Omega \geq \prod_{i=1}^n \left(1 - \frac{4\varepsilon^2}{(x_{i,2} - x_{i,1})^2} \right). \quad (5.23)$$

Since $\Omega \subset \mathbb{R}^n$, one can derive that

$$1 = \int_{\mathbb{R}^n} \delta_{\varepsilon}(\mathbf{x} - \mathbf{x}') d\Omega \geq \int_{\Omega} \delta_{\varepsilon}(\mathbf{x} - \mathbf{x}') d\Omega \geq \prod_{i=1}^n \left(1 - \frac{4\varepsilon^2}{(x_{i,2} - x_{i,1})^2} \right) \geq \left(1 - \frac{4\varepsilon^2}{[\min_{i \in \{1, \dots, n\}} (x_{i,2} - x_{i,1})]^2} \right)^n.$$

By using the Squeeze Theorem [83], we conclude

$$\lim_{\varepsilon \rightarrow 0^+} \int_{\Omega} \delta_{\varepsilon}(\mathbf{x} - \mathbf{x}') d\Omega = 1.$$

(iii) Now we consider

$$\int_{\Omega} \delta_{\varepsilon}(\mathbf{x} - \mathbf{x}') f(\mathbf{x}) d\Omega = \int_{\Omega} \frac{1}{(2\pi\varepsilon^2)^{n/2}} \exp\left\{-\frac{\|\mathbf{x} - \mathbf{x}'\|^2}{2\varepsilon^2}\right\} f(\mathbf{x}) d\Omega.$$

Firstly, we integrate over the infinite domain:

$$\begin{aligned} & \int_{\mathbb{R}^n} \delta_{\varepsilon}(\mathbf{x} - \mathbf{x}') f(\mathbf{x}) d\Omega \\ &= \frac{1}{(2\pi\varepsilon^2)^{n/2}} \int_{-\infty}^{+\infty} \cdots \int_{-\infty}^{+\infty} \exp\left\{-\frac{\|\mathbf{x} - \mathbf{x}'\|^2}{2\varepsilon^2}\right\} f(\mathbf{x}) dx_n \cdots dx_1 \\ &= \frac{1}{(2\pi\varepsilon^2)^{n/2}} \int_{-\infty}^{+\infty} \exp\left\{-\frac{(x_1 - x'_1)^2}{2\varepsilon^2}\right\} \cdots \int_{-\infty}^{+\infty} \exp\left\{-\frac{(x_n - x'_n)^2}{2\varepsilon^2}\right\} f(\mathbf{x}) dx_n \cdots dx_1. \end{aligned}$$

Again let $s_i = \frac{x_i - x'_i}{\sqrt{2\varepsilon}} - \frac{x_{i,1} + x_{i,2}}{2}$, and furthermore $\xi_i = s_i + \frac{x_{i,1} + x_{i,2}}{2}$, $i = \{1, 2, \dots, n\}$. We denote $\mathbf{x}_1 = (x_{1,1}, x_{2,1}, \dots, x_{n,1})$, $\mathbf{x}_2 = (x_{1,2}, x_{2,2}, \dots, x_{n,2})$ and $\mathbf{x}' = (x'_1, x'_2, \dots, x'_n)$. By Taylor Expansion, $f(\mathbf{x})$ can be rewritten as

$$\begin{aligned} f(\mathbf{x}) &= f\left(\sqrt{2\varepsilon}\mathbf{s} + \sqrt{2\varepsilon}\frac{\mathbf{x}_1 + \mathbf{x}_2}{2} + \mathbf{x}'\right) \\ &= f(\mathbf{x}') + \nabla f\left(\mathbf{x}'\right)\left(\sqrt{2\varepsilon}\mathbf{s} + \sqrt{2\varepsilon}\frac{\mathbf{x}_1 + \mathbf{x}_2}{2}\right) \\ &\quad + \frac{1}{2!}\left(\sqrt{2\varepsilon}\mathbf{s} + \sqrt{2\varepsilon}\frac{\mathbf{x}_1 + \mathbf{x}_2}{2}\right)^T \mathbf{H}(\mathbf{x}')\left(\sqrt{2\varepsilon}\mathbf{s} + \sqrt{2\varepsilon}\frac{\mathbf{x}_1 + \mathbf{x}_2}{2}\right) + \mathcal{O}(\varepsilon^3) \\ &= f(\mathbf{x}') + \nabla f\left(\mathbf{x}'\right)\sqrt{2\varepsilon}\left(\mathbf{s} + \frac{\mathbf{x}_1 + \mathbf{x}_2}{2}\right) \\ &\quad + \varepsilon^2\left(\mathbf{s} + \frac{\mathbf{x}_1 + \mathbf{x}_2}{2}\right)^T \mathbf{H}(\mathbf{x}')\left(\mathbf{s} + \frac{\mathbf{x}_1 + \mathbf{x}_2}{2}\right) + \mathcal{O}(\varepsilon^3) \\ &= f(\mathbf{x}') + \nabla f(\mathbf{x}')\sqrt{2\varepsilon}\boldsymbol{\xi} + \varepsilon^2\boldsymbol{\xi}^T \mathbf{H}(\mathbf{x}')\boldsymbol{\xi} + \mathcal{O}(\varepsilon^3) \end{aligned}$$

where $\mathbf{H}(\mathbf{x}')$ is Hessian matrix of $f(\mathbf{x})$. For any non-negative integer d ,

$$\int_{-\infty}^{+\infty} z^d e^{-z^2} dz = \begin{cases} 0, & \text{if } d \text{ is odd,} \\ \Gamma\left(\frac{d+1}{2}\right), & \text{if } d \text{ is even.} \end{cases}$$

First we calculate

$$\begin{aligned}
& \int_{\mathbb{R}^n} \delta_\varepsilon(\mathbf{x} - \mathbf{x}') f(\mathbf{x}) d\Omega \\
&= \frac{1}{(2\pi\varepsilon^2)^{n/2}} \int_{-\infty}^{+\infty} \exp\left\{-\frac{(x_1 - x'_1)^2}{2\varepsilon^2}\right\} \cdots \int_{-\infty}^{+\infty} \exp\left\{-\frac{(x_n - x'_n)^2}{2\varepsilon^2}\right\} f(\mathbf{x}) dx_n \cdots dx_1 \\
&= \frac{1}{\pi^{n/2}} \int_{-\infty}^{+\infty} \exp\left\{\left(-s_1 + \frac{x_{1,1} + x_{1,2}}{2}\right)^2\right\} \cdots \int_{-\infty}^{+\infty} \exp\left\{\left(-s_n + \frac{x_{n,1} + x_{n,2}}{2}\right)^2\right\} \\
& f(\sqrt{2\varepsilon}\mathbf{s} + \sqrt{2\varepsilon}\frac{\mathbf{x}_1 + \mathbf{x}_2}{2} + \mathbf{x}') ds_n \cdots ds_1 \\
&= \frac{1}{\pi^{n/2}} \int_{-\infty}^{+\infty} e^{-\xi_1^2} \cdots \int_{-\infty}^{+\infty} e^{-\xi_n^2} f(\sqrt{2\varepsilon}\boldsymbol{\xi} + \mathbf{x}') d\xi_n \cdots d\xi_1 \\
&= \frac{1}{\pi^{n/2}} \int_{-\infty}^{+\infty} e^{-\xi_1^2} \cdots \int_{-\infty}^{+\infty} e^{-\xi_n^2} [f(\mathbf{x}') + \nabla f(\mathbf{x}')\sqrt{2\varepsilon}\boldsymbol{\xi} + \varepsilon^2 \boldsymbol{\xi}^T \mathbf{H}(\mathbf{x}')\boldsymbol{\xi} + \mathcal{O}(\varepsilon^3)] d\xi_n \cdots d\xi_1 \\
&= \frac{f(\mathbf{x}')}{\pi^{n/2}} \int_{-\infty}^{+\infty} e^{-\xi_1^2} \cdots \int_{-\infty}^{+\infty} e^{-\xi_n^2} d\xi_n \cdots d\xi_1 \\
&+ \frac{\sqrt{2\varepsilon}}{\pi^{n/2}} \int_{-\infty}^{+\infty} e^{-\xi_1^2} \xi_1 f'_{x_1}(\mathbf{x}') \cdots \int_{-\infty}^{+\infty} e^{-\xi_n^2} \xi_n f'_{x_n}(\mathbf{x}') d\xi_n \cdots d\xi_1 \\
&+ \frac{\varepsilon^2}{\pi^{n/2}} \int_{-\infty}^{+\infty} e^{-\xi_1^2} \int_{-\infty}^{+\infty} e^{-\xi_1^2} \cdots \int_{-\infty}^{+\infty} e^{-\xi_n^2} \left(\sum_{i=1}^n f''_{x_i, x_i}(\mathbf{x}') \xi_i^2 + \sum_{i=1}^n \sum_{j=1, j \neq i}^n f''_{x_i, x_j}(\mathbf{x}') \xi_i \xi_j \right) d\xi_n \cdots d\xi_1 \\
&+ \mathcal{O}(\varepsilon^3) \\
&= f(\mathbf{x}') + \frac{\varepsilon^2}{\pi^{1/2}} \Gamma\left(\frac{3}{2}\right) \sum_{i=1}^d f''_{x_i, x_i}(\mathbf{x}') + \mathcal{O}(\varepsilon^3) \rightarrow f(\mathbf{x}'), \text{ as } \varepsilon \rightarrow 0^+.
\end{aligned}$$

For the integral over the given domain $\Omega = (x_{1,1}, x_{1,2}) \times \cdots \times (x_{n,1}, x_{n,2})$, it can be written as

$$\begin{aligned}
& \int_{x_{1,1}}^{x_{1,2}} \cdots \int_{x_{n,1}}^{x_{n,2}} dx_n \cdots dx_1 = \int_{-\infty}^{+\infty} \cdots \int_{-\infty}^{+\infty} dx_n \cdots dx_1 \\
& - \sum_{i=1}^n \int_{x_{1,1}}^{x_{1,2}} \cdots \int_{-\infty}^{x_{i,1}} \cdots \int_{x_{n,1}}^{x_{n,2}} dx_n \cdots dx_1 - \sum_{i=1}^n \int_{x_{1,1}}^{x_{1,2}} \cdots \int_{x_{i,2}}^{+\infty} \cdots \int_{x_{n,1}}^{x_{n,2}} dx_n \cdots dx_1 \\
&= (\sqrt{2\varepsilon})^n \left[\int_{-\infty}^{+\infty} \cdots \int_{-\infty}^{+\infty} ds_n \cdots ds_1 \right. \\
& \left. - \sum_{i=1}^n \int_{s_{1,1}}^{s_{1,2}} \cdots \int_{-\infty}^{s_{i,1}} \cdots \int_{s_{n,1}}^{s_{n,2}} ds_n \cdots ds_1 - \sum_{i=1}^n \int_{\xi_{1,1}}^{\xi_{1,2}} \cdots \int_{\xi_{i,2}}^{+\infty} \cdots \int_{\xi_{n,1}}^{\xi_{n,2}} d\xi_n \cdots d\xi_1 \right] \\
&= (\sqrt{2\varepsilon})^n \left[\int_{-\infty}^{+\infty} \cdots \int_{-\infty}^{+\infty} d\xi_n \cdots d\xi_1 \right. \\
& \left. - \sum_{i=1}^n \int_{\xi_{1,1}}^{\xi_{1,2}} \cdots \int_{-\infty}^{\xi_{i,1}} \cdots \int_{\xi_{n,1}}^{\xi_{n,2}} d\xi_n \cdots d\xi_1 - \sum_{i=1}^n \int_{\xi_{1,1}}^{\xi_{1,2}} \cdots \int_{\xi_{i,2}}^{+\infty} \cdots \int_{\xi_{n,1}}^{\xi_{n,2}} d\xi_n \cdots d\xi_1 \right],
\end{aligned}$$

where $\xi_{i,1} = \frac{x_{i,1}-x'_i}{\sqrt{2\varepsilon}}$ and $\xi_{i,2} = \frac{x_{i,2}-x'_i}{\sqrt{2\varepsilon}}$. Therefore,

$$\begin{aligned}
& \left| \int_{\Omega} \delta_{\varepsilon}(\mathbf{x} - \mathbf{x}') f(\mathbf{x}) d\Omega - f(\mathbf{x}') \right| \\
&= \left| f(\mathbf{x}') + \frac{\varepsilon^2}{\pi^{n/2}} \Gamma\left(\frac{3}{2}\right) \sum_{i=1}^d f''_{x_i, x_i}(\mathbf{x}') + \mathcal{O}(\varepsilon^3) - \frac{1}{\pi^{n/2}} \left[\sum_{i=1}^n \int_{\xi_{1,1}}^{\xi_{1,2}} e^{-\xi_1} \dots \int_{-\infty}^{\xi_{i,1}} e^{-\xi_i} \right. \right. \\
&\quad \dots \int_{\xi_{n,1}}^{\xi_{n,2}} e^{-\xi_n} f(\sqrt{2\varepsilon}\boldsymbol{\xi} + \mathbf{x}') d\xi_n \dots d\xi_1 + \sum_{i=1}^n \int_{\xi_{1,1}}^{\xi_{1,2}} e^{-\xi_1} \dots \int_{\xi_{i,2}}^{+\infty} e^{-\xi_i} \\
&\quad \left. \dots \int_{\xi_{n,1}}^{\xi_{n,2}} e^{-\xi_n} f(\sqrt{2\varepsilon}\boldsymbol{\xi} + \mathbf{x}') d\xi_n \dots d\xi_1 \right] - f(\mathbf{x}') \Big| \\
&\leq \left| \frac{\varepsilon^2}{\pi^{1/2}} \Gamma\left(\frac{3}{2}\right) \sum_{i=1}^d f''_{x_i, x_i}(\mathbf{x}') + \mathcal{O}(\varepsilon^3) \right| \\
&\quad + \frac{M}{2^{n-1}} \sum_{j=1}^n \prod_{i=1, i \neq j}^n [\operatorname{erf}(\xi_{j,2}) - \operatorname{erf}(\xi_{j,1}) + 2] \times [\operatorname{erf}(\xi_{i,2}) - \operatorname{erf}(\xi_{i,1})] \\
&\leq \left| \frac{\varepsilon^2}{\pi^{1/2}} \Gamma\left(\frac{3}{2}\right) \sum_{i=1}^d f''_{x_i, x_i}(\mathbf{x}') + \mathcal{O}(\varepsilon^3) \right| + \frac{M}{2} \sum_{j=1}^n [\operatorname{erf}(\xi_{j,1}) - \operatorname{erf}(\xi_{j,2}) + 2] \\
&\rightarrow 0, \text{ as } \varepsilon \rightarrow 0^+,
\end{aligned}$$

since $\|f(\mathbf{x})\| < M < +\infty$, $\xi_{i,1} \rightarrow -\infty$ and $\xi_{i,2} \rightarrow \infty$ respectively. Using $1 - \operatorname{erf}(y) < \frac{2}{\sqrt{\pi}} \exp\{-y\}$ for $y > 0$ and the fact that $\exp\{y\} < \frac{1}{y^\alpha}$ as $y \rightarrow \infty$, we see that the second term approximates zero faster than the first term. Hence, we conclude that there is a $C > 0$ such that

$$\left| \int_{\Omega} \delta_{\varepsilon}(\mathbf{x} - \mathbf{x}') f(\mathbf{x}) d\Omega - f(\mathbf{x}') \right| \leq C\varepsilon^2 \text{ as } \varepsilon \rightarrow 0^+.$$

□

As a remark we add that setting $f(\mathbf{x}) = 1$, immediately shows that there is a $C > 0$ such that

$$\left| \int_{\Omega} \delta_{\varepsilon}(\mathbf{x} - \mathbf{x}') d\Omega - 1 \right| \leq C\varepsilon^2, \text{ as } \varepsilon \rightarrow 0^+.$$

Using the result above, we start with analysing different approaches with only one relatively big cell in the computational domain. According to the model described in Eq (5.4), the forces released on the boundary of the cell are the superposition of point forces on the midpoint of each surface element. For example, if we use a square shape to approximate the biological cell, then the forces are depicted in Figure 5.1. Therefore, in n dimensional case ($n > 1$), if the biological cell is a n -dimensional hypercube, then the

forces can be rewritten as

$$\begin{aligned} \mathbf{f}_t &= \sum_{j=1}^{N_S} P(\mathbf{x}_j) \mathbf{n}(\mathbf{x}_j) \delta(\mathbf{x} - \mathbf{x}_j) \Delta S(\mathbf{x}_j) \\ &= P \sum_{i=1}^n \left\{ \mathbf{e}_i (\Delta x)^{n-1} \left[\delta \left(x_1 - x'_1, \dots, x_i - \left(x'_i + \frac{\Delta x}{2} \right), \dots, x_n - x'_n \right) \right. \right. \\ &\quad \left. \left. - \delta \left(x_1 - x'_1, \dots, x_i - \left(x'_i - \frac{\Delta x}{2} \right), \dots, x_n - x'_n \right) \right] \right\}. \end{aligned} \quad (5.24)$$

where \mathbf{e}_i is the standard basis vector with 1 in the i -th coordinate and 0's elsewhere, and Δx is the length of cell boundary in each coordinate. For the smoothed force approach, we set $\delta(\mathbf{x}) \approx \delta_\varepsilon(\mathbf{x})$. The force is given by

$$\begin{aligned} \mathbf{f}_\varepsilon &= P \sum_{i=1}^n \left\{ \mathbf{e}_i (\Delta x)^{n-1} \left[\delta_\varepsilon \left(x_1 - x'_1, \dots, x_i - \left(x'_i + \frac{\Delta x}{2} \right), \dots, x_n - x'_n \right) \right. \right. \\ &\quad \left. \left. - \delta_\varepsilon \left(x_1 - x'_1, \dots, x_i - \left(x'_i - \frac{\Delta x}{2} \right), \dots, x_n - x'_n \right) \right] \right\}. \end{aligned} \quad (5.25)$$

Following the same process in two dimensions [54] and thanks to the continuity of the Gaussian distribution, as $\Delta x \rightarrow 0$, the force converges to

$$\mathbf{f}_S = P(\Delta x)^n \nabla \delta_\varepsilon(\mathbf{x} - \mathbf{x}'). \quad (5.26)$$

Theorem 5.6. Let $\mathbf{u}_h \in \mathbf{V}_h(\Omega)$ be the Galerkin solution to the problem

$$(BVP^n) \begin{cases} \text{Find } \mathbf{u}_h \in \mathbf{V}_h(\Omega) \text{ such that} \\ a(\mathbf{u}_h, \boldsymbol{\phi}_h) = \int_{\Omega} \mathbf{f}_t \boldsymbol{\phi}_h d\Omega, \text{ for all } \boldsymbol{\phi}_h \in \mathbf{V}_h(\Omega), \end{cases} \quad (5.27)$$

and \mathbf{u}_h^ε be the Galerkin solution to

$$(BVP_\varepsilon^n) \begin{cases} \text{Find } \mathbf{u}_h^\varepsilon \in \mathbf{V}_h(\Omega) \text{ such that} \\ a(\mathbf{u}_h^\varepsilon, \boldsymbol{\phi}_h) = \int_{\Omega} \mathbf{f}_\varepsilon \boldsymbol{\phi}_h d\Omega, \text{ for all } \boldsymbol{\phi}_h \in \mathbf{V}_h(\Omega). \end{cases} \quad (5.28)$$

Then there is an $L_1 > 0$ such that $\|\mathbf{u}_h^\varepsilon - \mathbf{u}_h\|_{\mathbf{H}^1(\Omega)} \leq L_1 (\Delta x)^{(n-1)/2} \varepsilon$.

Proof. Using bilinearity of $a(\cdot, \cdot)$ gives upon setting $\mathbf{w} = \mathbf{u}_h - \mathbf{u}_h^\varepsilon$ the following equation:

$$a(\mathbf{w}, \boldsymbol{\phi}_h) = \int_{\Omega} (\mathbf{f}_t - \mathbf{f}_\varepsilon) \cdot \boldsymbol{\phi}_h d\Omega.$$

Using the result from Lemma 5.7 and the Triangle Inequality, bearing in mind that $\|\mathbf{e}_i\| = 1$ and that the basis field functions $\boldsymbol{\phi}_h$ are bounded, and after some algebraic manipulations, we can write the right-hand side as

$$\left| \int_{\Omega} (\mathbf{f}_t - \mathbf{f}_\varepsilon) \cdot \boldsymbol{\phi}_h d\Omega \right| \leq C(\Delta x)^{n-1} \varepsilon^2. \quad (5.29)$$

Coerciveness, see Lemma 5.4, and using $\boldsymbol{\phi}_h = \mathbf{w}$, gives

$$K \|\mathbf{w}\|_{H_1(\Omega)}^2 \leq a(\mathbf{w}, \mathbf{w}) \leq C(\Delta x)^{n-1} \varepsilon^2,$$

hence there is an $L_1 > 0$ such that

$$\|\mathbf{w}\|_{H_1(\Omega)} \leq L (\Delta x)^{(n-1)/2} \varepsilon,$$

which immediately implies that

$$\|\mathbf{u}_h - \mathbf{u}_h^\varepsilon\|_{H_1(\Omega)} \leq L_1 (\Delta x)^{(n-1)/2} \varepsilon.$$

□

Theorem 5.7. Let \mathbf{u}_h^ε be the solution to the boundary value problems in Eq (5.28), and \mathbf{u}_h^S the solution to

$$(BVP_{SP}^n) \left\{ \begin{array}{l} \text{Find } \mathbf{u}_h^\varepsilon \in \mathbf{V}_h(\Omega) \text{ such that} \\ a(\mathbf{u}_h^\varepsilon, \boldsymbol{\phi}_h) = \int_{\Omega} \mathbf{f}_S \boldsymbol{\phi}_h d\Omega, \text{ for all } \boldsymbol{\phi}_h \in \mathbf{V}_h(\Omega). \end{array} \right. \quad (5.30)$$

Then there is an $L_2 > 0$ such that

$$\frac{1}{(\Delta x)^n} \|\mathbf{u}_h^S - \mathbf{u}_h^\varepsilon\|_{\mathbf{H}^1(\Omega)} \leq L_2 \frac{(\Delta x)^2}{\varepsilon^3}.$$

Proof. Using bilinearity of $a(\cdot, \cdot)$ gives upon setting $\mathbf{w} = \mathbf{u}_h^\varepsilon - \mathbf{u}_h^S$ the following equation:

$$a(\mathbf{w}, \boldsymbol{\phi}_h) = \int_{\Omega} (\mathbf{f}_\varepsilon - \mathbf{f}_S) \cdot \boldsymbol{\phi}_h d\Omega.$$

Using Taylor's Theorem for multivariate functions on smoothed delta distributions, we get the following result for the right-hand side:

$$\int_{\Omega} (\mathbf{f}_\varepsilon - \mathbf{f}_S) \cdot \boldsymbol{\phi}_h d\Omega = \int_{\Omega} \frac{P(\mathbf{x}')}{48} (\Delta x)^{n+2} \sum_{i=1}^n \mathbf{e}_i \frac{\partial^3 \delta_\varepsilon(\hat{\mathbf{x}} - \mathbf{x}')}{\partial x_i^3} \cdot \boldsymbol{\phi}_h d\Omega, \quad (5.31)$$

for $\hat{\mathbf{x}}$ between \mathbf{x} and \mathbf{x}' . The magnitude of the above expression can be estimated from above by

$$\left| \int_{\Omega} (\mathbf{f}_\varepsilon - \mathbf{f}_S) \cdot \boldsymbol{\phi}_h d\Omega \right| \leq \frac{P(\mathbf{x}')}{48} (\Delta x)^{n+2} \left\| \sum_{i=1}^n \mathbf{e}_i \frac{\partial^3 \delta_\varepsilon(\hat{\mathbf{x}} - \mathbf{x}')}{\partial x_i^3} \right\|_{L^\infty(\Omega)} \|\boldsymbol{\phi}_h\|_{\mathbf{H}^1(\Omega)}. \quad (5.32)$$

Using Lemma 5.4, this gives

$$K \|\mathbf{w}\|_{\mathbf{H}^1(\Omega)}^2 \leq a(\mathbf{w}, \mathbf{w}) \leq \frac{P(\mathbf{x}')}{48} (\Delta x)^{n+2} \left\| \sum_{i=1}^n \mathbf{e}_i \frac{\partial^3 \delta_\varepsilon(\hat{\mathbf{x}} - \mathbf{x}')}{\partial x_i^3} \right\|_{L^\infty(\Omega)} \|\boldsymbol{\phi}_h\|_{\mathbf{H}^1(\Omega)}.$$

Division by $K\|\mathbf{w}\|_{\mathbf{H}^1(\Omega)}^2$ gives

$$\|\mathbf{w}\|_{\mathbf{H}^1(\Omega)} \leq \frac{P(\mathbf{x}')}{48} (\Delta x)^{n+2} \left\| \sum_{i=1}^n \mathbf{e}_i \frac{\partial^3 \delta_\varepsilon(\hat{\mathbf{x}} - \mathbf{x}')}{\partial x_i^3} \right\|_{L^\infty(\Omega)}.$$

We bear in mind that $\frac{\partial^3 \delta_\varepsilon}{\partial x_i^3} = \mathcal{O}(\varepsilon^{-3})$, this implies that there is an $L_2 > 0$ such that

$$\frac{1}{(\Delta x)^n} \|\mathbf{u}_h^S - \mathbf{u}_h^\varepsilon\|_{\mathbf{H}^1(\Omega)} \leq L_2 \frac{(\Delta x)^2}{\varepsilon^3}.$$

□

With the two theorems above, we have proved that the solution to (BVP_ε^n) converges to the solution to (BVP^n) , and the solution to (BVP_{Sp}^n) converges to the solution to (BVP_ε^n) . Hence, we can derive the following theorem:

Theorem 5.8. *Let \mathbf{u}_h be the Galerkin solution to (BVP^n) and \mathbf{u}_h^S be the solution to (BVP_{Sp}^n) , let $\varepsilon = \mathcal{O}(\Delta x)^p$ and $\Delta x \rightarrow 0$. If $0 < p < (2+n)/3$ then \mathbf{u}_h^S converges to \mathbf{u}_h in the H^1 -norm, and \mathbf{u}_h^S converges to \mathbf{u} in the H^1 -norm.*

Proof. Denote \mathbf{u}_h and \mathbf{u}_h^S to be the Galerkin solution to (BVP_ε^n) and (BVP_{Sp}^n) . Firstly, we consider

$$\begin{aligned} \|\mathbf{u}_h - \mathbf{u}_h^S\| &= \|\mathbf{u}_h - \mathbf{u}_h^\varepsilon + \mathbf{u}_h^\varepsilon - \mathbf{u}_h^S\| \\ &\leq \|\mathbf{u}_h - \mathbf{u}_h^\varepsilon\| + \|\mathbf{u}_h^\varepsilon - \mathbf{u}_h^S\| \\ &\leq L_1 (\Delta x)^{(n-1)/2} \varepsilon + L_2 \frac{(\Delta x)^{2+n}}{\varepsilon^3} \\ &= L_1 (\Delta x)^{(n-1)/2+p} + L_2 (\Delta x)^{2+n-3p} \rightarrow 0, \\ &\text{as } \Delta x \rightarrow 0, \text{ if } 0 < p < (2+n)/3. \end{aligned}$$

From this inequality, we conclude that the finite element solution of the smooth particle method converges to the solution of the immersed boundary method upon letting $\Delta x \rightarrow 0$ and choosing $\varepsilon = \mathcal{O}(\Delta x)^p$ for $0 < p < (2+p)/3$. □

5.4. NUMERICAL RESULTS

In this section, results in two dimensions using all aforementioned alternatives are presented. From the results listed below, the consistency of all approaches is proved computationally. Some of the results displayed below are part of other manuscripts which are under review now.

We consider only one big cell in the computational domain, and the boundary of the cell is split into finite line segments. Based on the special case of square (see Eq (5.17) and Figure 5.1) and since the magnitude relation between the direct approach and the smoothed particle approaches is still unclear, we will use the area of the cell as the magnitude ratio. Subsequently, we will investigate the new cell area after deformation, as well as a region near the cell. Further, the computational time will be compared, since

in our wound healing model, there are a large number of cells in the computational domain.

In Figure 5.2, the bandwidth around the cell in the smoothed particle approach is wider than the direct approach, which is mainly because of the continuity of the smoothed particle approach, whereas it is hard to see the difference from the plots between the immersed boundary approach and the mixed approach, except for the displacement in the mixed approach is smaller than the direct approach.

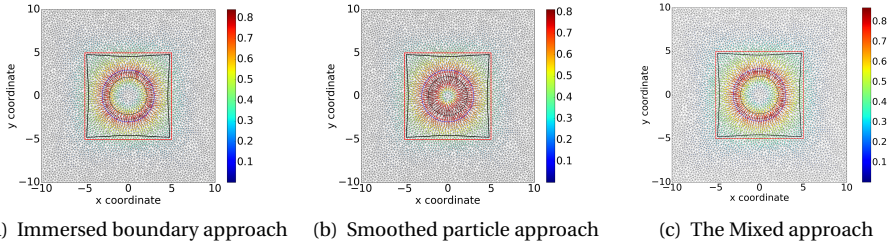


Figure 5.2: For the constant stiffness of the computational domain, it is hard to see the difference between three subplots. Black curves show the deformed region of vicinity and the cell, and blue curve represents the cell

Table 5.1 shows the L^2 -norm of the solution \mathbf{u} and the convergence rate. Compared to the immersed boundary approach, with the linear Lagrangian test functions, the other two approaches illustrate a better convergence rate with a quadratic order. In particular, the mixed approach, in which the order of the PDEs is reduced, appears to be the most favourable approach in the perspective of error estimation. Furthermore, the similar convergence rate in the immersed boundary approach and the smoothed particle approach implies that the Gaussian distribution is a suitable replacement for the Dirac Delta distribution as long as the variance of the Gaussian distribution is small enough.

Table 5.1: The L^2 -norm of the solution (i.e. the displacement) with different mesh size in each approach, if the stiffness is constant over the computational domain

	Immersed Boundary Approach	Smoothed Particle Approach	The Mixed Approach
h	6.5928365	6.9064864	6.5992660
h/2	6.5940614	6.9132492	6.5957506
h/4	6.5944070	6.9147421	6.5948781
Convergence rate	1.82566	1.94870	2.01038

Table 5.2 displays the numerical results of the reduction in the volume of the vicinity region and the cell, as well as the computational cost. Using the cell volume as the ratio between the force magnitude in the immersed boundary and smoothed particle ap-

proach, the area results hardly show any difference and the computational time is nearly the same. However, for the mixed approach, since two unknowns are solved in mixed function spaces, the computation takes longer comparing to the other two approaches, which is a significant drawback considering the large amount of cells in our wound healing model and multiple time iterations. Therefore, the smoothed particle approach is a promising alternative to the immersed boundary approach.

Table 5.2: The percentage of area reduction of the cell and the vicinity region, and time cost of the direct approach, the smoothed particle approach and the mixed approach, if the stiffness is constant over the computational domain

	Immersed Boundary Approach	Smoothed Particle Approach	The Mixed Approach
Cell Area Reduction Ratio(%)	47.81624	43.38118	48.30546
Vicinity Area Reduction Ratio(%)	12.85195	12.88194	12.85095
Time Cost(s)	1.70716	1.83455	6.96180

5

On the other hand, we set the stiffness inside the cell close to zero, and the results are displayed in Table 5.3, Table 5.4 and Figure 5.3. For the accuracy of all these approaches, the 'hole' approach has a significant improvement in the convergence rate of the solution, since it does not contain the Dirac Delta distributions in the boundary value problem.

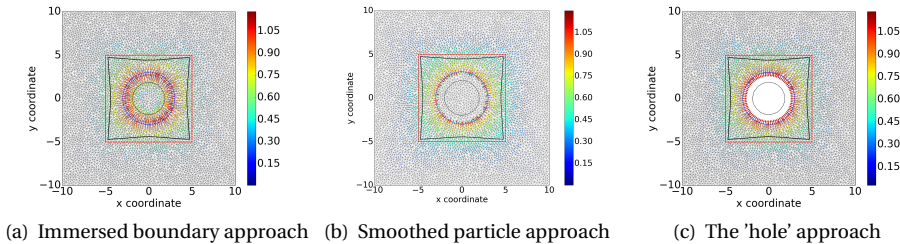


Figure 5.3: For the different stiffness inside and outside of the cell, the magnitude of the displacement shows significant difference, however, it is hard to see the differences on deformation between three approaches. Black curves show the deformed region of vicinity and the cell, and blue curve represents the cell.

From Table 5.4, it is notable that cell area reduction ratio and the vicinity area reduction are all more or less the same. However, for the cell region in smoothed particle approach, we noticed that the displacement of nodal points are much larger than the outside region, which is resulted from the low stiffness inside of the cell. Since we are not interested in that part in general, the displacement inside the cell is not plotted in Figure 5.3. Both smoothed particle approach and the 'hole' approach have the advantage

Table 5.3: The L^2 -norm of the solution (i.e. the displacement) with different mesh size in each approach, if the stiffness is different inside and outside the cell

	Immersed Boundary Approach	Smoothed Particle Approach	The 'Hole' Approach
h	7.9745554	7.1597432	8.0323264
h/2	8.0374314	7.2149243	8.0677711
h/4	8.0601776	7.2350698	8.0759127
Convergence rate	1.46688	1.45371	2.12220

of conducting non-singular solution, however, the 'hole' approach takes more than eight times as much computation time as the other two approaches, and new mesh structure needs to be regenerated after each iteration, which is too expensive for a model with a large number of moving cells and multiple time iterations. Therefore, taking the advantage of a smooth force into consideration, the smoothed particle approach has the potential to be incorporated into the model containing multiple cells.

Table 5.4: The percentage of area change of cell and vicinity region, and time cost of the direct approach, the smoothed particle approach and the 'hole' approach, when the stiffness inside and outside the cell differs

	Immersed Boundary Approach	Smoothed Particle Approach	The 'Hole' Approach
Cell Area Reduction Ratio(%)	61.92051	61.43349	61.92605
Vicinity Area Reduction Ratio(%)	17.50153	17.48103	17.52235
Time Cost(s)	1.99139	1.92355	8.71979

5.5. CONCLUSION

For dimensionalities larger than one, the Dirac Delta distribution results into a singular solution. We developed various alternative methods. The smoothed approach, in which the Dirac Delta distributions at the midpoint of the boundary segments of the cell are replaced by the Gaussian distributions directly, is discussed. The second alternative method is the smoothed particle approach, which considers the gradient of the Gaussian distribution at the centre of the cell. The variance of the Gaussian is related to the size of the cell. We claimed that the Gaussian distribution is a proper replacement for the Dirac Delta distribution and proved the convergence between these two approaches and the immersed boundary approach. The mixed finite-element approach reduces the order of the PDEs from the original boundary value problem but creates mixed function spaces

and solves two unknowns. In the 'hole' approach, we removed the region covered by the cell, and used a boundary condition to describe the force exerted on the boundary of the cell. We have shown that the smoothed particle approach and the 'hole' approach are consistent with the immersed boundary approach.

In two dimensions, we are still working on the exact ratio between the direct approach and the smoothed particle approach. However, inspired by the special case of square-shaped cell, we use the cell area as the ratio to investigate the discrepancy, which turns out to be negligible. All the numerical results of different approaches illustrate and confirm the consistency, while the computational costs differ significantly. The mixed approach and the 'hole' approach are not suited for the wound healing model which consists of many moving cells and a large number of time iterations. Furthermore, the smoothed particle approach costs nearly the same time as the immersed boundary approach, which is a promising method to be adapted into the general healing model, considering the advantage of smooth forces.

The findings in two dimensions have been extended to general dimensionality. Currently, all the analytical and numerical analysis has been carried out for simple linear elasticity. In the future, we plan to extend our findings to the viscoelasticity equations. This viscoelastic model contains a damping term, and still retains a linear nature. Furthermore, we are also interested in analyzing the above considered principles for a morphoelastic model. A morphoelastic model has the major advantage of incorporating permanent deformations, of which a major complication is its nonlinear nature.

6

UPSCALING BETWEEN AN AGENT-BASED MODEL (SMOOTHED PARTICLE APPROACH) AND A CONTINUUM-BASED MODEL FOR SKIN CONTRACTIONS

In general, there are two categories of mathematical models in multiple scales: agent-based modelling on the microscale and continuum-based modelling on the macroscale. No quantitative connection between these two categories of models has been built yet. In this chapter, we present some results from our study of the connection between these scales regarding the momentum equilibrium equations that are used to simulate the traction forces exerted on the extracellular matrix (ECM) by the cells during wound healing. For the one-dimensional case, we managed to rigorously establish the link between the two modelling approaches for both closed-form solutions and finite-element approximations. For the multiple dimensional case, we computationally evidence the connection between the agent-based and continuum-based modelling approaches.

6.1. INTRODUCTION

In our previous work (Chapter 2) [1], a formalism to describe the mechanism of the displacement of the ECM has been used, which is firstly developed by Boon *et al.* [41] and improved further by Koppenol [17]. Regarding the elasticity equation with point forces, we realized that the partial differential equation is singular for dimensionalities that ex-

This chapter has been submitted to conference proceedings of PARTICLE 2021 and Journal of Mathematical Biology.

ceeds one. Hence, we developed various alternatives to improve the accuracy of the solution in Chapter 4 and 5 [54, 82].

We have been working with agent-based models so far, which model the cells as individuals and define the formalism of pulling forces by superposition theory. However, once the wound scale is larger, the agent-based model is increasingly expensive from a computational perspective, and hence, the cell density model is preferred, which considers many cells as one collection in a unit. In this chapter, we investigate and discover the connections between these two models, in the perspective of modelling the mechanism of pulling forces exerted by the (myo)fibroblasts. As the consistency between the smoothed particle approach (SP approach) and the immersed boundary approach has been proven both analytically and numerically [54, 82], we select the SP approach here due to its continuity and smoothness, to compare with the cell density model using finite-element methods.

The chapter is structured as follows. We start introducing both models in one dimension in Section 6.2, then in Section 6.3 we extend the models to two dimensions. Section 6.4 displays the numerical results in one and two dimensions. Finally, some conclusions are shown in Section 6.5.

6.2. MATHEMATICAL MODELS IN ONE DIMENSION

Considering one-dimensional force equilibrium, the equations are given by

$$\begin{aligned} -\frac{d\sigma}{dx} &= f, & \text{Equation of Equilibrium,} \\ \epsilon &= \frac{du}{dx}, & \text{Strain-Displacement Relation,} \\ \sigma &= E\epsilon, & \text{Constitutive Equation.} \end{aligned}$$

By substituting $E = 1$, the equations above can be combined to Laplacian equation in one dimension:

$$-\frac{d^2u}{dx^2} = f. \quad (6.1)$$

6.2.1. SMOOTHED PARTICLE APPROACH

In Chapter 4 and 5 [54], a smoothed particle approach (SP approach) is developed as an alternative of the Dirac Delta distribution describing the point forces exerted by the biological cells, in the application of wound healing:

$$(BVP_{SP}) \begin{cases} -\frac{d^2u}{dx^2} = P_{SP} \sum_{i=1}^{N_s} \delta'_\epsilon(x - s_i), & x \in (0, L), \\ u(0) = u(L) = 0, \end{cases} \quad (6.2)$$

where P_{SP} is the magnitude of the forces, $\delta_\epsilon(x)$ is the Gaussian distribution with variance ϵ and s_i is the centre position of biological cell i . One can solve the partial differential equations (PDEs) with finite-element methods. The corresponding weak form is given

by

$$(WF_{SP}) \begin{cases} \text{Find } u \in H_0^1((0, L)), \text{ such that} \\ \int_0^L u' \phi' dx = \int_0^L \sum_{i=1}^{N_s} P_{SP} \delta'_\varepsilon(x - s_i) \phi dx, \text{ for all } \phi \in H_0^1((0, L)). \end{cases}$$

Without this knowledge, the existence and uniqueness of the H_0^1 -solution follows as well from the application of the Lax–Milgram theorem [80], where it is immediately obvious that the bilinear form in the left–hand side is symmetric and positive definite.

6.2.2. CELL DENSITY APPROACH

A cell density approach is often used in the large scale, so that the computational efficiency is much improved compared with the agent-based model. According to the model in [17], the force in two dimensions can be determined by the divergence of $n_c \cdot \mathbf{I}$, where n_c is the local density of the biological cells and \mathbf{I} is the identity tensor. In one dimension, the cell density approach is expressed as:

$$(BVP_{den}) \begin{cases} -\frac{d^2 u}{dx^2} = P_{den} \frac{dn_c}{dx}, x \in (0, L), \\ u(0) = u(L) = 0, \end{cases} \quad (6.3)$$

where P_{den} is the magnitude of the forces. The corresponding weak form is given by

$$(WF_{den}) \begin{cases} \text{Find } u \in H_0^1((0, L)), \text{ such that} \\ \int_0^L u' \phi' dx = \int_0^L P_{den} n'_s \phi dx, \text{ for all } \phi \in H_0^1((0, L)). \end{cases}$$

6.2.3. CONSISTENCY BETWEEN TWO MODELS

ANALYTICAL SOLUTIONS WITH SPECIFIC LOCATIONS OF BIOLOGICAL CELLS

To express the analytical solution, it is necessary to determine the locations of the biological cells, such that the cell density can be written as an analytical function of the positions. We assume, there are N_s cells distributed uniformly in the subdomain (a, b) of the computational domain $(0, L)$. Hence, the distance between the center position of any two adjacent biological cells is constant, which we denote $\Delta s = (b - a)/N_s$ and the first and the N_s -th cell are located at $x = a + \Delta s/2$ and $x = b - \Delta s/2$, respectively. With homogeneous Dirichlet boundary conditions, and suppose $P_{SP} = P\Delta s$ and variance $\varepsilon = \Delta s$, the boundary value problem of the SP approach is expressed as

$$(BVP_{SP}^1) \begin{cases} -\frac{d^2 u_1}{dx^2} = P\Delta s \sum_{i=1}^{N_s} \delta'_{\Delta s}(x - s_i), x \in (0, L), \\ u_1(0) = u_1(L) = 0, \end{cases} \quad (6.4)$$

where P is a positive constant and s_i is the centre position of the biological cells. Utilizing the superposition principle, the analytical solution is given by

$$u_1(x) = P\Delta s \sum_{i=1}^{N_s} \frac{1}{2} \left\{ \left(\frac{x}{L} - 1 \right) \operatorname{erf} \left(\frac{s_i}{\sqrt{2}\Delta s} \right) + \frac{x}{L} \operatorname{erf} \left(\frac{L - s_i}{\sqrt{2}\Delta s} \right) - \operatorname{erf} \left(\frac{x - s_i}{\sqrt{2}\Delta s} \right) \right\}, \quad (6.5)$$

where $\text{erf}(x)$ is the error function defined as $\text{erf}(x) = \frac{2}{\sqrt{\pi}} \int_0^x \exp(-t^2) dt$ [77]. Since the biological cells are uniformly located between a and b ($0 < a < b < L$), $\frac{dn_c}{dx}$ can be rephrased as

$$\frac{dn_c}{dx} = \begin{cases} \frac{1}{t}, & a - \frac{t}{2} < x < a + \frac{t}{2}, \\ -\frac{1}{t}, & b - \frac{t}{2} < x < b + \frac{t}{2}, \\ 0, & \text{otherwise,} \end{cases}$$

where t is a small positive constant. Taking the limit of t to zero, the above expression converges to $\delta(x - a) - \delta(x - b)$. Hence, the boundary value problem of the cell density model can be written as

$$(BVP_{den}^1) \begin{cases} -\frac{d^2 u_2}{dx^2} = P \frac{dn_c}{dx} \rightarrow P(\delta(x - a) - \delta(x - b)), x \in (0, L), \\ u_2(0) = u_2(L) = 0, \end{cases} \quad (6.6)$$

where $\delta(x)$ is the Dirac Delta distribution and a and b are the left and right endpoint of the subdomain (where biological cells are uniformly located) respectively. The analytical solution is then expressed as

$$u_2(x) = P(G(x, a) - G(x, b)), \quad (6.7)$$

where $G(x, x')$ is the Green's function [88], defined by

$$G(x, x') = \left(1 - \frac{x'}{L}\right)x - \max(x - x', 0),$$

in the computational domain $(0, L)$.

Actually, the convergence between $u_1(x)$ and $u_2(x)$ can be proven as $\Delta s \rightarrow 0^+$ by a proposition. Firstly, we introduce Chebyshev's Inequality:

Lemma 6.1. (Chebyshev's Inequality [86]) Denote X as a random variable with finite mean μ and finite variance σ^2 . Then for any positive $k \in \mathbb{R}$, the following inequality holds:

$$\mathbb{P}(|X - \mu| \geq k) \leq \frac{\sigma^2}{k^2},$$

where $\mathbb{P}(A)$ is the probability of event A . The above inequality can also be rephrased as

$$\mathbb{P}(|X - \mu| \leq k) \geq 1 - \frac{\sigma^2}{k^2}.$$

Proposition 6.1. Let $u_1(x)$ as described in Eq (6.4) be the exact solution to (BVP_{SP}^1) and $u_2(x)$ as described in Eq (6.6) be the exact solution to (BVP_{den}^1) . As $\Delta s \rightarrow 0^+$, $u_1(x)$ converges to $u_2(x)$.

Proof. For the standard Gaussian distribution in one dimension, the cumulative distribution function is given by $F(x) = \frac{1}{2} \left(1 + \text{erf}\left(\frac{x}{\sqrt{2}}\right)\right)$. Thus, we obtain

$$\text{erf}\left(\frac{x}{\sqrt{2}}\right) = 2F(x) - 1. \quad (6.8)$$

By Chebyshev's Inequality (see Lemma 6.1), one can conclude that for any positive k ,

$$F(k) - F(-k) \geq 1 - \frac{1}{k^2}. \quad (6.9)$$

Note that $1 - F(k) = F(-k)$ due to the symmetry of standard Gaussian distribution. Hence, Eq (6.9) implies

$$\begin{aligned} F(k) &\geq 1 - \frac{1}{k^2} + F(-k) = 1 - \frac{1}{k^2} + 1 - F(k) \\ \Leftrightarrow 1 - \frac{1}{k^2} &\leq F(k) \leq 1, \end{aligned}$$

and analogously, $0 \leq F(-k) \leq \frac{1}{k^2}$ is implied. Together with Eq (6.8), it gives

$$\begin{cases} 1 - \frac{1}{k^2} \leq \operatorname{erf}\left(\frac{k}{\sqrt{2}}\right) \leq 1, \\ -1 \leq \operatorname{erf}\left(-\frac{k}{\sqrt{2}}\right) \leq -1 + \frac{1}{k^2}. \end{cases}$$

Let $k = \frac{s_i}{\Delta s} > 0$, for any $s_i \in (a, b) \subset (0, L)$, $i = \{1, \dots, N_s\}$, then

$$\begin{cases} 1 - \left(\frac{\Delta s}{s_i}\right)^2 \leq \operatorname{erf}\left(\frac{s_i}{\sqrt{2}\Delta s}\right) \leq 1, \\ -1 \leq \operatorname{erf}\left(-\frac{s_i}{\sqrt{2}\Delta s}\right) \leq -1 + \left(\frac{\Delta s}{s_i}\right)^2. \end{cases}$$

As it has been defined earlier that $\Delta s = (b - a)/N_s$, we obtain

$$\begin{aligned} \sum_{i=1}^{N_s} \left(1 - \left(\frac{\Delta s}{s_i}\right)^2\right) \Delta s &\leq \sum_{i=1}^{N_s} \operatorname{erf}\left(\frac{s_i}{\sqrt{2}\Delta s}\right) \Delta s \leq \sum_{i=1}^{N_s} \Delta s \\ \Rightarrow (b - a) - (\Delta s)^3 \sum_{i=1}^{N_s} \frac{1}{s_i^2} &\leq \sum_{i=1}^{N_s} \operatorname{erf}\left(\frac{s_i}{\sqrt{2}\Delta s}\right) \Delta s \leq (b - a). \end{aligned}$$

Since $\lim_{\Delta s \rightarrow 0^+} (\Delta s)^3 \sum_{i=1}^{N_s} \frac{1}{s_i^2} = 0$ for any $s_i \in (a, b) \subset (0, L)$, the Squeeze Theorem [83] implies that

$$\lim_{\Delta s \rightarrow 0^+} \sum_{i=1}^{N_s} \operatorname{erf}\left(\frac{s_i}{\sqrt{2}\Delta s}\right) \Delta s = b - a. \quad (6.10)$$

Analogously, we obtain that for any $s_i \in (a, b) \subset (0, L)$,

$$\lim_{\Delta s \rightarrow 0^+} \sum_{i=1}^{N_s} \operatorname{erf}\left(-\frac{s_i}{\sqrt{2}\Delta s}\right) \Delta s = a - b. \quad (6.11)$$

Thus, it can be concluded that for any series of real number $\{x_i\} \in \mathbb{R}^n$, when $x_{i+1} - x_i = \Delta s$ and x_i is either all positive or all negative for any $i = \{1, \dots, N_s\}$,

$$\lim_{\Delta s \rightarrow 0^+} \sum_{i=1}^{N_s} \operatorname{erf}\left(\frac{x_i}{\sqrt{2}\Delta s}\right) \Delta s = (b - a) \operatorname{sgn}(x_i), \quad (6.12)$$

where $\text{sgn}(x)$ is sign function defined by

$$\text{sgn}(x) = \begin{cases} 1, & \text{if } x > 0, \\ 0, & \text{if } x = 0, \\ -1, & \text{if } x < 0. \end{cases}$$

We rewrite $u_1(x)$ as

$$u_1(x) = P \left[\frac{1}{2} \left(\frac{x}{L} - 1 \right) \sum_{i=1}^{N_s} \text{erf} \left(\frac{s_i}{\sqrt{2}\Delta s} \right) \Delta s + \frac{1}{2} \frac{x}{L} \sum_{i=1}^{N_s} \text{erf} \left(\frac{L-s_i}{\sqrt{2}\Delta s} \right) \Delta s - \frac{1}{2} \sum_{i=1}^{N_s} N_s \text{erf} \left(\frac{x-s_i}{\sqrt{2}\Delta s} \right) \Delta s \right].$$

Combining Eq (6.10), (6.11) and (6.12), $u_1(x)$ is given by

$$\begin{aligned} u_1(x) &= P \left[\frac{1}{2} \left(\frac{x}{L} - 1 \right) (b-a) + \frac{1}{2} \frac{x}{L} (b-a) + \frac{1}{2} [(x-b) \text{sgn}(x-b) - (x-a) \text{sgn}(x-a)] \right] \\ &= P \left[\left(\frac{x}{L} - \frac{1}{2} \right) (b-a) + \frac{1}{2} [(x-b) \text{sgn}(x-b) - (x-a) \text{sgn}(x-a)] \right] \\ &= P \left[\left(\frac{x}{L} - \frac{1}{2} \right) (b-a) + \frac{1}{2} [|x-b| - |x-a|] \right] \\ &= \begin{cases} P \frac{x}{L} (b-a), & 0 \leq x \leq a, \\ P \frac{x}{L} (b-a) - x + a, & a < x \leq b, \\ P \left(\frac{x}{L} - 1 \right) (b-a), & b < x \leq L, \end{cases} \end{aligned}$$

Rewriting $u_2(x)$ regarding different domain gives

$$u_2(x) = \begin{cases} P \frac{x}{L} (b-a), & 0 \leq x \leq a, \\ P \frac{x}{L} (b-a) - x + a, & a < x \leq b, \\ P \left(\frac{x}{L} - 1 \right) (b-a), & b < x \leq L. \end{cases}$$

Hence, we conclude that $u_1(x)$ converges to $u_2(x)$ as $\Delta s \rightarrow 0^+$. \square

FINITE-ELEMENT METHOD SOLUTIONS WITH ARBITRARY LOCATIONS OF BIOLOGICAL CELLS

For the finite-element method, we select the piecewise Lagrangian linear basis functions. We divide the computational domain into N_e identical mesh elements, with the nodal point $x_1 = 0$ and $x_{N_e+1} = L$. For the implementation, we define the cell density as the count of biological cell in every mesh element divided by the length of the mesh element, hence, it is a constant within every mesh element, which is denoted by $n_c([x_j, x_{j+1}])$. In other words, in the mesh element $[x_j, x_{j+1}]$, the count of the biological cell (denoted by $N_c([x_j, x_{j+1}])$) is defined by

$$N_c([x_j, x_{j+1}]) = \int_{x_j}^{x_{j+1}} n_c([x_j, x_{j+1}]) dx = h n_c([x_j, x_{j+1}]),$$

for any $j \in \{1, \dots, N_e\}$, where h is the size of every mesh element. Different from (BVP_{SP}^1) where Δs is the variance of δ_ε , for finite-element methods, we set $\varepsilon = h/3$, such that the integration of $\delta_{h/3}(x - x')$ for any $0 < x' < L$ over any mesh element with size h , is close to 1 (see Lemma 6.2). With the two approaches, the boundary value problems with Dirichlet boundary condition are defined by

$$(BVP_{SP}^2) \begin{cases} -\frac{d^2 u_1}{dx^2} = Ph \sum_{i=1}^{N_s} \delta'_{h/3}(x - s_i), x \in (0, L), \\ u_1(0) = u_1(L) = 0, \end{cases} \quad (6.13)$$

and

$$(BVP_{den}^2) \begin{cases} -\frac{d^2 u_2}{dx^2} = Ph \frac{dn_c}{dx}, x \in (0, L), \\ u_2(0) = u_2(L) = 0, \end{cases} \quad (6.14)$$

where s_i is the position of biological cells, h is the mesh size and N_s is the total number of cells in the computational domain. The consistency between (BVP_{SP}^2) and (BVP_{den}^2) can be verified by the following lemma and theorem.

Lemma 6.2. (Empirical rule [87]) *Given the Gaussian distribution of mean μ and variance ε :*

$$\delta_\varepsilon(x - \mu) = 1/\sqrt{2\pi\varepsilon^2} \exp\{-(x - \mu)^2/(2\varepsilon^2)\},$$

then the following integration can be computed:

1. $\int_{\mu-\varepsilon}^{\mu+\varepsilon} \delta_\varepsilon(x - \mu) dx \approx 0.6827$;
2. $\int_{\mu-2\varepsilon}^{\mu+2\varepsilon} \delta_\varepsilon(x - \mu) dx \approx 0.9545$;
3. $\int_{\mu-3\varepsilon}^{\mu+3\varepsilon} \delta_\varepsilon(x - \mu) dx \approx 0.9973$.

Theorem 6.1. *Denote $u_1^h(x)$ and $u_2^h(x)$ respectively the solution to (BVP_{SP}^2) and (BVP_{den}^2) . With Lagrangian linear basis functions for the finite element method, $u_1^h(x)$ converges to $u_2^h(x)$, as the size of the mesh element $h \rightarrow 0^+$, regardless of the positions of biological cells.*

Proof. We define $v^h(x) = u_1^h(x) - u_2^h(x)$, then the boundary value problem to solve $v^h(x)$ is given by

$$(BVP_v^1) \begin{cases} -\frac{d^2 v^h}{dx^2} = Ph \left(\sum_{i=1}^{N_s} \delta'_{h/3}(x - s_i) - \frac{dn_c}{dx} \right), x \in (0, L), \\ v(0) = v(L) = 0. \end{cases} \quad (6.15)$$

The corresponding Galerkin's form reads as

$$(GF_v^1) \begin{cases} \text{Find } v^h \in H_0^1((0, L)), \text{ such that} \\ \int_0^L \frac{dv^h}{dx} \phi' dx = \int_0^L Ph \left(\sum_{i=1}^{N_s} \delta'_{h/3}(x - s_i) - \frac{dn_c}{dx} \right) \phi dx, \\ \text{for all } \phi \in H_0^1((0, L)). \end{cases}$$

Using integration by parts and letting $\phi = \phi_j$, $j \in \{1, \dots, N_e + 1\}$, the equation in (GF_v^1) can be rewritten by

$$\begin{aligned}
 \int_0^L \frac{dv^h}{dx} \phi_j' dx &= \int_0^L Ph \left(\sum_{i=1}^{N_s} \delta'_{h/3}(x-s_i) - \frac{dn_c}{dx} \right) \phi_j dx \\
 &= [Ph \sum_{i=1}^{N_s} \delta_{h/3}(x-s_i) \phi_j]_0^L - [Ph n_c \phi_j]_0^L - \int_0^L Ph \left(\sum_{i=1}^{N_s} \delta_{h/3}(x-s_i) - n_c \right) \phi_j' dx \\
 (\text{Boundary condition}) &= - \int_0^L Ph \left(\sum_{i=1}^{N_s} \delta_{h/3}(x-s_i) - n_c \right) \phi_j' dx \\
 &= Ph \sum_{j=1}^{N_e} \left\{ \int_{x_j}^{x_{j+1}} n_c \phi_j' dx - \int_{x_j}^{x_{j+1}} \sum_{i=1}^{N_s} \delta_{h/3}(x-s_i) \phi_j' dx \right\} \\
 &= P \sum_{j=1}^{N_e} \left\{ [N_c([x_j, x_{j+1}]) - \int_{x_j}^{x_{j+1}} \sum_{i=1}^{N_s} \delta_{h/3}(x-s_i) dx] \right\} \\
 (h \rightarrow 0^+, \text{ Lemma (6.2)} &\rightarrow 0,
 \end{aligned}$$

since it can be defined that $N([x_j, x_{j+1}]) = \int_{x_j}^{x_{j+1}} \sum_{i=1}^{N_s} \delta(x-s_i) dx$. \square

6

6.3. MATHEMATICAL MODELS IN TWO DIMENSIONS

In this section, the smoothed particle approach and the cell density approach are introduced in \mathbb{R}^2 . The relation between both approaches is investigated in terms of convergence with respect to the mesh size and model parameters.

6.3.1. SMOOTHED PARTICLE APPROACH AND CELL DENSITY APPROACH

In multi dimensional case, the equation of conservation of momentum over the computational domain Ω , without considering inertia, is given by

$$-\nabla \cdot \boldsymbol{\sigma} = \mathbf{f}.$$

We consider a linear, homogeneous and isotropic domain, with Hooke's Law, the stress tensor $\boldsymbol{\sigma}$ is defined as

$$\boldsymbol{\sigma} = \frac{E}{1+\nu} \left\{ \boldsymbol{\epsilon} + \text{tr}(\boldsymbol{\epsilon}) \left[\frac{\nu}{1-2\nu} \right] \mathbf{I} \right\}, \quad (6.16)$$

where E is the Young's modulus of the material, ν is Poisson's ratio and $\boldsymbol{\epsilon}$ is the infinitesimal strain tensor:

$$\boldsymbol{\epsilon} = \frac{1}{2} [\nabla \mathbf{u} + (\nabla \mathbf{u})^T].$$

Considering a subdomain $\Omega_w \subset \Omega$, where the center positions of the biological cells are located, then the SP approach and cell density approach with homogeneous Dirichlet boundary condition are derived by

$$(BVP_{SP}^3) \begin{cases} -\nabla \cdot \boldsymbol{\sigma} = P_{SP} \sum_{i=1}^{N_s} \nabla \delta_\varepsilon(\mathbf{x} - \mathbf{s}_i), \mathbf{x} \in \Omega, \\ \mathbf{u}_1(\mathbf{x}) = \mathbf{0}, \mathbf{x} \in \partial\Omega, \end{cases} \quad (6.17)$$

and

$$(BVP_{den}^3) \begin{cases} -\nabla \cdot \boldsymbol{\sigma} = P_{den} \nabla \cdot (n_c \mathbf{I}), \mathbf{x} \in \Omega, \\ \mathbf{u}_2(\mathbf{x}) = \mathbf{0}, \mathbf{x} \in \partial\Omega. \end{cases} \quad (6.18)$$

6.3.2. CONSISTENCY BETWEEN TWO APPROACHES IN FINITE-ELEMENT METHOD

To prove the consistency between these two approaches, we define that for the triangular mesh element $e_k, k \in \{1, \dots, N_e\}$, where N_e is the total number of mesh elements in Ω , the density of biological cell $n_c(e_k)$ is constant and the count of biological cells $N_c(e_k)$ is expressed by

$$N_c(e_k) = \int_{e_k} n_c(e_k) d\Omega = A(e_k) n_c(e_k),$$

where $A(e_k)$ is the area of mesh element e_k . Similar to the process of proof in one dimension, we state the following theorem:

Theorem 6.2. Denote $\mathbf{u}_1^h(\mathbf{x})$ and $\mathbf{u}_2^h(\mathbf{x})$ respectively the solution to (BVP_{SP}^3) and (BVP_{den}^3) with $P_{SP} = P_{den} = P$. With Lagrange linear basis functions for the finite element method, $\mathbf{u}_1^h(\mathbf{x})$ converges to $\mathbf{u}_2^h(\mathbf{x})$, as the size of a triangular mesh element is taken to zero, regardless of the positions of biological cells.

Proof. We consider $\mathbf{v}^h(\mathbf{x}) = \mathbf{u}_1^h(\mathbf{x}) - \mathbf{u}_2^h(\mathbf{x})$, then the boundary value problem to solve $\mathbf{v}^h(\mathbf{x})$ is given by

$$(BVP_v^3) \begin{cases} -\nabla \cdot \boldsymbol{\sigma} = P \left[\sum_{i=1}^{N_s} \nabla \delta_\varepsilon(\mathbf{x} - \mathbf{s}_i) - \nabla \cdot (n_c \mathbf{I}) \right], \mathbf{x} \in \Omega, \\ \mathbf{v}(\mathbf{x}) = \mathbf{0}, \mathbf{x} \in \partial\Omega. \end{cases} \quad (6.19)$$

The corresponding Galerkin's form reads as

$$(GF_v^3) \begin{cases} \text{Find } \mathbf{v}^h \in \mathbf{H}_0^1(\Omega), \text{ such that} \\ \int_{\Omega} \boldsymbol{\sigma}(\mathbf{v}^h) : \nabla \boldsymbol{\phi}^h d\Omega = \int_{\Omega} P \left[\sum_{i=1}^{N_s} \nabla \delta_\varepsilon(\mathbf{x} - \mathbf{s}_i) - \nabla \cdot (n_c \mathbf{I}) \right] \cdot \boldsymbol{\phi}^h d\Omega, \\ \text{for all } \boldsymbol{\phi}^h \in \mathbf{H}_0^1(\Omega). \end{cases}$$

With integral by parts and letting $\boldsymbol{\phi}^h = \boldsymbol{\phi}_k^h, k \in \{1, \dots, N_e\}$, the equation in (GF_v^3) can be rewritten by

$$\begin{aligned} \int_{\Omega} \boldsymbol{\sigma}(\mathbf{v}^h) \nabla \boldsymbol{\phi}_k^h d\Omega &= \int_{\Omega} P \left[\sum_{i=1}^{N_s} \nabla \delta_\varepsilon(\mathbf{x} - \mathbf{s}_i) - \nabla \cdot (n_c \mathbf{I}) \right] \cdot \boldsymbol{\phi}_k^h d\Omega \\ &= P \left\{ \left[\int_{\partial\Omega} \sum_{i=1}^{N_s} \delta_\varepsilon(\mathbf{x} - \mathbf{s}_i) \boldsymbol{\phi}_k^h \mathbf{n} d\Gamma - \int_{\Omega} \sum_{i=1}^{N_s} \delta_\varepsilon(\mathbf{x} - \mathbf{s}_i) \nabla \cdot \boldsymbol{\phi}_k^h d\Omega \right] \right. \\ &\quad \left. - \left[\int_{\partial\Omega} n_c (\mathbf{I} \boldsymbol{\phi}_k^h) \cdot \mathbf{n} d\Gamma - \int_{\Omega} n_c \mathbf{I} : \nabla \boldsymbol{\phi}_k^h d\Omega \right] \right\} \\ \text{(Boundary condition)} &= -P \int_{\Omega} \sum_{i=1}^{N_s} \delta_\varepsilon(\mathbf{x} - \mathbf{s}_i) \nabla \cdot \boldsymbol{\phi}_k^h - n_c \mathbf{I} : \nabla \boldsymbol{\phi}_k^h d\Omega \end{aligned}$$

$$\begin{aligned}
&= -P \sum_{k=1}^{N_e} \int_{e_k} \sum_{i=1}^{N_s} \delta_\varepsilon(\mathbf{x} - \mathbf{s}_i) \nabla \cdot \boldsymbol{\phi}_k^h - n_c \mathbf{I} : \nabla \boldsymbol{\phi}_k^h d\Omega \\
&= -P \sum_{k=1}^{N_e} \nabla \cdot \boldsymbol{\phi}_k^h \int_{e_k} \sum_{i=1}^{N_s} \delta_\varepsilon(\mathbf{x} - \mathbf{s}_i) - n_c d\Omega \\
&= P \sum_{k=1}^{N_e} \nabla \cdot \boldsymbol{\phi}_k^h \left[N_c(e_k) - \int_{e_k} \sum_{i=1}^{N_s} \delta_\varepsilon(\mathbf{x} - \mathbf{s}_i) d\Omega \right] \\
&(\varepsilon \rightarrow 0^+) \rightarrow 0,
\end{aligned}$$

since it can be defined that $N_c(e_k) = \int_{e_k} \sum_{i=1}^{N_s} \delta(\mathbf{x} - \mathbf{s}_i) d\Omega$. Note that in two dimensions, ε needs to be sufficiently small compared to the size of a triangular mesh element. \square

6.4. RESULTS

Results in both one and two dimensions are discussed in this section. Since the objective of this chapter is to investigate the consistency and the connections between the SP approach and the cell density approach, all parameters are dimensionless.

6

6.4.1. ONE-DIMENSIONAL RESULTS

We show the results by analytical solutions in Figure 6.1 with various values of Δs (i.e. depending on different number of biological cells in the subdomain (a, b)). Here, the computational domain is $(0, 7)$ with $L = 7$ and the subdomain where the biological cells locate uniformly is $(2, 5)$ with $a = 2$ and $b = 5$. With the decrease of the variance in the Gaussian distribution in (BVP_{SP}^2) , the curves gradually overlap, which verifies the convergence between the analytical solutions to these two approaches.

To implement the model, there are two different algorithms shown in Figure 6.2 and 6.3. Depending on different circumstances, the implementation method is chosen. The cell density in one dimension is defined as the number of cells per length unit. In other words, the cell count in a given domain can be computed by integrating the cell density over the domain. If the cell density function can be expressed analytically and the first order derivative of the function exists, then a certain bin length d is chosen and the cell count in every bin of length d is calculated. Then we generalize the center positions of cells in every bin of length d , thus, the SP approach can be implemented, as it is indicated in Figure 6.2. However, it is not always straightforward to obtain the analytical expression of cell density. If the center positions of cells are given, the number of cells in each mesh element can be counted, hence, the cell density will be computed analogously at each mesh points. Therefore, the boundary value problem of cell density approach is solved by numerical methods, for example, the finite-element methods.

In this chapter, all numerical results are derived by finite-element methods with Lagrangian linear basis functions. Regarding the first implementation method (see Figure 6.2), we show the results with a Gaussian distribution and sine function as cell density functions; see Figure 6.4 and 6.5. We start with the simulations in which we keep the number of cells and the center positions of the cells the same, then we refine the mesh.

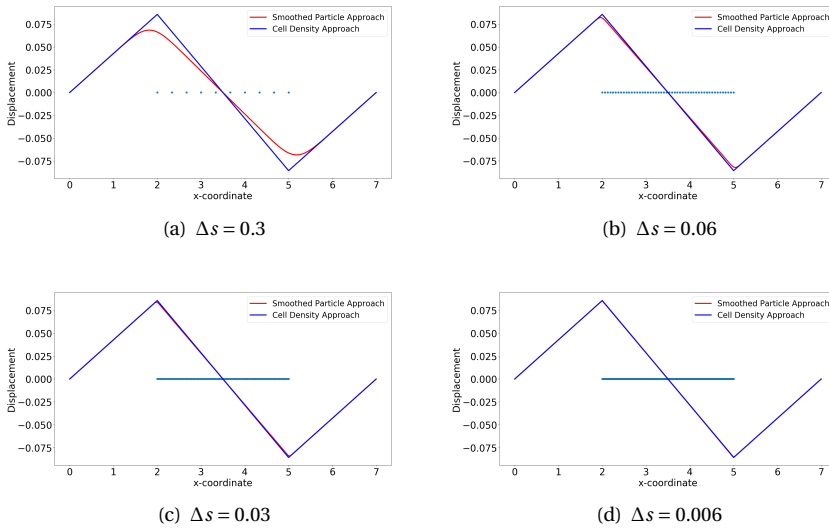


Figure 6.1: The solutions to (BVP_{SP}^1) and (BVP_{den}^1) are shown, with various values of Δs , which is the distance between centre positions of any two adjacent biological cells. Blue points are the centre positions of biological cells. Red curves represent the solutions to (BVP_{SP}^1) and blue curves represent the solutions to (BVP_{den}^1) .

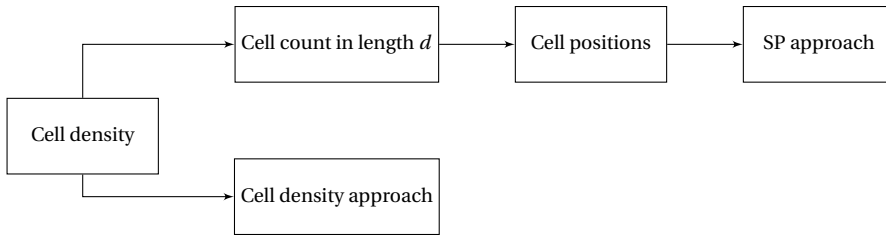


Figure 6.2: With the exact expression of cell density function and if the first order derivative of the function exists, the cell density approach is implemented directly. Based on the cell density, the number of cells in a certain region with length d is determined and subsequently, the center positions of cells can be generalized. Hence, the SP approach is implemented.

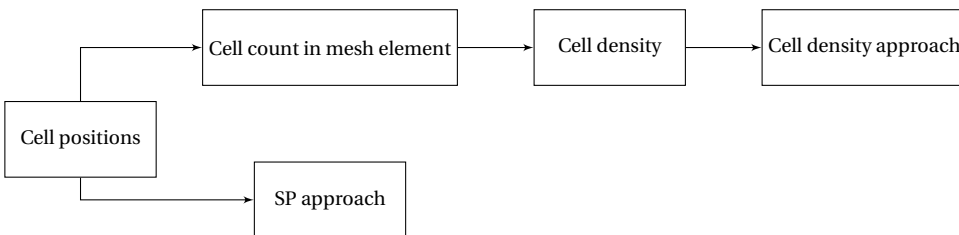


Figure 6.3: Given the center positions of cells, one can directly implement the SP approach. Computing the number of cells in every mesh element and divided by the length of the mesh element results into the cell density. Subsequently, cell density approach can be implemented.

Table 6.1: Numerical results of two approaches in one dimension, where the cell density function is in the form of the Gaussian distribution: $n_c(x) = 50 \times 1/\sqrt{2\pi \times 0.1^2} \exp\{-(x - 3.5)^2/(2 \times 0.1^2)\}$. Here, we define $N_s = 88$ and the mesh size $h = 0.07$. The results are solved by finite-element method with algorithm in Figure 6.2.

	SP Approach	Cell Density Approach
$\ u\ _{L^2((0,L))}$	0.5441481069175041	0.36197930815501245
$\ u\ _{H^1((0,L))}$	0.9642151731656272	0.871720645462775
Convergence rate of L^2 -norm	1.75281178	1.826378221
Convergence rate of H^1 -norm	1.70114233	1.716659924
Reduction ratio of the subdomain (a, b) (%)	13.88062	9.52381
Time cost (s)	0.045070	0.0032084

In Figure 6.5(a)-(c), the bin length d is 0.35, and the mesh size is a function of d . The results obtained by the SP approach become smoother. With various values of d , the solutions to the approaches are overlapping only if the factor between the d and mesh size is closer to 1. From Figure 6.5(d) to (f), the mesh is fixed and we vary the value of d . We note that in Figure 6.5(f), the solution to the SP approach is significantly different from the solution to the cell density approach. It is mainly caused by the fact that d is too small and there is barely any fluctuation with the count of cells in every d length subdomain, while with the Gaussian distribution as the cell density function, the majority of the cells are centered around $x = 3.5$. Hence, the solution to the SP approach still manages to be comparable with the solution to the cell density approach; see Figure 6.4(f). Numerical results of the simulation in Figure 6.4 are displayed in Table 6.1. There are some noticeable differences between two approaches, in particular the convergence rate in the H^1 -norm: thanks to the given, differentiable cell density function, the cell density approach converges faster. In addition, the cell density approach requires less computational time with a factor of 15.

We consider cells that are located uniformly in the subdomain $(2, 5)$, which implies that the gradient or divergence of the cell density vanishes inside the subdomain but does not exist at two endpoints of the subdomain. Hence, we utilize the implementation method in Figure 6.3, as the center positions of the cells are given, then the local cell density can be calculated per unit area. Compared with the results shown in Figure 6.1, the results in Figure 6.6 and Figure 6.7 show the solutions to (BVP_{SP}^2) and (BVP_{den}^2) respectively. Note that, in the finite-element method solutions, the magnitude of the forces in both approaches are the same, and the variance of $\delta_\varepsilon(x)$ is related to h rather than Δs (the distance between any two neighbouring biological cells). Furthermore, these figures verify that the convergence between SP approach and cell density approach is determined by the mesh size rather than by the distance between any two adjacent cells. Table 6.2 displays the numerical results of the simulation in Figure 6.6, in the perspective of the solution, the reduction ratio of the subdomain and the computational cost. Similarly to the figures, there is no significant difference between the norms and the deformed length of the subdomain. However, the simulation time in the cell density approach is much shorter than in the SP approach with a factor of 35.

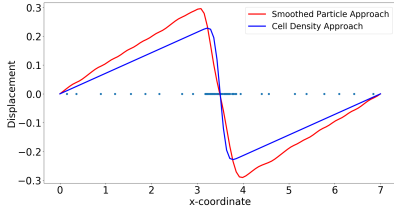
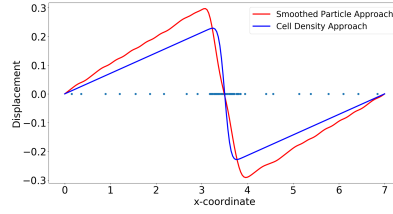
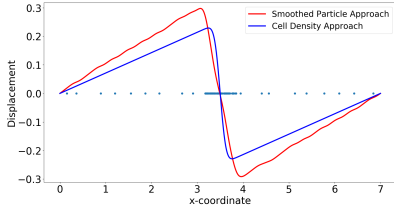
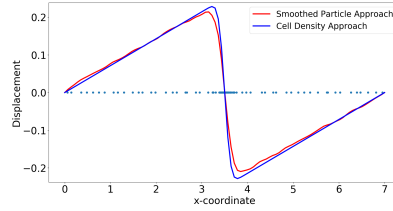
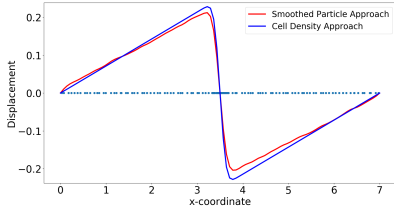
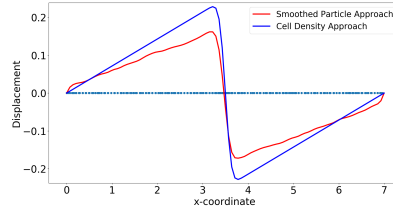
(a) $h(d) = d/5, h = 0.07, d = 0.35$ (b) $h(d) = d/10, h = 0.035, d = 0.35$ (c) $h(d) = d/50, h = 0.007, d = 0.35$ (d) $d(h) = 2h, h = 0.07, d = 0.14$ (e) $d(h) = h, h = 0.07, d = 0.07$ (f) $d(h) = h/4, h = 0.07, d = 0.0175$

Figure 6.4: The cell density function is in the form of the Gaussian distribution and using the algorithm in Figure 6.2, different simulations are carried out with various mesh size and the total number of cells. Blue curves represent the solutions to (BVP_{SP}^2) , and red curves are the solutions to (BVP_{den}^2) with $n_c(x) = 50 \times 1/\sqrt{(2\pi \times 0.1^2)} \exp\{-(x-3.5)^2/(2 \times 0.1^2)\}$. In Subfigure (a)-(c), we set $d = 0.35$ and cell positions are fixed, as h is decreasing. From Subfigure (d) to Subfigure (f), we use the same finite-element method settings (where h is sufficiently small with $h = 0.07$), and simulations are carried out with various values of d .

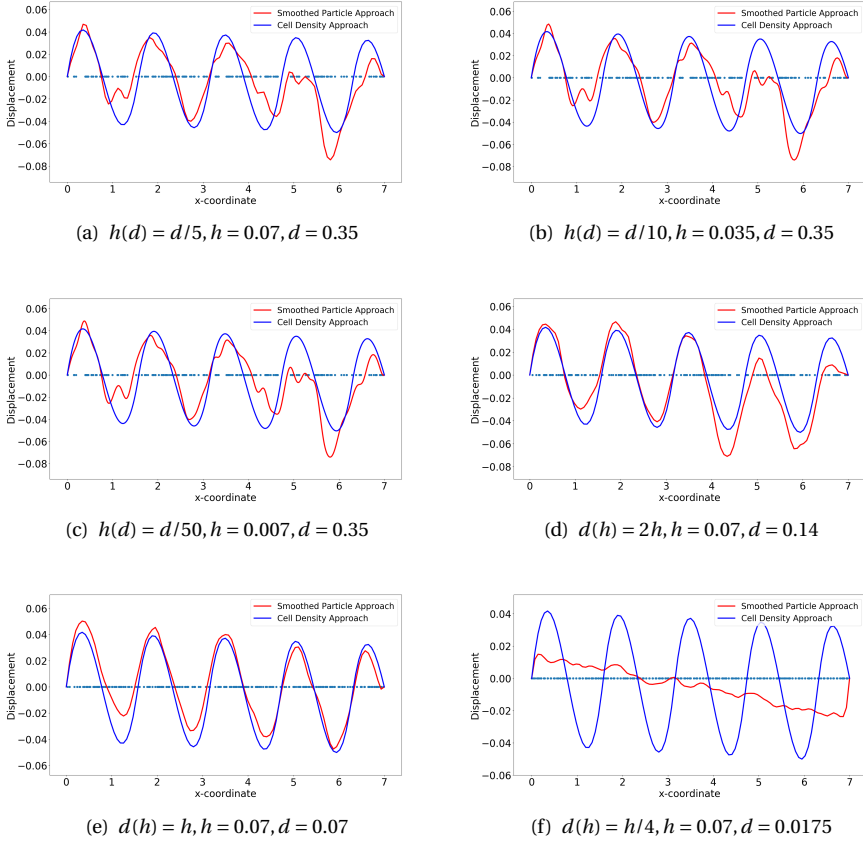
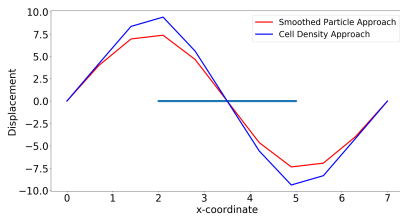


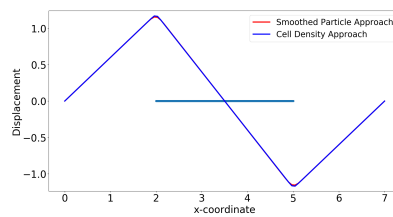
Figure 6.5: The cell density function is the sine function and using the algorithm in Figure 6.2, different simulations are carried out with various mesh size and the total number of cells. Blue curves represent the solutions to (BVP_{SP}^2) , and red curves are the solutions to (BVP_{den}^2) with $n_c(x) = 40|\sin(2x)|$. In Subfigure (a)-(c), we set $d = 0.35$ and cell positions are fixed. From Subfigure (d) to Subfigure (f), we use the same finite-element method settings (where h is efficiently small with $h = 0.07$), and we take different values of d .

Table 6.2: Numerical results of two approaches in one dimension with biological cells located uniformly. Here, we define mesh size $h = 0.07$ and $N_s = 50$, which means $\Delta s = 0.06$. The results are solved by finite-element method with algorithm in Figure 6.3.

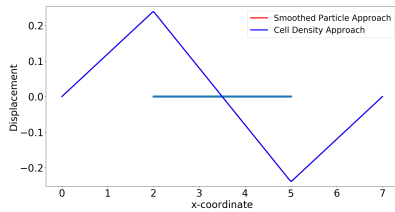
	SP Approach	Cell Density Approach
$\ u\ _{L^2((0,L))}$	0.1858655201	0.1858660118
$\ u\ _{H^1((0,L))}$	0.2780804415	0.2914497482
Convergence rate of L^2 -norm	0.9940317098	0.9985295706
Convergence rate of H^1 -norm	1.002001685	1.004380036
Reduction ratio of the subdomain (a, b) (%)	7.96908	7.98821
Time cost (s)	0.10391	0.0030458



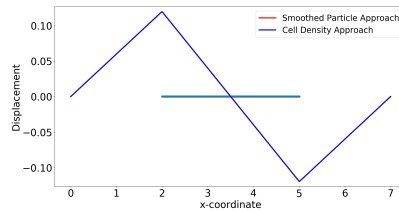
(a) $h = 0.7$



(b) $h = 0.07$



(c) $h = 0.014$



(d) $h = 0.007$

Figure 6.6: The finite-element method solutions to (BVP_{Sp}^2) and (BVP_{den}^2) are shown where cells are uniformly located. With the fixed positions of cells, the solutions are convergent as $h \rightarrow 0^+$. Blue points are the centre positions of biological cells. Red curves represent the solutions to (BVP_{Sp}^2) and blue curves represent the solutions to (BVP_{den}^2) .

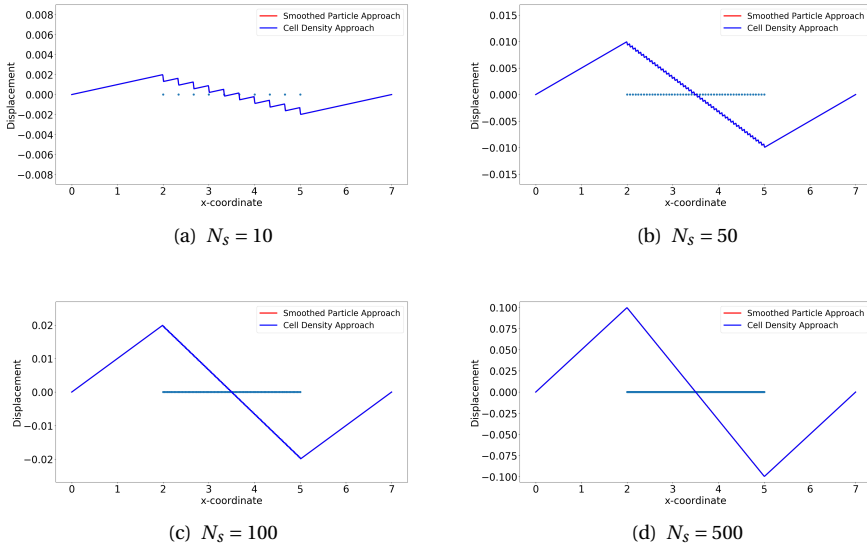


Figure 6.7: The finite-element method solutions to (BVP_{SP}^2) and (BVP_{den}^2) are shown with uniform distribution. Compared to the analytical result, the consistency between two approaches are unrelated to the number of cells, and the solutions are convergent as $h \rightarrow 0^+$. Here, we use $h = 0.007$. Blue points are the centre positions of biological cells. Red curves represent the solutions to (BVP_{SP}^2) and blue curves represent the solutions to (BVP_{den}^2) .

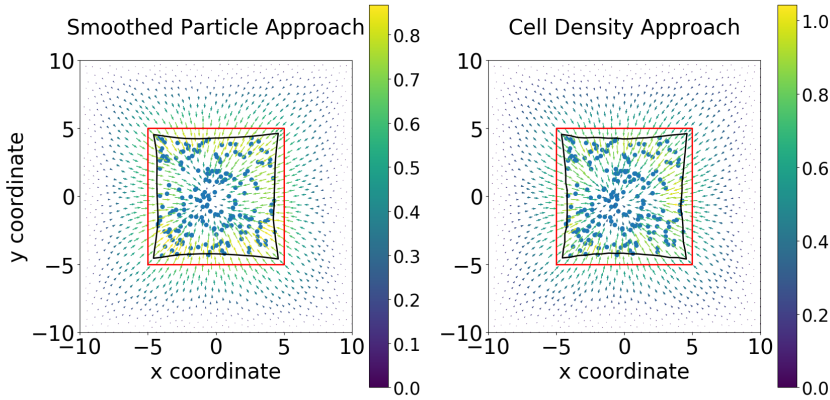


Figure 6.8: The displacement results are shown, which are solved from (BVP_{SP}^3) and (BVP_{den}^3) when cells are randomly located in the subdomain $(-5, 5) \times (-5, 5)$. In other words, it is impossible to write the analytical expression of $n_c(\mathbf{x})$, subsequently, the algorithm in Figure 6.3 is selected. There are 196 biological cells in the computational domain. Blue points are the center positions of biological cells, red curves are the original shapes of the subdomain, and the black curves represent the deformed boundary of the subdomain.

6.4.2. TWO-DIMENSIONAL RESULTS

In the multi-dimensional case, we are not able to find the analytical solution to the boundary value problems. The results are all solved by the use of the finite-element method applied to (BVP_{SP}^3) and (BVP_{den}^3) . Note that the force magnitude of both boundary value problems is the same. Following the same implementation methods as in one dimension, simulations are carried out with two formulas of cell density: (1) cells are located inside the subdomain Ω_w randomly by the uniform distribution; (2) the cell density function is in the form of the standard Gaussian distribution over the computational domain with $n_c(\mathbf{x}) = 50 \times \frac{1}{2\pi} \exp\left\{-\frac{\|\mathbf{x}\|^2}{2}\right\}$. Implementation methods in Figure 6.3 and Figure 6.2 are applied respectively in Simulation (1) and (2).

For Simulation (1), no analytical expression for (the derivative of) the density function is available. Therefore, the implementation starts with generating the cell positions, according to the principles outlined in Figure 6.3. In Figure 6.8, the displacement results are displayed. From the figures, hardly any significant differences between the solutions can be observed, which indicates that these two approaches are numerically consistent. Table 6.3 displays more details about the two approaches regarding the numerical analysis: most data are more or less the same. Thanks to the continuity of the SP approach, the convergence rate between two approaches is similar. However, as it has been mentioned earlier, the agent-based model is computationally more expensive than the continuum-based model; here, the difference is a factor of 240.

According to the setting of the simulation, we define the cell density function by

$$n_c(\mathbf{x}) = 50 \times \frac{1}{2\pi} \exp\left\{-\frac{\|\mathbf{x}\|^2}{2}\right\}, \text{ in } \Omega,$$

Table 6.3: Numerical results of two approaches in two dimensions with random distribution for the positions of biological cells. Due to the nonexistence of divergence or gradient of cell density function, implementation method in Figure 6.3 is used.

	SP Approach	Cell Density Approach
$\ u\ _{L^2((0,L))}$	10.105858093727422	12.314518769308366
$\ u\ _{H^1((0,L))}$	10.890035548437087	16.67100195050636
Convergence rate of L^2 -norm	2.012144067	2.061050246
Convergence rate of H^1 -norm	2.011995299	2.03760311
Reduction ratio of the subdomain Ω_w (%)	24.24192	23.33667
Time cost (s)	4.20677	1.77219×10^{-2}

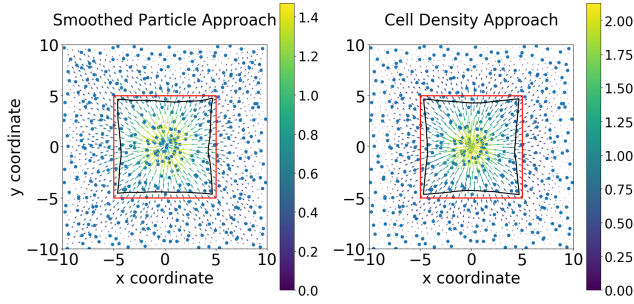
Table 6.4: Numerical results of two approaches in two dimensions with the form of the Gaussian distribution for the positions of biological cells. Figure 6.2 is implemented and there are 440 biological cells in the computational domain.

	SP Approach	Cell Density Approach
$\ u\ _{L^2((0,L))}$	11.14304909846569	13.188441094735877
$\ u\ _{H^1((0,L))}$	12.77795210802095	15.533928099123479
Convergence rate of L^2 -norm	1.724918322	1.856132219
Convergence rate of H^1 -norm	3.059831229	2.455660849
Reduction ratio of the subdomain Ω_w (%)	19.65854	20.55949
Time cost (s)	0.62347	0.017315

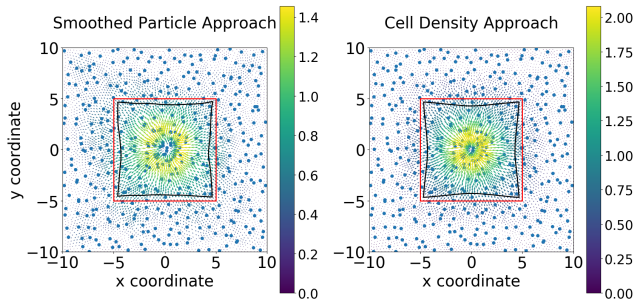
which is a Gaussian distribution multiplied by a positive constant. Similarly, in two dimensions, the cell density is defined by the number of biological cells per unit area. In other words, the cell count is computed by the local cell density multiplied by the area of selected region. Here, we assume that the selected region is a 1×1 square, then we generate the center positions of biological cells in every unit square based on the local number of cells. Figure 6.9 shows the numerical results regarding two approaches. There is no significant difference if the same mesh structure resolution is used. As the mesh is refined, the solution to the SP approach is smoother, since the "ring" in the center becomes more dominant. In Table 6.4, it can be concluded that there are no significant differences between two approaches except for the computational efficiency and the convergence rate of H^1 -norm. If the mesh is not fine enough, then the solution to the SP approach is less smooth, hence, the determination of the gradient of the solution is less accurate.

6.5. CONCLUSIONS

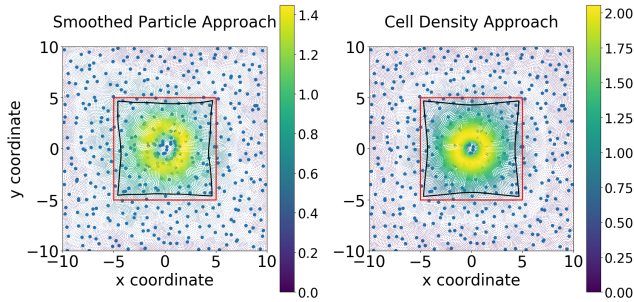
In this chapter, we discussed the different models to simulate the pulling forces exerted by the (myo)fibroblasts depending on different scales of the wound region. We started



(a) $h = 0.6435$



(b) $h = 0.3218$



(c) $h = 0.1609$

Figure 6.9: The displacement results are shown, which are solved from (BVP_{SP}^3) and (BVP_{den}^3) when cells are located according to the cell density function $n_c(\mathbf{x}) = 50 \times \frac{1}{2\pi} \exp\left\{-\frac{\|\mathbf{x}\|^2}{2}\right\}$. Hence, implementing algorithm in Figure 6.3 is used. There are 440 biological cells in the computational domain. Blue points are the center positions of biological cells, red curves are the original shapes of the subdomain, and the black curves represent the deformed boundary of the subdomain.

from one dimension and later extended the models to two dimensions. In one dimension, we can write explicitly the solution to the boundary value problem with specific distribution of the locations of biological cells. The consistency of the solutions indicates the possibility to prove the analytical connection between the two approaches. In both one and two dimensions, the numerical solutions delivered by finite-element methods with Lagrange linear basis functions implied that these two models are consistent under certain mesh conditions (when the mesh size is sufficiently small) and regardless the locations of the biological cells and the implementation methods. In summary, regarding the displacement of the ECM from the mechanical model, the agent-based model and the cell density model are consistent from a computational point of view. This could be used to transfer one type of model to the other one regarding the force balance in the wound healing model, as the connection between these two models has been suggested. We want to use the developed insights for the analysis of upscaling between agent-based and continuum-based model formulations.

III

MODELLING THE EVOLUTION OF CELL GEOMETRY DURING CELL MIGRATION

7

A FORMALISM FOR MODELLING TRACTION FORCES AND CELL SHAPE EVOLUTION DURING CELL MIGRATION IN VARIOUS BIOMEDICAL PROCESSES

The phenomenological model for cell shape deformation and cell migration [37, 90] is extended with the incorporation of cell traction forces and the evolution of cell equilibrium shapes as a result of cell differentiation. Plastic deformations of the extracellular matrix are modelled using morphoelasticity theory. The resulting partial differential equations are solved by the use of the finite element method. The paper treats various biological scenarios that entail cell migration and cell shape evolution. The experimental observations in [91], where transmigration of cancer cells through narrow apertures is studied, are reproduced using a Monte Carlo framework.

7.1. INTRODUCTION

In this chapter, an agent-based model is selected to develop a phenomenological model describing the cell geometry evolution during migration. This work is an extension of [90] and [37]. In [90], a model of the deformation of both the cell and the nucleus is developed. Furthermore, a parameter sensitivity analysis is carried out on the basis of Monte Carlo simulations. However, the study in [90] does not consider the traction forces applied by the cell and the impact on the substrates. Compared to the work of Vermolen and Gefen [37], we use finite-element methods to solve all partial differential equations,

This chapter has been published in *Biomech Model Mechanobiol* [89].

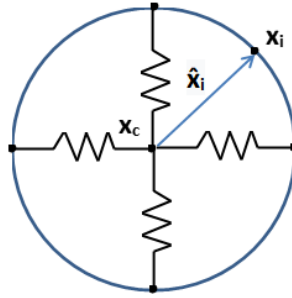


Figure 7.1: A schematic of the distribution of the nodal points on the cell membrane. In our model, we assume the equilibrium shape of the cell is maintained by a collection of springs.

rather than Green's functions. Therefore, a more precise solution is delivered. Furthermore, we implement a more intricate approach to model the traction forces applied by cells in various applications. In addition to circular projections of cells in [90] and [37], we model elliptic and hypocycloid-shaped cells in this chapter.

This chapter is structured as follows: Section 7.2 explains the agent-based model of cell migration, in the form of a set of partial differential equations. Possible applications of this model and the corresponding numerical results are exhibited in Section 7.3. Finally, conclusions are shown in Section 7.4.

7

7.2. MATHEMATICAL MODELLING

In this chapter, the phenomenological model of cell deformation is extended from the work in [37, 90], in particular, in two dimensions. With essential biological assumptions and simplifications, the model mainly describes the impact of extracellular components on the cell deformation and displacement. Subsequently, more applications can be developed, for instance, cell differentiation and cell repulsion. Different from the work in [92], where they also model the dynamics of intercellular adhesion by connecting a certain series of points inside the cell with elastic springs, the model in this chapter neglects the intracellular environment, hence, it is not capable to present the Poisson's effect of the cell.

The cell membrane is split into finite line segments by the nodal points, and the centre position of cell is determined by the mean of all the positions of the nodal points. The equilibrium shape of the cell is kept by a collection of springs, which connects each nodal point on the cell membrane to the centre of the cell, respectively; see Figure 7.1. For each nodal point, the displacement is determined by various mechanisms of directed motion and random turning [16], which will be discussed in details in the following contents. Regarding different applications of this model, there will be some model adjustments.

7.2.1. CONCENTRATION OF GENERIC SIGNAL

We assume that cell migration is mainly driven by chemotaxis (or mechanotaxis), which is commonly observed in wound healing and cancer cell metastasis with various types of signalling molecules. In wound healing, immune cells are directed to chase a bacterium or virus; high concentration of Transforming Growth Factor-beta (TGF-beta) induces the migration of (myo)fibroblasts towards the wound from the uninjured skin [2, 3]. Cancer metastasis is triggered by cancer cell proliferation and cell migration. On a cellular level, chemotaxis or haptotaxis is an essential cue for cancer cell migration and hence for the dissemination of tumours [18]. Numerous studies indicate that the availability of oxygen and nutrients is one of most crucial factors for the growth of tumours [93]. During tumour growth, the concentration of oxygen and nutrients depletes in the vicinity of the tumour [19]. Therefore, cancer cells have a tendency to migrate towards regions with higher concentrations of oxygen and nutrients.

Point sources and forces are modelled by the use of Dirac delta distribution in a d -dimensional framework. Let $\Omega \subset \mathbb{R}^d$ be an open region, then this distribution is defined by the following two characteristics:

1. $\delta(\mathbf{x}) = 0$, for all $x \in \mathbb{R}^d \setminus \{\mathbf{0}\}$;
2. $\int_{\Omega} \delta(\mathbf{x}) d\Omega = 1$, if $\mathbf{0} \in \Omega$.

The biophysical interpretation of the Dirac delta distribution is that the cell exerts force by the focal adhesion points. Since these points are many orders of magnitude smaller than the mesh size in the computational domain, we assume their sizes to be negligible. For this reason, we consider point forces by the use of Dirac delta distributions. Regarding the chemical signal, which makes the cancer cells move, we consider a point source. This is just a working hypothesis, since this could be changed to any type of source.

Together with the reaction-diffusion equation, the concentration of the signal is determined by:

$$\frac{\partial c(\mathbf{x}, t)}{\partial t} + \nabla \cdot (\mathbf{v}c(\mathbf{x}, t)) - \nabla \cdot (D\nabla c(\mathbf{x}, t)) = k\delta(\mathbf{x}(t) - \mathbf{x}_s), \mathbf{x} \in \Omega, t > 0, \quad (7.1)$$

where $c(\mathbf{x}, t)$ is the concentration of the signalling molecule, D is the diffusion rate which has been taken constant in the current study, k is the secretion rate of the signal source, \mathbf{x}_s is the position of the source, and \mathbf{v} is the displacement velocity of the substrate that results from the cellular forces exerted on their surroundings. The velocity is computed by solving the balance of the momentum, which will be discussed in the Section 7.2.2.

Initially, we assume there is no signalling molecules over the computational domain, that is,

$$c(\mathbf{x}, 0) = 0, \text{ in } \Omega.$$

As a boundary condition, we use the following Robin condition

$$\frac{\partial c}{\partial \mathbf{n}} + \kappa_s c = 0, \text{ on } \partial\Omega, t > 0,$$

which deals with a balance between the diffusive flux across the boundary and the flux between the boundary and the region far away from the domain of computation. The

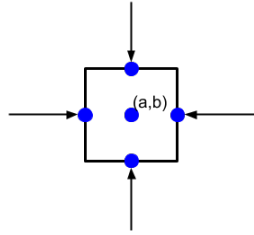


Figure 7.2: An example of pulling point forces, tractions applied by a cell, in which the cell membrane is split by four nodal points.

symbol κ_s , which is non-negative, represents the mass transfer coefficient. Note that as $\kappa_s \rightarrow 0$ then the Robin condition tends to a homogeneous Neumann condition, which represents no flux (hence isolation). Whereas as $\kappa_s \rightarrow \infty$ represents the case that $c \rightarrow 0$ on the boundary, which, physically, is reminiscent to having an infinite mass flow rate at the boundary into the surroundings. The Robin condition, also referred to as a mixing boundary condition, is able to deal with both these two limits and all cases between these limits.

7

7.2.2. PASSIVE CONVECTION OF SUBSTRATE

In wound healing, (myo)fibroblasts exert forces on their direct environment, i.e. extracellular matrix, which result into contraction of the tissue [2, 3, 6, 7]. For cancer cells, Massalha and Weihs [14] indicate that the metastatic cells exert traction forces ranged from $100 - 600 nN$ on the gel, of which the Young's modulus ranged from $2.2 - 10.9 kPa$. Furthermore, for stiffer substrates, the cancer cells remain rounded with changing area and they exert large traction forces with large magnitudes to its direct environment. Hence, the model includes passive convection of the substrate, which can provide a more realistic model in various applications.

As the cell membrane is broken into multiple line segments by nodal points, point forces are implemented here to depict the forces exerted by the cell, which are applied on the midpoint of each line segment; see Figure 7.2 as an example of a square-shape cell. Among different applications, the force direction may differ. For example, if the cell encounters an obstacle, a repulsive force will be exerted to resist the compression of the cell; in wound contraction, (myo)fibroblasts exert pulling forces on the extracellular matrix (ECM).

Morphoelasticity is widely used in the biological modelling to describe elastic growth, for instance, the growth of tumours [70], the seashell growth [71] and large contractions in wound healing [17, 72] etc. In wound healing, morphoelasticity describes the phenomena when the deformation of the skin is so large that the deformations are plastic. Conservation of momentum, combined with the evolution equation for the effective Eu-

lerian strain, results into the following modelling equations [17]:

$$\begin{cases} \rho \left[\frac{D\mathbf{v}}{Dt} + \mathbf{v}(\nabla \cdot \mathbf{v}) \right] - \nabla \cdot \boldsymbol{\sigma} = \mathbf{f}, \text{ in } \Omega, t > 0, \\ \frac{D\boldsymbol{\epsilon}}{Dt} + \boldsymbol{\epsilon} \text{skw}(\mathbf{L}) - \text{skw}(\mathbf{L})\boldsymbol{\epsilon} + [\text{tr}(\boldsymbol{\epsilon}) - 1] \text{sym}(\mathbf{L}) = -\alpha \boldsymbol{\epsilon}, \text{ in } \Omega, t > 0, \\ \mathbf{v}(\mathbf{x}, t) = \mathbf{0}, \text{ on } \partial\Omega, t > 0, \end{cases} \quad (7.2)$$

where ρ is the density of the extracellular matrix, $\mathbf{L} = \nabla \mathbf{v}$ and α is a non-negative constant. Note that if $\alpha = 0$, then as soon as the force $\mathbf{f} = \mathbf{0}$, then the tissue will gradually recover to its original shape and volume. Here, $\frac{D\mathbf{y}}{Dt} = \frac{\partial \mathbf{y}}{\partial t} + \mathbf{v} \nabla \cdot \mathbf{y}$ is material derivative where \mathbf{y} is any tensor field and \mathbf{v} is the migration velocity of any point within the domain of computation. In order to have a fixed boundary, we use a homogeneous Dirichlet boundary condition for the velocity. This condition implies that the the overall domain boundary Ω does not deform. Hence, the overall Ω is constant over time. However, due to the cellular traction forces, the tissue, and hence the computational domain, is subject to local deformations, which result into local strains and stresses. These deformations, indeed, give rise to local displacements within the domain of computation. Since the momentum balance equations are solved over the entire domain of computation, the local deformations, stresses and displacements are taken into account over the entire domain of computation. These local displacements induce the passive convection term $c(x, t)(\nabla \cdot \mathbf{v})$ in Eq (7.1). From a mechanical point of view, we treat the computational domain as a continuous linear isotropic domain. Further, as a result of the presence of liquid phases in the tissue, the mechanical balance is also subject to viscous, that is friction, effects. Therefore, we use Kelvin–Voigt’s viscoelastic dashpot model, of which the stress tensor reads as

$$\begin{aligned} \boldsymbol{\sigma} &= \boldsymbol{\sigma}_{elas} + \boldsymbol{\sigma}_{visco} \\ &= \frac{E}{1 + \nu_s} \{ \boldsymbol{\epsilon} + \text{tr}(\boldsymbol{\epsilon}) \left[\frac{\nu_s}{1 - 2\nu_s} \right] \mathbf{I} \} + \mu_1 \text{sym}(\mathbf{L}) + \mu_2 \text{tr}(\text{sym}(\mathbf{L})) \mathbf{I}, \end{aligned} \quad (7.3)$$

where ν_s is the Possion’s ratio of the substrate, $\boldsymbol{\epsilon}$ is the strain tensor, μ_1 and μ_2 are the shear and bulk viscosity respectively. The morphoelasticity model consists of a set of two non-linear partial differential equations, where both the velocity \mathbf{v} and strain tensor $\boldsymbol{\epsilon}$ are unknowns. The deformation of the domain is actually determined by the strain tensor. The displacement of the domain can be approximated by integrating the velocity over time: $\mathbf{u}(t) \approx \int_0^t \mathbf{v}(s) ds$, where the velocity is determined by Eq (7.2). The approximate solution is then known on the moving finite-element meshpoints. This is the discrete counterpart of the displacement. Further, we need the displacement (velocity) at the positions of the nodal points on the cell boundary. Since these positions do not coincide with the positions of the finite-element meshpoints, we need a mapping from the displacement velocity obtained at the finite-element meshpoints onto the, continuous, positions of the cell boundary nodes. This is obtained through interpolation procedures based on the Lagrangian finite-element framework. The obtained displacement velocities are substituted into the equation for the migration of the cell boundary nodes.

In the application of wound healing, (myo)fibroblasts are the cells pulling the ECM

and causing the contractions. The traction force \mathbf{f} of each (myo)fibroblast reads as

$$\mathbf{f}(\mathbf{x}; t) = \sum_{j=1}^N P(\mathbf{x}; t) \mathbf{n}(\mathbf{x}(t)) \delta(\mathbf{x}(t) - \mathbf{x}_j(t)) \Delta\Gamma^j, \mathbf{x} \in \Omega, t > 0, \quad (7.4)$$

where N is the number of nodal points on the cell membrane, $P(\mathbf{x}; t)$ is the magnitude of the force exerted by each (myo)fibroblast per unit length of the cell membrane. We have constructed the model such that local differences of the cellular traction force over the cell boundary can be incorporated. In the current study, however, we have assumed the cellular traction force to be constant over the entire cell boundary and for all the cells. Furthermore, $\mathbf{n}(\mathbf{x}(t))$ is the unit inward pointing normal vector (towards the cell centre) at $\mathbf{x}(t)$ (see Figure 7.2 as a schematic), $\mathbf{x}_j(t)$ is the midpoint of line segment j , and $\Delta\Gamma^j$ is the length of line segment j . Note that here \mathbf{x} refers to any position in Ω , hence possibly, but not necessarily on the cell boundary, or on the finite-element mesh points. The positions $\mathbf{x}_j(t)$ represent the positions of the nodal points on the cell boundary (hence not on the finite-element mesh), where the cellular traction force is exerted.

Further, we consider (myo)fibroblasts colliding with each other, then the cells exert repelling forces on the other one. Here, cells are not allowed to intersect each other; see Figure 7.3 as a schematic. Suppose for (myo)fibroblast i , there are $N_m^i = \{j_1^i, \dots, j_m^i\}$ line segments of cell membrane mechanically contacting with other (myo)fibroblasts. Then, on line segments $j \in N_m$, the (myo)fibroblast exert repelling force, while on the rest of the line segments, (myo)fibroblast releases pulling forces on the ECM. Hence, the traction force of the (myo)fibroblast i is given by

$$\begin{aligned} \mathbf{f}^i(\mathbf{x}; t) = & \sum_{j=1, j \notin N_m^i}^N P(\mathbf{x}, t) \mathbf{n}(\mathbf{x}(t)) \delta(\mathbf{x}(t) - \mathbf{x}_j^i(t)) \Delta\Gamma^{i,j} \\ & - \sum_{j \in N_m^i} Q(d(\mathbf{x}), t) \mathbf{n}(\mathbf{x}(t)) \delta(\mathbf{x}(t) - \mathbf{x}_j^i(t)) \Delta\Gamma^{i,j}, \end{aligned} \quad (7.5)$$

where l_m is the portion of the (myo)fibroblast membrane mechanically contacting with other cell, $Q(d(\mathbf{x}), t)$ is the force magnitude per length and $d(\mathbf{x})$ is the penetration depth. According to two-dimensional Hertz theory [94–96], for each elastic body, the explicit relation between the total force and the penetration depth is not clear. We assume the total force magnitude $\tilde{Q}(d(\mathbf{x}), t)$ is linearly proportional to the penetration depth $d(\mathbf{x})$:

$$\tilde{Q}(d(\mathbf{x}), t) = \frac{\pi}{4} d(\mathbf{x}) E^*, \quad (7.6)$$

where E^* is the total equivalent Young's modulus derived by

$$\frac{1}{E^*} = \frac{1 - \nu_1^2}{E_1} + \frac{1 - \nu_2^2}{E_2}.$$

Here, ν_i and E_i with $i \in \{1, 2\}$ represent the Poisson ratio and Young's modulus of two elastic bodies, respectively. In particular, if two bodies have the same elastic characteristics (i.e. $\nu_1 = \nu_2 = \nu$ and $E_1 = E_2 = E$), then

$$E^* = \frac{E}{2(1 - \nu^2)}.$$

We assume that the magnitudes of the repulsive force, which is exerted on the boundary segments of cell i that are in contact with another cell, are identical. In other words, $Q(d(\mathbf{x}), t)$ is given by

$$Q(d(\mathbf{x}), t) = \frac{\tilde{Q}(d(\mathbf{x}), t)}{\|l_m\|} = \frac{\pi}{4} d(\mathbf{x}) E^* / \|l_m\|, \quad (7.7)$$

where $\|l_m\|$ is the total length of the portion of the membrane of (myo)fibroblast i mechanically contacting with other (myo)fibroblast (i.e. the sum of the length of $\Delta\Gamma^{i,j}$, $j \in N_m^i$). Subsequently, the total traction force is $\mathbf{f} = \sum_{i=1}^{N_C} \mathbf{f}^i$, where N_C is the number of (myo)fibroblasts that are in contact with each other.

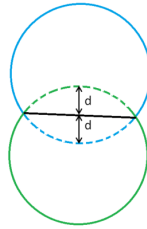


Figure 7.3: When cells collide with each other, they will deform and exert repulsive forces. The dashed curves show the equilibrium shape of cells, and the black curve is the overlapping membrane of both cells.

Another application is metastasis and invasion of cancer cell. Usually, in vitro, a microtube experiment is conducted [91]. To simplify the model, here we only consider one cancer cell going through a microtube; see Figure 7.4. Similar to the case when (myo)fibroblasts collide, we assume that $N_m = \{j_1, \dots, j_m\}$ is the line segments of cell membrane mechanically contacting with the wall of the microtube. Here, we will exclude the pulling force. In other words, the force released by the cancer cell is only the repelling force exerted on the wall of the microtube:

$$\mathbf{f}_m(\mathbf{x}; t) = - \sum_{j \in N_m} Q_m(d(\mathbf{x}), t) \mathbf{n}(\mathbf{x}(t)) \delta(\mathbf{x}(t) - \mathbf{x}_j(t)) \Delta\Gamma^j. \quad (7.8)$$

The magnitude of the force $Q_m(d(\mathbf{x}), t)$ here follows the same definition as in Eq (7.7), where $d(\mathbf{x})$ is the radius subtracting the distance from the cell membrane to the cell centre.

7.2.3. CELL DEFORMATION

According to [37, 90], the cell cytoskeleton is depicted as a collection of springs between the centre position of the cell and the nodal points on the cell membrane. Therefore, the equilibrium shape of the cell is kept by these springs, regardless of the original cell shape. In this chapter, we consider circular, elliptic and star-shape cells as two-dimensional projections. Combining chemotaxis (or mechanotaxis), passive convection and random

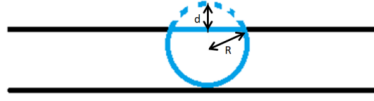


Figure 7.4: The cell is compressed by the wall of the microtube. To inhibit any changes from its equilibrium shape, it exerted the repelling force on the wall of the microtube, which is proportion to the compressed distance d .

walk, the displacement of the nodal point j on the cell membrane is given by

$$d\mathbf{x}_j = \beta(CSI(\Omega_C), A(\Omega_C)) \frac{\nabla c(\mathbf{x}, t)}{\|\nabla c(\mathbf{x}, t)\| + \gamma} dt + E_c(\mathbf{x}_c(t) + \hat{\mathbf{x}}_j - \mathbf{x}_j(t)) dt + \mathbf{v} dt + \sigma_{rw} d\mathbf{W}(t), \text{ in } \Omega_m \subset \Omega. \quad (7.9)$$

Here, Ω_C represents the cell region, Ω_m is the domain occupied by the microtube, E_c represents the cell elasticity; $\hat{\mathbf{x}} = \mathbf{x}_c(t) - \hat{\mathbf{x}}_j(t)$ is the vector connecting the equilibrium position of nodal point j on the cell membrane to the cell centre, \mathbf{x}_c is the central position of the cell and $\hat{\mathbf{x}}_j$ represents the equilibrium position of the nodal point j corresponding to the cell centre \mathbf{x}_c (see Figure 7.1); γ is a small positive constant to prevent the denominator being zero; \mathbf{v} is the velocity of the substrate determined by Eq (7.2); σ_{rw} is the portion of random walk, and $d\mathbf{W}(t)$ is a vector-Wiener process, which accounts for random walk. Furthermore, $\beta = \beta(CSI(\Omega_C), A(\Omega_C))$ is the weight of chemotaxis (or mechanotaxis), where we define the Cell Shape Index (CSI) of cell Ω_C by

$$CSI(\Omega_C) = \frac{4\pi A(\Omega_C)}{l^2(\partial\Omega_C)},$$

where $A(\Omega_C)$ is the cell area, $l(\partial\Omega_C)$ is the circumference of the cell membrane. According to [13], reduction of cell area and deformation of cell shape reduce the mobility of cell. For simplicity, we propose a linear relation here:

$$\beta(CSI(\Omega_C), A(\Omega_C)) = \beta_0 \times \mu_m \times (CSI(\Omega_C)/CSI_0(\Omega_C) + A(\Omega_C)/A_0(\Omega_C))/2,$$

where β_0 is the maximal response from the cell to the signal, μ_m is the mobility reduction coefficient, and $CSI_0(\Omega_C)$ and $A_0(\Omega_C)$ represent the CSI and volume of the equilibrium cell.

In order to maintain the right orientation of the cell, we introduce a matrix after rotation of an angle ϕ , as in [90]:

$$\mathbf{B}(\phi) = \begin{pmatrix} \cos(\phi) & -\sin(\phi) \\ \sin(\phi) & \cos(\phi) \end{pmatrix}, \quad (7.10)$$

such that ϕ can be computed from

$$\tilde{\phi} = \arg \min_{\phi \in [0, 2\pi)} \left(\sum_{i=1}^N \|\mathbf{B}(\phi) \tilde{\mathbf{x}}_i(t) - \mathbf{x}_i(t)\|^2 \right). \quad (7.11)$$

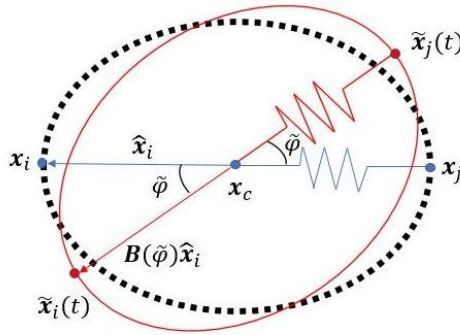


Figure 7.5: The orientation of the cell is taken into account, which is maintained by the rotation matrix which is quantified in Eq (7.10). The dashed ellipse represents the initial position of the cell and the red solid ellipse is the newly oriented cell.

The orientation of the cell is important in the context of how the cell has rotated from its initial position. The orientation of the cell is represented by the angle of the vector connecting the ‘front and tail’ of the cell; see Fig 7.5 as a schematic. The overall displacement of the nodes of the cell boundary are determined by translation and rotation. The matrix $\mathbf{B}(\phi)$ monitors the angle of rotation of the cell with respect to the cell position (and hence boundary nodes) at the previous time step. This orientation, and hence the angle of rotation is important for the determination of the equilibrium points of the cell boundary nodes. The equilibrium points reflect the position to which the cell boundary nodes will converge to if the cell does not move (that is the chemical signal is set to zero), and if the extracellular matrix is not subject to displacement velocities. If this orientation, that is the angle, would not be incorporated, then the cell will always return to its initial orientation.

Hence, the displacement of nodal point j is adapted to

$$\begin{aligned} d\mathbf{x}_j = & \beta(CSI(\Omega_C), A(\Omega_C)) \frac{\nabla c(\mathbf{x}, t)}{\|\nabla c(\mathbf{x}, t)\| + \gamma} dt \\ & + E_c(\mathbf{x}_c(t) + \mathbf{B}(\tilde{\phi})\hat{\mathbf{x}}_j - \mathbf{x}_j(t))dt + \mathbf{v}dt + \sigma_{rw}d\mathbf{W}(t). \end{aligned} \quad (7.12)$$

If there is an obstacle encountered by the cell, adjusting the displacement is necessary. Denote $\partial\Omega_{ob}$ as the boundary of the obstacle, which is possibly another cell or the wall of the microtube. For the nodal point colliding the obstacle, it cannot pass over the boundary of the obstacle. Hence, for the displacement of nodal point j , the normal direction of the boundary of the obstacle in $d\mathbf{x}_j(t)$ is vanished. To rephrase it, we adjust the displacement of the nodal point if it collides with the obstacle (see Figure 7.6) by

$$d\mathbf{x}_j(t) \leftarrow d\mathbf{x}_j(t) - (d\mathbf{x}_j(t), \mathbf{n}_{ob}(\mathbf{x}_j(t)))\mathbf{n}_{ob}(\mathbf{x}_j(t)), \text{ if } \mathbf{x}_j(t) \in \partial\Omega_{ob}, \quad (7.13)$$

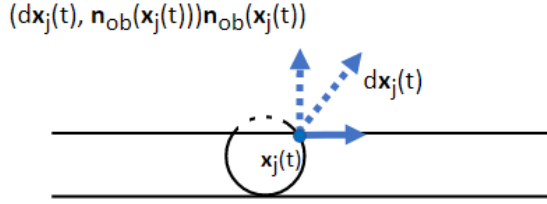


Figure 7.6: A schematic to show that the adjustment of the displacement of the nodal point on the cell membrane, when the nodal point contacts the wall of the microtube.

where $\mathbf{n}_{ob}(\mathbf{x})$ is unit pointing normal vector (outward the cell centre).

Furthermore, if a cell tries to go through a microtube, which mimic the cancer cell metastasis and invasion, not only the direction of the cell migration is limited (since the cell cannot pass over the microtube), but also the microtube will slow down the velocity of the cell as a result of friction. Note that the magnitude of the friction is proportional to the repelling force. In our model, we simply distract part of the velocity in the tangential direction of the obstacle. Hence, the displacement of the nodal point which collides the wall of the microtube is given by

$$d\mathbf{x}_j(t) \leftarrow d\mathbf{x}_j(t) - \mu_f \|\mathbf{f}(\mathbf{x}_j(t))\| \times (d\mathbf{x}_j(t), \boldsymbol{\tau}_{ob}(\mathbf{x}_j(t))) \boldsymbol{\tau}_{ob}(\mathbf{x}_j(t)), \text{ if } \mathbf{x}_j(t) \in \partial\Omega_{ob}, \quad (7.14)$$

where μ_f is the cell friction coefficient, $\mathbf{f}(\mathbf{x}_j(t))$ is the repelling force exerted by the cell and $\boldsymbol{\tau}_{ob}(\mathbf{x})$ is the tangential direction of the obstacle boundary $\partial\Omega_{ob}$.

This model provides a simple computational framework to describe the dynamics of the cell shape under multiple circumstances. However, the model does not describe the Poisson effect of the cell if the cell is compressed, since the model mainly considers the extracellular environment. Hence, in this chapter, the cell length will not be investigated.

7.3. APPLICATIONS AND NUMERICAL RESULTS

We exhibit several possible applications in this section, namely, cells migrating as a result of chemotactic signals, cells differentiating to another phenotype, cells repelling each other and one cell migrating through a microtube. Some parameters are the same in every application. If there is no specification, the parameter values are shown in Table 7.1. Note that parameter values are partially determined by experimental data from the references and partially estimated in this study, as they are indicated in all parameter tables. We try to use the clinical/experimental data from the literature as much as possible, however, some parameter values are unknown. Hence, to estimate these unknown parameter values, we determined the value by reproducing the experiment as much as possible.

In particular, to validate and calibrate the model, we tried to reproduce the key results in [91] like the probability of the occurrence of Phase 3 and the time interval of each phase. We ran four different Monte Carlo simulations to calibrate the model and to see

the impact of different settings of the model.

Table 7.1: Parameter values used in all the applications

Parameter	Description	Value	Units	Source
E_s	Substrate elasticity	100	$kg/(\mu m \cdot min^2)$	[65]
E_c	Cell elasticity	5	$kg/(\mu m \cdot min^2)$	[44]
μ_f	Cell friction coefficient	0.03	–	[97]
ν_s	Poisson's ratio of the ECM	0.49	–	[17]
ν_c	Poisson's ratio of (myo)fibroblast and cancer cell	0.32	–	[98]
k	Secrete rate of the signal	2.5	$kg/(\mu m^3 \cdot min)$	[1]
κ_s	Parameter in Robin's boundary condition to solve Eq (7.1)	100	μm^{-1}	[1]
μ_1	Shear viscosity of the ECM	33.783	$kg/(\mu m \cdot min)$	[1]
μ_2	Bulk viscosity of the ECM	22.523	$kg/(\mu m \cdot min)$	[1]
β_0	Maximal mobility of points on cell membrane	10	min^{-1}	Estimated in this study
N	Number of nodal points on the cell membrane	40	–	Estimated in this study
μ_m	The coefficient of cell mobility reduction	1	–	Estimated in this study
σ_{rw}	Weight of random walk	1	–	Estimated in this study
α	Degree of permanent deformation in Eq (7.2)	0.1	min^{-1}	Estimated in this study

7.3.1. FINITE-ELEMENT METHODS

In this chapter, all boundary value problems are solved by the finite-element methods with Lagrange linear basis functions. Regarding the time-integration, we use a backward Euler method. From the theory, it is known that smooth solutions would be subject to errors of the order $\mathcal{O}(h^2)$ and $\mathcal{O}(\Delta t)$ in the L^2 norm of the numeric error.

Here, we solved the boundary value problem in Eq (7.2) with the traction forces expressed in Eq (7.4). For the sake of investigating the convergence of the finite-element method, the parameters are dimensionless. We consider one large non-moving cell in the computational domain (see Figure 7.7), of which the membrane is divided into finite line segments, and there is a traction force applied on the midpoint of each line segment as in Eq (7.4). With the refinement of the mesh, the convergence rate of L^2 -norm of the solution to Eq (7.2) (i.e. the velocity) is computed, which is 1.899828112 that is close to the theoretical value 2.

7.3.2. CELLS MOVING TOWARDS THE POINT SOURCE

The basic application is that cell migrates towards the concentration gradient of a signalling molecule, which can be oxygen, growth factors or virus. The displacement is mainly determined by the gradient of the concentration of the signal. Subsequently, the closest part of the cell to the emitting source will develop a "nose"; see Figure 7.8. All parameter values have been documented in Tables 7.1 and 7.2. The 'nose' behaviour

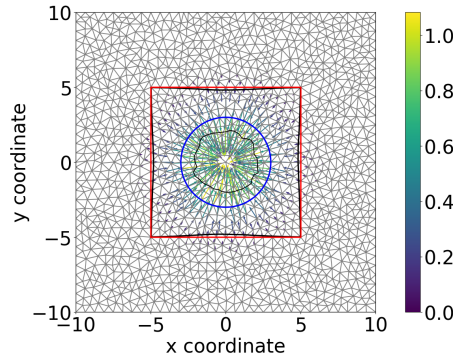


Figure 7.7: The plot shows the solution Eq (7.2), as an example to investigate the convergence of the finite-element methods. Blue curve represents the initial cell membrane, and red curve represents the original subdomain boundary. Black curves show the deformed shape of the cell and the subdomain.

(or so-called a triangular tailed shape) has also been observed in biological experiments, which is due to the locations of the adhesion sites over the cell membrane [10]. In the simulation we accommodate for the engulfment of the chemical source by switching off the chemical signal once the cell physically contacts it. Once this signal has been switched off, the concentration gradient flattens as a result of diffusion processes and therewith the cell recesses back to its equilibrium (original) shape and volume. At that moment, the cell geometry is no longer determined by chemotaxis.

From $t = 0$, the cells are attracted towards the centre of the computational domain, which is the location of the source of signalling molecules. Due to the difference of the gradient of the concentration of the signal over the domain, cells are deformed into a droplet shape, where the "nose" points in the direction of the point source. As the diffusion of the signal proceeds, the "nose" gradually disappears and cells recover to the equilibrium shape. To evaluate the cell geometry quantitatively, we provide the evolution of the CSI and cell area as a function of time in Figure 7.9. These quantities are of interest from a clinical point of view [13]. Resulting from the displacement of the direct environment, the volume of the cell decreases. The permanent volume changes of the cell are imposed by the permanent displacements from the morphoelastic model. Furthermore, the cells are tethered within a rigid deformed structure, hence, it makes cells deform as well. We note that cells have already recovered to the original shape but not the volume. It can be implied that a stiffer cell deforms less compared to a softer one.

7.3.3. DIFFERENTIATION OF CELLS

Cell differentiation is a process of a cell changing from one phenotype to another one, for example, a stem cell differentiates into various phenotypes, like blood cells and nerve cells etc. In this chapter, we mainly focus on the cellular differentiation in wound healing. In the proliferative phase of wound healing, some regular fibroblasts (which are spindle-shaped [99, 100]) differentiate into myofibroblasts (which are dendritic-shaped [101, 102]), which pull the skin ever harder and cause the permanent contractions. It

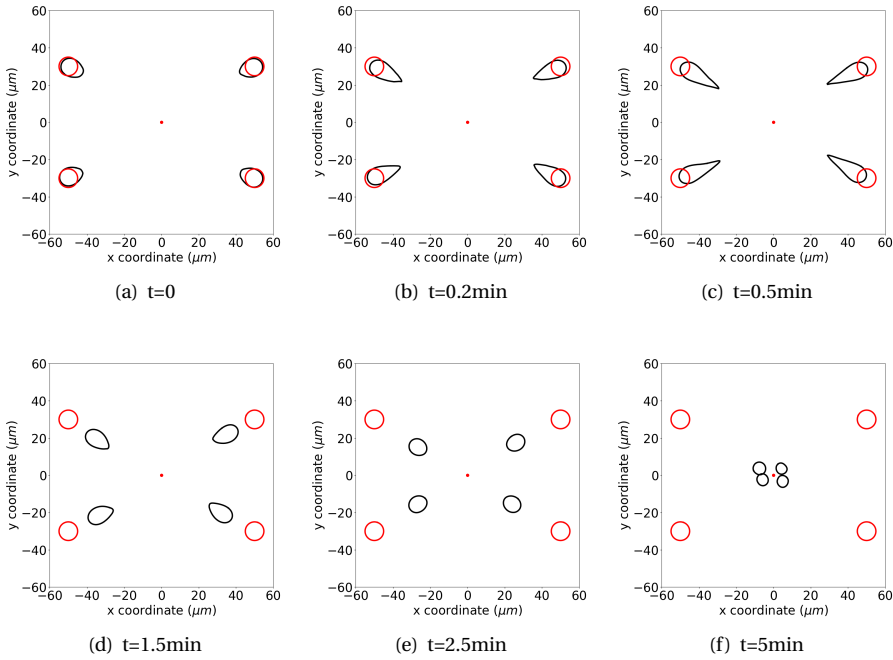


Figure 7.8: The figure shows the positions of cells at consecutive times. The red circles show the original shape and position of cells, and the red dots in the centre is the point source of a generic signal.

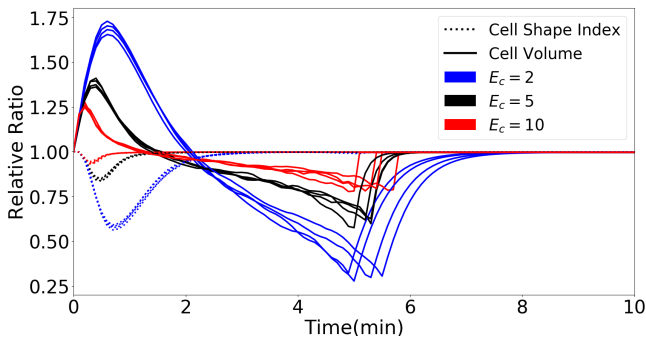


Figure 7.9: The cell shape index and relative ratio of cell area of all cells in Figure 7.8 are shown in the plot. The solid curves represent the cell area, and the dashed curves are the cell shape index. Different colours of curves indicate different stiffness of the cells.

Table 7.2: Parameter values estimated in the application of cell migrating toward the signal source

Parameter	Description	Value	Units
R	Cell radius	5	μm
Δt	Time step	0.1	min
D	Diffusion rate of the signal	200	$\mu m^2 / min$
x_0	Length of computational domain in x-coordinate	120	μm
y_0	Length of computational domain in y-coordinate	120	μm
x_w	Length of the subdomain in the centre of computational domain in x-coordinate	40	μm
y_w	Length of the subdomain in the centre of computational domain in y-coordinate	40	μm

is commonly recognized that high concentration of TGF-beta induces the fibroblast-to-myofibroblast differentiation [3, 13, 102]. In this section, since we mainly want to present a model of differentiation, only differentiation from fibroblasts to myofibroblasts is exhibited as an example: the signal is TGF-beta and initially, there are four regular fibroblasts in unwounded region, which are simulated by ellipses.

We assume that the two phenotypes of cells have the same volume if they are in the equilibrium status. Here, for ellipse and hypocycloid, there are two parameters to determine each shape: long (denoted by a_e) and short axis's (denoted by b_e) determine the ellipse; the radius of basis circle (de noted by a_h) and rotating circle (denoted by b_h) determine the hypocycloid. Note that the hypocycloid-shaped cell may not be realistic, and it is mainly to show that the model is capable to model the differentiation of cells, in which mostly the cellular skeleton and geometry are altered. To develop a smooth differentiation process, we introduce a function such that each parameter changes over time:

$$\begin{cases} R_a(\omega) = a_h\omega + a_e(1 - \omega), \\ R_b(\omega) = b_h\omega + b_e(1 - \omega), \end{cases} \quad (7.15)$$

where $R_a(\omega)$ and $R_b(\omega)$ represent two parameters to determine the shape, and $\omega = 1 - \exp\{-\lambda_\omega(t - t_\omega)\}$. Here, λ_ω is the parameter of the exponential distribution and t_ω is the time point when the fibroblast starts differentiating.

Figure 7.10 presents the cells positions at different time. In this chapter, we only consider a phenomenological modelling formulation in the sense that the cell differentiates if it is exposed to concentrations of signalling molecule that exceed a given threshold. The shape evolution is determined by the parameters in Eq (7.15).

As regular fibroblasts approach to the region with high concentration of TGF-beta, some of them start differentiating into myofibroblasts gradually. Subsequently, they exert larger forces on the ECM and contractions are developed in the wound, which is marked with red curves as a subdomain. The parameter values of the simulations are from Table 7.1 and Table 7.3.

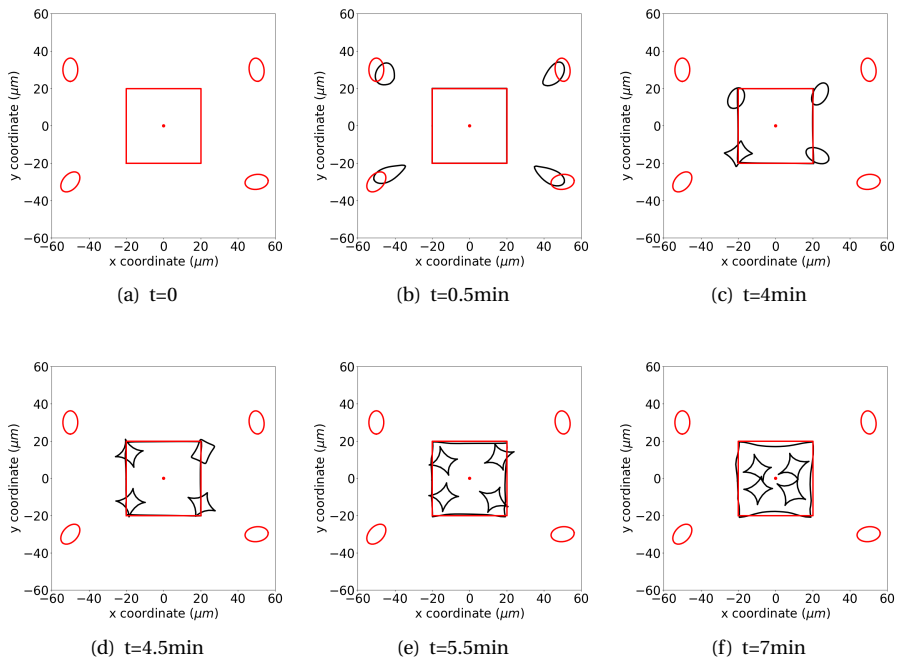


Figure 7.10: The figure shows the positions of cells at consecutive times by the black curves. The red circles show the original shape and position of cells, and the red dots in the centre is the point source of TGF-beta which triggers the differentiation from regular fibroblasts to myofibroblasts.

Table 7.3: Parameter values estimated in the application of cell differentiation

Parameter	Description	Value	Units
a_e	Length of long axis in elliptic cell	6.25	μm
b_e	Length of short axis in elliptic cell	4	μm
a_h	Radius of the basis circle to draw hypocycloid-shape cell	$20/\sqrt{6}$	μm
b_h	Radius of the rotating circle to draw hypocycloid-shape cell	$5/\sqrt{6}$	μm
λ_ω	Parameter in the exponential distribution to compute ω	10	–
Δt	Time step	0.1	min
D	Diffusion rate of the signal	233.2	$\mu m^2/min$
x_0	Length of computational domain in x-coordinate	120	μm
y_0	Length of computational domain in y-coordinate	120	μm
x_w	Length of the subdomain in the centre of computational domain in x-coordinate	40	μm
y_w	Length of the subdomain in the centre of computational domain in y-coordinate	40	μm

7.3.4. REPULSION BETWEEN TWO COLLIDING CELLS

Cells will deform when they encounter each other or an obstacle. On the contacting surface, cells will exert a repelling force (as it is shown in Eq (7.7)) to recover to its equilibrium shape. We consider two cells colliding with each other and adjust the displacement of nodal points on the cell membrane by Eq (7.13). Here, cells are not allowed to intersect with each other. Hence, initially, cells are located with a small distance between each other. In Figure 7.11, we present the cell positions at different times, and cells deform due to mechanical contact (hard impingement). The parameter values are from Table 7.1 and Table 7.2.

7.3.5. CELL MOVING THROUGH A MICROTUBE

Metastasis is a difficult phenomenon to study due to its large variation in spatiotemporal scales. Hence, studying the mechanics of one single cell is essential since the individual cell needs to break out from the tumour and invade through the ECM. To achieve that, Mak *et al.* [91] developed an active microfluidic system with several features to mimic the metastasis and invasion of the cancer cell. In this section, we will use our model to reproduce results of the experiment in [91].

Mak *et al.* [91] introduced a device and procedure to investigate mechanical transition effects of invading cancer cells. They constructed a set up with periodic microfluidic channels with various lengths and widths. This set up consists of a repeated pattern of large channel (LC) and subnuclear barriers (SNB). Mak *et al.* [91] let cancer cells load at the reservoir. Subsequently, cells move simultaneously through the microtubes and data regarding the velocity and cell length are collected.

SIMULATION SETTINGS

Following the settings in the experiment, we define a microtube with a varying width: a $15\mu m$ larger channel (LC) and $3.3\mu m$ subnucleus barriers with length $10\mu m$ (SNB10). Since the main reason for the active migration of the cell is not evident in [91], we keep

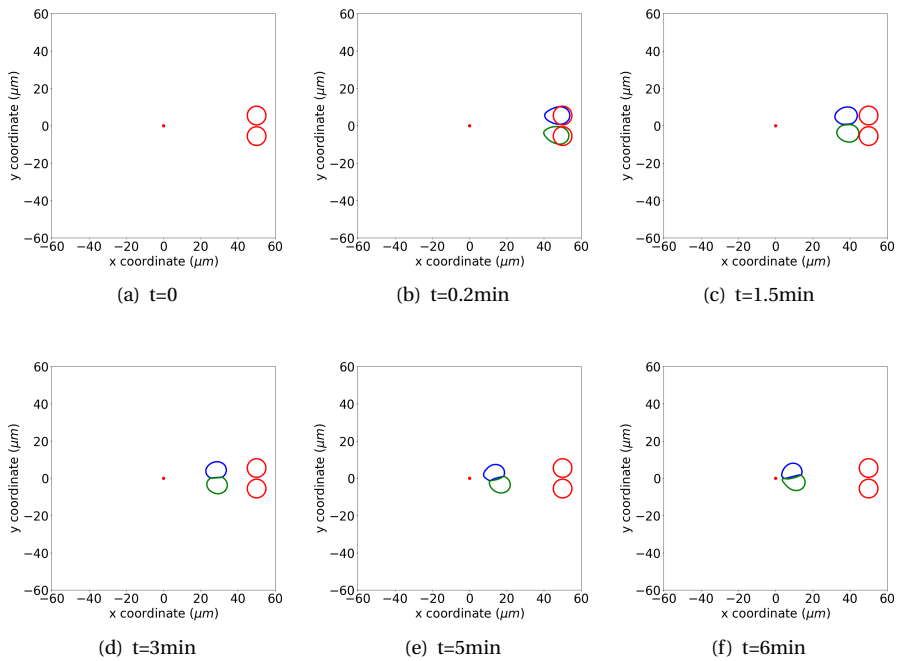


Figure 7.11: The figure shows the positions of cells in blue and green at consecutive times when two cells collide. The red circles show the original shape and position of cells, and the red dots in the centre is the point source of a signal.

on using random walk, with either chemotaxis or fixed velocity of the cell. Rather than having a periodic setting of subnucleus barriers (SNBs), we have one SNB in the middle connected with two LCs and run the simulations respectively. In this chapter, we only run the simulations regarding SNB10 in [91].

We consider the reduction of the cell mobility caused by cell shape and cell area [13], which is explained in Eq (7.12), the repelling forces exerted by the cell on the obstacles in Eq (7.13) and the friction between the cell and the wall of the microtube in Eq (7.14).

The position and shape of the cell are shown in Figure 7.12, which indicates how the cell migrates through the microtube. Since the repelling force on the wall of the microtube is included, we investigate the results regarding the cell velocity, pressure and the cell shape index over time; see Figure 7.13. The parameter values are taken from Table 7.1 and 7.4.

Table 7.4: Parameter values used in the application of cell going through a microtube

Parameter	Description	Value	Units	Source
R	Cell radius	9	μm	[91]
Δt	Time step	0.07	min	Estimated in this study
D	Diffusion rate of the signal	874.5	$\mu m^2/min$	Estimated in this study
x_0	Length of computational domain containing SNB10 in x-coordinate	400	μm	Estimated in this study
y_0	Length of computational domain containing SNB10 in y-coordinate	400	μm	Estimated in this study

7

Initially, there is a short distance before the cell enters the microtube, here the cell encounters no distraction. Therefore, the the cell travels at maximal speed and the cell is not compressed in the beginning. Next to this, the gradient of the signal results into the 'nose' behaviour and hence, the cell shape index changed. As the cell enters the wider part of the microtube, it slows down due to friction, and the cell is compressed, therefore, the cell starts exerting pushing forces on the wall of the tube. In the LC part, the cell shape index stays stable around 0.95. Further, the cell approaches the SNB, which is much more narrow than the LC, the cell suffered more from the friction and the compression from the microtube. As a consequence, the minimal cell velocity, the cell shape index and the maximal pressure is recorded when the cell is in the SNB. After that, cell moves further towards the signal source through the LC again. Hence, the cell velocity and cell shape index increase again, while the cell pressure reduces. According to [97] and [103], we manage to keep the cell velocity and pressure in a reasonable range: $6 - 20 \mu m/min$ and the maximal pressure that a cell can handle is around $12 kPa$.

Monte Carlo Simulations

In [91], the displacement of the cell is categorised as four phases:

- Phase 1: the cell enters the microtube via the LC, and slows down in particular when it is approaching the SNB;
- Phase 2: the cell is compressed strongly to enter the SNB;

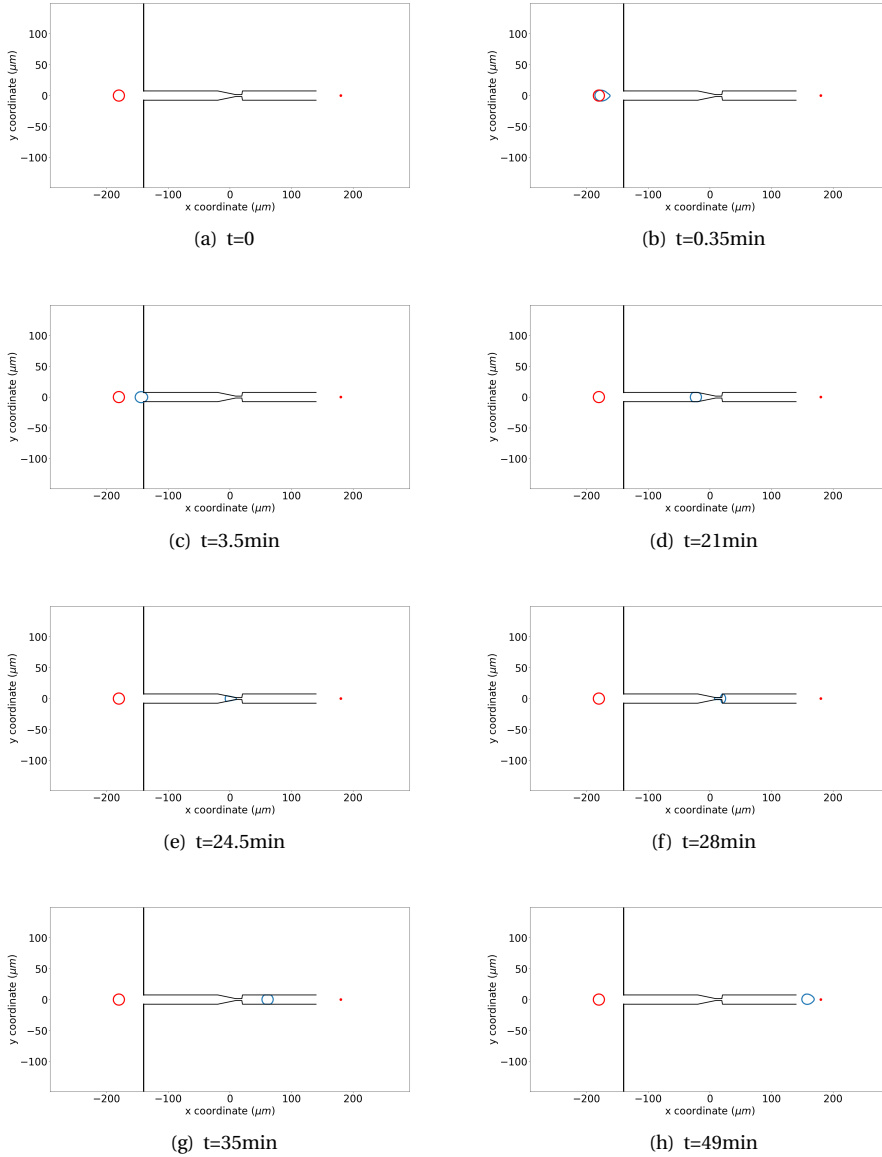
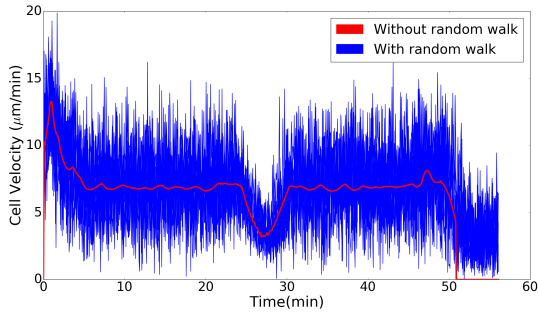
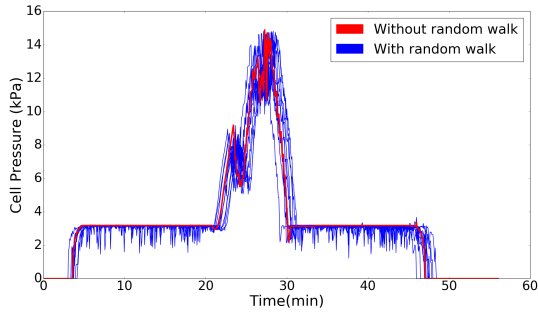


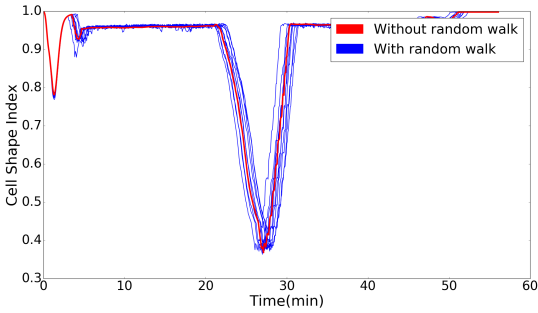
Figure 7.12: The figure shows the positions and shapes of cells at consecutive times by the blue contours when it travels through a microtubule. The red circles show the original shape and position of cells, and the red dots in the end of the microtubule is the point source of a signal.



(a) Cell Velocity



(b) Cell Pressure



(c) Cell Shape Index

Figure 7.13: The cell velocity, pressure and shape index over time when the cell migrates through the micro-tube, where there is a $10\mu\text{m}$ subnucleus barrier. The simulation mimics the experiment in [91].

- Phase 3: the cell fails to migrate monotonically forward when it is in the SNB;
- Phase 4: the cell enters the LC again and continues to migrate monotonically.

Hence, in the simulations, we try to collect the data and distinguish these different phases. Different from [91] that the microtube is designed periodically (such that the sample can be collected multiple times with one individual cell), one cell is supposed to go through one set of the microtube in each simulation. To reproduce the experimental results, Monte Carlo simulations are conducted to estimate the probability of the occurrence of phase 3 and the time costs for each phase, with different aforementioned reasons of active migration. The input values for the Monte Carlo simulations are shown in Table 7.5. In our simulation, we determine phase 3 when the cell stops moving monotonically forward when it is in the SNB until it leaves the SNB completely and reenters the LC.

Table 7.5: Parameter values used in the application of cell going through a microtube

Parameter	Description	Distribution	Source
μ_f	Friction coefficient for the cell going through the microtube	$U(0.03, 0.06)$	[97]
μ_m	The coefficient of cell mobility reduction	$U(0.6, 1)$	Estimated in this study

We run the simulations with four assumptions of the main mechanism provoking the active cell displacement: chemotaxis, fixed velocity with $10\mu m/min$, velocity generated from $(6, 15)\mu m/min$ and $(6, 20)\mu m/min$ in horizontal direction according to [103]. The number of samples and the Monte Carlo error of the occurrence of phase 3 collected from the Monte Carlo simulations of each aforementioned category are displayed in Table 7.6. Figure 7.14 illustrates the probability of the occurrence of phase 3, which is the stage when the cell stops monotonic forward migration. The mechanism that makes the cell move forward is not clear in [91], hence this could be reason for a mismatch between the experimental and simulated results. However, the results are significantly close regarding the probability of the occurrence of phase 3. Coincidentally, according to our current simulations, with either chemotaxis or velocity $10\mu m/min$, the probability of the occurrence of phase 3 is the same in the first 3 digits.

Table 7.6: Monte Carlo simulations of various models, in which the main mechanisms of cell active displacement differ

	Mechanism of Cell Active Displacement	Number of Samples from Monte Carlo Simulations	Monte Carlo Error of the Occurrence of Phase 3
Simulation 1	Chemotaxis	1400	9.2171×10^{-3}
Simulation 2	Fixed velocity $v = 10$	1390	9.7022×10^{-3}
Simulation 3	Fixed velocity $v \in (6, 15)$	1360	1.2102×10^{-2}
Simulation 4	Fixed velocity $v \in (6, 20)$	1378	1.0621×10^{-2}

Furthermore, the time cost of each phase is recorded and shown in Figure 7.15. The results with different modelling settings or simulations do not show many differences,

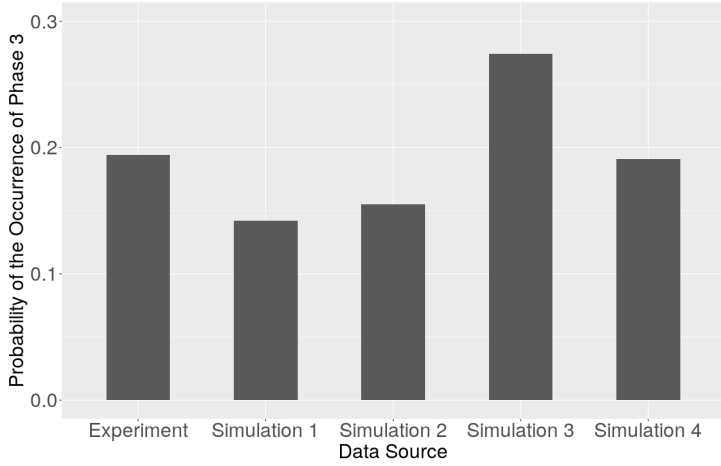


Figure 7.14: The probability of the occurrence phase 3 in [91] and from Monte Carlo simulations by implementing different mechanisms of cell active displacement (see Table 7.6 for more information). The parameter values are taken from Table 7.5.

7

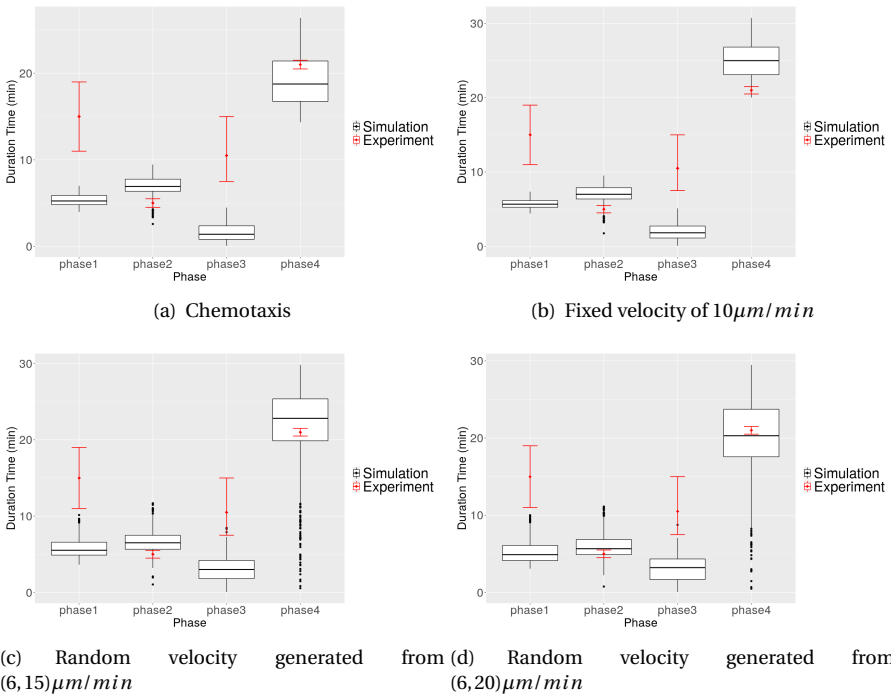


Figure 7.15: The figure shows the time costs of each phase in [91] and from Monte Carlo simulations by using the model. Red dots with the error bar represent the experimental data from [91] and the box plots are the data collected from the simulations.

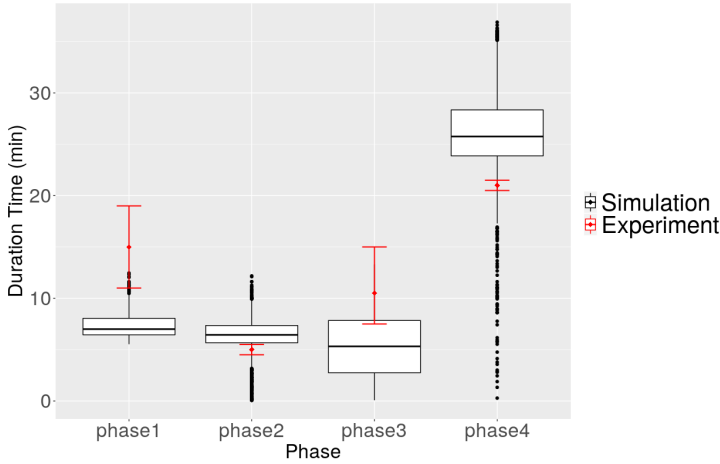


Figure 7.16: The time cost of each phase from the Monte Carlo simulation, in which the cell stiffness is $E_c = 1$ and the cell velocity is randomly generated from $(6, 20)$. Red dots with error bar represent the experimental data from [91] and the box plots are the data collected from the simulation.

in particular between chemotaxis and fixed velocity $v = 10$. The reason is that the microtubule restricts the displacement of the cell in the vertical direction, therefore, the cell mainly migrates in the horizontal direction. In general, the results between any simulation and the experiment differ more, compared with the results of the occurrence of phase 3, in particular, phase 1 and phase 3. Therefore, to investigate the possible reasons of mismatching results in phase 1 and phase 3 in phase time, we reran the simulation with the same settings as Simulation 4 in Table 7.6, except for the cell stiffness modified to $E_c = 1$. The results are shown in Figure 7.16. With a softer cell, the simulation data in phase 3 match better with the experimental data. However, now a discrepancy between simulation and experiments results in phase 4 instead.

There are several possible reasons causing the discrepancy in the time interval of each phase. Firstly, for phase 3, we only obtain valid data when the cell moves non-monotonically, which results in a reduction of the sample size of the simulation data. Apparently the cell ‘dwells’ and ‘doubts’ whether it ‘wants’ to keep on going if its pathway is (partially) obstructed. Secondly, the length of LC is not stated clearly in [91], therefore, we could only estimate that from the scale in the figures. Thirdly, it is not clear if the velocity of active migration of the cell is constant, while in our simulation, the velocity can change over time, depending on the gradient of the chemotactic signal. Despite all these uncertainties, we still managed to reproduce the results which are close to the experimental results. Fourthly, the transaction of each phase from [91] to our simulations may cause a mismatch of the duration time of each phase. Fifthly, it has been observed in [104] that after the first time moving through the narrow channel, cells deform easier to move faster through the following narrow channels, which may indicate that the cell characteristics change regarding its geometry.

7.4. CONCLUSIONS

A phenomenological model for cell shape evolution and migration has been developed, with primary focus on the mechanics of the extracellular environment. Furthermore, the impact of passive convection, due to local displacements within the extracellular matrix, on the evolution of the cell shape has been taken into account. A morphoelastic model has been used in the current study to incorporate permanent deformations of the extracellular tissue. The model can be applied to mimic several microscopic biological observations such as cell deformation and migration during wound contraction and cancer metastasis. To validate the model, the experimental setup in [91] has been modeled. This experiment entailed cell migration through microtubes with different widths and with a varying width over the length. The model is able to reproduce the most important trends that were observed in the experimental data despite some experimental uncertainties such as the determination of which phase a cell is in during the transmigration process. Furthermore, the current model provides a basis that can be expanded to describe more experimentally observed phenomena in cell geometry.

8

CONCLUSIONS AND DISCUSSIONS

8.1. GENERAL CONCLUSIONS

In this thesis, the research has been categorised as three connected parts: an agent-based model on wound contraction, consistency analysis of various approaches for the transition between agent-based and continuum-based models, and a cell-based model on the evolution of cell geometry. Mathematical modelling is an important and necessary tool to help us have better insights into biological phenomena. Since there are many biological processes taking place in *in vitro* and *in vivo* experiments, mathematical modelling can help to quantitatively understand complex biological processes in skin and tissue, and hence help clinicians to optimize and improve therapies. In addition, the value of many input parameters are unknown because of lack of data or because of patient-specific variations. By linking the outcomes of mathematical models to (clinical) experiments, one can estimate some of the input parameters. Despite the potential to use the mathematical models as a predictive tool for clinical scenarios, still a significant amount of uncertainty remains due to the patient-specific nature of many of the input parameters. For this reason, it is necessary to investigate the impact of parameter variation of the models. This parameter variation is done by means of a Bayesian parameter sensitivity analysis.

Therefore, this thesis treats our insights in mathematical modelling on various biological phenomena, in particular, scar contraction and cell geometry evolution. Furthermore, we developed multiple approaches to improve the accuracy of the numerical approximations if the Dirac Delta distributions are utilized to accommodate for the difference between the cell size and size of domain of computation. Conclusions on each part of this theses will be listed in subsequent subsections.

8.2. CONCLUSIONS ON PART I

Some agent-based models for the contraction of scars have been described in this part of the thesis. The agent-based models consist of initial-boundary value problems for the mechanical balance and material balances. Mechanical balances mimic the defor-

mation of tissue as a result of pulling forces that are exerted by (myo)fibroblasts. Mass balances mimic the level of growth factors over the tissue. These equations are coupled nonlinearly and the force and source terms are characterized by Dirac Delta distributions. These Dirac distributions are used to account for the huge difference in order of magnitude of the tissue domain and the size of the multiple cells. In Chapter 2, a qualitative model validation is presented on the basis of literature and educated guesses. Furthermore, a Bayesian sensitivity analysis using Monte Carlo simulation techniques is carried out to estimate the probability that particular scenarios regarding scar contraction take place. The results from the sensitivity analysis are beneficial to further optimization of therapy.

In the sensitivity analysis in Chapter 2, we observed that a stronger immune system will result into an "immune cells barrier" preventing fibroblasts entering the wound. Provided that there is no difference in cell size regardless of the cell phenotype, one can reduce the barrier by altering the size of the immune cells and/or increase the death rate of the immune cells. Furthermore, as cells are in a fixed circular shape, it may improve the model further by modifying the equilibrium shape of various phenotype of cells. This effect may be caused by the fact that the considered scar region is extending over micrometers only, which is relatively small, hence causing a very high cell number density. It is questionable whether this "immune cells barrier" is biologically sound.

In Chapter 2, the permanent deformations (plasticity) of the extracellular matrix have been simulated using a phenomenological model. In Chapter 3, this phenomenological model for the extracellular matrix was replaced with a morphoelastic formulation. The latter formulation describes the underlying physics more accurately, however, its implementation is more complicated. It has turned out that the solution of the resulting partial differential equations in case of morphoelasticity take more CPU time than the phenomenological approach. However, since the cell-based computations predominantly determine the overall computation time, the eventual net difference in CPU time is not significant. The numerical results show that both models can simulate the deformation of the ECM taking place during the scar contraction. With proper selection of parameter values, two approaches are numerically—at least qualitatively—consistent. However, the two models differ in the prediction of the correlation between the degree of scar contraction and the density of collagen.

8.3. CONCLUSIONS ON PART II

The agent-based models, based on Dirac Delta distributions, are used extensively in Part I of this thesis and in various studies in literature. These Dirac distributions simulate point sources in order to accommodate for the large difference in scales between cells and computational domain. The disadvantage of the use of Dirac distributions is that they cause singularities, at those points where they are acting, of the solution. Solutions will not exist in the finite element spaces that we employ. This problem arises in problems with higher dimensionality for both mass- and momentum balance equations. The advantage of this approach is that the cell-based method involves relatively easy-to-measure parameters. For this reason, several alternative formulations have been developed and compared to approaches with Dirac distributions. These alternative approaches are based on regularization of the Dirac distributions, as well as on more continuum-

based approaches.

The final objective is to link the agent-based models to continuum-based models through upscaling arguments. For this reason, several transitional models, such as the 'smoothed particle approach', that are merely hybrid versions between full continuum-based and agent-based models have been introduced. The transition between these various approaches has been analyzed mathematically as well as computationally. In Chapter 6, consistency between some of these approaches has been demonstrated.

8.4. CONCLUSIONS ON PART III

If one models the biological phenomena in the cellular scale, one should be aware that the cell shape can have a significant impact on cellular events. In Part III, we developed a phenomenological model that is able to model the morphology of the cell during migration. In the model, the cellular skeleton is maintained by a series of elastic springs connecting the mass center and the cell boundary. Furthermore, a morphoelasticity model is used to quantify the impact of the traction forces on the cell geometry. The model can simulate the processes like cell differentiation and cancer cell invasion. To validate the model, we managed to reproduce important experimental results in [91] to some extent, despite some uncertainties in the model. In summary, this model provides a basis that can be expanded further to simulate more microscopic observations, such that it can suggest the design of experiments.

8.5. DISCUSSIONS AND OUTLOOK

In this thesis, we firstly developed an agent-based model on skin contraction post wounding. Provided that agent-based modelling tracks the cellular events and cell positions precisely, the model is capable of visualizing the inflammation and proliferation phases regarding important elements, and quantifying the cause of the occurrence of the scar contraction. Furthermore, some important parameter values are adopted directly from clinical and experimental data, which is beneficial to develop a more empirically based model. Thanks to the flexibility of altering the parameter values, this model has the potential to be extended as a simulation tool which is patient-characterized. Furthermore, since the agent-based model treats each cell individually, various shapes of cells or even deformable cells can be accounted for; similar extension holds for a more complicated and irregular geometry of the scar.

To achieve the long-term goal of this scar contraction model as a simulation tool for a large wound, it is necessary to transit the model from two dimensions to three dimensions. From a mathematical point of view, it is not difficult to achieve that, which may be done in future research. We note that an extension to three spatial coordinates not only makes the numerical treatment of the partial differential equations more expensive, such an extension also necessitates larger numbers of cells in the agent-based models. The latter factor mostly determines the increase of computational cost.

The improvement of computational efficiency may be reached by the use of parallel computing, such as the use of the Graphical Processing Unit (using CUDA). In particular, the cell-based computations will benefit from such implementations. The implementation should be done in programming language like C++. In this research, the first steps

in the direction of a C++ implementation has been made during the supervision of an MSc-project. The resulting linear systems of algebraic equations from finite element discretization have been solved using Krylov subspace methods. Such a computational framework allows the simulation of larger, three-dimensional, domains with very many cells.

The modeling framework contains very many input parameters and stochastic processes (for cell division, cell death, cell migration etc.). Many of the input parameters have not been measured or suffer from ill documentation. Besides this inconvenience, a large number of input parameters are patient-specific, in the sense that they depend on several characteristics of the patient, such as gender, race, pigmentation, age and lifestyle. In this sense the current modeling framework is still unfeasible for use in clinical settings. In order to make this model valuable, upscaling is an important step. Upscaling, which is the translation between small and large scales can be done in two ways: (1) a functional analytic approach, in which one uses an averaging technique in combination with a rigorous treatment of the set of point force problems to arrive at a continuum-based formulation; (2) a statistical approach where one uses multiple simulations to predict what is happening on the smallest scales. The latter approach can be accomplished by the use of machine learning. Furthermore, machine learning could also be applied on larger domains so that the doctors obtain quick access to simulation results. The latter option requires a large investment in the development of a computational framework in order to have reasonable training times for the machine learning algorithms.

Next to this, the model may benefit from regression techniques (inverse modeling) in order to match the model to (clinical) experiments. For this framework, which contains a lot of uncertainty via random (cellular) processes, this will be a challenging task. *In vitro* laboratory tests could also be helpful for the validation of parts of the current model.

The work in Part II develops several alternative approaches to the Dirac Delta distributions to model the point forces exerted by the cells. Given the numerical and analytic consistency between the alternatives and the immersed boundary approach, one can choose between them since they provide comparable results if the other parameter values are kept the same. Based on the number of cells in the computational domain, guidelines for the most convenient approach are given in Part 2 of this thesis. We, however, remark that the analysis has only been done for a simple elasticity model, and not for the more complicated viscoelastic approach or the morphoelastic model that have been used as well in this thesis.

Since the cell-based model requires relatively many computational resources compared to the fully continuum-based approach, we have made the first attempts to upscaling between these modeling frameworks. The first results are based on a regularization of the Dirac Delta distribution, and the subsequent Gaussian-inspired smoothed particle approach. These first results show convergence between the finite element solutions to these approaches under mild conditions between mesh size and 'particle size'. The proof has been entirely completed for the one-dimensional case, and we suspect that an extension to higher dimensionality is possible.

The cell deformation model that is used to simulate the evolution of the cell geometry during cell migration does not yet include the Poisson effect. The reason for this is

that the current implementation only treats the cell membrane (cell boundary) by decomposition into boundary segments and boundary points. The boundary points are all connected via springs (upon neglecting inertia) to the cell center. In a more advanced setting, the boundary points are both connected to next-neighbors on the boundary and to the cell center. In fact, this makes the model more complicated since one effectively obtains a partial differential equations-like structure over the cellular outer surface. This will make the simulations more expensive, but also more realistic, so that both curvature- and Poisson effects are incorporated in a more physical manner.

REFERENCES

- [1] Q. Peng and F. Vermolen, *Agent-based modelling and parameter sensitivity analysis with a finite-element method for skin contraction*, *Biomechanics and Modeling in Mechanobiology* **19**, 2525 (2020).
- [2] S. Enoch and D. J. Leaper, *Basic science of wound healing*, *Surgery (Oxford)* **26**, 31 (2008).
- [3] B. D. Cumming, D. L. S. McElwain, and Z. Upton, *A mathematical model of wound healing and subsequent scarring*, *Journal of The Royal Society Interface* **7**, 19 (2009).
- [4] N. H. Advisor, *Wound healing process*, <http://www.newhealthadvisor.com/wound-healing-process.html> (2016), accessed: 19-07-2018.
- [5] J. Rosińczuk, J. Taradaj, R. Dymarek, and M. Sopol, *Mechanoregulation of wound healing and skin homeostasis*, *BioMed Research International* **2016**, 1 (2016).
- [6] E. Haertel, S. Werner, and M. Schäfer, *Transcriptional regulation of wound inflammation*, *Seminars in Immunology* **26**, 321 (2014).
- [7] B. Li and J. H.-C. Wang, *Fibroblasts and myofibroblasts in wound healing: Force generation and measurement*, *Journal of Tissue Viability* **20**, 108 (2011).
- [8] J. P. O’Leary, A. Tabuenca, and L. R. Capote, *The physiologic basis of surgery* (Lippincott Williams & Wilkins, 2008).
- [9] T. F. Deuel, R. M. Senior, J. S. Huang, and G. L. Griffin, *Chemotaxis of monocytes and neutrophils to platelet-derived growth factor*. *Journal of Clinical Investigation* **69**, 1046 (1982).
- [10] A. Mogilner and K. Keren, *The shape of motile cells*, *Current Biology* **19**, R762 (2009).
- [11] P. G. Robey, “*mesenchymal stem cells*”: *fact or fiction, and implications in their therapeutic use*, *F1000Research* **6**, 524 (2017).
- [12] E. L. Barnhart, K.-C. Lee, K. Keren, A. Mogilner, and J. A. Theriot, *An adhesion-dependent switch between mechanisms that determine motile cell shape*, *PLoS Biology* **9**, e1001059 (2011).
- [13] K. Keren, Z. Pincus, G. M. Allen, E. L. Barnhart, G. Marriott, A. Mogilner, and J. A. Theriot, *Mechanism of shape determination in motile cells*, *Nature* **453**, 475 (2008).

- [14] S. Massalha and D. Weihs, *Metastatic breast cancer cells adhere strongly on varying stiffness substrates, initially without adjusting their morphology*, [Biomechanics and Modeling in Mechanobiology](#) **16**, 961 (2016).
- [15] M. Saeed and D. Weihs, *Finite element analysis reveals an important role for cell morphology in response to mechanical compression*, [Biomechanics and Modeling in Mechanobiology](#) **19**, 1155 (2019).
- [16] H. Ebata, A. Yamamoto, Y. Tsuji, S. Sasaki, K. Moriyama, T. Kuboki, and S. Kidoaki, *Persistent random deformation model of cells crawling on a gel surface*, [Scientific Reports](#) **8** (2018), 10.1038/s41598-018-23540-x.
- [17] D. Koppenol, *Biomedical implications from mathematical models for the simulation of dermal wound healing*, PhD-thesis at the Delft University of Technology, the Netherlands (2017).
- [18] R. C. Wek and K. A. Staschke, *How do tumours adapt to nutrient stress?* [The EMBO Journal](#) **29**, 1946 (2010).
- [19] D. W. Siemann and M. R. Horsman, *Modulation of the tumor vasculature and oxygenation to improve therapy*, [Pharmacology & Therapeutics](#) **153**, 107 (2015).
- [20] K. Safferling, T. Sütterlin, K. Westphal, C. Ernst, K. Breuhahn, M. James, D. Jäger, N. Halama, and N. Grabe, *Wound healing revised: A novel reepithelialization mechanism revealed by in vitro and in silico models*, [The Journal of Cell Biology](#) **203**, 691 (2013).
- [21] A. J. Singer and R. A. Clark, *Cutaneous wound healing*, [New England Journal of Medicine](#) **341**, 738 (1999).
- [22] P. Friedl and D. Gilmour, *Collective cell migration in morphogenesis, regeneration and cancer*, [Nature Reviews Molecular Cell Biology](#) **10**, 445 (2009).
- [23] L. Rittié, *Cellular mechanisms of skin repair in humans and other mammals*, [Journal of Cell Communication and Signaling](#) **10**, 103 (2016).
- [24] F. J. Vermolen and E. Javierre, *A finite-element model for healing of cutaneous wounds combining contraction, angiogenesis and closure*, [Journal of Mathematical Biology](#) **65**, 967 (2011).
- [25] P. Rousselle, F. Braye, and G. Dayan, *Re-epithelialization of adult skin wounds: Cellular mechanisms and therapeutic strategies*, [Advanced Drug Delivery Reviews](#) **146**, 344 (2019).
- [26] N. Gal and D. Weihs, *Intracellular mechanics and activity of breast cancer cells correlate with metastatic potential*, [Cell Biochemistry and Biophysics](#) **63**, 199 (2012).
- [27] J. Guck, S. Schinkinger, B. Lincoln, F. Wottawah, S. Ebert, M. Romeyke, D. Lenz, H. M. Erickson, R. Ananthakrishnan, D. Mitchell, J. Käs, S. Ulvick, and C. Bilby, *Optical deformability as an inherent cell marker for testing malignant transformation and metastatic competence*, [Biophysical Journal](#) **88**, 3689 (2005).

- [28] S. E. Cross, Y.-S. Jin, J. Rao, and J. K. Gimzewski, *Nanomechanical analysis of cells from cancer patients*, *Nature Nanotechnology* **2**, 780 (2007).
- [29] V. Swaminathan, K. Mythreye, E. T. O'Brien, A. Berchuck, G. C. Blobe, and R. Superfine, *Mechanical stiffness grades metastatic potential in patient tumor cells and in cancer cell lines*, *Cancer Research* **71**, 5075 (2011).
- [30] A. M. Turing, *The chemical basis of morphogenesis*, *Philosophical Transactions of the Royal Society of London. Series B, Biological Sciences* **237**, 37 (1952).
- [31] J. T. Bonner, *On development: the biology of form*, Vol. 2 (Harvard University Press, 1974).
- [32] F. Markowetz, *All biology is computational biology*, *PLOS Biology* **15**, e2002050 (2017).
- [33] M. C. Mackey and P. K. Maini, *What has mathematics done for biology?* *Bulletin of Mathematical Biology* **77**, 735 (2015).
- [34] A. Friedman, *What is mathematical biology and how useful is it*, *Notices of the AMS* **57**, 851 (2010).
- [35] J. D. Murray, *Vignettes from the field of mathematical biology: the application of mathematics to biology and medicine*, *Interface Focus* **2**, 397 (2012).
- [36] R. T. Tranquillo and J. Murray, *Continuum model of fibroblast-driven wound contraction: Inflammation-mediation*, *Journal of Theoretical Biology* **158**, 135 (1992).
- [37] F. J. Vermolen and A. Gefen, *A phenomenological model for chemico-mechanically induced cell shape changes during migration and cell-cell contacts*, *Biomechanics and Modeling in Mechanobiology* **12**, 301 (2012).
- [38] N. Brusselaers, S. Monstrey, D. Vogelaers, E. Hoste, and S. Blot, *Severe burn injury in europe: a systematic review of the incidence, etiology, morbidity, and mortality*, *Critical Care* **14**, R188 (2010).
- [39] W. H. Organization, *Cancer*, (2018), <https://www.who.int/news-room/fact-sheets/detail/cancer>, Last accessed on 30-12-2020.
- [40] H. Dillekås, M. S. Rogers, and O. Straume, *Are 90% of deaths from cancer caused by metastases?* *Cancer Medicine* **8**, 5574 (2019).
- [41] W. Boon, D. Koppenol, and F. Vermolen, *A multi-agent cell-based model for wound contraction*, *Journal of Biomechanics* **49**, 1388 (2016).
- [42] F. J. Vermolen and A. Gefen, *A semi-stochastic cell-based formalism to model the dynamics of migration of cells in colonies*, *Biomechanics and Modeling in Mechanobiology* **11**, 183 (2011).

- [43] S. D. Talia, H. Wang, J. M. Skotheim, A. P. Rosebrock, B. Futcher, and F. R. Cross, *Daughter-specific transcription factors regulate cell size control in budding yeast*, [PLoS Biology](#) **7**, e1000221 (2009).
- [44] J. Chen, D. Weihs, and F. J. Vermolen, *A model for cell migration in non-isotropic fibrin networks with an application to pancreatic tumor islets*, [Biomechanics and Modeling in Mechanobiology](#) **17**, 367 (2017).
- [45] M. Yamao, H. Naoki, and S. Ishii, *Multi-cellular logistics of collective cell migration*, [PLoS ONE](#) **6**, e27950 (2011).
- [46] H. P. Langtangen and A. Logg, *Solving PDEs in Python: The FEniCS Tutorial I*, Vol. 1 (Springer International Publishing, 2016).
- [47] P. V. Liedekerke, A. Buttenschön, and D. Drasdo, *Off-lattice agent-based models for cell and tumor growth*, in *Numerical Methods and Advanced Simulation in Biomechanics and Biological Processes* (Elsevier, 2018) pp. 245–267.
- [48] M. Dudaie, D. Weihs, F. J. Vermolen, and A. Gefen, *Modeling migration in cell colonies in two and three dimensional substrates with varying stiffnesses*, [In Silico Cell and Tissue Science](#) **2** (2015), 10.1186/s40482-015-0005-9.
- [49] F. J. Vermolen and A. Gefen, *Semi-stochastic cell-level computational modelling of cellular forces: application to contractures in burns and cyclic loading*, [Biomechanics and Modeling in Mechanobiology](#) **14**, 1181 (2015).
- [50] J. E. Marsden and A. Tromba, *Vector calculus* (Macmillan, 2003).
- [51] L. G. Leal, *Advanced transport phenomena: fluid mechanics and convective transport processes*, Vol. 7 (Cambridge University Press, 2007).
- [52] G. Dziuk and C. M. Elliott, *Finite elements on evolving surfaces*, [IMA Journal of Numerical Analysis](#) **27**, 262 (2007).
- [53] A. Madzvamuse and U. Z. George, *The moving grid finite element method applied to cell movement and deformation*, [Finite Elements in Analysis and Design](#) **74**, 76 (2013).
- [54] Q. Peng and F. Vermolen, *Point forces and their alternatives in cell-based models for skin contraction*, Reports of the Delft Institute of Applied Mathematics, Delft University, the Netherlands **1389-6520** (2019).
- [55] J. C. Dallon, J. A. Sherratt, and P. K. Maini, *Mathematical modelling of extracellular matrix dynamics using discrete cells: Fiber orientation and tissue regeneration*, [Journal of Theoretical Biology](#) **199**, 449 (1999).
- [56] A. Gefen, *Effects of virus size and cell stiffness on forces, work, and pressures driving membrane invagination in a receptor-mediated endocytosis*, [Journal of Biomechanical Engineering](#) **132** (2010), 10.1115/1.4001888.

- [57] J. C. Dallon, J. A. Sherratt, and P. K. Maini, *Modeling the effects of transforming growth factor-beta on extracellular matrix alignment in dermal wound repair*, *Wound Repair and Regeneration* **9**, 278 (2001).
- [58] R. B. Dickinson, S. Guido, and R. T. Tranquillo, *Biased cell migration of fibroblasts exhibiting contact guidance in oriented collagen gels*, *Annals of Biomedical Engineering* **22**, 342 (1994).
- [59] A. L. F. Meister, *Generalia de genesi figurarum planarum et inde pendentibus earum affectionibus* (1769).
- [60] L. Gould, P. Abadir, H. Brem, M. Carter, T. Conner-Kerr, J. Davidson, L. DiPietro, V. Falanga, C. Fife, S. Gardner, E. Grice, J. Harmon, W. R. Hazzard, K. P. High, P. Houghton, N. Jacobson, R. S. Kirsner, E. J. Kovacs, D. Margolis, F. M. Horne, M. J. Reed, D. H. Sullivan, S. Thom, M. Tomic-Canic, J. Walston, J. A. Whitney, J. Williams, S. Zieman, and K. Schmader, *Chronic wound repair and healing in older adults: Current status and future research*, *Journal of the American Geriatrics Society* **63**, 427 (2015).
- [61] R. G. Wells, *Tissue mechanics and fibrosis*, *Biochimica et Biophysica Acta (BBA) - Molecular Basis of Disease* **1832**, 884 (2013).
- [62] D. R. Thomas, *Age-related changes in wound healing*, *Drugs & Aging* **18**, 607 (2001).
- [63] J. Larouche, S. Sheoran, K. Maruyama, and M. M. Martino, *Immune regulation of skin wound healing: Mechanisms and novel therapeutic targets*, *Advances in Wound Care* **7**, 209 (2018).
- [64] N. D. Evans, R. O. Oreffo, E. Healy, P. J. Thurner, and Y. H. Man, *Epithelial mechanobiology, skin wound healing, and the stem cell niche*, *Journal of the Mechanical Behavior of Biomedical Materials* **28**, 397 (2013).
- [65] X. Liang, V. Crecea, and S. A. Boppart, *Dynamic optical coherence elastography: A review*, *Journal of Innovative Optical Health Sciences* **03**, 221 (2010).
- [66] J. Solon, I. Levental, K. Sengupta, P. C. Georges, and P. A. Janmey, *Fibroblast adaptation and stiffness matching to soft elastic substrates*, *Biophysical Journal* **93**, 4453 (2007).
- [67] A. Wakhlu, A. C. Chowdhury, N. Mohindra, S. R. Tripathy, D. P. Misra, V. Agarwal, et al., *Assessment of extent of skin involvement in scleroderma using shear wave elastography*, *Indian Journal of Rheumatology* **12**, 194 (2017).
- [68] S. S. Shapiro and M. B. Wilk, *An analysis of variance test for normality (complete samples)*, *Biometrika* **52**, 591 (1965).
- [69] J. De la Torre and A. Sholar, *Wound healing: Chronic wounds*, (2006).
- [70] A. Goriely and D. Moulton, *Morphoelasticity: A theory of elastic growth*, in *New Trends in the Physics and Mechanics of Biological Systems* (Oxford University Press, 2011) pp. 153–176.

- [71] S. Rudraraju, D. E. Moulton, R. Chirat, A. Goriely, and K. Garikipati, *A computational framework for the morpho-elastic development of molluskan shells by surface and volume growth*, *PLOS Computational Biology* **15**, e1007213 (2019).
- [72] M. B. Amar, M. Wu, M. Trejo, and M. Atlan, *Morpho-elasticity of inflammatory fibrosis: the case of capsular contracture*, *Journal of The Royal Society Interface* **12**, 20150343 (2015).
- [73] Y. Kuwahara, Y. Shima, D. Shirayama, M. Kawai, K. Hagihara, T. Hirano, J. Arimitsu, A. Ogata, T. Tanaka, and I. Kawase, *Quantification of hardness, elasticity and viscosity of the skin of patients with systemic sclerosis using a novel sensing device (vesmeter): a proposal for a new outcome measurement procedure*, *Rheumatology* **47**, 1018 (2008).
- [74] A. Klenke, *Probability theory: a comprehensive course*, 1st ed., Universitext (Springer London, 2008).
- [75] C. O'Rourke, R. A. Drake, G. W. Cameron, A. J. Loughlin, and J. B. Phillips, *Optimising contraction and alignment of cellular collagen hydrogels to achieve reliable and consistent engineered anisotropic tissue*, *Journal of Biomaterials Applications* **30**, 599 (2015).
- [76] B. Laud, *Electromagnetics* (New Age International, 1987).
- [77] E. Weisstein, *Erf. from mathworld—a wolfram web resource*, URL: <http://mathworld.wolfram.com/Erf.html> (2010).
- [78] Q. Peng and F. Vermolen, *Point forces and their alternatives in cell-based models for skin contraction in two dimensions*, in *2020 International Conference on Mathematics and Computers in Science and Engineering (MACISE)* (IEEE, 2020).
- [79] S. Bertoluzza, A. Decoene, L. Lacouture, and S. Martin, *Local error estimates of the finite element method for an elliptic problem with a dirac source term*, *Numerical Methods for Partial Differential Equations* **34**, 97 (2018).
- [80] D. Braess, *Finite Elements: Theory, Fast Solvers, and Applications in Solid Mechanics* (Cambridge University Press, 2007).
- [81] R. Scott, *Finite element convergence for singular data*, *Numerische Mathematik* **21**, 317 (1973).
- [82] Q. Peng and F. Vermolen, *Numerical methods to solve elasticity problems with point sources*, Reports of the Delft Institute of Applied Mathematics, Delft University, the Netherlands **1389-6520** (2019).
- [83] T. M. Apostol and C. Ablow, *Mathematical analysis*, *Physics Today* **11**, 32 (1958).
- [84] K. Atkinson and W. Han, *Theoretical numerical analysis*, Vol. 39 (Springer, 2005).
- [85] L. Lacouture, *A numerical method to solve the stokes problem with a punctual force in source term*, *Comptes Rendus Mécanique* **343**, 187 (2015).

- [86] I. Olkin and J. W. Pratt, *A multivariate tchebycheff inequality*, [The Annals of Mathematical Statistics](#) **29**, 226 (1958).
- [87] F. Pukelsheim, *The three sigma rule*, [The American Statistician](#) **48**, 88 (1994).
- [88] R. Haberman, *Elementary Applied Partial Differential Equations*, Vol. 987 (Prentice Hall Englewood Cliffs, NJ, 1983).
- [89] Q. Peng, F. J. Vermolen, and D. Weihs, *A formalism for modelling traction forces and cell shape evolution during cell migration in various biomedical processes*, [Biomechanics and Modeling in Mechanobiology](#) **20** (2021), 10.1007/s10237-021-01456-2.
- [90] J. Chen, D. Weihs, M. V. Dijk, and F. J. Vermolen, *A phenomenological model for cell and nucleus deformation during cancer metastasis*, [Biomechanics and Modeling in Mechanobiology](#) **17**, 1429 (2018).
- [91] M. Mak, C. A. Reinhart-King, and D. Erickson, *Elucidating mechanical transition effects of invading cancer cells with a subnucleus-scaled microfluidic serial dimensional modulation device*, [Lab Chip](#) **13**, 340 (2013).
- [92] J. Zhao, F. Manuchehrfar, and J. Liang, *Cell–substrate mechanics guide collective cell migration through intercellular adhesion: a dynamic finite element cellular model*, [Biomechanics and Modeling in Mechanobiology](#) **19**, 1781 (2020).
- [93] E. T. Roussos, J. S. Condeelis, and A. Patsialou, *Chemotaxis in cancer*, [Nature Reviews Cancer](#) **11**, 573 (2011).
- [94] V. L. Popov, *Contact Mechanics and Friction* (Springer Berlin Heidelberg, 2010).
- [95] S. Liu, A. Peyronnel, Q. Wang, and L. Keer, *An extension of the hertz theory for 2d coated components*, [Tribology Letters](#) **18**, 505 (2005).
- [96] J. H. Tripp, *Hertzian contact in two and three dimensions*, NASA Technical Reports **NASA-TP-2473** (1985).
- [97] T. E. Angelini, A. C. Dunn, J. M. Urueña, D. J. Dickrell, D. L. Burris, and W. G. Sawyer, *Cell friction*, [Faraday Discussions](#) **156**, 31 (2012).
- [98] W. R. Trickey, F. P. Baaijens, T. A. Laursen, L. G. Alexopoulos, and F. Guilak, *Determination of the poisson's ratio of the cell: recovery properties of chondrocytes after release from complete micropipette aspiration*, [Journal of Biomechanics](#) **39**, 78 (2006).
- [99] R. Chaudhari, *Myofibroblasts: Functions, evolution, origins, and the role in disease*, [SRM Journal of Research in Dental Sciences](#) **6**, 234 (2015).
- [100] S. H. Phan, *Biology of fibroblasts and myofibroblasts*, [Proceedings of the American Thoracic Society](#) **5**, 334 (2008).

- [101] I. Hirahara, Y. Ogawa, E. Kusano, and Y. Asano, *Activation of matrix metalloproteinase-2 causes peritoneal injury during peritoneal dialysis in rats*, [Nephrology Dialysis Transplantation](#) **19**, 1732 (2004).
- [102] V. D. Desai, H. C. Hsia, and J. E. Schwarzbauer, *Reversible modulation of myofibroblast differentiation in adipose-derived mesenchymal stem cells*, [PLoS ONE](#) **9**, e86865 (2014).
- [103] C. P. McCann, P. W. Kriebel, C. A. Parent, and W. Losert, *Cell speed, persistence and information transmission during signal relay and collective migration*, [Journal of Cell Science](#) **123**, 1724 (2010).
- [104] M. Mak and D. Erickson, *A serial micropipette microfluidic device with applications to cancer cell repeated deformation studies*, [Integrative Biology](#) **5**, 1374 (2013).

ACKNOWLEDGEMENTS

Rest and be thankful.

—William Wordsworth

Since the first day of my PhD life, I have foreseen that it is going to be a relatively long acknowledgement. It is not only because of me as a talkative person, but also without those sweet, kind and adorable people, I could never make this. Sorry that it will take quite some time to finish reading this part.

Firstly, my sincere appreciations are to **Prof. dr. ir. Fred Vermolen**. We met in Shanghai and at that time, I would never have believed that this smart, nice, kind and interesting person would be my supervisor in the future. Afterwards, we still talked to each other frequently till you offered me a position. Since I arrived in the Netherlands, you have been guiding me step by step how to become a researcher, and helping me to integrate in this country better. I felt really honored and lucky that I can accomplish my PhD life under your supervision. I think you are really the person that changes my entire life, and I really appreciate how many efforts you have put in my project and also to establish my confidence. Furthermore, thanks for introducing me to your kind family: **Petra, Luca** and **Evi**, and inviting me to join you all sometimes — that may be the reason why others are saying that I am like the third child in your family.

I would like to thank **Prof. dr. ir. Kees Vuik** for providing such a nice atmosphere in the group and many supports for SIAM-SC when I was the president—I might be the one bothering you the most among all the SIAM-SC boards. Even though we did not have regular meetings, I appreciate all the suggestions and advice you gave during my progress meetings and on my thesis, in particular, regarding my future career. It is very kind and nice of you when you initialized the meeting with me discussing the possibilities of the postdoctoral position in the group. Besides, I really enjoyed our "snacks communication" during the pandemic period, and I hope my baking brings you delights.

Thank you, my committee members: **Prof. dr. Amir Zadpoor, Prof. dr. Roeland Merks, Prof. dr. Amit Gefen, Dr. Daphne Weihs, Prof. dr. ir. Geurt Jongbloed** and **Dr. Neil Budko**, for reading this thesis and providing me with kind suggestions.

I had thought that I would not have any other cooperation during PhD, until I met **Dr. Daphne Weihs**, who is a nice, smart and inspiring scientist and with whom I started a new topic in my research. I feel grateful to meet you and am appreciated with all the help on the manuscript and with writing a very nice reference letter for me. More importantly, I am grateful for your inspiring email to me after Christmas holiday in 2020. Soon after Fred's leaving, **Dr. Lisanne Rens** became one of the new owners of the office. Coincidentally, she is also working on computational biology, which makes me not the only one in this topic in DIAM again. This was also the first time I stepped out my comfort zone to look for cooperation. Thank you for showing interest in cooperating with me. Besides work, it is incredibly sweet of you that you are willing to share your own

experience in academia with me and connect me with other people who might be able to help me.

The coolest office definitely deserves enormous amount of my appreciations: **Merel, Mo, Gaby, Xiaoshan** and **Roel** (adopted 10% office mate). All of you gave me unlimited supports and care. I really enjoyed all our office events: carting, boat trip and fondue nights etc. **Mo**, you are like a big sweet brother to me and always encourages me to be confident. Especially when we went carting, you prepared all the stuff for me to prevent me getting injured. **Gaby**, thanks for all the company and warm smiles, since I became your office mate. You are the one helping me integrate into the group and know other colleagues. **Xiaoshan**, you are always so kind to others and willing to help others. Thank you for exploring various restaurants together with me and I miss our weekly hotpot very much. **Roel**, as the most rational person among us, thanks for expanding my sports list and offering yourself as a good badminton partner. I hope we still have a chance to play a tournament together at some time. More importantly, you are always there to help me solve different problems in life, as well as translating my propositions into Dutch. I still want to apologize that I failed to take good care of you when we were in China.

Our office competitive princess, **Merel**, let me experience bankrupt the first time ever (I hope that was the only time) in my life when we were travelling in China. Even though my first impression told me we might not be friends at all, we become quite close at some moment. I am glad to hear that in front of me you can completely be yourself, regardless of any emotions you have. I am so happy to have you and we carried each other's hands to walk through (perhaps the most stressful) 4 years in the life, with lots of tears and laughter, and quite a few arguments (especially during board games). Furthermore, I really appreciate your excellent work in translating my summary into Dutch.

I want to thank **Ana** and **Prajakta** for giving me company in my leisure time and giving me advice when I need to write serious emails. **Ana**, you are the only friend I met, who is neither from the group nor the badminton. I really miss the weekend we spent together, when we hunted for nice coffee and brunch. Furthermore, thank you for introducing me to **Marisa**, with whom I can not only explore nice restaurants but also play squash together. **Prajakta**, I guess you were the first one seeing me crying so badly due to the pressure from the work. Thanks for always supporting me and cooking non-spicy butter chicken for me, which is still the best I have ever had.

I still remember how clueless I was when I joined the group, and how clumsy I am (still) with computer stuff. Thank you, the best secretary **Deborah**, for giving me so much help, especially regarding SIAM-SC. In particular, you made sure I received nice gift from DIAM for Christmas of the depressive year 2020. Whenever I need help with computer or destroy the system or feel that my English is not good, I know it is time to bring a piece of cookie/cake and talk to **Kees Lemmens**. Also thank **Reinaldo** for tutoring me about python and sharing his working experience with me.

It is a luxury to have these kind supervisors in our group: **Dr. ir. Martin van Gijzen**, **Dr. Matthias Möller** and **Dr. Neil Budko**. Having a chat with any of you always inspires me and encourages me to improve myself, in particular as a researcher. As a teaching assistant, **Prof. dr. Kristof Cools** and **Dr. Deepash Toshniwal** make me realize my value, even though in the end the only thing I did is sharing my notes. I want to thank **Prof. dr. ir. Kees Oosterlee** for his kind help with SIAM-SC, and his sweet and warm smile

whenever we encounter each other. Appreciations also go to **Ingeborg** for her advice on how to advertise SIAM-SC and always being interested in my homemade cakes. Thank you **Dennis** for sharing with me all those nice TV series — it will take me quite some time to go through all of them.

It is a pleasure to be colleagues with **Baljaa, Behrouz, Menel, Thomas, Luis** and **Lisa**. I miss the time when we had lunch together, which helped me integrate in this group and really know you all rather than only face and name. Thank you, **Shuaiqiang** and **Jiao** for giving me lots of suggestions, especially on how to adapt to this country. Thanks **Linlin** for teaching me cooking new dishes and for feeding me sometimes when I was too tired or lazy to cook. I am grateful that "quantum computing" **Merel** always shows enthusiasm when I propose some events and hope you will like and enjoy your PhD in our lovely group! **Mousa**, thanks for taking the English course together with me and always being a big fan of my cooking. I want to express my gratitude to **Anne, Vandana** and **Jochen**, with whom I always had nice coffee and chat to release my stress, then realize I am not the only one suffering from the backside of doing a PhD. Furthermore, I want to thank **Hugo** and **Elisa** that took over SIAM-SC and take good care of it. Thanks to **Wilbert**, besides a PhD candidate, I got a new identity as a supervisor, which I hope I did it well. I would like to thank you for improving the computational efficiency of my wound healing model and writing the paper together with me. Later, I also cosupervised **Thomas** together with Lisanne for the Bachelor project, and we always have nice discussion on the research and all the issues during a PhD journey. Coincidentally, both **Wilbert** and **Thomas** are now teachers in the school, and I never doubt that you two can definitely be nice teachers!

Without **Otto** and **Thomas** from Computer Science department as my "IT support", I assumed that I would not have finalized my PhD smoothly in the last half year, when there was no official office for us. Thank you both for lending me the monitor and keyboard, so that I can still have a proper and decent place to work on the campus.

It is never easy to find a job in industrial or a position in academia, in particular during the COVID time and as a foreigner who cannot speak fluent Dutch in the Netherlands. I thought I would spend a relaxing year to finalize my PhD but I broke down during the journey of looking for a postdoc/industrial position. I would like to thank all the people who gave me unlimited supports and company, and listened to me crying and underestimating myself as a failure almost every day in that Chinese Spring Festival week. Without any of you, I guess I might have finalized my PhD in sorrow. In particular, I want to thank **Prof. dr. Roeland Merks** from Leiden University, who showed great interest in my work and willingness to cooperate with me. After the first time virtual meeting, you were already putting a lot of efforts in improving my CV and motivation letter. Besides, I really appreciated that you always reply me kind and long email which contains a lot of useful information regarding my research and my career. Appreciations also go to **Dr. Hermen Jan Hupkes** with offering me the postdoctoral position at Mathematical Institute at Leiden University.

Without the encouragement from **Dr József Lőrinczi, Dr Cheng Zhang, Dr Emma Eastoe, Dr Chao Zheng, Dr Qin Jiang** and **Dr Hong Xu**, I would never have thought of applying for a PhD position. Thank you all for convincing me to do a PhD.

I always know that I am not a sportive or competitive person, unless I am on a badminton court. I met a lot of badminton buddies with whom I enjoy badminton even

more: **Jie Ren, Xuan Tao, Roger Zhe Li, Xuzheng Chai, Jing Li, Kailun Yang, Zhi Hong, Meng Wang, Kevin Pun, Varun Nair, Bo Fan and Owen Clark.** Special thanks to **Jie, Chunyan** and **Xuan**, who always treat me as their younger sister, take care of me and talk to me when I am stressed out from my work.

Since the first day I arrived in the Netherlands, **Roger, Yancong, Kailun** and I have been living in the same building. I enjoy our gathering for hotpot and board games, especially when we share our worries and concerns with each other. I wish all of you have a smooth graduation soon! Thank you **Yifan Fu** for lending me your folding bike when I sold my bike since I overthought that I was not going to pass my go/no go meeting.

I will never have such a beautiful cover without the generous help from **Susana Vieira**. If one calls PhD an adventure, then having a nice printed thesis is definitely the last challenge and the most difficult one for me, because I know nothing about it and my friend cannot help me entirely in the end. Besides the humorous amount of appreciation, I would like to apologize to **Susana** as well for making you work on my cover in the weekend.

Outside the Netherlands but inside the Europe, I have two "second homes", where I always feel I am welcome and not alone. Thank you, **Xiulan** and your kind family. Only with you will I stay up late for drinking multiple types of alcohol and still stay lucid (I guess). I really enjoyed spending my birthday and Christmas with you, even though most time I was just staying with the kids, I still had a lot of fun. As a travelling-lover, **Luiz** always sends me dozens of nice and sweet postcards and tries to make me jealous. Meeting you is also one of the unexpected things in my life, which offers me the opportunity to visit Porto whenever I want.

From this paragraph, I would like to write something in Chinese to my family, teachers and friends in China. Even though we are separated by long distance and time difference, you are always there for me.

首先，多谢我的父母，不仅仅是养育之恩，更多的是给予了我自由和宽松的成长环境，以至于有时候你们甚至有些后悔给我的自由是不是太过了，因为在我成年之后，大部分时间我都不在你们身边。我很感激你们还是决定松开手里的风筝线，让我探索自己的天空，也告诉我只要我想，我随时都可以回家。这应该就是家的意义吧，不管自己成为了什么样的人，好或者不好，成功抑或是失败，自己在这茫茫世界终究是有容身之所。同时，也感谢家人们一路的陪伴和支持，我希望现在的我没有让你们担心，也没有让你们失望，尤其是爷爷和公公，希望他们在另一个世界会感到欣慰。

其次，很感谢我的老师们：**吴丽敏老师，汤琼瑶老师，赵志凌老师，冯延春老师，章雅珍老师，谢冬英老师，蔡少华 (Boss) 老师，沙建东老师和王云贵老师。**谢谢你们一直在关注着我，有时候会听着我的抱怨。除了家人之外，你们真的是看着我成长，看着我一直这么轴，然后又一直把我当女儿似的宠着。吴老师，谢谢你给我的英语打下了坚实的基础，尤其是口语，不然我想我在国外连个敲门砖都没有。Boss，如果没有你做我的数学老师，我想我可能不会选择数学专业（因为真的是太难了），我还是时常会梦见你啊，每次梦见你的时候，我都在想是不是我又不够努力或者不够快乐了，所以你会跑来看看我。沙老师，谢谢你每次都能接我的电话，听我在这头一直哭，然后说好多烂笑话哄我开心。赵老师，请允许我称呼你为我的“忘年交”，谢谢你一直喜欢我的性格，每次回去都带我去吃好吃的或者给我做饭。汤老师、冯老师，谢谢你们一直都在鼓励我。

在上海大学的三年，我很幸运遇上了很多很好很照顾我的老师：盛万成老师，侯磊老师，徐洪老师，姜勤老师，许万美老师和白岸杨老师。谢谢各位老师给我的机会和提点，给了我一个很好的平台，让我有机会能够出国交流，然后继续深造。特别感谢侯磊老师，允许我在上海期间做Fred的助教，不然我也不会有机会和他继续学习。

最后，我要感谢我的朋友们：吴楠，狄子涵，黄怡青，李凌云，贾希源。楠楠，不管我和你说什么，你都很快能理解我的感受，其实“善良”是一个很大的优点：即使你知道这个世界遍布荆棘，你仍然愿意友好相待，不是每个人都有这样的勇气和坚持。狄，和你之间我们更像是彼此操心和支持的姐妹，很多事情只要和对方说出来了，就已经少了很多的烦恼。阿青，我们认识了12年了，很多时候，我说上半句你就已经知道下半句是什么了，这个默契只有我们之间才有。凌云，谢谢你毫不犹豫地答应帮我设计封面，没有想到当时在我姐婚礼上偶然遇见的我们，之后能够成为好朋友。贾书记，我工作上最好的搭档，谢谢你让我体验了一把做伴郎的感觉，也谢谢你很多时候点醒我。

Last but not least, thanks for everyone who has ever been in my life. Every of you builds me up as a person and teaches me how to get along with this world.

Qiyao Peng (彭琪瑶)
Delft, October 2020

CURRICULUM VITÆ



Qiyao PENG

13-07-1994 **Born in Nanchang Jiangxi, China.**

EDUCATION

- 2012 - 2016** **Bachelor's Degree in Mathematics and Applied Mathematics**
Shanghai University, Shanghai, China (2012-2015)
Loughborough University, Loughborough, United Kingdom (2015-2016)
Thesis: Isospectrality and Isoperimetric Inequalities for Domain Laplacians
Supervisor: Dr. J. Lörinczi
- 2016 - 2017** **Master's Degree in Statistics**
Lancaster University, Lancaster, United Kingdom
Thesis: Extreme Values applied to Alumni Fundraising
Supervisor: Dr. J. Park
- 2017 - 2021** **PhD. in Applied Mathematics**
Delft University of Technology, Delft, The Netherlands
Thesis: Mathematical Aspects of Cell-Based and Agent-Based Modelling for Skin Contraction after Deep Tissue Injury
Promotors: Prof. dr. ir. C. Vuik and Prof. dr. ir. F. J. Vermolen

WORKING EXPERIENCE

- 2020 - 2021** **Visiting Researcher**
Hasselt University, Hasselt, Belgium
- 2022 -** **Postdoctoral Researcher**
Leiden University, Leiden, The Netherlands

PUBLICATIONS AND SCIENTIFIC ACTIVITIES

JOURNAL PAPERS

1. Q. Peng and F. J. Vermolen. *Agent-based modelling and parameter sensitivity analysis with a finite-element method for skin contraction*. Biomech Model Mechanobiol 19, 2525–2551 (2020).
2. Q. Peng, F. J. Vermolen and D. Weihs. *A Formalism for Modelling Traction forces and Cell Shape Evolution during Cell Migration in Various Biomedical Processes*. Biomech Model Mechanobiol 20, 1459–1475 (2021).
3. Q. Peng and F. J. Vermolen. *Numerical Methods to Compute Stresses and Displacements from Cellular Forces: Application to the Contraction of Tissue*. Journal of Computational and Applied Mathematics. January 2020. (Under review)
4. Q. Peng and F. J. Vermolen. *Point Forces in Elasticity Equation and Their Alternatives in Multi Dimensions*. Journal of Mathematics and Computers in Simulation. April 2021. (Under review)
5. Q. Peng and F. J. Vermolen. *Upscaling between an Agent-Based Model (Smoothed Particle Approach) and a Continuum-Based Model for Skin Contractions*. Journal of Mathematical Biology. May 2021. (Under review)
6. Q. Peng, W. S. Gorter and F. J. Vermolen. *Comparison between a Phenomenological Approach and a Morphoelasticity Approach regarding the Displacement of Extracellular Matrix*. Journal Biomechanics and Modeling in Mechanobiology. July 2021. (Under review)

PROCEEDINGS

1. Q. Peng and F. J. Vermolen. *Point Forces and Their Alternatives in Cell-Based Models for Skin Contraction in Two Dimensions*. In 2020 International Conference on Mathematics and Computers in Science and Engineering (MACISE), pp. 250-259. IEEE, 2020.
2. Q. Peng and F. J. Vermolen. *Point Forces and Their Alternatives in Cell-Based Models for Skin Contraction*. In 2019 European Numerical Mathematics and Advanced Applications Conference (ENUMATH), pp. 763-771. Springer, 2021.

3. Q. Peng and F. J. Vermolen. *Upscaling between an Agent-Based Model (Smoothed Particle Approach) and a Continuum-Based Model for Skin Contractions in One Dimension*. In 2021 VII International Conference on Particle-Based Methods (PARTICLES). 2021. (Under Review)

TECHNICAL REPORTS

1. Q. Peng, and F. J. Vermolen. *Point Forces and Their Alternatives in Cell-Based Models for Skin Contraction*. Reports of the Delft Institute of Applied Mathematics, 19-03, 2019.
2. Q. Peng, and F. J. Vermolen. *Numerical Methods to Solve Elasticity Problems with Point Sources*. Reports of the Delft Institute of Applied Mathematics, 19-02, 2019.
3. Q. Peng, and F. J. Vermolen. *Point Forces in Elasticity Equation and Their Alternatives in Multi Dimensions*. Reports of the Delft Institute of Applied Mathematics, 20-05, 2020.

ORAL PRESENTATIONS

1. *Cell-Based Model for Wound Contractions*. Annual Scientific Day of Burn Institution. Amersfoort, The Netherlands. 08 March 2019. (Invited speaker)
2. *Various Mathematical Approaches to Mechanical Simulations in Wound Healing Processes*. The Mathematics of Finite Elements and Applications (MAFELAP). London, United Kingdom. 18 - 21 June 2019.
3. *Combined Agent-Based and Finite-Element Modelling of Wound Contraction*. European Numerical Mathematics and Advanced Applications Conference (ENUMATH). Egmond aan zee, The Netherlands. 30 September - 04 October 2019.
4. *Point Forces and Their Alternatives in Cell-Based Models for Skin Contraction in Two Dimensions*. Applied Mathematics and Computers in Simulation (AMACS). Lisbon, Portugal (Online). 11 - 13 April 2020.
5. *Various Mathematical Approaches to Mechanical Simulations in Wound Healing Processes*. International Society for Porous Media Annual Meeting (INTERPORE). Qingdao, China (Online). 31 August - 03 September 2020.
6. *Cell-Based Modelling of Contraction Phenomena in Skin after Injury*. Virtual Physiological Human Conference (VPH). Paris, France (Online). 25-28 August 2020.
7. *Upscaling between an Agent-Based Model (Smoothed Particle Approach) and a Continuum-Based Model for Wound Contractions*. International Society for Porous Media Annual Meeting (INTERPORE). Online. 31 May - 04 June 2021.
8. *A Cell Shape Evolution Model for Wound Contraction and Cancer Cell Metastasis using Morphoelasticity*. Society of Mathematical Biology Annual Meeting (SMB). Online. 13 - 17 June 2021. (Invited Speaker)

9. *A Cell Shape Evolution Model for Cell Migration using Morphoelasticity*. 17th International Symposium on Computer Methods in Biomechanics and Biomedical Engineering and the 5th Conference on Imaging and Visualization (CMBBE). Bonn, Germany (Online). 07 - 09 September 2021.
10. *Various Mathematical Approaches to Mechanical Simulations in Wound Healing Processes*. VII International Conference on Particle-Based Methods (PARTICLES). Hamburg, Germany (Online). 04 - 06 October 2021.

POSTER PRESENTATIONS

1. *Agent-Based Modeling of Contractions of Burns*. Virtual Physiological Human Conference (VPH). Zaragoza, Spain. 05 - 07 September 2018.
2. *Agent-Based Modeling of Contractions of Burns*. 43rd Woudschoten Conference. Zeist, The Netherlands. 03 - 05 October 2018.
3. *Point Forces and Their Alternatives in Cell-Based Models for Skin Contraction*. Society for Industrial and Applied Mathematics (SIAM) Conference on Mathematical and Computational Issues in the Geosciences (GS). Milan, Italy (Online). 21 - 24 June 2021.

TEACHING ASSISTANT WORK

1. Mathematical Methods For Physics: Finite-Element Analysis (wi4243-III). Delft University of Technology, September 2018 - November 2019.
2. Applied Finite Elements. Mastermath. September 2018 - March 2019.

SUPERVISING WORK

1. Master project (together with Prof. dr. ir. F. J. Vermolen): *Embedding Morphoelasticity in Agent-Based Model for Wound Contraction in Burn Injuries*. W. S. Gorter, Delft University of Technology. 2020 - 2021.
2. Bachelor project (together with Dr. E. Rens): *Mathematical Modeling of Collective Cell Migration*. T. van Vroonhoven, Delft University of Technology. 2021 - 2022.

ANCILLARY WORK

1. President of SIAM-SC TU Delft, 2019-2020.
2. Organizing Annual SIAM-SC Workshop Day 2020: Non-linear Equations. Delft, The Netherlands (Online). 2020